

Experimental investigation of cavitation in a cylindrical orifice

Author:

Stanley, Cameron

Publication Date:

2012

DOI:

<https://doi.org/10.26190/unsworks/15230>

License:

<https://creativecommons.org/licenses/by-nc-nd/3.0/au/>

Link to license to see what you are allowed to do with this resource.

Downloaded from <http://hdl.handle.net/1959.4/51608> in <https://unsworks.unsw.edu.au> on 2024-04-19

Experimental Investigation of Cavitation in a Cylindrical Orifice



UNSW
THE UNIVERSITY OF NEW SOUTH WALES

Cameron Stanley

School of Mechanical and Manufacturing Engineering

University of New South Wales

A thesis submitted for the degree of

Doctor of Philosophy

2012

COPYRIGHT STATEMENT

‘I hereby grant the University of New South Wales or its agents the right to archive and to make available my thesis or dissertation in whole or part in the University libraries in all forms of media, now or here after known, subject to the provisions of the Copyright Act 1968. I retain all proprietary rights, such as patent rights. I also retain the right to use in future works (such as articles or books) all or part of this thesis or dissertation.

I also authorise University Microfilms to use the 350 word abstract of my thesis in Dissertation Abstracts International.

I have either used no substantial portions of copyright material in my thesis or I have obtained permission to use copyright material; where permission has not been granted I have applied/will apply for a partial restriction of the digital copy of my thesis or dissertation.’



Signed:

Date: February 15, 2012

AUTHENTICITY STATEMENT

‘I certify that the Library deposit digital copy is a direct equivalent of the final officially approved version of my thesis. No emendation of content has occurred and if there are any minor variations in formatting, they are the result of the conversion to digital format.’



Signed:

Date: February 15, 2012

ORIGINALITY STATEMENT

‘I hereby declare that this submission is my own work and to the best of my knowledge it contains no materials previously published or written by another person, or substantial proportions of material which have been accepted for the award of any other degree or diploma at UNSW or any other educational institution, except where due acknowledgment is made in the thesis. Any contribution made to the research by others, with whom I have worked at UNSW or elsewhere, is explicitly acknowledged in the thesis. I also declare that the intellectual content of this thesis is the product of my own work, except to the extent that assistance from others in the project’s design and conception or in style, presentation and linguistic expression is acknowledged.’



Signed:

Date: February 15, 2012

Acknowledgements

Firstly I would like to gratefully acknowledge the guidance and support of my supervisors, Associate Professors Gary Rosengarten and Tracie Barber. Throughout this testing experience they were a constant source of positivity and continually encouraged me to endure the setbacks and forge ahead. I also thank Emeritus Professor Brian Milton for his assistance during the various stages of this work.

The completion of this work would not have been possible without the assistance of the skillful workshop staff in the School of Mechanical Engineering. I would like to thank Russell Overhall, Ian Cassapi and Andy Higley for your generous technical advice and support during the fabrication of the test rig. A special thanks must go to Vince Carnevale who was always happy to discuss my design concerns and share his technical wisdom. I truly could not have completed this task without his assistance.

I would especially like to thank my comrade, cellmate and brother, Alex Sinclair. Thanks for sharing my office and tolerating me for these past years. You taught me a lot about engineering, fluid mechanics and life in general. Without you by my side I may never have made it to this point and would definitely not have had as many laughs along the way.

I must also thank my family and close friends whose patience and enduring support have been greatly appreciated. Finally I would like to thank my girlfriend Tracey Hollings for her continual encouragement and positivity.

List of Publications

1. C. Stanley, T. Barber, B. Milton and G. Rosengarten, *Periodic cavitation shedding in a cylindrical orifice*, Experiments in Fluids, DOI: 10.1007/s00348-011-1138-7, Available Online (2011)
2. C. Stanley, G. Rosengarten, T. Barber and B. Milton, *Investigation of the effects of cavitation on atomization of a high speed liquid jet*, The 5th International Students/Young Birds Seminar on Multi-scale Flow Dynamics, 4-6 November, Sendai, Japan (2009)
3. C. Stanley, G. Rosengarten, B. Milton and T. Barber, *Investigation of cavitation in a large-scale transparent nozzle*, FISITA World Automotive Congress - Student Congress, F2008-SC-001, 14-19 September, Munich, Germany (2008)

Abstract

The atomisation of liquid jets is of crucial importance to a wide range of applications including industrial processing, automotive fuel injectors and agriculture. The presence of cavitation in plain orifice atomisers is known to enhance this process; however the complex flow mechanisms that result within the nozzle remain incompletely understood. Periodic cavitation shedding has been widely observed for external cavitating flows, but has received little attention for nozzle flows.

A new cavitation research rig was designed and built to facilitate the investigation of influence of cavitation on atomisation in large-scale plain orifice nozzles. Refractive index matching with a $8.25mm$ diameter acrylic nozzle was achieved using aqueous sodium iodide as the test fluid, which allowed unabated access to the flow structures near the orifice wall. High-resolution images of the internal flow and near nozzle spray structures were recorded using high-speed visualisation. Digital processing was then used to extract cavitation cloud shedding frequencies, collapse lengths, re-entrant jet motion and spray angles across a range of Reynolds numbers from 4.8×10^4 to 2.2×10^5 . Nozzle discharge coefficient was also measured and revealed an interesting tendency for the nozzle to revert from the hydraulically flipped state to supercavitation.

Periodic shedding of cavitation clouds was found to occur for a narrow range of cavitation numbers corresponding to partial cloud cavitation. Spectral analysis of the recordings found the frequencies associated with this shedding to vary linearly with cavitation number, K , from approximately $500Hz$ at $K = 1.8$ to approximately $2500Hz$ at $K =$

2.1. Comparison of the shedding behaviour with water revealed strong agreement. The mechanism behind this periodicity appears to be the motion of the re-entrant jet, which appears to be largely driven by the adverse pressure gradient around the flow reattachment zone.

Discontinuities were observed in collapse length and spray angle corresponding to the transition from partial cloud cavitation to developed cavitation at approximately $K = 1.8$. It is believed this transition is related to the slope of the pressure gradient in the stream wise direction.

Spray angles were shown to be significantly enhanced by the presence of cavitation in the nozzle with the angle directly related to the distance of the collapse region to the nozzle exit. Peak angles occur for supercavitation where the cavitation clouds collapse directly near the exit plane of the nozzle. Further reductions in cavitation number resulted in transition to the hydraulically flipped state. Transition from hydraulic flip to supercavitation was regularly observed for cavitation numbers below $K = 1.7$. This unusual tendency contravenes typical jet behaviour and was shown to be related to the vertical inclination of the nozzle and the disturbance of the separated jet by liquid falling back down the nozzle under the action of gravity. Discharge coefficient measurements closely follow the 1D model predictions within the literature except for the region of periodic cavitation shedding. In this region the presence of cavitation had minimal effect on the nozzle discharge coefficient, with peak C_d values occurring here.

Contents

Abstract	ix
List of Figures	xv
List of Tables	xviii
Nomenclature	xix
1 Introduction	1
1.1 Background	1
1.2 Atomisation of Liquid Jets	3
1.3 Cavitation Fundamentals	5
1.3.1 Phase Change and Cavitation	5
1.3.2 Nucleation Theory	7
1.3.3 Bubble Dynamics and Collapse	8
1.3.4 Cavitating Flows	12
1.4 Thesis Outline	13
2 Literature Review	15
2.1 Early Studies on Liquid Jet Atomisation	15
2.2 The Influence of the Nozzle on Atomisation	16
2.2.1 Effects of Length to Diameter Ratio	17
2.2.2 Effects of Inlet Rounding	19
2.2.3 Ambient Conditions	21
2.3 The Effects of Cavitation on Nozzle Flow	23
2.3.1 Cavitating Flow Structures	23
2.3.2 Nozzle Turbulence and Jet Breakup	27
2.3.3 Nozzle Discharge Coefficient	30
2.3.4 Injector Specific Observations	34

2.4	Periodic Cloud Shedding	36
2.4.1	Re-entrant Jet	37
2.4.2	Shedding Frequency	40
2.5	Summary of the Literature	42
2.6	Thesis Objectives	43
3	Experimental Rig Design	44
3.1	General Description	44
3.2	Test Section	49
3.2.1	Nozzle Design	49
3.2.2	Analytical Stress Calculations	52
3.2.3	Finite Element Analysis	55
3.2.4	Hydrostatic Testing	57
3.3	Liquid Supply Piping	58
3.3.1	Flow Development	58
3.3.2	Computational Fluid Dynamics Modeling	59
3.4	Hydraulic Actuation System	61
3.5	Optical Access Pressure Vessel	65
3.6	Support Frame	69
3.7	Test Liquid Characterisation - Sodium Iodide	70
3.7.1	Refractive Index Matching	70
3.7.2	Kinematic Viscosity	73
3.7.3	Density	74
3.7.4	Vapour Pressure	75
3.8	Data Acquisition and Cylinder Control	75
4	Measurement Techniques and Experimental Uncertainty	77
4.1	Data Extraction	77
4.1.1	Non-dimensional Parameters	78
4.2	High-speed Visualisation	81
4.2.1	Illumination	81
4.2.2	Camera Lens and Region of Interest	83
4.3	Image Processing Techniques	83

4.3.1	Cavity Collapse length	85
4.3.2	Spray Angle	87
4.3.3	Signal Spectral Analysis	90
4.3.3.1	Power Spectral Density	90
4.3.3.2	Calculation Method	93
4.3.4	Measurement Limitations	95
4.4	Experimental Uncertainty	96
4.4.1	Analysis Methodology	96
4.4.2	Bias Error	97
4.4.3	Precision Error for Single Measurements	98
4.4.4	Precision Error for Multiple Measurements	98
5	Results and Discussion	101
5.1	Cavitating Flow Regimes	101
5.2	Test Parameters	104
5.3	Collapse Length	104
5.4	Partial Cavitation	110
5.4.1	Periodic Cloud Shedding	110
5.4.2	Re-entrant Jet	111
5.4.2.1	Re-entrant Jet Motion	113
5.4.2.2	Estimation of Re-entrant Jet Velocity	117
5.4.2.3	Asymmetric Cloud Shedding	121
5.4.3	Measurement of Periodic Shedding Frequencies	124
5.5	Developed Cavitation	128
5.5.1	Cavity Appearance	128
5.5.2	Transient Motion of Closure Region	129
5.5.3	Sublayer Motion	131
5.6	Nozzle Discharge Coefficient	131
5.6.1	Comparison to 1-dimensional theory	133
5.6.2	Transition from Hydraulic Flip to Supercavitation	135
5.7	Near-Nozzle Spray Structure Visualisation	137
5.7.1	Spray Surface Appearance	137
5.7.2	Measurements of Spray Angle Variation with Cavitation	139

5.7.3 Ligament and Droplet Formation	141
6 Conclusions and Recommendations	144
6.1 Key Findings	144
6.2 Recommendations for Future Work	146
A Uncertainty Analysis	148
B Instrumentation Calibration	173
C Pressure Vessel Drawings	178
D Hydraulic Equipment	189
References	192

List of Figures

1.1	Common diesel fuel injector geometry	2
1.2	Typical phase change diagrams	6
1.3	Heterogeneous nucleation formed from a crevice	8
1.4	Micro-bubble in equilibrium	9
1.5	Equilibrium of a spherical bubble	10
2.1	Sharp-edged and rounded inlet nozzle producing the same spray angle	19
2.2	Droplet size dependence on mean flow velocity	20
2.3	Breakup length stability curve	23
2.4	Plug Cavitation	25
2.5	One-dimensional cavitating nozzle flow	31
2.6	Compilation of experimental nozzle discharge coefficient	33
2.7	Schematic representation of the re-entrant jet formation	37
3.1	Experimental rig schematic	45
3.2	Overall view showing pressure vessel and support frame	47
3.3	Hydraulic and test fluid cylinder configuration	48
3.4	Acrylic test piece	51
3.5	Stress calculations cross-sectional area	53
3.6	Finite Element Analysis stress calculations	56
3.7	Nozzle supply-pipe centerline dimensions	60
3.8	Cross-section of CFD pipe mesh	61
3.9	Secondary velocity fields	62
3.10	CFD velocity profiles	63

LIST OF FIGURES

3.11	Pressure vessel	66
3.12	Pressure vessel and test section configurations	68
3.13	Experimental refractive index matching	72
3.14	NaI kinematic viscosity regression	73
3.15	NaI density as a function of solution concentration	74
3.16	NaI vapour pressure as a function of temperature	75
4.1	Pressure trace	79
4.2	Schematic of near-nozzle spray visualisation setup	82
4.3	Schematic of visualisation region of interest	84
4.4	Collapse length image processing	86
4.5	Spray images for $Re = 6.5 \times 10^4$ and $K = 1.83$	88
4.6	Spray angle definition - right side shown	89
4.7	Schematic of the signal segmentation using Welch's averaged peri- odogram	92
4.8	Schematic of interrogation spots used for cavitation frequency anal- ysis	94
5.1	Representative nozzle cavitation structures	102
5.2	Time-averaged, normalised cavitation collapse length	106
5.3	Cavitation collapse length comparison	108
5.4	Periodic cavitation shedding sequence	112
5.5	Cavitation shedding sequence showing detailed re-entrant jet motion	114
5.6	Schematic illustration of typical re-entrant jet motion	116
5.7	Re-entrant jet interface deformation image sequence	118
5.8	Re-entrant jet interface tracking	118
5.9	Ratio of re-entrant jet travelling wave velocity, V_j to mean nozzle velocity, V_n	120
5.10	Bubble motion in the re-entrant	121
5.11	Image sequence showing asymmetric motion of re-entrant jet . . .	123
5.12	Power spectral density analysis	125
5.14	Turbulent reattachment with sporadic cavitation shedding, $K =$ 1.79 , $Re = 6.9 \times 10^4$	129
5.15	Power spectral density analysis	130

LIST OF FIGURES

5.16	Nozzle discharge coefficient as a function of cavitation number . .	132
5.17	Discharge coefficient for partial cavitation	134
5.18	Pressure data showing fluctuations between hydraulic flip and supercavitation	136
5.19	Nozzle discharge coefficient comparison from early injection to late	137
5.20	Representative images of spray structure	138
5.21	Near nozzle spray angle as a function of cavitation number	140
5.22	Ligament formations sequence for partial and supercavitation . . .	142
B.1	Pressure vessel gas pressure sensor calibration	174
B.2	Injection pressure sensor calibration	174
B.3	Gas temperature thermocouple calibration	175
B.4	Liquid temperature thermocouple calibration	175
B.5	LDT piston position calibration	176
B.6	Piston velocity calibration	177
C.1	Pressure vessel - drawing sheet 1	179
C.2	Pressure vessel - drawing sheet 2	180
C.3	Pressure vessel - drawing sheet 3	181
C.4	Pressure vessel - drawing sheet 4	182
C.5	Pressure vessel - drawing sheet 5	183
C.6	Pressure vessel - drawing sheet 6	184
C.7	Pressure vessel - drawing sheet 7	185
C.8	Pressure vessel - drawing sheet 8	186
C.9	Pressure vessel - drawing sheet 9	187
C.10	Pressure vessel - drawing sheet 10	188
D.1	Hydraulic System Schematic	190
D.2	Test Fluid Cylinder End Cap	191

List of Tables

3.1	Experimental rig schematic component list	46
3.2	Nozzle Parameters	50
3.3	Material Properties of Cast Acrylic	52
3.4	Analytical nozzle stresses	55
3.5	FEA nozzle stresses	57
3.6	Pressure vessel design parameters	67
3.7	Pressure vessel assembly component list	69
3.8	Physical Properties of Aqueous Sodium Iodide	76
4.1	Measurement parameters and estimated uncertainties	100
5.1	Experimental Parameters	105
5.2	Measured re-entrant jet velocity for various conditions	119

Nomenclature

Roman Symbols

Δz	vertical height difference
\dot{m}_{act}	actual mass flow rate
\dot{m}_{th}	theoretical mass flow rate
\hat{S}_{AVPER}	averaged periodogram power spectral density estimator
\hat{S}_{PER}	periodogram power spectral density estimator
\hat{S}_W	Welch's averaged power spectral density estimator
A	nozzle cross-sectional area
C	sodium iodide concentration
C_c	contraction coefficient
C_d	discharge coefficient
C_v	velocity coefficient
D_c	test fluid cylinder bore diameter
D_n	nozzle diameter
D_p	supply pipe diameter
f	frequency

NOMENCLATURE

f_s	sampling frequency
g	gravitational constant
K	cavitation number
L	nozzle length
L/D	nozzle length to diameter ratio
L_{cav}	cavity length
L_{cav}/L	dimensionless cavity collapse length
P	static pressure
P_1	nozzle injection pressure
P_2	ambient gas pressure
P_g	partial pressure of gas
P_v	vapour pressure
P_{gO}	initial gas partial pressure
R	bubble radius
r	radial variable
r/R	nozzle inlet rounding to nozzle radius ratio
R_c	critical bubble radius
r_i	inner radius
R_O	initial bubble radius
r_o	outer radius
R_{sp}	supply pipe bend curvature radius
Re	Reynolds number

NOMENCLATURE

S	liquid surface tension
S_{XX}	power spectral density
T	Temperature
U	data window power scaling factor
V	velocity
V_c	piston velocity
V_j	re-entrant jet velocity
V_n	average nozzle velocity
V_o	LDT output voltage
V_∞	free-stream velocity
V_{liq}	liquid velocity within re-entrant jet
V_{nth}	theoretical nozzle velocity
$w(n)$	data window
We	Weber number
x	stream-wise co-ordinate
x_p	piston axial position
x_{LL}	spray angle analysis - lower left gas/liquid interface position
x_{LU}	spray angle analysis - upper left gas/liquid interface position
x_{RL}	spray angle analysis - lower right gas/liquid interface position
x_{RU}	spray angle analysis - upper right gas/liquid interface position
y_{LL}	spray angle analysis - vertical lower-limit
y_L	spray angle analysis - vertical position of lower gas/liquid interface

y_{UL}	spray angle analysis - vertical upper-limit
y_U	spray angle analysis - vertical position of upper gas/liquid interface

Greek Symbols

μ	dynamic viscosity
ν	kinematic viscosity
ν_p	Poisson's ratio
ρ	density
σ	traditional cavitation number
σ_a	axial stress
σ_h	hoop stress
σ_r	radial stress
σ_y	tensile yield strength
θ	spray angle
θ_L	left-side spray angle
θ_R	right-side spray angle

Acronyms

<i>ANSI</i>	American National Standards Institute
<i>CFD</i>	Computational Fluid Dynamics
<i>CI</i>	Compression Ignition
<i>CMOS</i>	Complementary MetalOxideSemiconductor
<i>CR</i>	Contraction Ratio
<i>DTFT</i>	Discrete-Time Fourier Transform

NOMENCLATURE

<i>FEA</i>	Finite Element Analysis
<i>fps</i>	Frames Per Second
<i>FSO</i>	Full Scale Output
<i>LDA</i>	Laser Doppler Anemometry
<i>LDT</i>	Linear Displacement Transducer
<i>LDV</i>	Laser Doppler Velocimetry
<i>PIV</i>	Particle Image Velocimetry
<i>PMMA</i>	Polymethyl Methacrylate - “Acrylic”
<i>PSD</i>	Power Spectral Density
<i>R – P</i>	Rayleigh-Plesset Equation
<i>ROI</i>	Region Of Interest
<i>TKE</i>	Turbulent Kinetic Energy
<i>VCO</i>	Valve Covered Orifice
<i>VOF</i>	Volume Of Fluid

Chapter 1

Introduction

1.1 Background

The atomisation of liquid jets is of central importance to a wide range of applications including industrial processing, automotive fuel injectors and agriculture. In essence, the process of atomisation involves the conversion of a liquid jet or sheet into a dispersed spray of small droplets within a gaseous environment (Lefebvre (1989)). The physical devices used to produce these sprays are generally termed *atomisers* or *nozzles*. Regardless of the method of atomisation, there are a number of key elements which influence the process, such as the hydraulics of the internal nozzle flow, the generation of liquid turbulence and the aerodynamic interaction of the jet with the gaseous medium. Each of these factors, together with the physical properties of the liquid and gas, has a marked influence on determining the shape and distribution of the final spray.

Combustion engines are heavily reliant on the effective atomisation of liquid fuels by the injector nozzle to produce a distribution of small droplets within the combustion chamber. The creation of small droplets of liquid fuel dramatically increases the surface area of the fuel, which promotes mixing and evaporation. This process is particularly important for diesel engines where fuel injection is the most important parameter affecting engine performance. In fact, the combustion efficiency and emission products of compression ignition (CI) engines are widely known to depend strongly upon the effectiveness of this process (Giffen & Muraszew (1953)).

Plain-orifice atomisers are a type of pressure atomiser which utilise a cylindrical contraction to increase the liquid velocity and generate jet breakup. The design of a typical diesel fuel injector incorporates multiple plain-orifice style nozzles due primarily to their simplicity, durability and relative ease of manufacture. A schematic showing basic diesel injector nozzle geometries can be seen in figure 1.1.

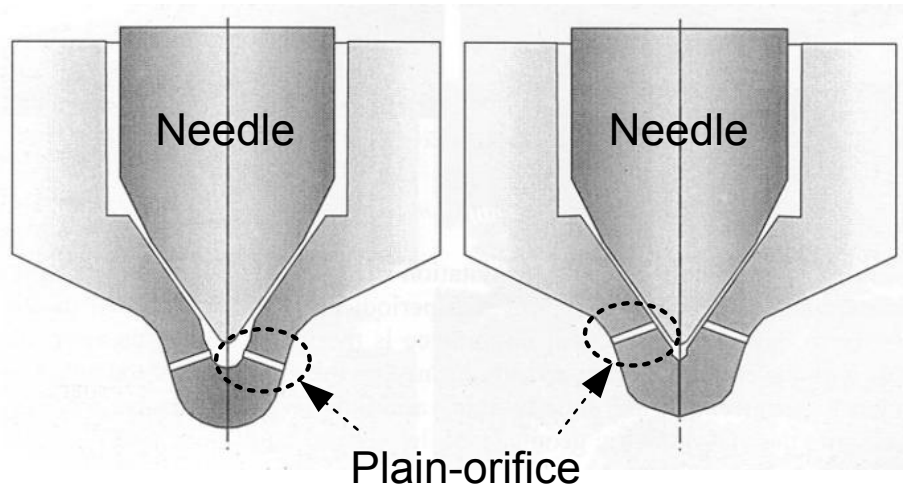


Figure 1.1: Common diesel fuel injector geometry for a mini-sac injector (left) and VCO injector (right). Both styles use a plain-orifice to atomise the liquid fuel. Image is modified from [Bae *et al.* \(2002\)](#).

The high velocities generated by the contraction cause a reduction of the static pressure within the nozzle and can subsequently result in cavitation. The presence of cavitation in the nozzle has been shown to have dramatic influence on the atomisation. Turbulence generated by the collapse of cavitation bubbles increases the disruption of the surface of the jet and helps overcome the consolidating force of surface tension. While this is advantageous to the atomisation process the cavitation collapse can also be highly destructive and may result in material degradation or ultimately failure of the injector.

The progressive introduction of increasingly stringent emissions standards for automobiles has reinforced the importance of improving the atomisation process

for diesel fuel injectors. Enhancements to current injector designs are underpinned by a need to further our understanding of the fundamental physics affecting the atomisation process. Owing to the complexity of the fluid mechanics involved, the exact mechanisms for the improvements to atomisation due to cavitation are not fully understood. However, experimental studies on real-sized fuel injector nozzle are very difficult due to the high velocities, high pressures and small physical scales. To overcome some of these limitations large scale replica nozzles are commonly used which significantly enhances the ability to conduct experimental investigations. Scaling the effects of cavitation between the large-scale replica nozzles and the real scale cannot be truly achieved due to the fundamental timescales associated with the bubble behaviour. Despite this obvious constraint large scale nozzle experiments have demonstrated very similar flow structures to small cavitating nozzles and offer dramatic improvements to the optical resolution of the cavitation phenomena. Complementary to the direct improvements to the understanding of the fundamental physics, experimental data obtained in large-scale orifice studies can also be valuable for the development and validation of cavitation models (Gavaises *et al.* (2009)). Regardless of efforts to downsize engines size and moves towards electric vehicles the social and economic inertia to change look certain to ensure diesel engines remain as a widespread transportation power supply for the foreseeable future. Irrespective of the alternatives, it is pertinent to continue efforts to improve the combustion efficiency and fuel economy of diesel engines.

1.2 Atomisation of Liquid Jets

Despite the importance and wide ranging applications of atomisation, a universal definition is rather elusive. Generally speaking the process involves the breakdown of a cohesive liquid jet into much smaller droplets. In fact the root word *atom* is perhaps a little misleading, as the dimensional scale of the droplets produced are many orders of magnitude larger. However, the connotation implies the desired outcome is a dispersion of very small droplets of the liquid phase in a continuous gaseous medium. Sprays can be produced in a variety of ways and essentially all that is required to achieve this breakdown is a high relative velocity between the

liquid and the surrounding gas. There are a number of different styles of atomiser which can achieve this aim including plain orifice, swirl, pintle and air blast. Each of these have certain capabilities and limitations which lend themselves to particular applications. Plain orifice atomisers, of interest to this work, are perhaps the most basic of all atomisers. They utilise a reduction of flow area to generate high liquid velocities. Typically the smaller the orifice the higher the liquid velocity the finer the droplet size produced.

In the study of atomising nozzles, atomisation is generally regarded as the condition whereby a liquid jet is broken up into droplets directly upon exiting the nozzle. In general the breakup of a liquid jet requires interaction with the gaseous medium, and so occurs over a finite length. A distance referred to as the *breakup length* is used to describe the stream-wise penetration of the spray from the nozzle exit until the jet is regarded as “atomised”. Generally this refers to the point where the solid liquid core has been broken into an array of smaller droplets by the interaction of aerodynamic shear forces. It is often difficult to establish this location, and often the technique used is highly dependent on the experimental conditions. The break-up length of a fuel spray in a high speed small direct injection diesel engine may be of the order of the distance between the injector and the combustion chamber wall. For this reason, the break-up length has a very important role in the spatial distribution of liquid fuel and also on the air-fuel ratio (Hiroyasu (1991)).

The mechanism by which the jet is physically broken into droplets is extremely complex and highly dependent on the liquid properties and flow conditions. Typically, for high velocity turbulent jet atomisation, perturbations are produced on the surface of the jet by turbulence, inertial effects or velocity profile relaxation. Once formed these perturbations are acted upon by aerodynamic shear forces and amplified. Eventually the disruptions to the surface structure protrude out laterally and get disintegrated into droplets by surface tension, in a process referred to as *primary* atomisation. For low enough relative velocities the cohesive force of viscosity allows the initial perturbations to form extended “finger-like” columns of liquid, known as *ligaments*. These ligaments, and any large droplets formed during the primary atomisation continue to be broken up due to the deforma-

tion of the droplet resulting from aerodynamic interaction, which is referred to as *secondary* atomisation.

The improvements to the atomisation process due to cavitation is generally attributed to the increased levels of turbulence created by the explosive growth and collapse of cavitation bubbles within the orifice. Increased turbulence strengthens the lateral velocity fluctuations and tends to increase the size of the surface perturbations, which promotes aerodynamic interaction. Experiments have shown the enhancements to atomisation improve as the proximity of the cavitation collapse region nears the nozzle. However, the collapse of bubbles, particularly in highly turbulent flow fields, is extremely complex. As such the exact mechanism linking the bubble collapse with the improvements of atomisation are not well understood. Particularly, characterising the influence of complex cavitating flow structures, such as periodic cavitation, have received little attention.

1.3 Cavitation Fundamentals

In simple terms, cavitation describes the change of phase from liquid to gas due to the reduction of pressure. At a low enough pressure, the originally homogeneous liquid medium will rupture and produce vapour, which can occur for cases where the liquid is both static and in motion. The type of cavitation of relevance to this thesis is known as *hydrodynamic* cavitation, which relates to cavitation occurring in flowing liquids.

The following sections provide a brief introduction to some of the fundamentals of the cavitation phenomenon. It is in no way exhaustive, but rather is intended as a refresher to some of the basic theory required to understand the physics of the cavitating flows described in this thesis. For comprehensive reviews of cavitation the reader can refer to [Knapp *et al.* \(1970\)](#), [Brennen \(1995\)](#) or [Franc & Michel \(2004\)](#).

1.3.1 Phase Change and Cavitation

Generally in considering the change of phase from liquid to gas, reference is made to a typical phase diagram, as shown in figure [1.2](#). For pure substances such

as water, the triple point is separated from the critical point by the saturated liquid/vapour line. Crossing this line represents a change of phase between liquid and gas. The process of cavitation and boiling are shown to demonstrate two such processes and illustrate the fundamental differences between the two. Boiling is the process of vapour formation due to the addition of heat at approximately constant pressure whereas cavitation is the formation of vapour due to the reduction of pressure at approximately constant temperature. In the case of hydrodynamic cavitation the reduction of pressure required for the phase change is due to localised high velocities caused, for example, by geometric constrictions.

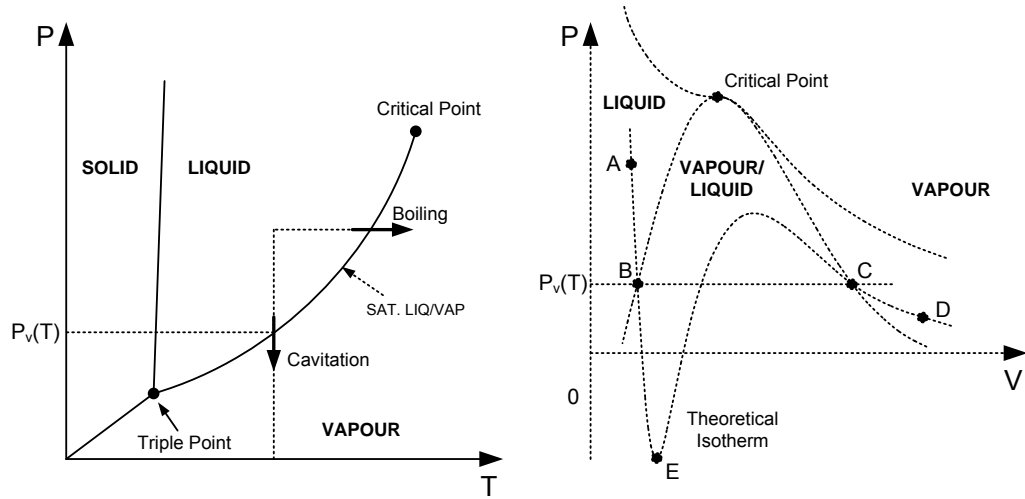


Figure 1.2: Typical phase change diagrams

Generally the transformation from liquid to vapour phase is thought to occur at the vapour pressure of the liquid, $P_v(T)$. This process is illustrated as the horizontal passage from point B to point C in the P - V diagram on the right of figure 1.2. In most practical situations and in the presence of sufficient bubble nucleation sites this is the case. However, other isotherms between the liquid and vapour state are possible. In the absence of nucleation sites a liquid may transition to vapour through “metastable” points, withstanding pressures below the vapour pressure without rupture. In fact, it is possible for the pressure to fall below absolute zero, at which point the liquid is under tension. Point E along the

theoretical isotherm shown represents a state of dynamic equilibrium whereby the liquid is experiencing tension. The presence of any localised impurities will lead to rupture and a transition to state D . Estimates derived from van der Waals equation of state indicate pure liquids are capable of withstanding tensions of around 500 atmospheres at room temperature. These enormous values have never been achieved experimentally, as invariably liquids contain local weaknesses which allow the fluid to rupture well before these limits are reached. These weaknesses are referred to as nucleation points.

1.3.2 Nucleation Theory

Nucleation is generally classified as either *homogeneous* or *heterogeneous*. Homogeneous nucleation is the generation of momentary microscopic voids in the bulk of the fluid due to thermal motion. It produces widespread and uniform vapour production. Alternatively, heterogeneous nucleation describes the formation of localised weakness within the flow which lead to liquid rupture. There are a number of sources of heterogeneous nucleation including “free-stream” nuclei created either by micro-bubbles of dissolved gases or microscopic contaminant particles, and “surface nuclei” which consist of gas caught in microscopic crevices of the boundary walls or guiding body which are not completely filled by the liquid. Typically, conical crevices such as shown in figure 1.3 are considered to exemplify the surface nucleation points created from such roughness topology (Brennen (1995)). As liquid pressure in the vicinity of these nucleation sites is reduced, the cavity expands allowing the generation and release of vapour bubbles into the bulk of the liquid.

Nuclei can also be produced by cavitation itself, particularly in the cloud cavitation regime. Each of these nucleation sites provide specific locations where the fluid can rupture when the pressure is reduced to the vapour pressure. In most practical engineering environments, heterogeneous nucleation will predominate.

Different levels of nucleation can significantly alter the observed cavitation structures. Observations of cavitation inception are particularly sensitive to the variations in the nucleation population, which have been shown to be the origin of discrepancies when tests on similar bodies were made at different facilities (Franc

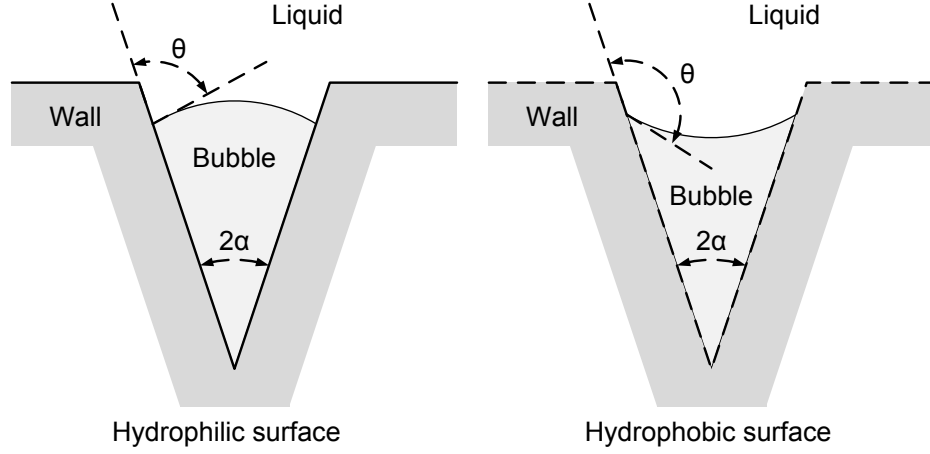


Figure 1.3: Heterogeneous nucleation formed from a crevice

& Michel (2004)). Quantification of the free-stream nuclei population within a liquid body is rather difficult, but a distribution of the nuclei number density can be measured with acoustic and optical techniques. Perhaps the most reliable methods for quantification of the nuclei present involves taking a holograph of the liquid and reconstructing the field to inspect the nuclei. A summary of the numerous methods employed at different research facilities was presented by Billet (1985). In general surface nuclei cannot be measured, but can be controlled to some degree by careful attention to the surface finish of the device.

1.3.3 Bubble Dynamics and Collapse

Interesting observations on the growth and stability of cavitation bubbles can be gained from considering the behaviour of an isolated spherical bubble in equilibrium with the surrounding liquid, shown in figure 1.4. The complete analysis will not be repeated here for brevity. For practical situations the bubble can be expected to contain both liquid vapour and dissolved gas. In this case a force balance yields;

$$P = P_g + P_v - \frac{2S}{R} \quad (1.1)$$

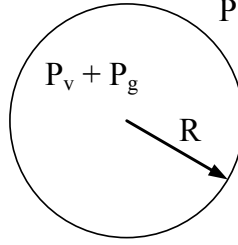


Figure 1.4: Micro-bubble in equilibrium

where R is the bubble radius, P_v is the vapour pressure, P_g is the partial pressure of the gas and S is the surface tension. If we now consider the action of such a bubble as it experiences an isothermal change in the external pressure field, ignoring gas diffusion and assuming the surface remains spherical. It is possible to re-write the equation 1.1 in terms of initial conditions so that the effects of changes in the pressure field can be predicted for different nuclei. For isothermal pressure variations the gas pressure within the nuclei is proportional to the volume, yielding the following expression;

$$P = P_{g0} \left[\frac{R_0}{R} \right]^3 + P_v - \frac{2S}{R} \quad (1.2)$$

where the subscript 0 refers to initial conditions for both the nuclei radius and gas pressure. There are two counteracting forces at play on the bubble; the internal pressure force tending to increase the bubble size, and the surface restoring surface tension force. Differentiating equation 1.2 yields the minimum or critical bubble radius, R_c , for the given initial conditions. Figure 1.5 is a plot showing a number of these equilibrium curves. As the pressure is reduced the bubble will expand. Provided the expansion produces a bubble radius less than the critical size, then the balance of forces will return the nuclei to its initial size. In other words, the mechanical equilibrium for the bubble on the branch of the curve to the left of the critical radius is stable. For pressure reductions beyond the critical pressure, the bubble is no longer stable and will grow explosively.

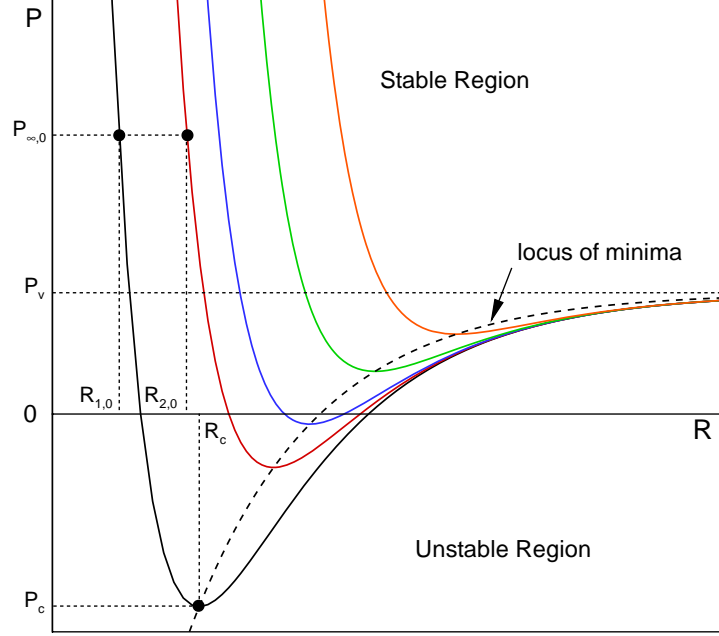


Figure 1.5: Equilibrium of a spherical bubble

The pressure difference between the vapour pressure and critical pressure is known as the static delay of cavitation. Importantly, the static delay is always positive and gets larger for smaller nuclei. However this analysis is highly simplified and provides a representational understanding of the influences of pressure reduction on the nuclei present in the liquid. Real fluids will contain a distribution of nuclei sizes. When subjected to low pressure some of these nuclei will be sufficiently small that they remain passive. Others may be large enough that the pressure will initiate violent expansion.

The applicability of this simplified quasi-static analysis is limited to situations where the time spent in the low-pressure region is long compared to the collapse time of the bubble. For longer time periods diffusion of dissolved gases can affect the growth. For shorter growth cycles inertial and viscous effects can become influential.

The dynamic response of spherical nuclei is somewhat more complex. The most common equation of motion is the *Rayleigh-Plesset* (R-P) equation;

$$\rho \left[R\ddot{R} + \frac{3}{2}\dot{R}^2 \right] = P_v - P_\infty(t) + P_{g0} \left[\frac{R_0}{R} \right]^3 - \frac{2S}{R} - 4\mu \frac{\dot{R}}{R} \quad (1.3)$$

In its earliest form the equation, derived by [Rayleigh \(1917\)](#), described the collapse of spherical bubbles modelled as voids in an infinite homogeneous incompressible liquid field. His work was later continued by [Plesset \(1949\)](#) to account for surface tension and vapour pressure within the bubble, which eliminated the infinite velocities of bubble collapse predicted by Rayleigh's model. The effects of contaminant gases on the bubble dynamics were later added. It is common for only the linear term in the full R-P equation to be used for increased numerical stability.

A detailed analysis of the bubble motion described by the R-P equation is beyond the scope of this work, although a few important points are worthy of noting. The non-linear nature of equation 1.3 alludes to the complexity of the bubble motion it describes. Attempts to numerically model the motion often make simplifying assumptions which ignore certain influences such as viscosity or surface tension. In doing so, they modify the true behaviour of the bubble. However, they do exhibit the main features of bubble growth and collapse, some of which can be summarised as follows:

- Bubble growth is fairly smooth, with the maximum bubble size occurring after the region of lowest pressure. Bubble collapse is catastrophic occurring over very short periods of time.
- During collapse the interface accelerates as the radius of the bubble reduces reaching extremely high collapse velocities which can exceed $1000m/s$. Successive rebound and collapse cycles occur, which are dissipated by viscosity. The actual growth and collapse of nuclei in cavitating devices is complicated further by turbulence and non-uniform pressure fields.
- An imbalance in the forces acting on the surface of bubbles can create asymmetric collapse. This promotes the formation of a liquid jet which is accelerated by the collapse and can impact the back of the bubble with

extremely high velocity. The impact of this water jet can cause significant damage when the asymmetric collapse occurs in the proximity of a surface.

1.3.4 Cavitating Flows

There are a number of different types of cavitating flow structures that form in hydrodynamics. Cavitating flows are almost invariably complex and varied but can be broadly classified based on the overall appearance and effects on the flow of the cavitation structures.

Bubble Cavitation - describes the formation and collapse of discrete vapour bubbles within low pressure regions of the flow. It is perhaps the simplest form of cavitation and is highly dependent on the nuclei size and distribution within the fluid, or the entrainment of nuclei from solid surfaces. Bubble collapse is characterised as being violent, noisy and can be highly destructive.

Sheet/Attached Cavitation - refers to cavitation structures which form at fixed locations, typically due to the low pressure regions created by the dynamic flow interaction with a solid body or obstacle. Often the cavitation structures occupy a flow recirculation zone and form large coherent cavities, the surface appearance of which is dependent on the upstream boundary layer flow. The cavity closure region is highly complex and large scale instabilities can result.

Partial Cavitation - is a type of sheet cavitation for which the cavity closure occurs on or within the body to which it is attached.

Supercavitation - is also a type of sheet cavitation. In studies of cavitation on hydrofoils, supercavitation refers to the situation where cavity closure occurs downstream from the trailing edge. Specifically, for cavitation in orifices, supercavitation refers to the condition where cavity closure occurs at or just past the exit plane of the orifice/nozzle.

Cloud Cavitation - is a form of partial cavitation which occurs when instabilities result in large-scale shedding of clusters of bubbles which appear as “clouds”. The coherent collapse of these structures can produce localised shock waves within the liquid. Following the collapse small bubbles of non-condensable gases remain, providing a source of nuclei for further cavitation events.

The propensity for the occurrence of cavitation within a liquid is described by a non-dimensional parameter called the cavitation number. In traditional cavitation studies it is defined as;

$$\sigma = \frac{P_{\infty} - P_v}{\frac{1}{2}\rho V_{\infty}^2} \quad (1.4)$$

and it relates the static pressure tending to suppress cavitation, to the dynamic pressure tending to promote it. However, there have been a number of alternative cavitation numbers proposed and used extensively in the study of cavitation orifices. Generally they are expressed in terms of the static pressures as they are easy to measure. The cavitation number used in this work is that used by Nurick (1976) which is defined as;

$$K = \frac{P_1 - P_v}{P_1 - P_2}. \quad (1.5)$$

where P_1 is the injection pressure and P_2 is the ambient gas pressure. As the cavitation number is reduced the flow conditions become more conducive to cavitation. It can be easily observed that this tendency is produced by increases in injection pressure, P_1 , or a decrease in the ambient gas pressure, P_2 . Conversely, reductions in injection pressure or increases in back pressure suppress the tendency for a nozzle to cavitate and result in increases in the cavitation number.

1.4 Thesis Outline

This thesis aims to provide a fundamental study of the effects of cavitation on orifice flow. It is a step back from the geometric specific applications of plain orifice atomisers such as diesel injectors but it serves to improve the understanding of the flow physics at play. As will be seen in Chapter 2, a substantial portion of the literature concerning cavitation in orifices is motivated by applications to fuel injector nozzles. However, the applications for cavitation orifices are more widespread. The aim of this research, while being motivated by diesel injector flows, is to carry out a fundamental investigation of the influence of cavitation on orifice flows.

The outline of this thesis is as follows. Chapter 2 provides a thorough review of the literature relating to cavitation in orifices. Attention is given to demonstrating the application of such flows to the atomisation of liquid jets. Chapter 3 provides a thorough description of the design and development of the experimental rig used for this study. As the design was complex and incorporated significant engineering considerations it will be discussed in detail. This study also uses a refractive index matching technique to improve the fidelity of the results. The characterisation of the fluid used for this will also be covered in this chapter. Chapter 4 describes the measurement and analysis techniques employed in this study. It also discusses the sources of measurement uncertainty within the work. Chapter 5 presents the results obtained in the study. A number of fundamental aspects of cavitation within an orifice are explored in detail. Finally Chapter 6 provides some conclusions obtained from the study and identifies possible future work. A comprehensive breakdown of the error analysis is presented in Appendix A, providing details of the elemental sources of error for the measurement of experimental parameters. Calibration curves for relevant measurements devices is then presented in Appendix B. Appendix C presents the engineering drawings of an optical access pressure vessel designed as part of this study. Appendix D presents schematics of the hydraulic circuitry presented in Chapter 3.

Chapter 2

Literature Review

2.1 Early Studies on Liquid Jet Atomisation

The breakup of liquid jets is crucial to a wide range of applications and has been a topic of research since the late nineteenth century. Early work by Plateau (1945) demonstrated the breakup of a cylindrical liquid column under the action of surface tension forces once its length exceeded its perimeter. Rayleigh (1917) used linear stability analysis to demonstrate that infinitesimal surface perturbations could rapidly grow and breakup low velocity inviscid liquid jets. Weber (1931) extended the work of Rayleigh to include viscosity and aerodynamic interaction. However, significant work on the breakup of high speed jets, which is relevant to the work of this thesis, did not begin in earnest until the 1920's and 1930's. Driven mainly by a need to increase the efficiency of solid¹ fuel injection systems for compression ignition (CI) engines, significant amounts of research were conducted in both Germany and the United States. This early research focused mainly on experimentally investigating the influence of fuel injection parameters such as injection pressure (Lee (1933), Kuehn (1925)), nozzle geometry (Lee (1933), Gelalles (1930)), chamber pressure (Lee (1933), Lee & Spencer (1934), Castleman (1932), Miller & Beardsley (1926)), discharge coefficient (Gelalles (1932)) and

¹Solid Injection refers to fuel injection incorporating a pump to deliver fuel to a nozzle in which the fuel is atomised as it enters the combustion chamber. The technology represented a fundamental improvement from the earlier “air-blast” style injection systems that used compressed air to aid in the atomisation of fuel.

2.2 The Influence of the Nozzle on Atomisation

fuel spray distribution (Kuehn (1925), Lee & Spencer (1934), Haenlein (1932)). Given the state of the injection equipment and measuring techniques available at the time, these experiments were often conducted at pressures and velocities that are far below those used in modern fuel injectors. Despite this, important observations and experimentally verified trends were established and paved the way for the research to come.

Castleman (1932) suggested that the mechanism behind the atomisation of fuel jets such as those produced in solid injection CI engines was due to the interaction of the liquid jet and the gas. Drawing on the analysis of Rayleigh, Castleman suggested that ligaments were formed on the jet surface due to shear forces and then collapse to form liquid droplets under the action of surface tension forces. Experimental observations by Kuehn (1925), that showed an “intact” length of jet was always present, were suggested to support his theory that the atomisation had to be related to the aerodynamic interaction of the jet and the gas.

Castleman’s aerodynamic interaction theory gained support when Taylor (1963) later developed a theory relating to the development of small capillary waves at the interface between a viscous liquid and an inviscid gas. He demonstrated that the density of the ambient gas had a profound effect on the breakup of the jet. Taylor showed that the diameter of the droplets forming at the liquid-gas interface from this break-up process might be expected to be comparable to the wavelength of the surface wave, and very much smaller than the jet diameter. This type of atomisation leads to very fine spray formation and is referred to as the Taylor mode of jet breakup (Reitz & Bracco (1982)).

2.2 The Influence of the Nozzle on Atomisation

The theory that aerodynamic interaction alone was responsible for the atomisation of liquid jets was not entirely supported by Castleman’s contemporaries. In fact it received criticism from some who reasoned that this aerodynamic mechanism requires a finite time to develop and therefore a length of intact jet should be observable near the exit of the nozzle.

2.2 The Influence of the Nozzle on Atomisation

In contrast to the findings of Kuehn, DeJuhasz (1931) observed that the liquid emerging from the nozzles in his experiments was in an atomised state, and reasoned therefore that the atomisation process was occurring due to the influence of internal nozzle effects. He suggested that the liquid turbulence levels played an important role in the atomisation process. This belief was supported in part by Schweitzer (1937) who argued that although turbulence wasn't the sole mechanism behind atomisation the radial velocity components of the turbulent jets had a strong influence on the breakup process. Schweitzer suggested that although aerodynamic effects were present, liquid turbulence levels acted to accelerate the disintegration of the jets. Under otherwise identical conditions, long smooth walled orifices were shown to increase breakup length, while short rough walled orifices reduced it.

Drawing upon the work of Taylor, the first attempt to directly link the internal nozzle characteristics to the observed atomisation trends was made by Ranz (1958). Conducting experiments on orifice flows discharging immiscible fluids into water Ranz proposed that the lateral velocity of the droplet was proportional to the initial lateral velocity of the infinitesimal surface wave disturbance which had created it. Using this approach Ranz suggested a correlation for the jet spray angle that incorporated an empirical constant which had to be varied for different nozzle geometries. Despite the observed trends Ranz was unable to establish a meaningful correlation between the spray angle and the nozzle.

Reitz & Bracco (1982) later compared their measured divergence angles to those predicted by Ranz and Taylor's theory and confirmed the need to vary the empirical constant to achieve agreement. It was suggested this implied there were additional phenomena, beyond the aerodynamic interaction between the liquid and gas flows, which must be present. This verified conclusively that the internal nozzle effects were indeed influencing the jet atomisation process.

2.2.1 Effects of Length to Diameter Ratio

One important geometric parameter that has received considerable attention was the influence of the nozzle length to diameter ratio, L/D , on both the breakup length and spray divergence angle. Reitz & Bracco (1982) found that increasing

2.2 The Influence of the Nozzle on Atomisation

the nozzle L/D ratios from 0.5 to 85 resulted in trends of decreasing spray divergence angle independently of liquid viscosity or gas density changes. Similar trends were often observed, however unlike the monotonic decrease in spray angle with increasing L/D observed by Reitz and Bracco, often a peak was observed in the relationship. Wu *et al.* (1983) varied L/D ratios from 1 to 50 and found a peak in spray angle for an L/D value of 10, and beyond a value of 20 their data showed a steady decrease in spray angle with increasing L/D . These trends were very closely echoed by Hiroyasu *et al.* (1982) and Arai *et al.* (1984) who found peaks in spray angle at L/D ratios of 20 and 4 respectively. Conversely to these trends, the breakup length was shown to have a minimum value which generally corresponded to the L/D ratio for maximum jet divergence. As with the spray angle, increasing the L/D beyond or below this optimal value resulted in longer breakup lengths.

Attempts have been made to explain these variations in breakup length with L/D ratio by considering the stability of the nozzle velocity profile (Hiroyasu *et al.* (1982), Reitz & Bracco (1982)). For short L/D ratios the flow is still expanding from the contraction at the nozzle inlet and is rather uniform. For large L/D ratios the flow is approaching a fully developed velocity profile which is either turbulent or laminar dependent on the liquid properties and injection conditions. For intermediate L/D ratios the flow has expanded after the vena contracta and is in a highly unstable reattachment zone. McCarthy & Molloy (1974) conducted an extensive review of the stability of liquid jets and suggested the L/D ratio has an influence on the spray structure up until the shear stress and pressure gradients are established. It was believed that once the jet emerges from the nozzle, losing the constraint of the boundary, lateral components in the liquid flow cause the jet to expand past the original surface. These surface disturbances are then acted upon by aerodynamic shear forces. Despite contributing to the breakup, velocity profile relaxation, irrespective of whether the jet is laminar or turbulent, was ruled out as being the sole mechanism behind atomisation by Reitz & Bracco (1982).

2.2.2 Effects of Inlet Rounding

The effects of nozzle inlet rounding on jet atomisation was also extensively investigated (Reitz & Bracco (1982), Kent & Brown (1982), Ohn *et al.* (1991a), Dodge *et al.* (1992), Karasawa *et al.* (1992), Marcer & Legouez (2001)) and was shown to introduce a stability to the flow in a similar fashion to increasing the L/D ratio. Rounding on the entrance of the orifice increases the tendency for the fluid to remain attached and avoid forming a vena contracta. As well as improving the discharge coefficient, the added stability in the velocity profile had the effect of lowering the jet divergence angle and increasing the breakup length. Reitz & Bracco (1982) demonstrated this influence by directly comparing the spray produced by a sharp edged nozzle (III) with an L/D ratio of 10.1 and a rounded inlet nozzle (XII) with an L/D ratio of 2.1 (see figure 2.1). Both nozzles were shown to produce a jet with the same divergence angle indicating the significant stabilising influence of the inlet rounding.

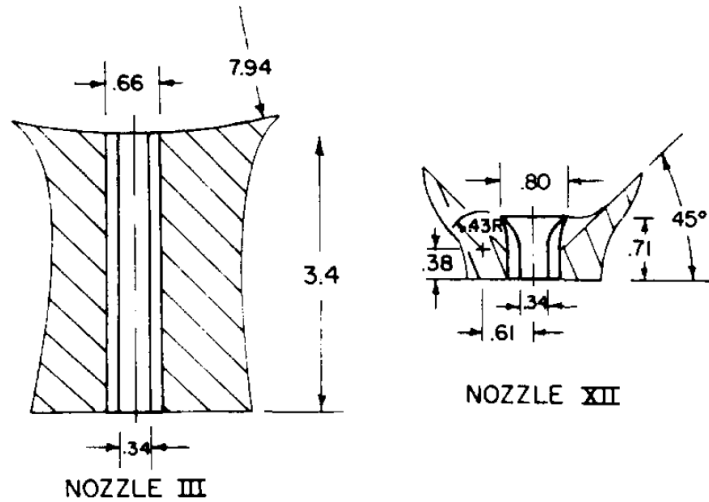


Figure 2.1: Sharp-edged nozzle III ($L/D = 10.1$) and rounded inlet nozzle XII ($L/D = 2.1$) produced the same jet divergence angle - Reitz & Bracco (1982).

The differences in observed spray structure for rounded nozzles compared to sharp-edged nozzles was suggested by Karasawa *et al.* (1992) to be a consequence of the higher velocities in the vena contracta established in sharp-edged nozzles.

2.2 The Influence of the Nozzle on Atomisation

To account for the influence of the flow contraction, and allow direct comparison the measured jet velocity was divided by the discharge coefficient of the nozzle. When the Sauter mean diameter of the droplets was plotted against this corrected velocity, the data was shown to correlate very well. Figure 2.2 shows data for four nominally identical nozzles with L/D of 4 and a diameter of 3mm. Manufacturing tolerances on the nozzle diameter, which affect the discharge coefficient, can clearly be seen to affect the raw data (left) but are eliminated when plotted against the corrected velocity (right).

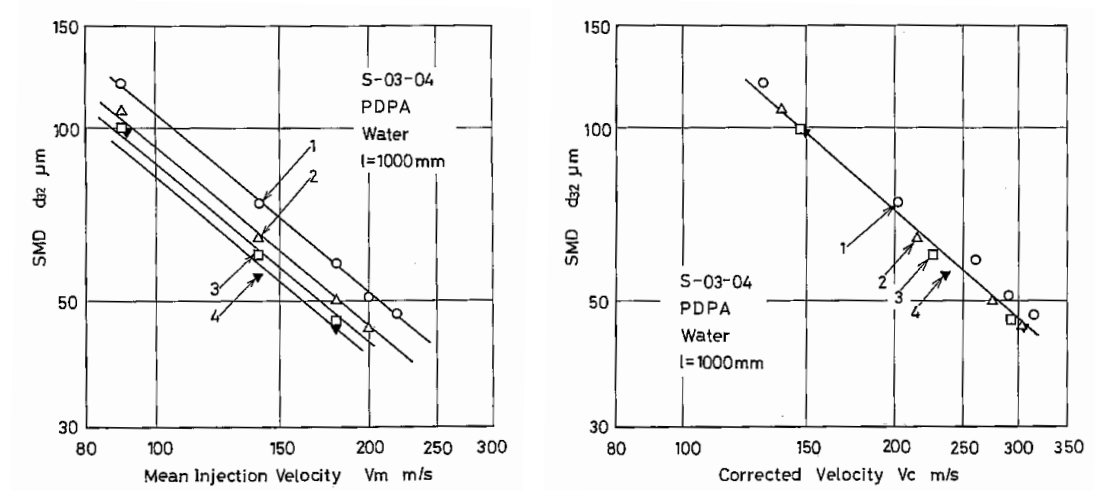


Figure 2.2: Droplet size dependence on mean flow velocity for 4 “identical” nozzles. Raw data (left), corrected data (right) - Karasawa *et al.* (1992).

These somewhat intuitive results were further supported by measurements conducted by Kent & Brown (1982) of the discharge coefficient and nozzle exit turbulence for incompressible air flow through two nozzles with rounded and square-edged inlet profiles. Large scale nozzles and air were used due to the extreme difficulties associated with experimental measurements of turbulence generation in small liquid atomising nozzles. This is a consequence of the high velocity flows and extremely small spatial resolution required. Spatially resolved RMS velocity fluctuations at the nozzle exit, measured using Laser Doppler Velocimetry

2.2 The Influence of the Nozzle on Atomisation

(LDV), demonstrated that the sharp edged nozzle had higher overall turbulence levels and significantly higher radial velocity fluctuations than the rounded nozzle.

Similar single-phase investigations were conducted by [Knox-Kelecy \(1992\)](#), [Knox-Kelecy & Farrell \(1992\)](#) and [Knox-Kelecy & Farrell \(1993\)](#) to investigate the influence of inlet rounding and L/D ratio on the turbulence development in 50 times scaled up nozzles. In the case of the sharp edged nozzles, prominent turbulent frequencies present in the upstream flow (e.g. pumping fluctuations) were redistributed by the turbulence within the nozzle. This was thought to be the result of the unique turbulence characteristics introduced by the reattachment of the boundary layer. For rounded nozzles the absence of the flow reattachment meant the upstream spectral signature was essentially passed through the nozzle. Increasing the L/D ratio in sharp edged nozzles shifted the turbulent spectrum from a concentrated, relatively narrow, band of low frequencies towards higher frequencies.

2.2.3 Ambient Conditions

An extensive number of studies have investigated the effects of ambient conditions on the atomisation process and the trends have been well established. Studies have shown for a given jet velocity, increasing the pressure (or density) of the ambient gas into which the jet was injected increased the jet spray angle and decreased the spray penetration (see for example [Miller & Beardsley \(1926\)](#), [Lee \(1933\)](#), [Iyer & Abraham \(1997\)](#)). This seemed an obvious consequence of the heightened aerodynamic shear forces exerted on the surface of the jet aiding in the disintegration of the solid liquid core. Interestingly, the density of the gas was shown to have a greater influence on the jet spray angle than the ambient pressure. [Reitz & Bracco \(1982\)](#) reinforced this by comparing the spray structures of two jets injected into gases that, due to their respective molecular masses, had a four-fold density difference. Under otherwise identical conditions the jet issuing into low density nitrogen gas was seen to have a continuous liquid core, whereas the jet issuing into xenon gas was seen atomising from the nozzle exit, divergent in shape and rippled in structure.

2.2 The Influence of the Nozzle on Atomisation

It was clear that the atomisation of liquid jets involved a complex combination of factors, in which aerodynamic interaction was “supplemented” by effects caused from within the nozzle (Wu *et al.* (1986)). The surface of the liquid jet leaving the nozzle was directly perturbed by events occurring within the nozzle. These perturbations are then acted upon by the aerodynamic shear forces until the surface of the jet is broken into droplets. The improvements to jet atomisation that resulted from increased injection pressure was also well known. Generally, as injection pressures increase, jet velocity increases directly. This increases the aerodynamic shear forces enhancing the atomisation. However, as injection pressures and consequently liquid velocities increased, conditions become increasingly conducive to cavitation forming in the orifice. Cavitation was quickly recognised as being highly important to the atomisation process due to the increased levels of turbulence, and heightened surface disturbances it introduced and received increased attention in the literature. In fact Reitz and Bracco concluded their extensive studies (Reitz & Bracco (1979a,b, 1982)) by suggesting that cavitation could not be ruled out as the sole cause for the observed trends in atomisation.

The complexity of the mechanisms responsible for the atomisation process is clearly illustrated by curves plotting spray breakup length against jet velocity, such as figure 2.3. The peaks and troughs in the relationship indicate regions where the atomisation is dominated by different forces such as laminar or turbulent breakup.

Various stability curves have been proposed (see for example McCarthy & Molloy (1974), Arai *et al.* (1984), Hiroyasu *et al.* (1991)) however there has been some disagreement in the shape of the curves, particularly in the high velocity spray region, where cavitation can have a significant influence. Three distinct possibilities can be seen for the break-up length at high velocities in figure 2.3, which have been attributed to various cavitating regimes present in the nozzle (see section 2.3.1). Schmidt & Corradini (2001) suggested that the disagreement may be partly due to the fact that changing the jet velocity simultaneously alters the external aerodynamic interactions and the internal flow structures.

The literature reveals a large number of similar experimental studies investigating jet atomisation, often with conflicting results. However, on close inspection, test conditions between studies are often markedly different. A particularly

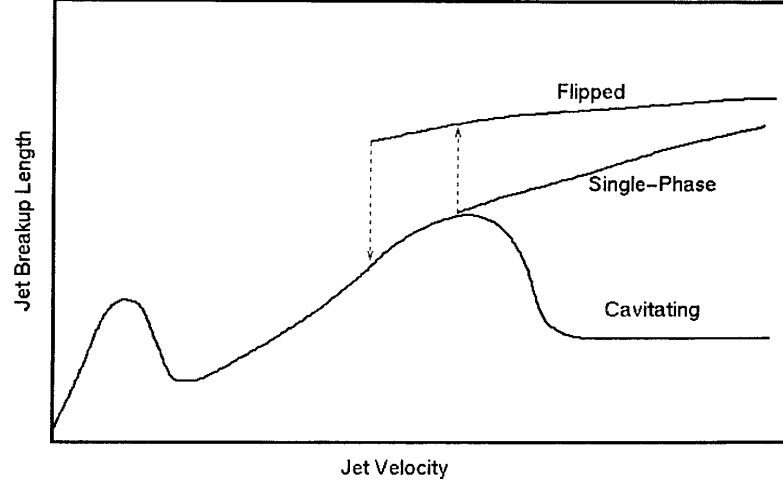


Figure 2.3: Breakup length stability curve - Schmidt & Corradini (2001)

common discrepancy is the comparison of studies injecting jets into quiescent air rather than pressurised gas, which is common owing to the significantly simpler experimental setup requirements. For example, the findings of Ohrn *et al.* (1991a) that “the shape and condition of the nozzle inlet have an important and sometimes overriding effect on spray cone angle”, was criticised by Dodge *et al.* (1992) owing to their use of atmospheric air. Atmospheric conditions are known to reduce to aerodynamic breakup forces and emphasise the contribution of the flow within the nozzle to the jet behaviour.

2.3 The Effects of Cavitation on Nozzle Flow

2.3.1 Cavitating Flow Structures

In a typical orifice style configuration the contraction of the flow causes an increase in the liquid velocity, and a subsequent reduction of static pressure. For sharp-edged orifices, the flow separates at the inlet corner and forms a *vena contracta* shortly inside the nozzle. The pressure distribution across the nozzle entrance is not uniform, and will be lowest near the corners of the nozzle where

2.3 The Effects of Cavitation on Nozzle Flow

the inertial effects of the contraction are the most pronounced. As the velocity through the nozzle increases the static pressure locally falls to the vapour pressure of the liquid. When this occurs cavitation bubbles form, originating from heterogeneous nucleation sites in the high shear flow region of the separated boundary layer. Studying cavitation in large scale transparent nozzles, Soteriou *et al.* (1995) referred to this as *geometric* cavitation. Alternatively, Chaves *et al.* (1995) demonstrated that cavitation could also be repeatedly initiated from geometrical imperfections around the nozzle entrance of real sized nozzles, which act as heterogeneous nucleation sites.

The appearance of the cavitation as it developed in the nozzle was found to be dependent on the scale of the nozzle and also the flow velocity. For large scale nozzles incipient cavitation bubbles grow and form foamy white clouds which occupy the entrance region of the nozzle. However, the extent of the nozzle cross-section occupied by the cavitation has been debated. Soteriou *et al.* (1999) used a laser light sheet to visualise cavitation formation in a 5.5mm diameter transparent nozzle. They believed that vapour bubbles initiating in the separated boundary layer near the sharp entrance quickly spread to occupy the entire cross section, and referred to this as *plug* cavitation, and later as *pre-film* cavitation by Arcoumanis *et al.* (1999). Figure 2.4 shows an image of this condition and a schematic indicating the author's interpretation of the cavitation structure.

However the plug cavitation condition was refuted in a study of the cavitation formation in small-scale nozzles by Badock *et al.* (1999). Also using a laser light sheet for illumination, and shadowgraphy to visualise the cavitation in acrylic nozzles with diameters between 0.18 and 0.30mm, an intact liquid core was seen to be present under all injection conditions studied. Chaves *et al.* (1995) also dispelled the idea that cavitation occupied the entire nozzle section for real sized nozzles and rather observed the cavitation to consist of large extended fixed cavities with smooth almost glassy appearance. Increasing flow velocity causes a roughening of the surface of the cavities. This particular regime of smooth surfaced, attached cavities was termed *film* cavitation Arcoumanis *et al.* (1999).

For sufficiently short nozzles further reductions in the cavitation number caused the fixed cavity to extend all the way to the exit. This results in cavity collapse occurring at the exit plane of the nozzle. This condition was referred

2.3 The Effects of Cavitation on Nozzle Flow

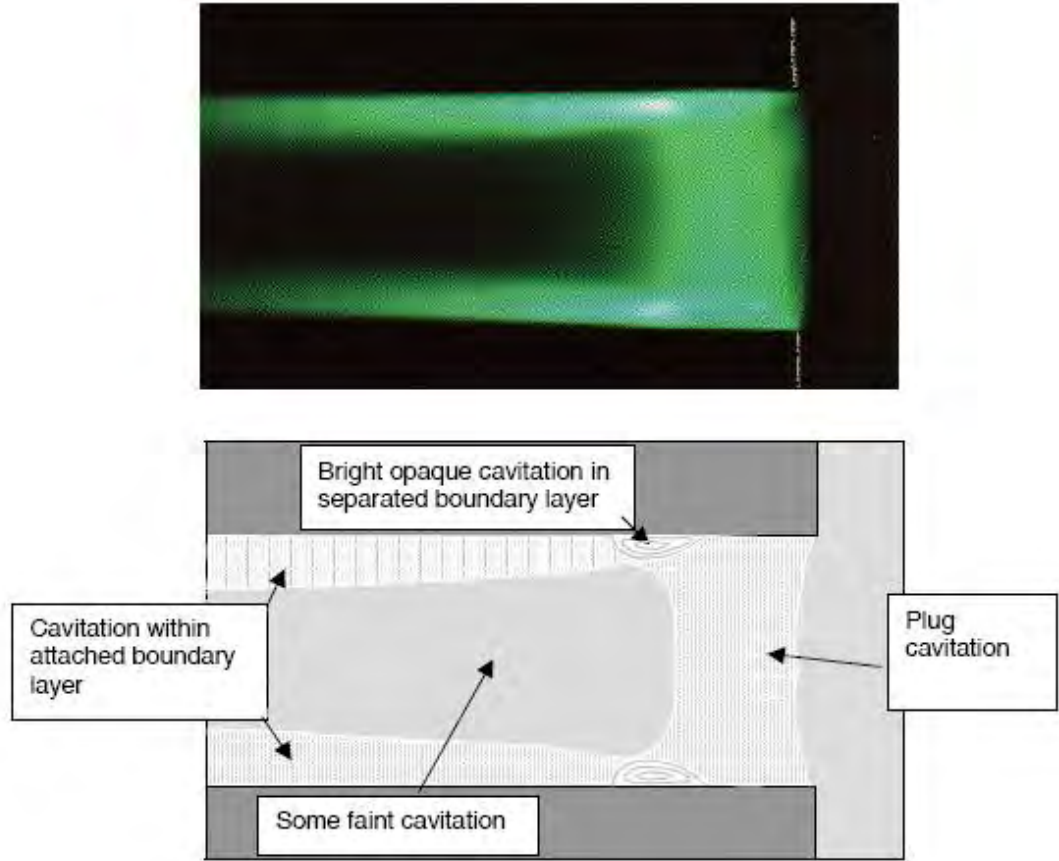


Figure 2.4: Plug cavitation as observed by - Soteriou *et al.* (1999)

to as *supercavitation* by Chaves *et al.* (1995), analogously to the common terminology used for hydrofoil cavitation. Under these conditions the driving force for the collapse of the cavitation bubbles is the pressure differences between the ambient gas pressure and the low pressure within the cavities. Supercavitation could be achieved in nozzles that, due to scale effects and disturbances around the entrance of the nozzle, were resistant to hydraulic flip.

As cavitation increases further from the supercavitation condition relatively high pressure ambient gas can force into the extended cavities collapsing near the nozzle exit. This causes the flow to separate from the nozzle entrance and remain detached the entire length of the nozzle. A complete cessation of cavitation and an absence of the interaction with the nozzle wall eliminates the internal

2.3 The Effects of Cavitation on Nozzle Flow

influences responsible for disrupting the jet. Consequently, with no surface perturbations which can be amplified by aerodynamic interaction, there is a sudden and discontinuous increase in the breakup length (see figure 2.3). In this detached state, later referred to as *hydraulic flip* in studies of rocket injectors, the constricted jet had a ‘glass-like’ appearance and broke up well downstream from the nozzle exit.

Hydraulic flip was originally reported by Bergwerk (1959), who was perhaps the first person to identify the significant influence of cavitation on jet breakup. Once a jet has transitioned to the flipped state reattaching the jet to the nozzle walls has been shown to be rather difficult. A hysteresis in this transition was observed in a number of studies (Ramamurthi & Patnaik (2002); Ramamurthi *et al.* (2001), Hiroyasu (2000); Hiroyasu *et al.* (1991)) and can be seen graphically in the stability curve (see figure 2.3).

Flow conditions inside small-scale cavitating nozzles such as those in fuel injectors are extreme; with very high pressures (up to 180MPa) and high fluid velocities ($> 300\text{m/s}$). These conditions, combined with the small physical scales ($\sim 250\mu\text{m}$), make gaining optical access for experimental studies extremely difficult. For this reason large scale transparent replica nozzles are often used (Arcoumanis & Gavaises (1998)). This assists with measurement of the flow and greatly facilitates the optical access and resolution of any flow visualisation. Fundamental studies, exploring the global flow characteristics and cavitation flow structure, were conducted using single-hole simple orifice atomiser nozzles (eg. Badock *et al.* (1999), Dan *et al.* (1997), Chaves *et al.* (1995)) and also two-dimensional slot orifices (Suh *et al.* (2008), Henry & Collicott (2000)). More complex multi-hole geometries representing realistic injector nozzle configurations, including the affects of pre-nozzle flow influences such as the needle and sac volume, were also explored (eg. Afzal *et al.* (1999)). In order to correlate the flow from the large scale nozzle to the real sized injector, dynamic similarity is used. Cavitation and Reynolds number are matched to the real size nozzles, although few have managed to achieve this simultaneously.

Differences in the observed flow structures for small scaled injector nozzles and large scale replicas were influenced by both the nucleation mechanics responsible for the formation of the cavities, and also the residence time for the bubbles in

2.3 The Effects of Cavitation on Nozzle Flow

the nozzle. In both cases the formation of cavitation is due to heterogeneous nucleation sites. Generally for large scale flows these nuclei grow into individual cavitation bubbles which have a foamy appearance. Eventually these individual bubbles can coalesce to form cavitation films. However the relative size of the heterogeneous nuclei from which the cavitation initiates (i.e crevices due to surface roughness and free stream microbubbles) does not scale with the size of the nozzle (Billet & Holl (1981)). As a result, the individual cavitation bubbles which form within small nozzles represent a larger fraction of the nozzle volume, which enhances the formation of film cavitation (Arcoumanis *et al.* (2000)).

The differences in the cavitation structure formed is also related to the unique length scale for cavitation related to the relative collapse time of the bubbles for the pressures characteristic to that scale. The high pressures of real scale nozzle flow result in short residence times which generally mean the cavitation bubbles collapse within the injection hole. Whereas the relatively low pressures for the larger nozzles produce longer residence times and the cavitation bubbles are often observed to last all the way to the exit of the nozzle (Arcoumanis *et al.* (1999)). As this length scale cannot be matched between the two different nozzles, the cavitating flow structure will be unavoidably different in nature. Considerations of cavitation scaling and the influences on cavitation are discussed in Brennen (1995) and Franc & Michel (2004). Despite the obvious differences associated with the scale of the flow, direct comparison between real and large scale nozzle cavitation have indicated very little deviation in the macroscopic flow structure (Arcoumanis & Whitelaw (2002)). This again reinforces that, with careful consideration of these influences and a tentative approach to extrapolating the results to real scale flows, large scale nozzles are a valuable tool for experimental investigation.

2.3.2 Nozzle Turbulence and Jet Breakup

The effect of the cavitation on the spray structure in both single-hole and multi-hole nozzles was obvious and pronounced. Jets emerging from cavitating nozzles had roughened surfaces directly from the nozzle exit. They quickly diverged into sprays with ragged appearance and were rapidly broken into droplets by the aerodynamic shear forces. The spray divergence angle was consistently larger (Wu

2.3 The Effects of Cavitation on Nozzle Flow

et al. (1983), Payri *et al.* (2004)) and the breakup length of the jets shorter (Arai *et al.* (1984), Hiroyasu *et al.* (1991)) compared to non-cavitating jets operating at otherwise identical conditions. It is believed these improvements in atomisation are the result of the heightened roughness to the liquid jet surface upon exit from the nozzle, which result from the flow turbulence created by the cavitation within the nozzle (Tamaki *et al.* (1998), Soteriou *et al.* (1995), Chaves *et al.* (1995)). The enhancements in atomisation with the presence of cavitation were experimentally observed to level off for further increases in injection pressures once a state of supercavitation was reached (Reitz & Bracco (1979a), Wu *et al.* (1983)). For supercavitation the degree of perturbation on the jet surface caused by the catastrophic bubble collapse were at such levels that further increases to flow turbulence had little influence on the atomisation.

Despite there being common agreement it is the increased levels of turbulence associated with the cavitation which is responsible for the enhanced atomisation, the exact mechanism responsible for this turbulence is not well understood. Some believe the primary influence of cavitation is the increased velocities that result as a consequence of the reduction in liquid flow area by the presence of vapour pockets (Dumont *et al.* (2000), Desantes *et al.* (2001), Benajes *et al.* (2004)). Others have suggested it is the liquid pressure fluctuations that result from the catastrophic bubble collapse that cause the increased levels of turbulence (Sou *et al.* (2006)).

Limited attempts have been made to measure turbulence levels within atomising nozzles under cavitating and non-cavitating conditions. Conducting such measurements in real scale nozzles is particularly difficult given the high sample rates and extremely small spacial resolution required. Typically the lower limit on the measurement volume of a laser system used to measure instantaneous velocities is of the order of the nozzle diameter, inhibiting the ability to determine local variations. This process is complicated further by the two phase flow associated with cavitation. Consequently, practically all studies have been conducted in scaled up nozzles, a number using simplified two dimensional slots rather than cylindrical nozzles and very few with cavitation present.

With the primary focus of investigating the influence of the cavitation on nozzle turbulence He & Ruiz (1995), and later Ruiz & He (1999), conducted Laser

2.3 The Effects of Cavitation on Nozzle Flow

Doppler Velocity (LDV) measurements of the flow through a 200 times scaled up two-dimensional step section. Interestingly turbulent intensities were found to be consistently 10-20% higher behind the vapour filled cavity than behind a recirculation region for non-cavitating nozzles at identical Reynolds numbers. However despite the higher turbulent intensity levels directly behind the cavities, the turbulence for cavitating conditions was shown to decay at a slower rate than the turbulence for non-cavitating nozzles. When the levels were compared at the nozzle exit, the turbulence intensity for the cavitating nozzle was roughly 25% higher than those for the non-cavitating nozzle.

It was also observed that the regions of highest turbulence intensity were quite localised to regions downstream of the cavity whereas the peak values occurred along the nozzle centreline for non-cavitating flows. The proximity of the higher levels of turbulence closer to the nozzle wall and the free surface once the jet exited the nozzle was suggested as a possible explanation for the more effective breakup of cavitating atomisers.

More recently, [Sou *et al.* \(2006, 2007\)](#) conducted similar measurements of the lateral velocity fluctuations within a large scale two-dimensional planar nozzle section using LDV. Sou used a systematic approach to explore the turbulence generation across a range of cavitation conditions, something that had previously been ignored. A significant increase in the lateral velocity fluctuations were seen just before the nozzle exit for the supercavitating flow. It is this fluctuating component of lateral velocity, not present for the other cavitation regimes, which the authors suggest is responsible for the significant increase in jet atomisation observed under supercavitating conditions. Sequences of high-speed images showing the internal flow and near nozzle spray structure provided strong evidence that collapsing cavitation bubbles were directly related to ligament formation on the liquid jet surface. Similar qualitative observations were also made by [Ganippa *et al.* \(2004\)](#) and also [Sou *et al.* \(2008\)](#) for ligament formation on the spray produced by a cavitating orifice.

Turbulence measurements were also conducted inside a large scale multi-hole sac-type injector by [Roth *et al.* \(2002\)](#). Turbulent Kinetic Energy (TKE) levels measured using LDV indicated that the string cavitation (see section 2.3.4) within the sac volume had a minimal effect on the turbulence levels prior to the

nozzle hole with the small increases immediately dissipating and diffusing into the bulk flow. Measurements of the TKE within the nozzle hole indicated that the turbulence levels were increased by increasing levels of cavitation and diffused more slowly.

2.3.3 Nozzle Discharge Coefficient

While cavitation within an orifice improved the atomisation of the liquid jet, it came at the expense of hydraulic resistance. This is typically measured using the discharge coefficient, C_d , which represents the ratio of the actual mass flow rate through an orifice to the theoretical mass flow for ideal conditions. Measurements conducted by [Spikes & Pennington \(1959\)](#) indicated that the onset of cavitation within an orifice resulted in reductions of nozzle discharge coefficient, although no reasonable explanation was provided.

[Pearce & Lichtarowicz \(1971\)](#) provided a very elegant description of the fluid mechanics involved and articulated the cause for the observed reduction in C_d . As a result of the fluid approaching the orifice from a larger cross section the flow has a component of velocity at 90° to the bore. Momentum causes the flow to separate from the inlet edge of the nozzle and form a *vena contracta*. It is typical to define a contraction ratio, C_c , expressing the ratio of area at the vena-contracta, A_c , to the nozzle cross section, A . The value of the contraction ratio is highly dependent on the rounding of the inlet edge. For an ideal square edge conformal mapping shows $C_c = \pi/(\pi + 2) \approx 0.61$ but it rapidly increases with increasing inlet radius. As the flow contracts the velocity increases and the static pressure decreases, reaching a minimum value at the vena contracta. Following the contraction the flow then expands causing a reduction in velocity and a sharp rise in static pressure. Provided the nozzle has sufficient length, the flow then reattaches. From this point till the exit, the flow represents regular turbulent pipe flow and experiences gradual loss of pressure occurs due to wall friction. For a constant injection pressure, reductions in back pressure cause an increase in the fluid velocity and a corresponding reduction of the pressure at the contraction. Flow conditions remain unaltered until the pressure at the vena contracta reaches the vapour pressure of the liquid. At this point cavitation

2.3 The Effects of Cavitation on Nozzle Flow

occurs. Further reductions in outlet pressure can no longer influence the upstream conditions as the static pressure cannot fall below the vapour pressure. In other words the flow is “choked”. Experimentally, this is observed as a reduction in the discharge coefficient and stabilisation of mass flow through the nozzle (see for example Randall (1952)).

Choking was also demonstrated in both small and large scale nozzles by Soteriou *et al.* (1995). However, they believed the choking was caused by the dramatic reduction of sonic speed associated with the transition to two-phase flow. This theory was based on their assertion that cavitation occupied the entire nozzle cross section (see figure 2.4), which seems more likely an artifact of their visualisation than a physical reality.

An analytical model expressing the relationship between discharge coefficient and cavitation was initially proposed by Bragg and Crosby in the correspondence to the paper of Spikes & Pennington (1959). Later Pearce & Lichtarowicz (1971) and Nurick (1976) also presented the same analysis which is based on the simplified cavitating nozzle flow as shown in figure 2.5. It is assumed that cavitation has no effect on the development of the vena contracta with the vapour fully occupying the recirculation zone.

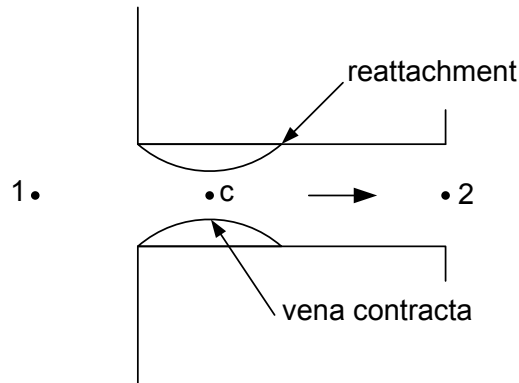


Figure 2.5: One-dimensional cavitating nozzle flow

Combining a Bernoulli analysis between point 1 and c and a mass continuity balance between c and 2 the following expression can be obtained:

2.3 The Effects of Cavitation on Nozzle Flow

$$\frac{P_1 - P_c}{\frac{1}{2}\rho V_2^2} = \left(\frac{1}{C_c}\right)^2 \quad (2.1)$$

where V_1 is assumed negligible. The nozzle discharge coefficient can be defined in terms of the total losses incurred by the flow from point 1 to point 2 (including friction, Borda-Carnot and turbulence losses):

$$V_2 = C_d \sqrt{2(P_1 - P_2)/\rho} \quad (2.2)$$

At this point an assumption is made that the pressure at the contraction for a cavitating nozzle is equal to the vapour pressure of the liquid. Substitution of equation 2.2 into equation 2.1 yields an expression for the discharge coefficient, C_d , in terms of the contraction coefficient, C_c ;

$$C_d = C_c \sqrt{\frac{P_1 - P_v}{P_1 - P_2}}. \quad (2.3)$$

Finally, identifying the expression under the radical as the cavitation number, K , as defined by Nurick, it can be written

$$C_d = C_c \sqrt{K}. \quad (2.4)$$

It can be seen that the discharge coefficient is predicted to be purely a function of the cavitation number. From a simple substitution of equation 2.3 into equation 4.5 it can be seen that

$$V_2 = C_c \sqrt{2(P_1 - P_v)/\rho} \quad (2.5)$$

which is independent of the back pressure, P_2 . In other words choking is predicted by the model at the onset of cavitation. The highest value of K for which cavitation occurred within the nozzle was referred to as the critical cavitation number K_{crit} , above this point the flow became single phase and the above analysis was invalid. For non cavitating conditions the discharge coefficient becomes a function of the Reynolds number, as shown by [Lichtarowicz *et al.* \(1965\)](#), and can be assumed to be nearly constant for $Re > 2 \times 10^4$.

2.3 The Effects of Cavitation on Nozzle Flow

This behaviour was experimentally validated by a number of studies (e.g. [Ohm *et al.* \(1991b\)](#), [Soteriou *et al.* \(1995\)](#), [Schmidt *et al.* \(1995\)](#)). Compiling the experimental results of a number of researchers, [Schmidt & Corradini \(2001\)](#) found that practically the discharge coefficient was often higher than that predicted by the one-dimensional theory (see figure 2.6). This was assumed to be the result of slight inlet rounding increasing the discharge coefficient.

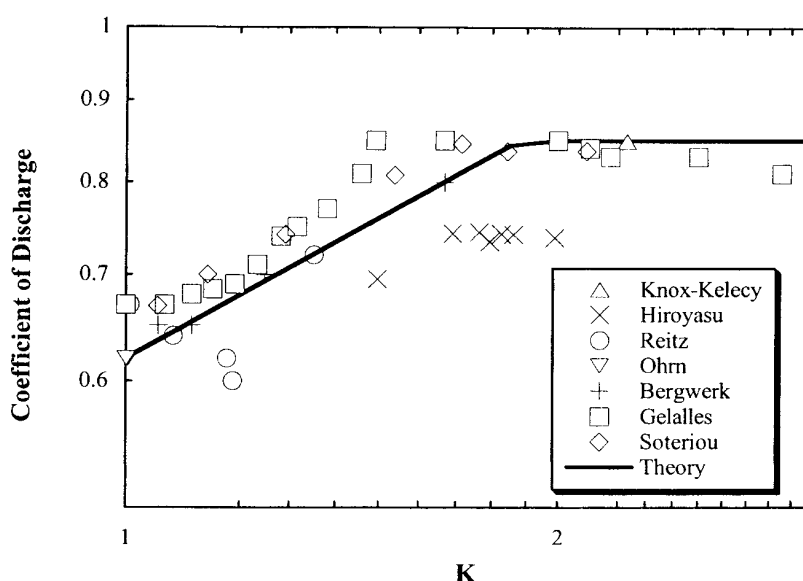


Figure 2.6: Compilation of experimental nozzle discharge coefficient - from [Schmidt & Corradini \(2001\)](#).

Nurick observed inlet rounding of $r/D > 0.14$ was sufficient to prevent the formation of the vena contracta and cavitation. Similar effects have been observed by the use of a converging conical nozzle ([Payri *et al.* \(2004\)](#), [Payri *et al.* \(2005\)](#)). In this case the acceleration of the liquid is more gradual than the case of the cylindrical section, preventing cavitation formation. No mass flow choking was observed regardless of the injection pressure used and the discharge coefficient continued to follow the single-phase approximation ([Benajes *et al.* \(2004\)](#), [Payri *et al.* \(2008\)](#)).

[Ruiz \(1991\)](#) and [Schmidt & Corradini \(1997\)](#) both extended Nurick's analysis to generate nozzle exit momentum relationships in terms of the nozzle parameters.

2.3 The Effects of Cavitation on Nozzle Flow

Both Ruiz and Schmidt and Corradini made a number of simplifying assumptions regarding the cavitation cavity interaction and reattachment to the nozzle wall. Schmidt and Corradini assumed that there was zero wall shear present and allowed their exit velocity profile to vary radially. Ruiz however, assumed the exit velocity profile was uniform and applied a momentum difference between the exit and contraction to determine the head losses of the fluid. These contrasting assumptions effectively form the bounds of possible exit momentum, with Schmidt and Corradini's zero shear approach forming the upper limit, and Ruiz's 'plug' flow model forming the lower limit. These one dimensional models have shown a limited ability to predict the global flow parameters, such as the discharge coefficient, rather well. However, they lack the ability to account for geometrical influences, nucleation mechanics and scale effects.

2.3.4 Injector Specific Observations

A number of experiments have been conducted for cavitating flows in more realistic injector based geometries on both small and large scale. Generally the flow structures differ from single hole configurations due to the difference in the way the fluid approached the orifice. Hole location and orientation with respect to the injector sac volume were shown by Kim *et al.* (1997) to alter the cavitation structure observed. In general the presence of the needle was shown to have a significant influence on the flow within the nozzle. The restriction of the flow path created by the needle means the fluid undergoes a greater change of direction on the upper corner. As a consequence cavitation was shown to initiate on the upper corner of the nozzle entrance and extend into the nozzle (e.g Afzal *et al.* (1999)). Eccentricity of the needle altered the pre-nozzle flow patterns introducing hole-hole variations in mass flow and consequentially, spray structure (Arcoumanis *et al.* (1999)).

The tendency for multi-hole injectors to reach the flipped state was shown to be inhibited by the presence of the needle. It was believed that the increased levels of flow turbulence introduced by the flow in the annular area around the needle were sufficient to promote reattachment of the boundary layer, preventing the flow cavities extending to the nozzle exit (Soteriou *et al.* (1995)). Partial

2.3 The Effects of Cavitation on Nozzle Flow

flip of the nozzle flow was sometimes seen, when cavitation appearing on the top surface of the nozzle extended to the exit whereas the flow on the bottom surface remained attached. In these conditions the spray produced was asymmetric with the top half of the jet appearing less divergent and ruffled than the lower half.

The understanding of nozzle cavitation was further complicated when Kim *et al.* (1997) discovered vortical, or “string”, cavitation structures which formed in the discharge hole and progressed to the sac volume of a 10 times scaled multi-hole sac-type injector. Under different needle lift conditions these highly transient vortical structures were seen to link between different discharge holes in the lower region of the sac. A number of studies used high speed visualisation to investigate the phenomenon, with focus placed on the processes required for the formation of string cavitation and its interaction with the bulk nozzle flow. Afzal *et al.* (1999) and Roth *et al.* (2002) found that the string cavitation was distinct from geometric cavitation but often coexisted.

Cavitation strings were seen to initiate in the pre-nozzle volume between the needle and needle seat where the fluid separates from the needle surface and forms large scale vortex structures Gavaises & Andriotis (2006). Nouri *et al.* (2007) attribute this vortex formation to the interaction of the high momentum annular flows and the cross flows that are induced by the intermittent throttling of individual holes by the already present geometric cavitation. This was later verified in the work of Andriotis *et al.* (2008) and Gavaises *et al.* (2009) exploring the origin, size and lifetime of string cavitation. Simulations revealed that string cavitation also initiated from a second separation point at the top corner of the nozzle. Primarily, string cavitation has been observed in large scale nozzles although evidence of the phenomenon existing in small scale injector geometries under realistic conditions has also been reported (Blessing *et al.* (2003), Roth *et al.* (2005), Arcoumanis *et al.* (2000)).

The destructive effects of cavitation due to bubble collapse in close proximity to a surface are well documented; see for example Knapp (1957) and Brennen (1995). The mechanism responsible for this damage is the frequent strain on the surface, partly due to the micro-liquid jets caused by the asymmetric collapse of vapour bubbles and partly due to the local shockwaves produced by local bubble collapse (Gavaises *et al.* (2007)). The presence of both geometric and string

cavitation within the nozzles of diesel fuel injectors renders them susceptible to cavitation damage and can result in catastrophic failure as noted by Asi (2006). The use of tapered nozzle holes has been shown to reduce and even eliminate the presence of geometric cavitation within the injector nozzles (Blessing *et al.* (2003), Gavaises *et al.* (2009)). However, the elimination of the cavitation can influence the effective atomisation of liquid fuel. Also, string cavitation, which is not eliminated by tapered holes have been shown to be responsible for increase exhaust emissions (Gavaises (2008)). These issues present concerns for designers who strive to meet the increasingly stringent vehicle emissions regulations. Increasing the understanding of nozzle cavitation is central to effectively utilising the benefits for improved liquid atomisation, whilst minimising the potential for structural damage.

2.4 Periodic Cloud Shedding

Attached cavities, such as those which form for geometric cavitation in plain orifices, are rarely stable and cavity lengths may oscillate significantly under certain conditions. These oscillations are often referred to as cavitation instabilities. Callenaere *et al.* (2001) distinguished two main types of attached cavity instability; intrinsic instabilities and system instabilities. Intrinsic instabilities referred to oscillations originating from within the cavity itself, whereas system instabilities were caused by influences external to the cavity such as flow conditions in the supply or interactions with other cavities.

One of the most interesting, and common, forms of intrinsic instability is the periodic shedding of cloud cavitation identified by Knapp (1955). Investigating fixed cavitation on 2-dimensional bodies, Knapp found that the cavity underwent a “continuous but somewhat irregular cyclical process” where the cavity attached to the guiding body would grow, reach roughly a fixed length, then shed as a coherent bubble cloud. In fact, three distinct phases were identified for this cycle; (a) formation and growth, (b) filling, and (c) breakoff. Central to this process was the motion of a jet of liquid moving upstream underneath the cavity, referred to as the re-entrant jet.

2.4.1 Re-entrant Jet

The formation of the re-entrant jet occurs in the region surrounding the flow reattachment to the wall behind the cavity. The expanding flow behind the cavity impinges on the wall and forms a stagnation point (Callenaere *et al.* (2001)). On the upstream side of this stagnation point momentum forces the fluid towards the nozzle entrance and under the cavity. On the downstream side of the stagnation point the flow reattaches to the wall and continues towards the nozzle exit. A schematic representation of the re-entrant jet formation can be seen in figure 2.7.

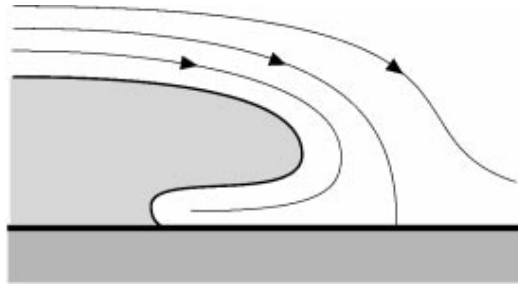


Figure 2.7: Schematic representation of the re-entrant jet formation in the closure region of a fixed cavity - Callenaere *et al.* (2001).

In the process referred to as filling by Knapp (1955) the re-entrant flow travels up-stream beneath the cavity while the cavity remains essentially a constant characteristic length. Eventually the jet reaches the vicinity of the leading edge and “pinches-off” the attached cavity allowing it to be shed from the leading edge and form a vapour cloud (Wade & Acosta (1966), Le *et al.* (1993)). As the cloud is shed a new fixed cavity forms at the leading edge and begins to grow. As the separated cloud is convected downstream it coalesces and forms a rolling vortex due to the momentum of the free-stream. The velocity of the cloud was measured by Kubota *et al.* (1989) using LDA and a selective sampling method. Results showed the cloud consisted of a large number of small bubbles, and was convected with a lower velocity than the bulk flow with concentrated vorticity at its core. As the cloud is convected downstream it eventually collapses in the high pressure region.

A number of attempts have been made to measure the upstream velocity of the re-entrant jet. In the study of cavitating hydrofoils, the re-entrant jet velocity, V_j , has been expressed in terms of the free-stream velocity, V_∞ , using steady potential theory. Assuming the cavity interface to be a line of constant pressure it can be shown that $V_j = V_\infty \sqrt{1 + \sigma}$, where σ is the classical cavitation number defined as $\sigma = (P_\infty - P_v) / \frac{1}{2} \rho V_\infty^2$. In reality the non-ideal cavity structure and skin friction combine to produce a jet velocity less than this prediction.

Pham *et al.* (1999) used surface mounted electrical impedance probes to measure the velocity of the re-entrant jet beneath the cavity. The jet velocity was found to be of the same order of magnitude as the free-stream, however it decreased as it progressed beneath the cavity towards the leading edge. Despite these measurements, the authors visualised perturbations on the surface of the jet which they conjectured were the result of the impact of the re-entrant jet with the cavity interface. The shedding periodicity corresponded well to the propagation of these perturbations. Similarly, Sakoda *et al.* (2001) measured the jet velocity from visualisation and found it decayed as it progressed.

Elucidating the motion of the liquid jet has proven difficult and often the re-entrant jet velocity has been inferred from the deformation of the cavity interface. In this way Le *et al.* (1993) found the velocity of perturbations traveling against the direction of flow were close to the magnitude of the free-stream, however the motion was difficult to interpret. To aid with the identification of the re-entrant jet fluorescein dye was injected from a location towards the back of the cavity. The cyclic nature of the jet became clear as coloured water could be seen near the leading edge at some instants of the period and only near the shed cloud in the wake at others. The injection of ink to aid with visualising the re-entrant jet motion was also been used by Jousselein *et al.* (1991) and Kawanami *et al.* (1997).

Generally, gaining visual access to the flow beneath the cavity is experimentally difficult to achieve. This is particularly true for axisymmetric cavitating bodies, for both external flow (eg. cavitating spheres) and internal flows (eg. cylindrical orifices). Sato & Saito (2002) and later Sugimoto & Sato (2009) visualised periodic cloud shedding in large scale cylindrical orifices. The general shedding cycle was observed to be similar to that described above. The authors

interpreted the progression of the re-entrant jet by observing the motion of the cavity “marching” towards the nozzle entrance and again found the velocity of the jet to be approximately equal in magnitude to the free-stream flow. However, the images used for this interpretation were affected by the refraction of the light passing through the cylindrical nozzle, obscuring access to liquid motion adjacent to the wall.

Experiments conducted by [Stutz & Reboud \(1997a\)](#) and [Stutz & Reboud \(1997b\)](#) on two-dimensional convergent-divergent nozzles provided improved optical access to the re-entrant jet and confirmed the role of the re-entrant jet in the periodic breaking off of the cavity. Using a double optical probe they also explored the two-phase nature of the cavity and found void fraction did not exceed 25% for unsteady cavities. [Kawanami *et al.* \(1997\)](#) demonstrated that by physically blocking the path of the re-entrant jet using an obstacle attached to a hydrofoil the cloud cavitation regime could be prevented, emphasising its role in the process.

The collapse of a shed bubble cloud is known to create pressure pulses in the vicinity of the guiding body, often orders of magnitude greater than the pressure in the mean flow ([Reisman & Brennen \(1996\)](#), [Reisman *et al.* \(1998\)](#)). Aside from being the cause of noise ([McKenney & Brennen \(1994\)](#)) it has been suggested that these pressure pulses may contribute to the motion of the re-entrant jet and the cavitation instability ([Leroux \(2004\)](#), [Leroux *et al.* \(2005\)](#)). Instantaneous pressure measurements across the span of the hydrofoil suggested that shock wave phenomena could also be responsible for the cavity destabilization. However experiments by [Coutier-Delgosha *et al.* \(2007\)](#) suggest the correlation between pressure pulses generated by the cloud collapse and the re-entrant jet motion was not systematic, but rather dependent on flow conditions.

Other studies by [Laberteaux & Ceccio \(2001a\)](#) and [Callenaere *et al.* \(2001\)](#) have suggested the adverse pressure gradient in the cavity wake has a strong influence on the development of the re-entrant jet. Studying the cavitating flow behind a backward facing step, [Callenaere *et al.* \(2001\)](#) investigated the effects of changing step height and the level of confinement of the bulk flow. Two important parameters were identified for the re-entrant jet instability: (1) the strength of the adverse pressure gradient in the region of closure, and (2) the cavity thickness

compared to the re-entrant jet thickness. Extended cavities collapse in regions of relatively flat pressure gradient which reduces the thickness and strength of the re-entrant jet pulse. Thin cavities for which the thickness of the jet was comparable to the cavity thickness produced strong interactions between the liquid jet and the interface which lead to regular shedding of smaller clouds.

Together with the combined influences of the over-pressure at the stagnation point, the adverse pressure gradient and pressure pulses from cloud collapse, re-entrant jet motion is also affected by the 3-dimensionality of the flow. The structure of the fixed cavity was shown to be concave following the shedding of a bubble cloud (see [Kubota *et al.* \(1989\)](#)). Significant portions of the cavities present on swept hydrofoils, where the axis of the body is inclined to the flow, have been shown to be remarkably steady when compared to regular two dimensional foils. It was found that when the closure line of the cavity is no longer normal to the flow, the re-entrant jet is reflected at an inclination angle due to the conservation of momentum tangential to the closure line (see [De Lange *et al.* \(1994\)](#), [Duttweiler & Brennen \(1998\)](#), [Laberteaux & Ceccio \(2001b\)](#)). The effect of this inclined jet is that portions of the cavity remain attached and steady, whereas others are regularly shed.

2.4.2 Shedding Frequency

Together with the analysis of the re-entrant jet, analysis of the frequencies associated with the cloud cavitation instability is often conducted. Generally, the frequency is reported in terms of the Strouhal number, defined as:

$$S = \frac{fL}{V_\infty} \quad (2.6)$$

where f is the shedding frequency, V_∞ is the free-stream velocity and L is a cavity length scale. Generally the maximum cavity length is chosen for the Length scale, although occasionally alternatives such as the mean cavity length have been used ([Sato & Saito \(2002\)](#)). A number of different techniques have been reported within the literature for measuring the shedding frequency. Stroboscopic lighting (eg. [Le *et al.* \(1993\)](#)) provides a simple way to obtain the characteristic frequencies, but becomes less effective as the limits of the coherent oscillation

region are reached. A more objective measure of the shedding frequency can be obtained from spectral analysis of pressure signals mounted on the guiding body (eg. Reisman *et al.* (1998), Leroux (2004)). Visual based methods have also been employed in a number of studies, with high-speed video recordings used to establish the temporal evolution of the cavity (Kawanami *et al.* (1997), Sato & Saito (2002)). These methods are attractive as they are non-intrusive and allow the visual exploration of the cavitation structure while providing sufficient temporal resolution to allow investigation of the shedding frequencies. Brandner *et al.* (2007) used a more complex wavelet analysis technique which uses the time variance of the mean pixel intensity in a small interrogation area to conduct spectral analysis of cloud cavitation on a sphere.

Reisman *et al.* (1998) identified two distinct kinds of shedding events. The first were high amplitude repeatable pressure pulses corresponding to the coherent shedding of a cloud, which they termed *global* pulses. The second were random pulses of smaller amplitude corresponding to localised passage of crescent-shaped regions of low void fraction, which they termed *local* pulses. Given the relative significance on the flow of these events, the Strouhal number is generally determined based on the shedding frequencies associated with these global events.

Chandra & Collicott (1999) investigated the shedding frequencies for cavitation in a slot orifice using a collimated laser beam and an optical receiver. Single point frequency measurements were obtained for a number of different injection pressures and axial locations. Spectral analysis revealed two major frequency components. The first low frequency component ($1 - 2kHz$) was thought to be related to the characteristic frequency of the flow, V/L and therefore related to large scale unsteadiness associated with global shedding events described by Reisman *et al.* (1998). A second high frequency component ($4 - 14kHz$) was thought to be associated with the smaller scale bubble shedding process.

In most studies it is common that only a single Strouhal number is reported for the shedding with typical values ranging between $0.2 \sim 0.3$ for cloud cavitation shedding. However, differences between various studies have indicated the specific geometry and cavitation number of the flow has an effect on the value obtained. For example, experiments by Arndt *et al.* (2000) showed that variations in the angle of attack of a hydrofoil caused a distinct change to the Strouhal number

of the cloud shedding. Occasionally, Strouhal number variation with cavitation number has been reported, such as by [De Lange & De Bruin \(1998\)](#). In their study they suggested that as the ideal re-entrant jet velocity was a function of the cavitation number, σ (see above), then there would be a dependence of the Strouhal number on cavitation number as well. Replacing V_∞ with $V_\infty\sqrt{1+\sigma}$ in equation 2.6, they determined an expression for S as a function of σ which was shown to have general agreement in the trend of the experimental data. Computation results of [Bunnell *et al.* \(1999\)](#) for cavitating slot orifices also showed the Strouhal number was dependent on cavitation number. However, they defined the Strouhal number in terms of slot length, which for periodic shedding will be significantly longer than the cavity length. For this reason their results were significantly higher in magnitude than the commonly reported values, with $S \approx 0.5 \sim 2$.

Experimental data for shedding instabilities in cylindrical orifices is particularly scant. [Sato & Saito \(2002\)](#) and [Sugimoto & Sato \(2009\)](#) both investigated cloud shedding in large scale orifices and measured Strouhal numbers in the range $S = 0.3 \sim 0.4$ and $S = 0.3 \sim 0.5$ respectively. Both papers focused primarily on describing the periodic motion of the shedding and present little discussion on the variations in frequency with cavitation number.

2.5 Summary of the Literature

- Improvements to atomisation that result from presence of cavitation within an orifice are related to the increased levels of turbulence. This turbulence enhances the surface perturbations of the liquid as it leaves the nozzle. These initial disturbances rapidly grow and are acted upon by the aerodynamic shear forces breaking the liquid into droplets.
- Due to the difficulties involved with measuring cavitating orifice flows, the vast majority of experimental studies have been performed on large-scale transparent nozzles. The results obtained from these experiments provide good macroscopic agreement with small scale cavitating flows.

- Cloud cavitation instability is an interesting phenomenon which causes periodic shedding of coherent bubble clouds. The periodic shedding produces large pressure spikes and localised vorticity in the cavity wake. This has received very little attention for cylindrical orifice flows.
- The motion of a re-entrant jet is central to the cloud shedding instability. The exact mechanism by which this motion produces periodic shedding is complex and has received little attention for cylindrical orifice flows.

2.6 Thesis Objectives

The effects of cavitation on the flow within an orifice is an important issue. However there are a number of fundamental aspects of this flow which are not fully understood. With consideration to the relevant literature outlined above, the technical objectives of the current work were as follows.

To experimentally investigate and characterise the cavitating flows in a large-scale cylindrical orifice. A deliberate attempt was made to adopt a fundamental approach, particularly in relation to the geometry of the orifice and upstream configuration. The work aimed to explore the relationships between the internal cavitation structures and important flow characteristics such as the jet spray structure and hydraulic resistance for a wide range of conditions. Particular attention was placed on addressing the lack of high-quality discharge coefficient measurements available within the literature for various cavitation regimes and relate the data to the internal flow structures.

The lack of understanding of the periodic shedding behaviour for orifice flows was also addressed. Particularly, this study aimed to conduct spectral analysis to identify the impact of the partial cavitation regime on nozzle flow and elucidate the role of the re-entrant jet in the cloud shedding process. Improved experimental techniques such as refractive index matching and high resolution high-speed visualisation were used to investigate the mechanism responsible for the cavitation instability.

Chapter 3

Experimental Rig Design

This chapter provides the details of design and specifications of the experimental nozzle cavitation facility used in this study. Complete design of a new and novel experimental cavitation research facility was undertaken and will be discussed in detail. Characterisation of the test fluid, as well the data acquisition and control systems, will also be discussed.

3.1 General Description

In order to meet the objectives outlined in section 2.6 the design and fabrication of a cavitation rig was completed, which allowed for interrogation of the cavitation inside a large-scale ($D = 8.25mm$) cylindrical orifice. Given the complexity of the undertaking, the design aimed to provide the functionality required for the current work, whilst offering the utility to meet future experimental needs. A schematic of the cavitation rig is shown in figure 3.1 with the critical components itemised in table 3.1. Photos indicating the overall scale of the rig are also shown in figure 3.2 and figure 3.3.

Flow through the test section was generated using a double acting hydraulic cylinder, which was coupled via a shaft to a second cylinder containing the test fluid. Forward motion of the hydraulic cylinder caused the test fluid to be driven through a delivery pipe to the test section, which consisted of an acrylic nozzle with a sharp-edged cylindrical orifice (see section 3.2). As the liquid velocity was controlled by the reciprocating motion of the driving piston, the liquid was

3.1 General Description

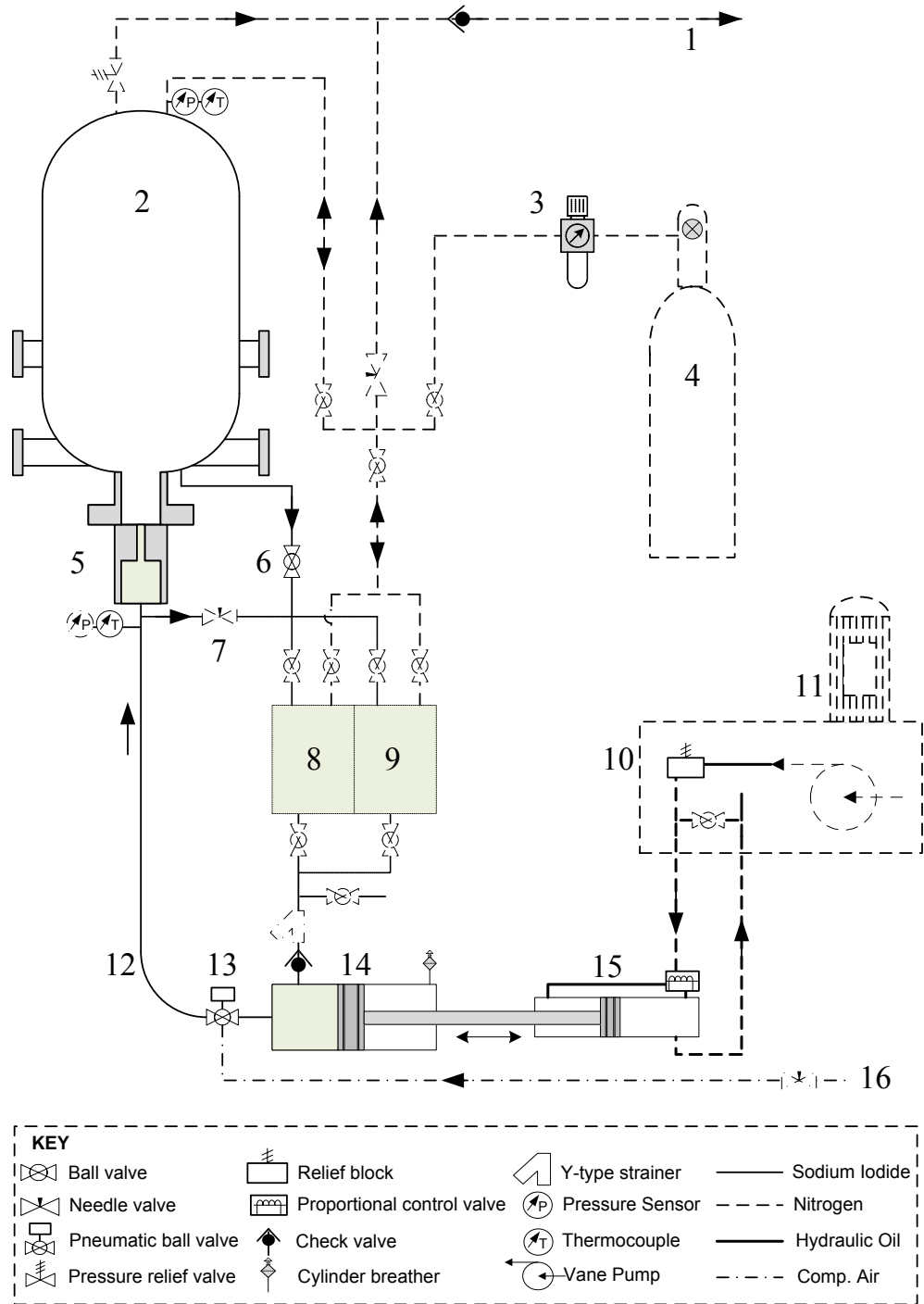


Figure 3.1: Experimental rig schematic. Major components are itemised in table 3.1.

3.1 General Description

Table 3.1: Experimental rig schematic component list (figure 3.1)

Item #	Description
1	Pressure vessel gas bleed line
2	Optical access pressure vessel
3	Pressure regulator
4	Nitrogen gas supply
5	Test section
6	Pressure vessel fluid drain line
7	Test section fluid drain line
8	Test fluid tank 1
9	Test fluid tank 2
10	160L hydraulic oil reservoir
11	15kW electric motor
12	Test fluid supply pipe
13	Pneumatically actuated ball valve
14	Test fluid cylinder
15	Double acting hydraulic cylinder
16	Compressed air supply valve

expelled in discrete volumes referred to as *injections*. The high speed jet which results from the nozzle contraction was then sprayed vertically upwards into an optical access pressure vessel. The rig allowed for the independent control of both the Reynolds number, Re , and the Cavitation number, K , of the flow. Specifying the velocity of the piston controlled the Re (for given fluid properties), while variation of the ambient pressure within the pressure vessel allowed for control of K (for a given Re).

The vertical orientation of the nozzle was a central feature of the design as it eliminated the need for a pre-nozzle valve to control the liquid. Typically these valves introduce turbulence prior to the nozzle entrance, which affects the flow within the test piece. In fact significant attention was paid to the uniformity of the flow entering the test section and remove potential sources of flow asymmetry.

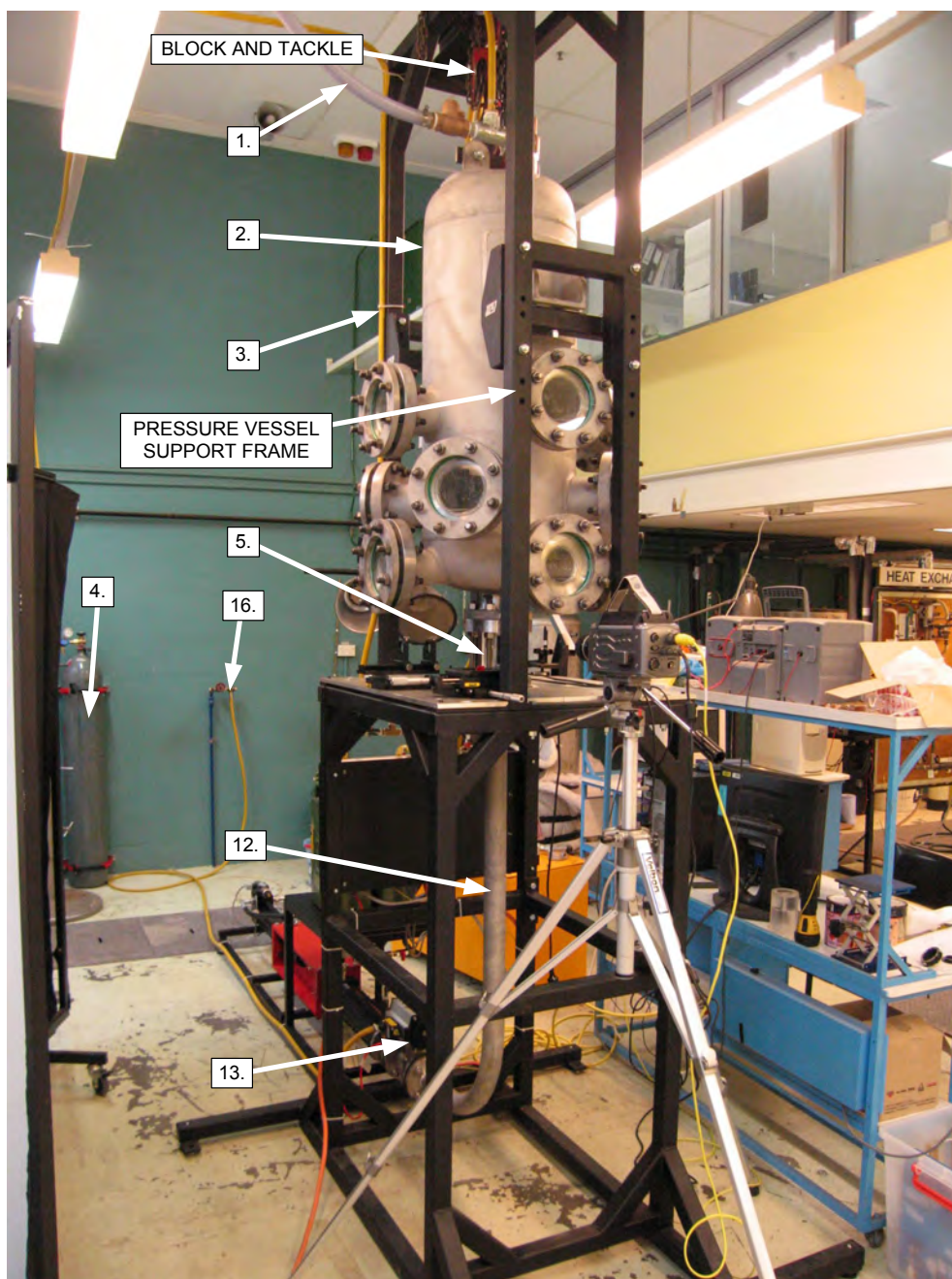


Figure 3.2: Overall view showing pressure vessel and support frame. Item numbers correspond to table 3.1.

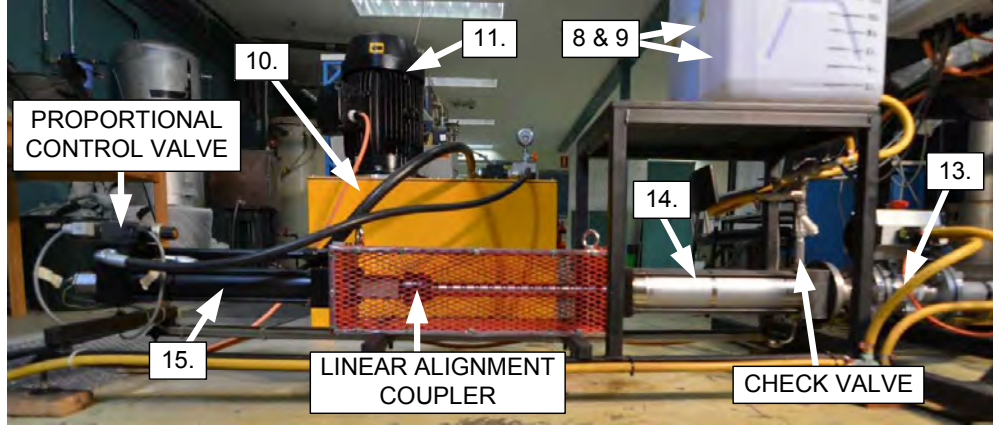


Figure 3.3: Hydraulic and test fluid cylinder configuration. Item numbers correspond to table 3.1.

This feature of the design will be discussed in more detail in section 3.3.

A full-bore pneumatic ball valve located directly at the outlet of the test fluid cylinder was used to control flow of fluid through the delivery pipe. Before each injection the ball valve was closed and the piston retracted. Suction pressure created behind the piston was used to draw liquid through a check valve and into the test fluid cylinder from one of two supply tanks. Once the cylinder was fully retracted the pneumatic ball valve was opened and the liquid driven through the 52mm diameter supply pipe into the test section.

The velocity of the fluid through the nozzle, and hence Reynolds number, was directly proportional to the hydraulic piston velocity. The motion of the double acting hydraulic cylinder was governed by the direction of flow of high pressure hydraulic oil from the hydraulic power unit. This was dictated by a position of a proportional control valve on the hydraulic fluid manifold which was controlled by an analog voltage input. The control of this system is discussed more in section 3.4.

A significant component of the rig was the optical access pressure vessel, located down-stream from the acrylic test piece. The primary function of this pressure vessel was to accurately regulate the ambient gas pressure, which allowed control of the cavitation number of the flow within the nozzle. Complementary to this, nine viewing windows in the pressure vessel provided optical access to

the spray structure of the jet. In fact, the rig was designed to operate in two distinct modes. For visualisation and measurement of the cavitation within the orifice the acrylic nozzle is positioned below the pressure vessel. Alternatively, the removal of a mounting flange allowed the acrylic nozzle to be inserted into the base of the pressure vessel, which provided optical access to the near nozzle spray region via the viewing windows. Further details of the pressure vessel are outlined in section 3.5.

Once the piston reaches the end of its stroke, ending the injection of test fluid, the pneumatic ball valve was closed and the driving piston stopped to prevent the gas pressure within the pressure vessel driving the cylinder backwards. The test fluid within the pressure vessel was then drained via a drainage port in the supply pipe. The location of this port was below the acrylic nozzle, ensuring that all liquid that was injected through the nozzle was drained out of the system. This allowed free bubbles, which can act as cavitation nucleation sites, to be dispersed and gas diffusion between the bubbles and the liquid to reach equilibrium. The fluid was drained to the storage tank which was not being used for liquid supply. Here it was allowed to settle in the tank while gases dissolved in the solution returned to equilibrium concentrations at atmospheric pressure before the being injected again. These measures were used to help prevent re-circulation of the fluid altering the observed cavitation structures.

During the injection a data acquisition system was used to record a number of different parameters including; fluid, gas and ambient temperature, pre-nozzle liquid pressure and gas pressure. A LabVIEW program was also written to monitor and control the position and velocity of the driving piston and synchronise and initiate high-speed visualisation. The details of these systems will be discussed in section 3.8.

3.2 Test Section

3.2.1 Nozzle Design

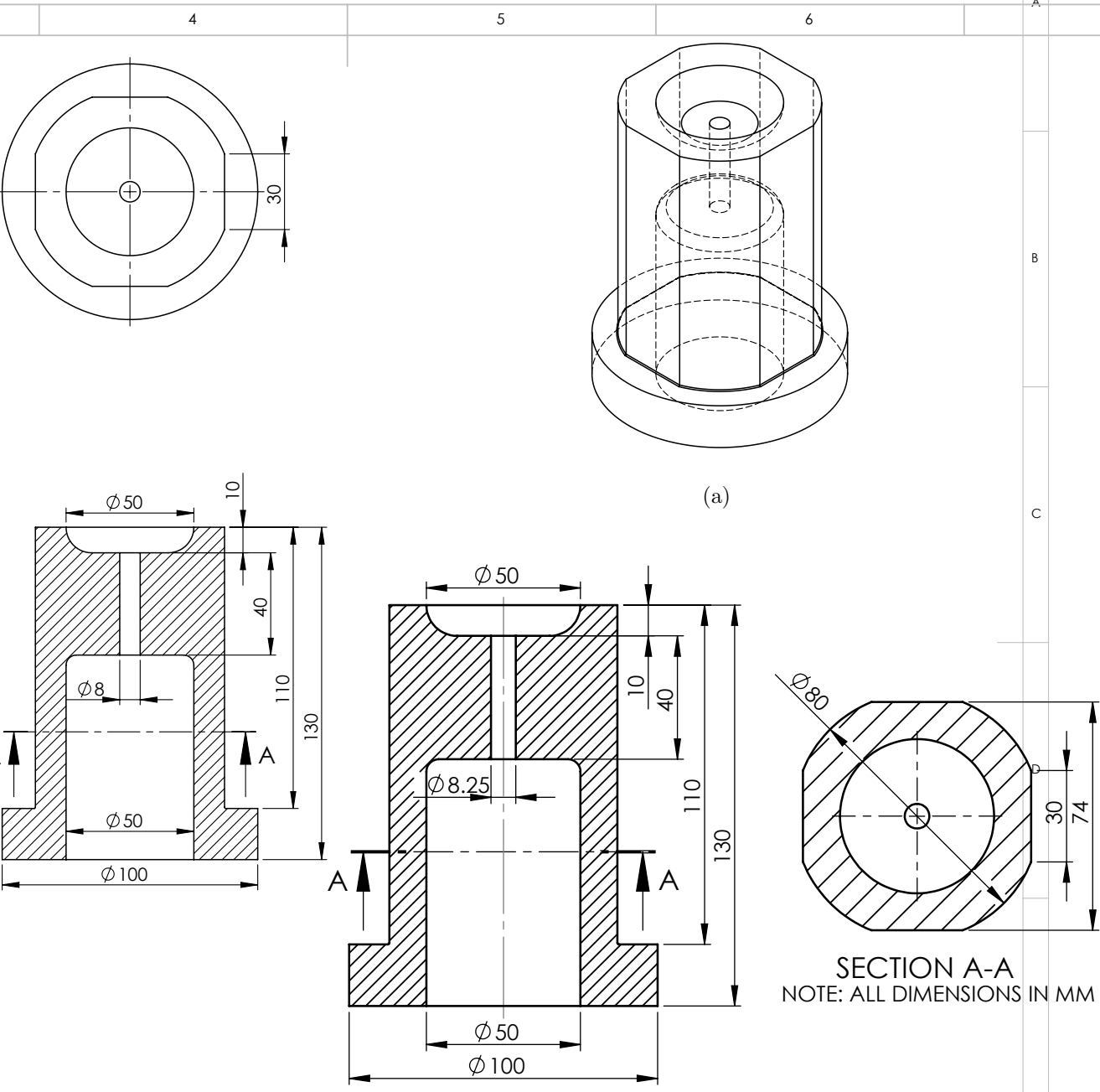
The nozzle geometry selected for these experiments is a plain orifice style cylindrical nozzle. This simplified geometry allows fundamental exploration of the

influence of cavitation on orifice flow structures without the introduced complications of upstream nozzle geometries. A schematic and cross-sectional views of the acrylic nozzle can be seen in figure 3.4(b). The orifice had a diameter of $D_n = 8.25mm$, a length of $L = 40mm$ and zero nominal inlet rounding. This resulted in an L/D_n ratio of 4.85, which is within the range expected to produce optimal spray divergence (see section 2.2.1), aiding in the study of the effects of cavitation on spray angle. For consistency with the literature nozzle length to diameter ratio will be referred to for the remainder of the thesis as L/D . The acrylic nozzle incorporated a $D_e = 50mm$ diameter entrance section allowing optical access to a small length of the supply pipe before the orifice. The resulting contraction ratio between the entrance section and the nozzle was $D_e/D_n = 6.06$. A summary of the important nozzle dimensions can be found in table 3.2.

The nozzle was machined from cast acrylic (polymethyl methacrylate - PMMA), which offers the benefits of chemical compatibility with a wide range of fluids, good machinability and relatively low cost. However, most importantly acrylic is optically clear and has one of the lowest refractive index of all transparent engineering plastics ($n \approx 1.49$). This allows for refractive index matching between the test liquid and the acrylic nozzle which helps to eliminate optical distortion during visualisation of the flow through the cylindrical orifice section. To further aid with optical access flat faces were machined onto the outer surface of the test section at 90° to each other. All surfaces of the acrylic used for optical measurements were polished to a glass like finish.

Table 3.2: Nozzle Parameters

Parameter	Value
Nozzle Length, $L(mm)$	40.00
Nozzle Diameter, $D_n(mm)$	8.25
L/D Ratio	4.85
Pre-nozzle Entrance Diameter, $D_e(mm)$	50.00
Supply Pipe Diameter, $D_p(mm)$	52.00



UNLESS OTHERWISE SPECIFIED: DIMENSIONS ARE IN MM SURFACE FINISH: 3.2/ TOLERANCES: ±0.5 MATERIAL: PERSPEX ROD	DEBUR AND BREAK SHARP EDGES	DO NOT SCALE DRAWING	REVISION 2	51	DEBUR AND BREAK SHARP EDGES	DO NOT SCALE DRAWING
Figure 3.4: Acrylic nozzle test piece showing (a) 3-dimensional projection, and (b) cross-sectional view.	CONTACT Cameron Stanley (02) 9385 6005	(b) UNSW	TITLE: 8mm Ø Acrylic Nozzle	DWG NO. 002_08_09	A3	UNSW
DATE: 09/08/2009	WEIGHT:	SCALE:1:2	SHEET 1 OF 1			

The relatively low yield strength of acrylic material provided the greatest limitation for the design and fabrication of the test section. Acrylic also has a tendency to exhibit brittle properties with age, which further emphasised the need for a comprehensive design process to ensure the nozzle was capable of withstanding the stresses it was subjected to during experiments. The design procedure followed the guidelines outlined in the Australian Standards governing the safe design of pressure vessels (AS1210) and pressure piping (AS4041). However as acrylic is not a material commonly used for components subjected to internal pressures, specifications regarding allowable stress limits and material standards were not available within the listed standards. To accommodate this lack of explicit guidance considerable attention was given to evaluating the stresses within the nozzle for the maximum design pressure of $1.5MPa$. Fundamental stress calculations were complemented by Finite Element Analysis (FEA) and hydrostatic testing of a full scale nozzle to ensure material integrity and operator safety. The material properties used for these calculations were chosen conservatively from data provided by the supplier, shown in table 3.3. Each of these procedures will now be briefly described.

Table 3.3: Material Properties of Cast Acrylic

Property	Supplier Data	Selected Value
Tensile Strength, $\sigma_y(MPa)$	55-76	55
Young's Modulus, $E(GPa)$	2.41-3.45	2.41
Poisson's Ratio, ν_p	0.35-0.41	0.37

3.2.2 Analytical Stress Calculations

Evaluating the design in figure 3.4 maximum material stresses were expected to occur in the wall of the nozzle in the region preceding the orifice. Material stresses were calculated analytically by considering the cross-section formed by a horizontal plane passing through this region, as shown on the right side of

figure 3.4(b). As a conservative estimation the cross-section was approximated as cylindrical, with inner diameter equal to the nozzle internal diameter and outer diameter equal to the reduced section diameter at the viewing flats, as shown in figure 3.5.

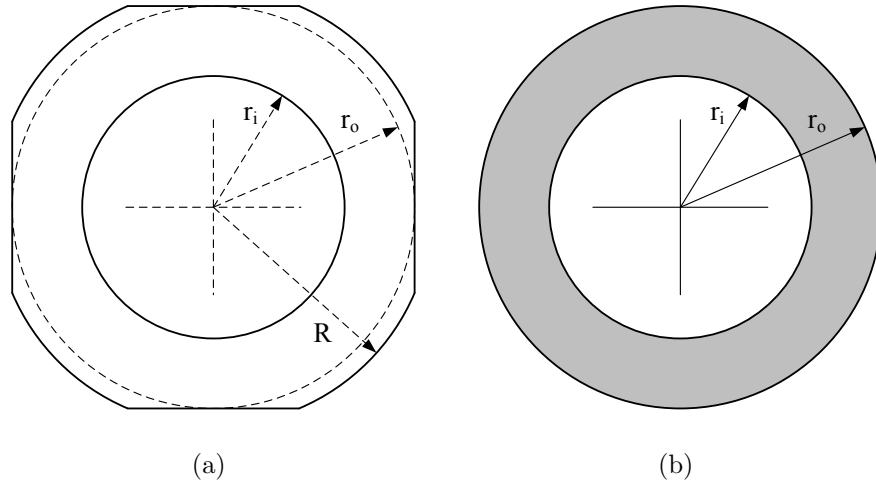


Figure 3.5: (a) Total nozzle cross-sectional area ($2827.8mm^2$) and (b) simplified cylindrical cross-section ($2356.2mm^2$) used for stress calculations. Radial dimensions can be found in figure 3.4(b).

Using this simplified cylindrical cross section, material stresses can now be calculated treating the nozzle as a “thick walled” pressure vessel. This analysis is suitable for cylindrical shells where the ratio of internal radius to thickness, $r_i/t < 10$ and in this case $r_i/t \approx 2.1$. For a cylinder subjected to internal pressure loading the distribution of hoop stress, σ_h , and radial stress, σ_r , are given by Lamé’s formulation (Young & Budynas (2002)):

$$\sigma_h = \frac{r_i^2 P}{(r_o^2 - r_i^2)} \left(1 + \frac{r_o^2}{r^2} \right) \quad (3.1)$$

$$\sigma_r = \frac{r_i^2 P}{(r_o^2 - r_i^2)} \left(1 - \frac{r_o^2}{r^2} \right) \quad (3.2)$$

and axial stress, σ_a , is given by:

$$\sigma_a = \frac{r_i^2 P}{(r_o^2 - r_i^2)} \quad (3.3)$$

where r_i is the inner radius, r_o is the outer radius, r is the radial variable and P is the applied pressure. It can be noted that the hoop and radial stresses (σ_h and σ_r) vary as a function of the nozzle radius, whereas the axial stress (σ_a) remains constant. Applying these relationships to the section in figure 3.5(b) for an internal pressure of $1.5MPa$ yields the following stresses:

$$\sigma_h = 1.26 \left(1 + \frac{37^2}{r^2} \right) \quad (3.4)$$

$$\sigma_a = 1.26 \quad (3.5)$$

$$\sigma_r = 1.26 \left(1 - \frac{37^2}{r^2} \right) \quad (3.6)$$

It can easily be seen that both the hoop and radial stresses vary with radial location, while the axial component remains invariant. To accurately represent realistic loading conditions the axial stress component must also include the compressive stresses introduced by the bolts holding the acrylic nozzle between the supply pipe and the bottom of the pressure vessel. O-ring seals were used at both ends of nozzle to provide liquid sealing against the mating components. These are classified as “self-energising” and technically require no pre-load to initiate sealing. In practice a minimal amount of axial loading is required to prevent joint separation. This value was determined according to the aforementioned Australian standards, and set to $25kN$. Applying this load to the conservative cross-sectional area and using the standard convention that compressive stresses are assigned as negative this preload results in a combined axial stress of $-9.35MPa$. Combining these components it can be seen that the maximum principal stress element is located on the inner surface of the nozzle. To evaluate the likelihood of material failure, Tresca stress were calculated. Table 3.4 presents the comparison between these stresses for on the inner and outer surface of the simplified cylindrical section.

Table 3.4: Analytical nozzle stresses

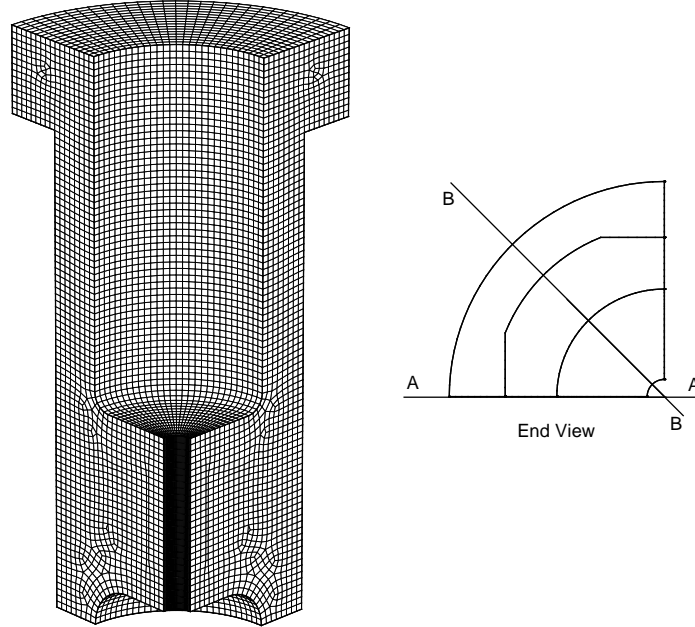
Name	Stress (MPa)	
	$r = r_i$	$r = r_o$
Hoop, σ_h	4.02	2.52
Radial, σ_h	-1.50	0.00
Axial, σ_h	-9.35	-9.35
Von Mises, σ_{vm}	6.69	5.94

3.2.3 Finite Element Analysis

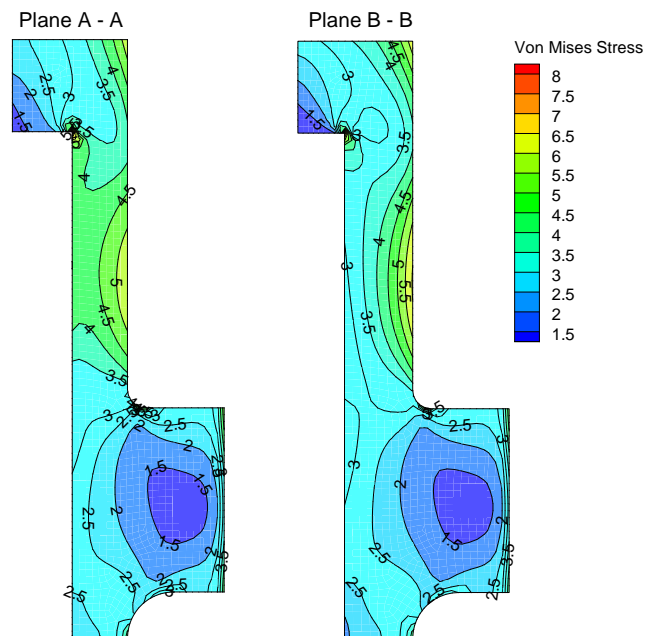
Finite Element Analysis (FEA) was used to complement the simplified stress analysis above. Pre and post processing were conducted using ANSYS version 13. Geometrical symmetry allowed the nozzle to be modelled as a quarter-section with the use of symmetry boundary conditions. A total of 41981 3-D quadratic tetrahedral elements were used to generate the computational mesh, with particular attention being paid to the internal fillet radii where stress concentrations were expected. The ratio of adjacent element size was kept below 2:1 and element aspect ratios for all elements were between 0.33 and 3. All FEA modelling specifications listed in Australian Standard AS1210 were met or exceeded.

Material properties used in the model are those listed in table 3.3. The maximum test injection pressure of $1.5MPa$ was set as the applied pressure for the model. The mesh and Von Mises stress fields generated by the model can be seen in figure 3.6.

Maximum Von Mises stresses of $8.23MPa$ were found to occur on the sharp edge on the corner of the expansion from the pre-nozzle section to the larger diameter section. This large section is required to support the nozzle when it is inserted into the pressure vessel for spray analysis (see section 3.5). The sharp edge, although detrimental for stress generation, where required to allow sufficient space for an o-ring seal on the protruding face. Wherever possible radii were used to reduce stress concentration factors. The resulting factor of safety determined from this maximum value of $8.23MPa$ was approximately 6.7 taking



(a) Nozzle quarter-section mesh and end projection showing cross-sections



(b) Von Mises stress contours for plane A-A (left) and plane B-B (right)

Figure 3.6: Finite Element Analysis stress calculations

a conservative material yield strength value of $55MPa$. For a comparison to the analytical calculations maximum Von Mises stresses for the pre-nozzle section for the cross-sections indicated in figure 3.6(b) are listed in table 3.5.

Table 3.5: FEA nozzle stresses

Plane	Von Mises Stress (MPa)	
	$r = r_i$	$r = r_o$
Plane A-A	5.32	4.50
Plane B-B	4.45	2.28

The calculated stresses were less than those determined from the analytical thick-walled pressure vessel equations. This was an expected consequence of the conservative approach taken by approximating the nozzle cross-section as cylindrical (see figure 3.5(b)). Further to this, the factor of safety of 6.7 under worse-case loading conditions indicated the material was capable of withstanding the imposed loads safely.

3.2.4 Hydrostatic Testing

To further ensure the material integrity of the acrylic under high load conditions a replica nozzle was machined and hydrostatically tested according to the guidelines in Australian Standard AS1210. The replica nozzle was bolted between two flat plates to closely simulate the bolting configuration during operation. A dual axis, 90° foil strain gauge was attached to the outer surface of the acrylic nozzle in the location of maximum indicated Tresca stress. A hand-operated hydraulic pump was used to increase the static pressure in increments of $10psi$ from $20psi$ to $330psi$ ($137kPa$ - $2270kPa$), 1.5 times the maximum design pressure of $1.5MPa$. The pressure was then released and the process repeated 10 times. No hysteresis was observed for the recorded strain indicating the material remained within the elastic limits for the applied pressure range. All tests and stress evaluations of the nozzle indicated the acrylic material was suitable for use in the test rig at injection pressures up to $1.5MPa$.

3.3 Liquid Supply Piping

The liquid supply pipe was used to connect the outlet of the pneumatic ball valve to the base of the test piece. It was fabricated from schedule 40, 50mm nominal bore (internal diameter, $D_p = 52mm$), 304 stainless steel pipe. ANSI 150 grade flanges were welded to both ends and used to fix the pipe in position. At the bottom end the pipe was bolted to the outlet of the 50mm full-bore pneumatic ball valve, which was attached to the outlet of the test fluid cylinder. The flange was sealed against the ball valve using rubber gaskets, which were cut to be flush with the pipe inner wall. At the top of the pipe, a recess in the flange accommodated the nozzle. Bolts between the pipe flange and the flange on the base of the pressure vessel sandwiched the acrylic nozzle in position. A bend in the pipe was required to turn the fluid 90° from the horizontal plane of the test fluid cylinder to the vertical injection plane. The 90° bend was mandrel bent to ensure no wrinkling on the inner surface which could introduce disturbances to the flow.

3.3.1 Flow Development

A great deal of importance was given to ensuring the upstream flow conditions had minimal effects on the nature of the cavitation which developed within the nozzle. Ideally, fully developed flow is desirable prior to the nozzle contraction. Asymmetries in the entry flow can manifest themselves as asymmetrical cavitation structures.

The pipe diameter was selected to be sufficiently large to minimise the liquid velocity and flow disturbances, whilst also minimising the volume of the system. The pipe diameter was then reduced slightly to $D_e = 50mm$ in the pre-orifice section of the test piece which provided a contraction ratio of $D_n/D_e \approx 0.165$. This value was sufficiently low that the influence of D_n/D_e on the discharge coefficient of the nozzle was unlikely to exceed 1% for any Reynolds number (Lichtarowicz *et al.* (1965)).

It is well known that curves in pipes introduce secondary flow fields, due to the difference in centrifugal force experienced by the higher velocity particles near the flow axis compared to the particles near the wall (Schlichting (1968)). The

effects of the secondary fields on the pressure distribution in the flow are more pronounced for laminar flow than turbulent, however, the influence on the flow in both regimes is communicated both upstream and downstream of the bend (Berger *et al.* (1983)). Experiments conducted by Ito (1960) for fully developed turbulent flow in a 90° bend indicate the flow remains affected 40-50 diameters downstream for a Reynolds number of 2×10^5 . For a $52mm$ diameter pipe this length of downstream straight section ($\approx 2.5m$) is impractical. As such, a $1m$ ($\approx 20D$) post bend straight section was used to dramatically reduce, albeit not entirely eliminate, secondary effects. Figure 3.7 shows a schematic of the supply pipe system indicating the major components and their relative lengths.

3.3.2 Computational Fluid Dynamics Modeling

Computational Fluid Dynamics (CFD) modeling was used to explore the influence of the pipe geometry on the flow asymmetries. Gambit version 2.3.16 and Fluent version 6.3.26 were used for pre-processing and processing respectively. The geometry modelled included the test fluid cylinder, full-bore ball valve, supply pipe and acrylic nozzle test section. For all cases the piston position was placed at the full extension position as it was assumed this introduced the greatest disturbance to the flow entering the supply pipe. Plug flow entry conditions were used as this accurately represents the piston motion driving the flow, with the highest piston velocity capable ($0.185m/s$) used for all simulations.

A number of pipe bend radii (200, 250, 300 and $350mm$) and post-bend straight lengths (200, 400, 600, $1000mm$) were investigated for a fixed pipe diameter of $52mm$. Structured computational meshes were used for all simulations with the final mesh having approximately 1.9 million cells. A hemispherical section of this mesh can be seen in figure 3.8. A range of turbulence models were explored to ensure the consistency of the results. Insignificant differences were observed between the models and as such the final simulations used the $k-\omega$ SST turbulence model. As the intention of these simulations was to explore the variation in nozzle flow asymmetry with variations in bend radii and post-bend straight length only single phase flow conditions were modelled.

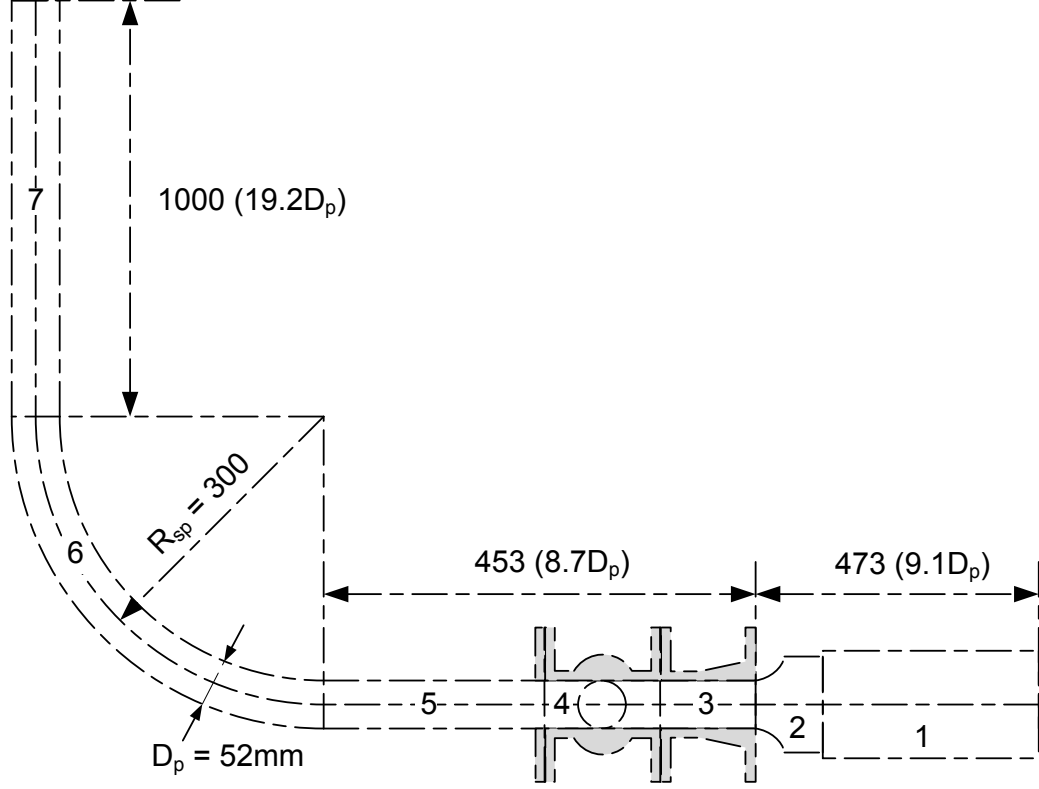


Figure 3.7: Nozzle supply-pipe centerline dimensions given in *mm* and pipe diameters. 1. Test fluid cylinder, 2. Cylinder end cap, 3. Outlet flange adapter, 4. Full-bore pneumatic ball valve, 5. Pre-bend straight, 6. 90° bend, 7. Post-bend straight

Results of the CFD simulations agreed with design predictions, indicating flow asymmetries introduced by the pipe bend were most effectively reduced by increasing the pipe bend radius and the length of the post-bend straight section. The final geometry which incorporated a pipe bend radius of $R_{sp} = 300\text{mm}$ and a 1m straight was shown to sufficiently eliminate these effects. Figure 3.9 shows the variations in isocontours of velocity magnitude for two different planes perpendicular to the pipe axis; the first (3.9(a)) is directly at the exit of the bend, while the second (3.9(b)) is located 20mm prior to the orifice contraction. Sec-

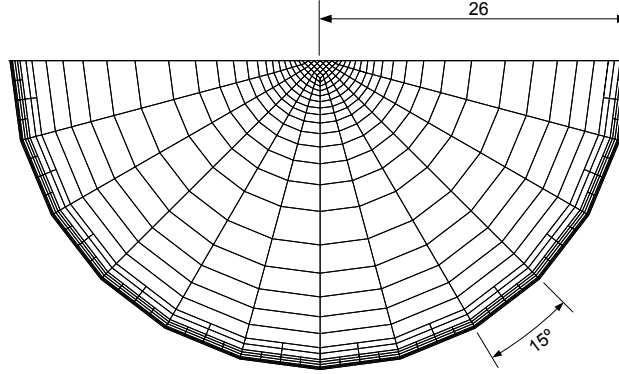


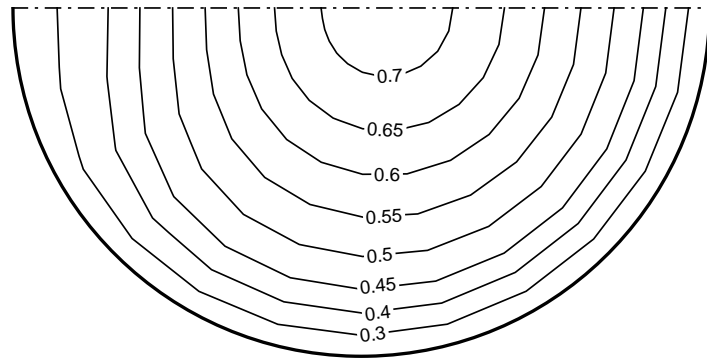
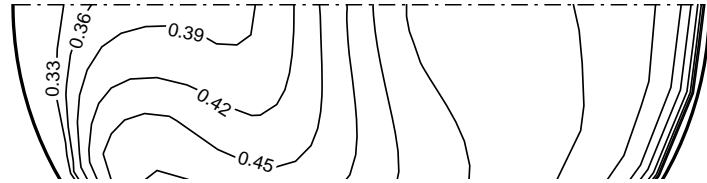
Figure 3.8: Cross-section of CFD pipe mesh

ondary velocity fields introduced by the bend are clearly visible at the bend exit but have been significantly suppressed before entrance to the nozzle. Together with the smoothing effect of the straight section on the flow profiles, the large contraction ratio between the pipe and nozzle diameters further serves to coerce the flow towards axisymmetry in the approach to the nozzle entrance. Axial velocity profiles on a plane bisecting the supply pipe can be seen in figure 3.10 and further illustrate the influence of the contraction ratio.

The “wing-shaped” velocity contours observed between 5 and 10mm into the nozzle (figure 3.10(b)) are consistent with the experimental observations of Soteriou *et al.* (1999), and result from the translation of strong radial flow components into axial velocity as the flow accelerates past the separated boundary region. Once the flow had proceeded to approximately 2 orifice diameters into the nozzle the ring of higher velocity had been smoothed out by the reattachment of the boundary layer. From this point on the flow progresses towards a fully developed profile, with insignificant asymmetries remaining in the flow.

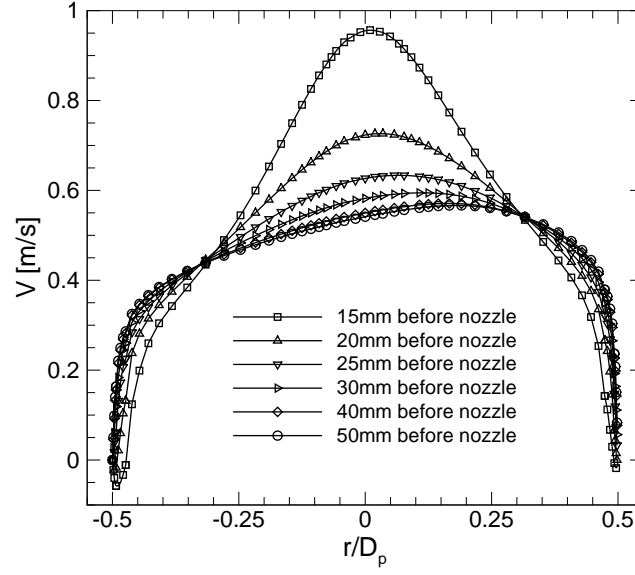
3.4 Hydraulic Actuation System

The injection of fluid through the nozzle into the pressure vessel is controlled by the motion of the hydraulic driving cylinder. The main elements of the hydraulic

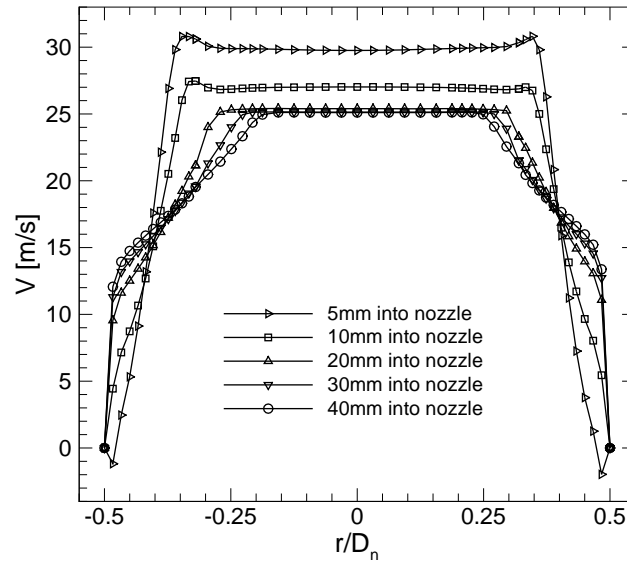


(b) plane 20mm before the nozzle entrance

Figure 3.9: Pipe half-sections showing isocontours of velocity magnitude (m/s). Secondary velocity contours clearly evident at the bend exit, (a), are greatly diminished before the flow enters the nozzle, (b).



(a)



(b)

Figure 3.10: Axial velocity profiles at various stream-wise distances (a) before entrance to the nozzle and, (b) into the nozzle from the entrance plane.

3.4 Hydraulic Actuation System

driving system are: 4" diameter test fluid cylinder, 2 1/2" diameter double-acting hydraulic cylinder, proportional control valve, fixed displacement vane pump (31.8ml/rev), 15kW Electric motor and a 160L oil reservoir. The area reduction ratio between the test fluid and hydraulic cylinder produces a maximum pressure in the test fluid of 6MPa and a maximum volume flow rate of 1.5L/s. Operational fluid pressure was limited to 1.5MPa by the design pressure of the acrylic nozzle and pressure vessel. A technical schematic of the hydraulic system can be found in appendix D.

As discussed in Section 3.1, injection of fluid through the test section is controlled by the motion of the test fluid cylinder. This cylinder is coupled to the double-acting hydraulic cylinder via a linear alignment coupler and shaft. The position of the proportional control valve on the driving cylinder, controlled via a $\pm 10V$ analog voltage sent from a control unit, governs the direction and flow rate of hydraulic oil into the cylinder from the pump and reservoir. A "dead-band" of cylinder movement existed between approximately -2.5V and +3V. After this dead-band the piston velocity became roughly parabolic with input; a '+' voltage moving the piston forward, a '-' voltage retracting the piston.

A Linear Displacement Transducer (LDT) within the piston bore allows for highly accurate measurement of the instantaneous position of the piston. The displacement signal was then differentiated to give piston velocity for each injection. The steady flow of hydraulic fluid from the fixed displacement vane pump produced highly stable and repeatable piston velocity and allowed precise control of the mass-flow through the test section.

To reduce disturbances to the flow in the supply pipe a custom end cap was designed for the test fluid cylinder (see appendix D). A smooth bell-mouth shaped contraction was used to transition the flow from the cylinder internal diameter (101.6mm) to that of the supply pipe (52mm). CFD simulations indicated complete removal of fluid recirculation zones in the end cap region under worst case flow conditions.

During the test fluid cylinder filling process, described briefly in section 3.1, suction pressure created by the retracting piston was used to drawn fluid into the cylinder via a check valve and y-type strainer. Pressure drop data provided by the check-valve manufacturer suggested a flow rate of less than 10L/min was

required to ensure that the liquid pressure remained above the vapour pressure (suppression of cavitation). However, experience showed a retraction velocity corresponding to $<1L/min$ was required to prevent cavitation damage of the spring-loaded ball within the check valve.

3.5 Optical Access Pressure Vessel

The optical access pressure vessel formed a critical part of the test facility and was designed and fabricated for this study. As well as providing a means to control the gas pressure downstream from the nozzle, and hence the cavitation within the nozzle, viewing windows in the wall of the pressure vessel provided direct visual access to the spray jet. This section provides an overview of the salient features of the pressure vessel, however a complete list of engineering drawings can be found in appendix C.

A schematic of the pressure vessel is shown in figure 3.11 and a list of the major design parameters can be found in table 3.6. Nitrogen gas was supplied to the vessel via a pressure regulator and supply valve, which provided coarse adjustment of the gas pressure. Fine adjustment was then achieved by bleeding gas from the vessel using a needle valve on a drainage line, allowing repeatability of gas pressure conditions to within approximately $\pm 3kPa$. The volume of the pressure vessel is such that the gas pressure increase due to the isothermal compression of the quiescent gas during the period of liquid injection is kept to less than 2.6%. A relief valve in the top of the vessel ensured gas pressures did not exceed $1.5MPa$.

The pressure vessel featured nine viewing windows arranged in three axially spaced sets of three orthogonal windows, referred to here as *triplets*. The location and size of the viewing windows was strictly controlled by the design code, AS1210-1997. The first triplet was positioned as close as possible to the base of the vessel, with a centre distance of $142.4mm$ from the face of the bottom flange. Each triplet was orientated 45° offset from the adjacent triplet to minimise the axial spacing, with centre-to-centre distances of $177mm$ and $215mm$ between the first and second, and second and third, triplets respectively. Heavy limitations on the size of holes allowed in the torispherical dished ends of the vessel restricted the

3.5 Optical Access Pressure Vessel

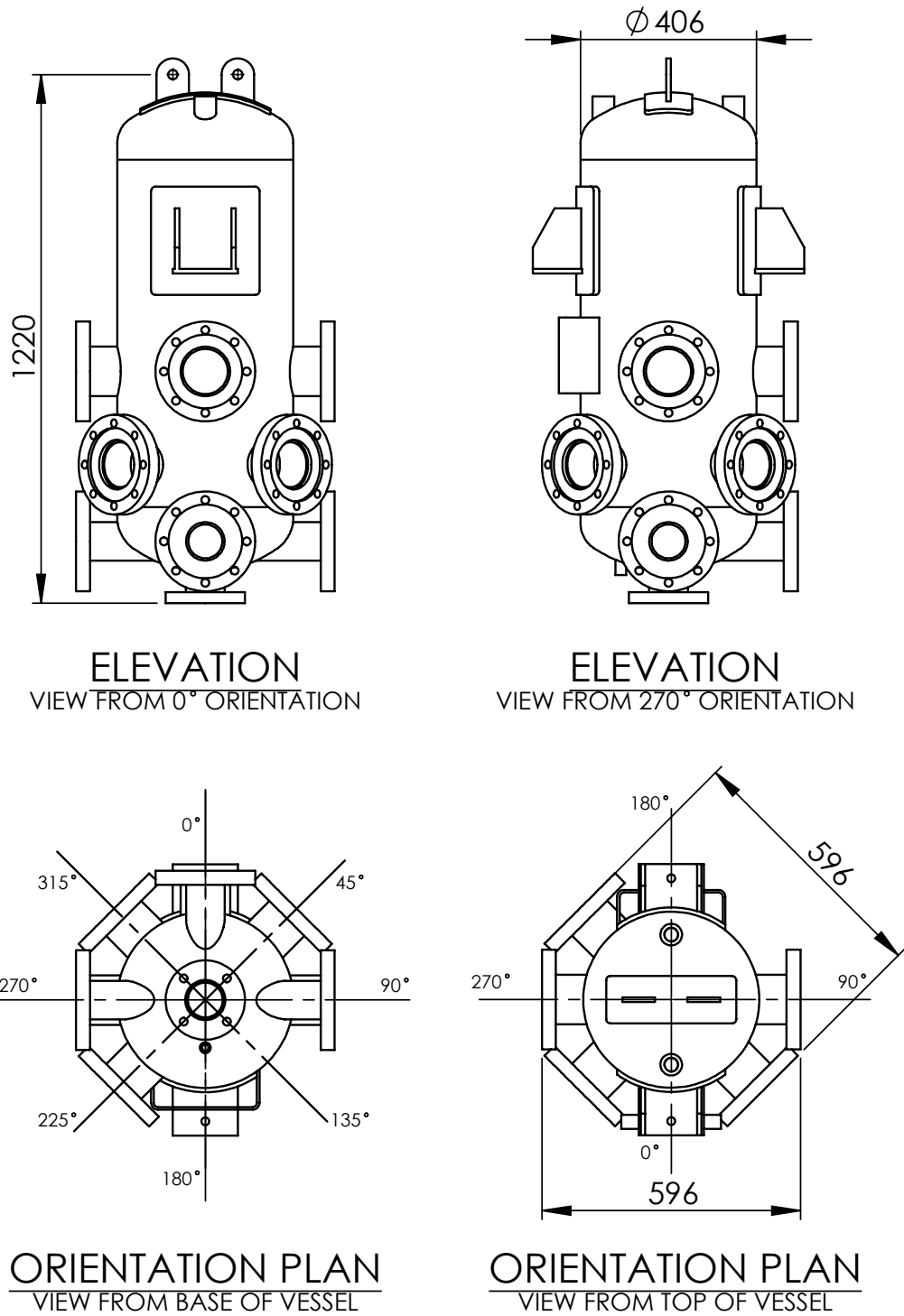


Figure 3.11: Pressure vessel - dimensions shown in *mm*.

3.5 Optical Access Pressure Vessel

Table 3.6: Pressure vessel design parameters

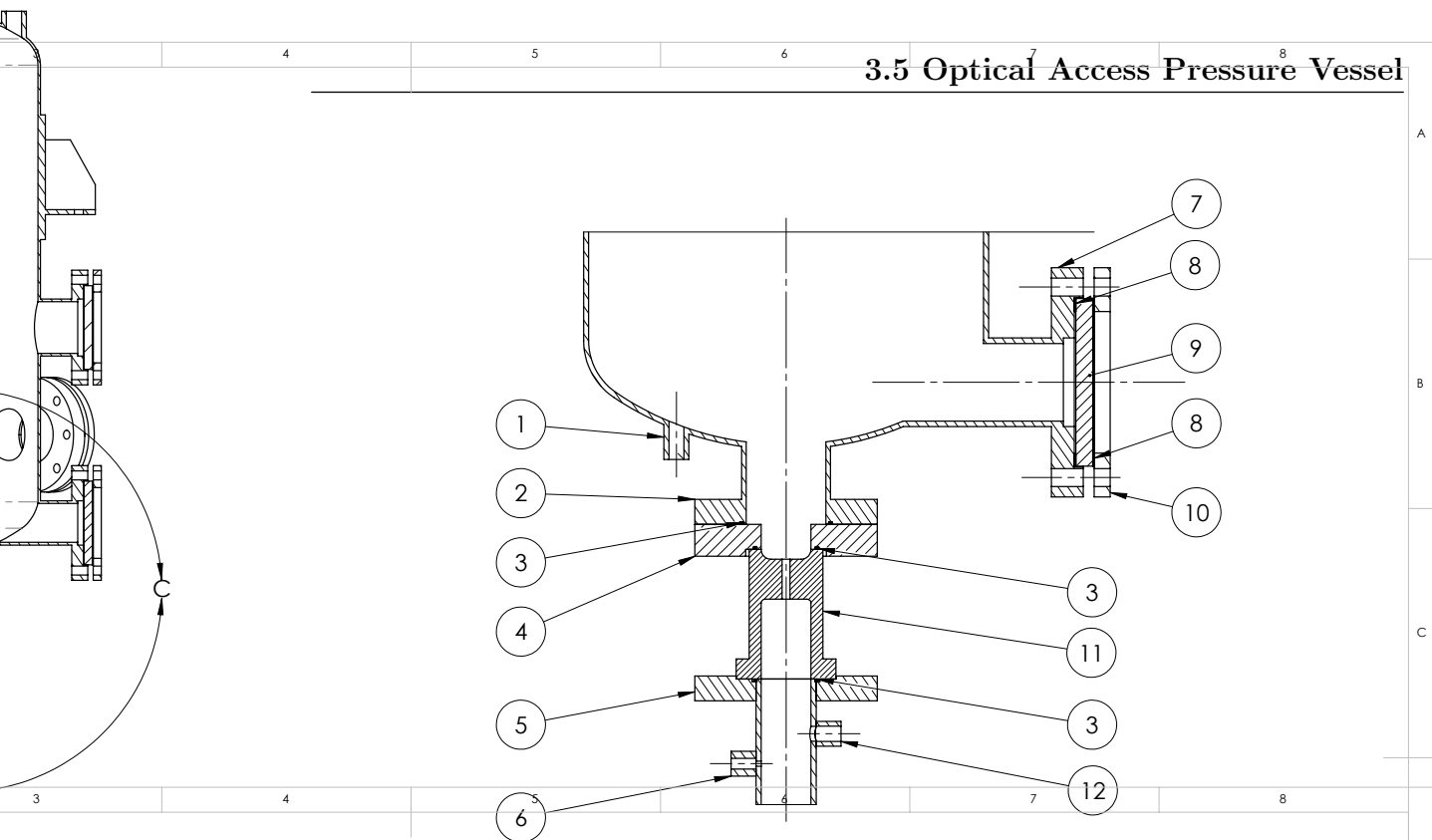
Property	Value
Design Code	AS1210-1997
Design Pressure ($kPag$)	1500
Test Pressure ($kPag$)	2260
Design Temperature ($^{\circ}C$)	50
Code Class	28
Hazard Level (AS4343)	C
Material	ASTM A240-304
Empty Weight (kg)	317
Volume (L)	123
Internal Diameter (mm)	388
Viewing port diameter (mm)	77.9 (bottom 3) 102.3 (top 6)

diameter of the lowest triplet ports to $77.9mm$, whereas the diameter for the second and third triplet was $102.3mm$. The orthogonal layout of each triplet meant back-lit photography, laser light-sheet illumination and Schlieren measurements of the spray structure are possible at each axial location.

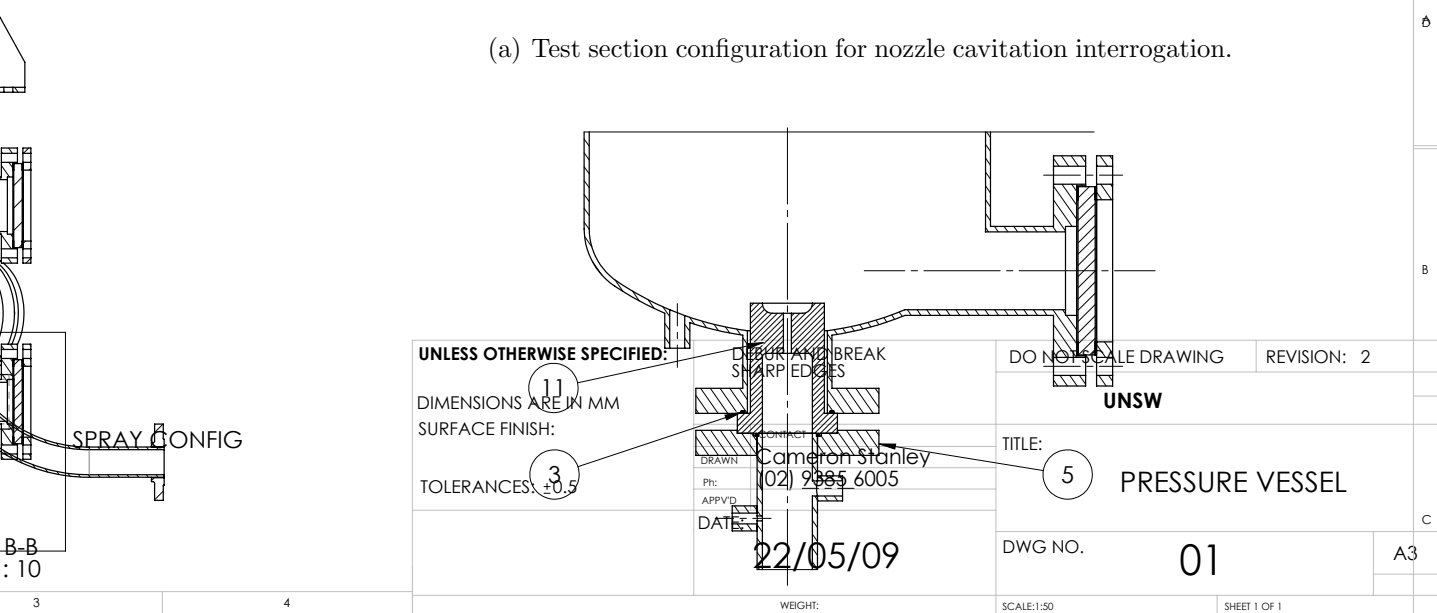
The design of the pressure vessel accommodated two major experimental configurations (see figure 3.12);

- visualization and measurement of the cavitation in the nozzle with the test section held outside the pressure vessel, and,
- interrogation of the near nozzle spray structures with the test section inserted into the base of the pressure vessel.

The test section is fixed in position between a flange on the upper end of the supply pipe and the bottom of the pressure vessel. When nozzle cavitation structure and turbulence is to be measured a removable adapter flange (item 4) is fixed to the base of the pressure vessel. A $10mm$ extension of the test piece



(a) Test section configuration for nozzle cavitation interrogation.



(b) Test section configuration for near-nozzle spray interrogation.
SCALE 1 : 5

Figure 3.12: Pressure vessel section view. Configuration (a) allows optical access to the test section for cavitation interrogation; Configuration (b) allows optical access to the exit plane of the nozzle for spray structure investigation.

Note: all bolts and piping connections are suppressed for clarity.

Table 3.7: Pressure vessel assembly component list (figure 3.12)

Item #	Description
1	Pressure vessel drainage port
2	Pressure vessel base flange
3	O-ring
4	Removable adapter flange
5	Supply pipe flange
6	Pressure sensor and thermocouple port
7	Pressure vessel viewing port flange
8	Gasket
9	Glass window
10	Window retaining ring
11	Acrylic nozzle test section
12	Supply pipe drainage port

beyond the exit plane of the orifice allows the tip of the test section to be inserted into a recess in the adapter flange, holding the nozzle outside of the vessel with the orifice entirely visible (see figure 3.12(a)).

For viewing and measurement of the near nozzle spray structure the locating flange is removed and the acrylic nozzle inserted into the base of the pressure vessel. In this configuration, the exit plane of the nozzle is vertically aligned with the lowest viewing window (figure 3.12(b)). Test fluid that accumulates in the base of the PV when the nozzle is in this configuration can be drained from the base of the PV through a drainage port (item 1) in the torispherical head, and returned to a settling tank.

3.6 Support Frame

The general frame structure was designed to support the major components of the rig, allow optical access to the acrylic nozzle for visualisation and diagnostics

and support measurement instrumentation. The major frame structure was broken into two components; the support frame for the pressure vessel and supply piping, and the support frame for the hydraulic and test fluid cylinders. Supplementary to these is an independent spacing structure between the two hydraulic cylinders. This ensured the large forces generated by the hydraulic cylinder were held independently of the light-weight cylinder support structure. Leveling feet under the base of both frame structures allows the test piece to be leveled.

To accommodate the two flow interrogation configurations discussed in Section 3.5 the pressure vessel is moved vertically relative to the test section. Lifting of the pressure vessel was performed using a block and tackle mounted to an I-beam at the top of the support frame and attached to lifting lugs on the top of the PV. Mounting brackets supporting the PV allow it to be bolted in various set positions.

Positioning of the high speed camera was controlled using a three-axis linear positioning stage attached to an aluminium plate mounted to the support frame roughly level with the base of the acrylic nozzle. An adapter plate was then used to attach the camera to the positioning stage at the correct working distance. This method ensured the camera was positioned at 90° to the flat faces on the acrylic nozzle and allowed accurate adjustments of lens focus or camera position.

3.7 Test Liquid Characterisation - Sodium Iodide

3.7.1 Refractive Index Matching

To prevent optical distortion during visualisation, refractive index matching between the acrylic nozzle and the test fluid was employed. A number of liquids exist which allow refractive index matching with acrylic ($n \approx 1.49$), each have their individual merits and shortcomings. Consideration must be given to chemical reactivity, harmfulness to the operator, solution viscosity and price. A tabulated list of solids and potential matching fluids can be found in Budwig (1994) and Miller *et al.* (2006). For this study aqueous sodium iodide solution was selected as the test fluid.

3.7 Test Liquid Characterisation - Sodium Iodide

Sodium iodide has been used in a number of studies to achieve refractive index matching. [Chen & Fan \(1992\)](#) and [Reese *et al.* \(1995\)](#) used a 55% *w/w* aqueous solution of NaI in a rectangular glass chamber enclosing their cylindrical Pyrex glass test section ($n \approx 1.47$) to improve optical access and minimise curvature effects during Particle Image Velocimetry (PIV) measurements. [Uzol *et al.* \(2002\)](#) employed a 64% *w/w* NaI solution as their test fluid to conduct PIV measurements in an axial turbo-pump constructed from acrylic (PMMA). In this article, the authors discuss some of the difficulties associated with using NaI mixtures, including chemical stability and variations in transmittance. Sodium iodide solutions are susceptible to discolouration due to the formation of I_3^- ions, a process accelerated by exposure to light, oxygen and elevations in temperature. Unlike I^- ions, I_3^- ions absorb light in the visible range, which can dramatically attenuate the passage of light and affect visualisation. This process can be minimised by limiting the solutions exposure to light and oxygen, the later of which is achieved by keeping the solution under the presence of Nitrogen gas. It has also been shown that I_3^- ions can be partially eliminated from the solution by the addition of either sodium borate 10-hydrate ($Na_2B_4O_7 \cdot 10H_2O$) (see [Uzol *et al.* \(2002\)](#)) or sodium thiosulphate ($Na_2S_2O_3$) (see [Narrow *et al.* \(2000\)](#)) at a concentration of 0.1% *w/w*. For the current work sodium thiosulphate has been used as the I_3^- ion mitigating agent.

A simple model for the prediction of refractive index, n_{NaI} , of NaI solutions as a function of temperature T , NaI concentration C , and wavelength λ was determined by [Narrow *et al.* \(2000\)](#) for moderate parameter variations:

$$n_{NaI}(T, C, \lambda) = 1.252 - (2.91 \times 10^{-4} C^{-1}) T + (0.365) C + (5542 \text{ nm}^2) \lambda^{-2} \quad (3.7)$$

Equation 3.7 provides a very good estimate of the solution concentration required to achieve refractive index matching with acrylic for a given liquid temperature and light wavelength, although it must be noted the range of conditions used within this work exceeds those used to form the correlation. In practice, it is common to obtain the solution concentration using a trial and error process,

3.7 Test Liquid Characterisation - Sodium Iodide

visually comparing the distortion of light passing through the mixture (see [Lim *et al.* \(1994\)](#) and [Miller *et al.* \(2006\)](#)).

For this work comparisons were made of the optical distortion of a uniform $1\text{mm} \times 1\text{mm}$ grid placed behind the test section as solution concentration was varied from 57% to 64% (w/w) in 1% increments. Photos of the mesh were taken for each concentration as the liquid temperature was slowly increased from 13°C to approximately 20°C . The coefficients of equation 3.7 indicate that changes in concentration have a greater influence on refractive index than changes in temperature. This agreed well with experimental observations. As such, a nominal concentration of $C = 63\%$ was selected for use in all tests as it exhibited the least distortion of the grid pattern at the temperature expected for experimental measurements ($T \approx 18^\circ\text{C}$). Despite this, no active temperature control was used. Figure 3.13 shows the effectiveness of the refractive index matching technique.

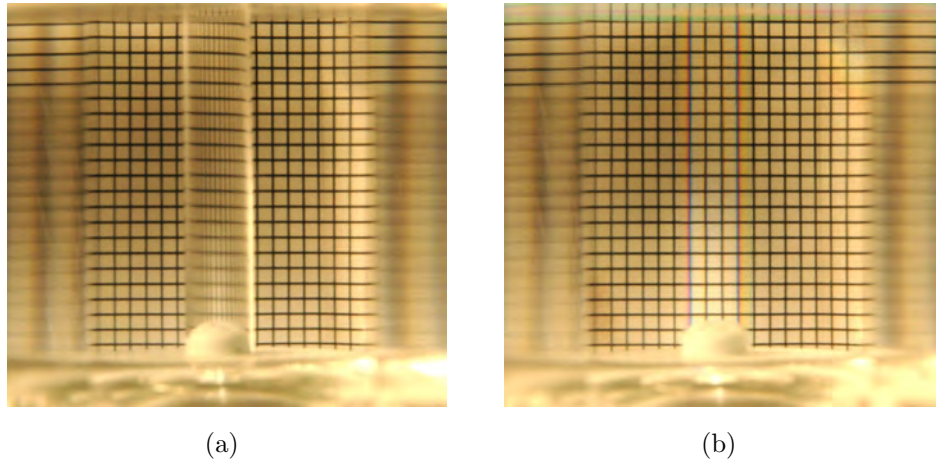


Figure 3.13: Experimental refractive index matching showing the distortion of a $1 \times 1\text{mm}^2$ mesh placed behind the test section. The nozzle diameter is clearly present for (a) distilled water (control) but is near invisible for (b) 63% w/w NaI solution.

3.7.2 Kinematic Viscosity

Data for viscosity and density of NaI solutions was rather limited in the literature. Some studies used the nominal values of 1.8 and $1.1 \times 10^{-6} \text{ m}^2/\text{s}$ for specific gravity and kinematic viscosity respectively (see [Uzol *et al.* \(2002\)](#)). Given the inevitable variations to these parameters with temperature and concentration, viscosity measurements were conducted using a Cannon-Fenske Routine viscometer for a range of NaI concentrations from 57% to 66% for temperatures between 13°C and 24°C . Measurements at each temperature were repeated twice to minimise measurement error. A multi-variable regression equation was then used to generate an expression for relate kinematic viscosity in terms of temperature and concentration. The resulting regression equation is:

$$\nu = 8.575 \times 10^{-6} e^{(-0.014T)} C^3 \quad (3.8)$$

where T is the liquid temperature in $^\circ\text{C}$ and C is solution concentration in $\%w/w$. A comparison of the measured viscosity to that predicted by equation 3.8 is shown in figure 3.14.

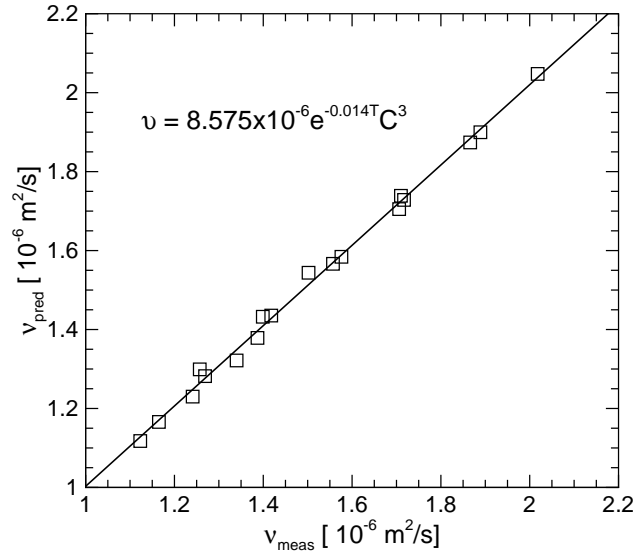


Figure 3.14: NaI kinematic viscosity regression

3.7.3 Density

Density measurements were also conducted for the same range of NaI concentrations at laboratory temperature ($T \approx 18^\circ\text{C}$). A nominal volume (20mL) of liquid was accurately transferred to a beaker using a high resolution pipette. This volume was then weighed and the density calculated. The process was repeated 5 times for each concentration to improve accuracy. The expected uncertainty in the density of the sodium iodide solution with temperature change was estimated using the percentage variation in density of saturated water across the expected experimental temperature variation. A plot of density variation with concentration can be seen in figure 3.15 together with a linear regression equation.

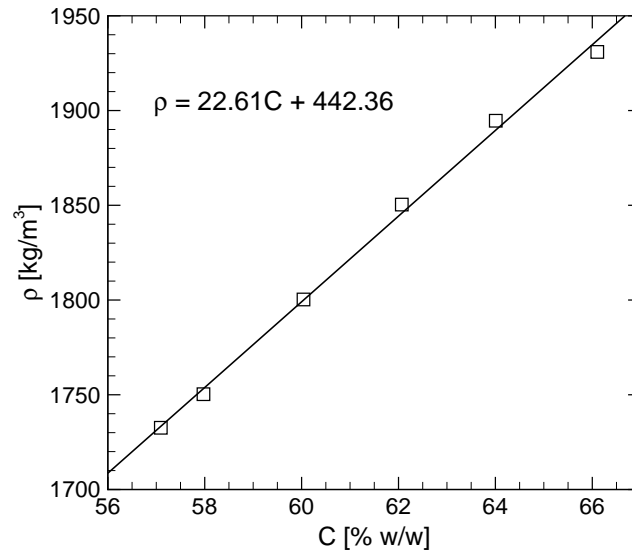


Figure 3.15: NaI density as a function of solution concentration

3.7.4 Vapour Pressure

Vapour pressure for the NaI solution was determined using an empirical formulation based on the Antoine type equation:

$$\log [P_v (kPa)] = A(m) + \frac{B(m)}{T(K)} + \frac{C(m)}{T(K)^2} \quad (3.9)$$

where $A(m)$, $B(m)$ and $C(m)$ are cubic functions of solution molarity. The constants for each of these equations were (Patil *et al.* (1991)): $A_0 = 6.642$, $A_1 = 0.491$, $A_2 = -0.101$, $A_3 = 0.005$, $B_0 = -1340.491$, $B_1 = -323.215$, $B_2 = 63.051$, $B_3 = -3.272$, $C_0 = -146462.900$, $C_1 = 51849.160$, $C_2 = -10123.010$, $C_3 = 525.534$. Figure 3.16 shows a plot of vapour pressure variation with temperature.

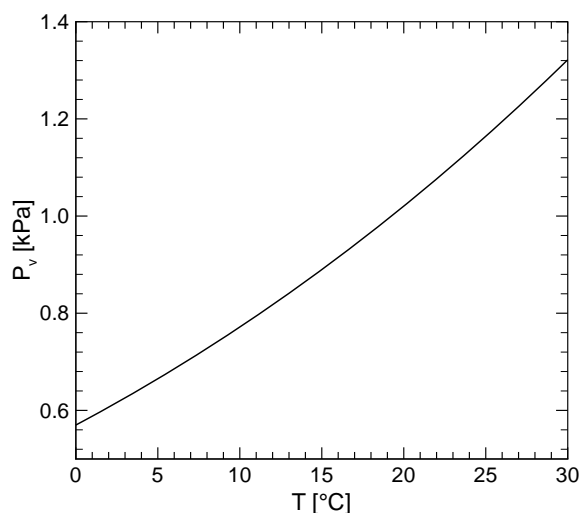


Figure 3.16: NaI vapour pressure as a function of temperature

A summary of the typical properties for a 63%w/w NaI solution at a nominal temperature of $T = 18^\circ\text{C}$ are listed in table 3.8.

3.8 Data Acquisition and Cylinder Control

A number of parameters were recorded during each injection using a National Instruments PCI6221 multifunction data acquisition (DAQ) card. The DAQ card

3.8 Data Acquisition and Cylinder Control

Table 3.8: Physical Properties of Aqueous Sodium Iodide

Property	Nominal Value
Concentration, C $\%(w/w)$	63
Refractive Index, n	1.49
Kinematic Viscosity, ν (m^2/s)	1.67×10^{-6}
Density, ρ (kg/m^3)	1866.79
Vapour Pressure, P_v (kPa)	0.97

was 16-bit resolution and with 16 analog input and 2 analog output channels, with a combined sample rate of $250kHz$. The DAQ card was interfaced with a standard PC using National Instruments LabVIEW 2009 program. A state machine style control program was written which allowed for various programmable piston motion sequences, such as that used to fill the test fluid cylinder with fresh NaI following an injection cycle. During the expulsion phase of the injection sequence, data was acquired and saved for injection pressure, P_1 , gas pressure, P_2 and piston position. Sample rates were limited to the response time of the pressure sensors and set to $1000Hz$ for all variables. Data acquired from each injection was later processed using Matlab, described in chapter 4.

As well as acquiring measurement data, the program used digital input/output from the DAQ card to operate a number of relays within the system including that used to control the pneumatically actuated ball valve and activation of the hydraulic control unit. Digital output synchronised to the position of the piston were also used to trigger the acquisition of high-speed video recordings. Piston velocity was controlled for each injection by selecting the analog voltage to be output to the hydraulic control unit.

Temperature measurements for the liquid, gas and ambient air were continually acquired using a Pico USB TC-08 Thermocouple Data Logger. Samples were acquired at 1 minute intervals over the duration of experiments each day. Later, the temperature used to evaluate the liquid properties for a particular injection was determined by correlating the time-stamps on the DAQ measurements.

Chapter 4

Measurement Techniques and Experimental Uncertainty

This chapter provides the details of the experimental techniques and methodologies used throughout this work. In order to process the high speed visualisation a number of image processing programs were written and used to determine the results presented in chapter 5. The mathematical formulations and techniques for determining flow features central to these programs will be discussed. Finally estimates of the sources of error and measurement uncertainty will be provided.

4.1 Data Extraction

Measurements of injection pressure, gas pressure and piston position were recorded during each injection at a sample rate of $1000Hz$ by the data acquisition system described in section 3.8. Injection pressure traces typically showed transient spikes associated with the initial motion of the piston and the end of injection. These sections of the data were removed before processing, to ensure all derived parameters were determined from steady state data only.

In many cases injections were composed of a number of distinctly different operating phases. These corresponded to the formation of different cavitation structures within the orifice and produced significant changes in the injection pressure. These changes in pressure are a consequence of the shifts in the discharge coefficient that result from the various degrees of cavitation. As the system

was driven by a constant mass flow (constant piston velocity), variations to the discharge coefficient cause the shifts in the injection pressure to satisfy mass continuity. Where possible, data for each of these discrete regions in the record was separated and processed individually. Figure 4.1 shows typical pressure traces indicating multiple steady state sections and the removal of transients in the data record of an injection.

A Matlab program was used to conduct all calculations from the steady state data. Injection and gas pressures are averaged over the steady state region before being used to calculate the non-dimensional parameters; cavitation number and nozzle discharge coefficient. Piston velocity was determined from the gradient of a linear regression of piston position data for the recorded interval. The mean nozzle velocity was then determined using continuity and the ratio of cylinder to nozzle diameters.

Temperature measurements of the pressure vessel gas, liquid in the supply pipe and ambient air were measured at 1 minute intervals for the duration of experiments each day using k-type thermocouples. The temperature used for the determination of fluid properties such as viscosity (section 3.7) was taken as the mean of the liquid temperature for the two data points either side of the actual injection time.

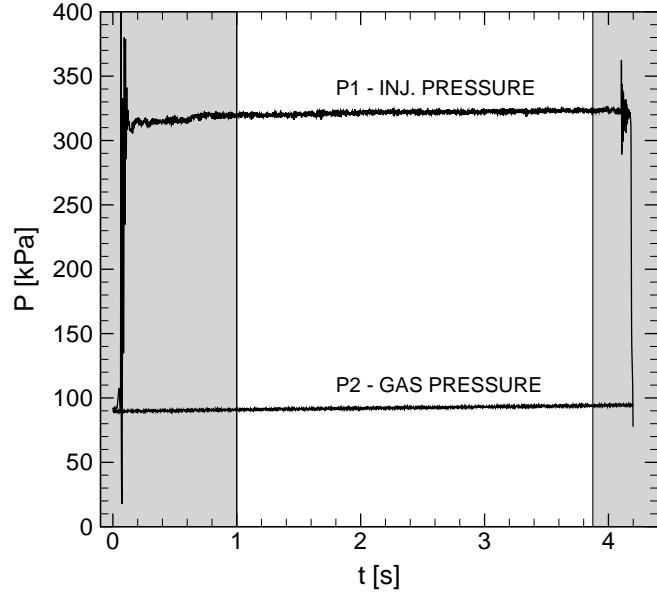
4.1.1 Non-dimensional Parameters

Data averaged over the steady state sections of the data record were used to calculate the non-dimensional parameters of interest; Reynold number, Re , cavitation number, K and discharge coefficient, C_d . Reynolds number was defined here as,

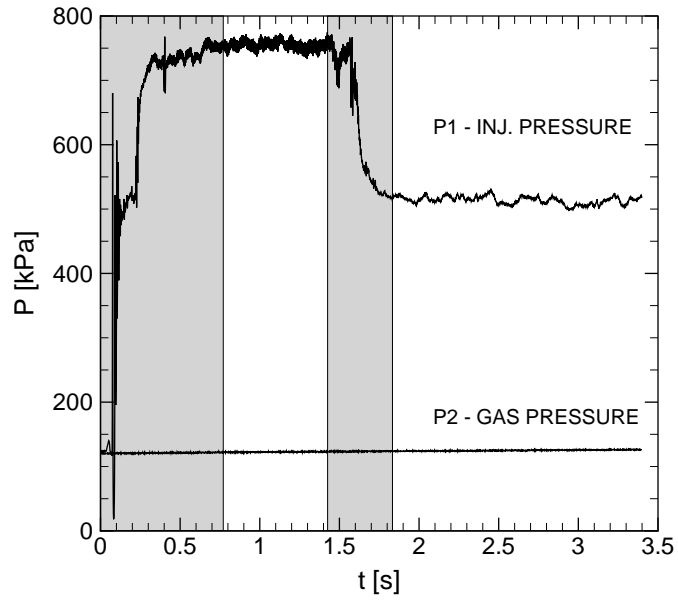
$$Re = \frac{V_n D_n}{\nu} \quad (4.1)$$

where V_n is the mean velocity through the nozzle, D_n is the nozzle diameter and ν is the kinematic viscosity.

As mentioned in section 1.3.4 the cavitation number used in this work is defined as,



(a)



(b)

Figure 4.1: (a) Single flow regime pressure trace for $Re = 6.62 \times 10^4$ and $K = 1.84$. (b) Multiple flow regime pressure trace for $Re = 8.0 \times 10^4$ with $K = 1.35$ initially and $K = 1.58$ late. Grey regions in the plot indicate transient data rejected in analysis.

$$K = \frac{P_1 - P_v}{P_1 - P_2}. \quad (4.2)$$

where P_1 is the injection pressure, P_2 is the gas pressure, and P_v is the vapour pressure. Both P_1 and P_2 were measured using Honeywell piezoresistive pressure transducers (gage) with a response time $< 1ms$. The pressure sensor for P_1 was mounted in a tapping in the supply pipe 202mm (item 6 in figure 3.12) below the nozzle entrance. Similarly, the pressure sensor for P_2 was mounted on a side branch of the filling port on the top of the pressure vessel (visible in figure 3.11). P_1 was converted to absolute pressure for use in equation 4.2 by the addition of atmospheric pressure, measured using a barometer in the laboratory, prior to commencement of experiments each day.

The discharge coefficient of a nozzle relates the actual mass flow rate through the nozzle, \dot{m}_{act} , to the theoretical mass flow rate, \dot{m}_{th} for an ideal fluid under identical conditions,

$$C_d = \frac{\dot{m}_{act}}{\dot{m}_{th}}. \quad (4.3)$$

The theoretical mass flow rate can be expressed in terms of the Bernoulli velocity through the nozzle, V_{nth} , the nozzle cross sectional area, A , and the liquid density, ρ ,

$$C_d = \frac{\dot{m}_{act}}{\rho A V_{nth}}. \quad (4.4)$$

The actual mass flow rate through the nozzle can be expressed in terms of the piston velocity, V_c , and test fluid cylinder diameter, D_c . An expression for the theoretical velocity through the nozzle can be obtained by combining Bernoulli's equation and mass continuity between points upstream of the entrance and nozzle exit. Substitution of these expressions into equation 4.4 yields

$$C_d = \frac{D_c^2 V_c}{\frac{D_n^2}{\sqrt{1-\beta^4}} \sqrt{\frac{2(P_1^* - P_2^*)}{\rho}}} \quad (4.5)$$

where $P_i^* = P_i + \rho g z_i$, denotes piezometric pressure at point i , D_n is the nozzle diameter, and $\beta = D_n/D_p$ is ratio of the nozzle to supply pipe diameters.

Discharge coefficient is often expressed as the product of two different parameters: the velocity coefficient, C_v , and the area contraction or contraction coefficient, C_c . The velocity coefficient accounts for the reduction from ideal velocity, and the contraction coefficient accounts for the loss of cross-sectional area due to flow contraction. In this way the the discharge coefficient can be expressed as

$$C_d = C_v C_c \quad (4.6)$$

The expression in equation 4.6 is helpful for analysing the elemental sources of loss and will be called upon in the discussion of chapter 5.

4.2 High-speed Visualisation

High-speed visualisation provided a non-intrusive means of exploring the temporal evolution of the cavitation structures within the nozzle and the near nozzle spray structure. A Phantom V7.3 CMOS camera (800 x 600 pixel) was used for all high-speed visualisation in this work. This camera has a full resolution frame rate of 6688 frames per second (*fps*), with frame rates in excess of $100kfps$ capable at reduced resolution. These capabilities allowed for visualisation at high resolution on temporal scales that provided great insight into the cavitation initiation and development, bubble shedding process and spray ligament formation. Acquisition of the images was initiated by a trigger pulse synchronised to the piston position. The axial position of the piston chosen as the trigger point for the camera was dependent on the piston velocity and desired frame rate of the camera.

4.2.1 Illumination

The appropriate choice and application of light to the test piece is arguably the most important and complex element of scientific photography (Blaker (1965)).

4.2 High-speed Visualisation

This is particularly true for high-speed visualisation where correct illumination of the subject ensures the recoding reveals the most pertinent information from the flow. The basic principles of lighting for high-speed applications are very similar to those of conventional photography, except that amounts of light required are often orders of magnitude higher (Ray (2002)).

A number of different illumination techniques were trialled, however it was found that backlit illumination provided the greatest contrast between the cavitation structures and liquid. This technique has been broadly applied to the visualisation of cavitation bubbles (see for example Lauterborn & Ohl (1997)) and produces images in which cavitation structures appear as dark silhouettes surrounded. These bubble shadows enhance the detection of cavitation in the flow and particularly aid with the digital processing techniques used in this work.

Illumination was provided by a 500W halogen lamp placed behind the nozzle, or optical access window, in direct line with the camera. A light sheet diffuser made from silicone baking paper was used to create a diffuse light source and minimise specular reflections in the images. A schematic of the visualisation setup can be seen in Figure 4.2.

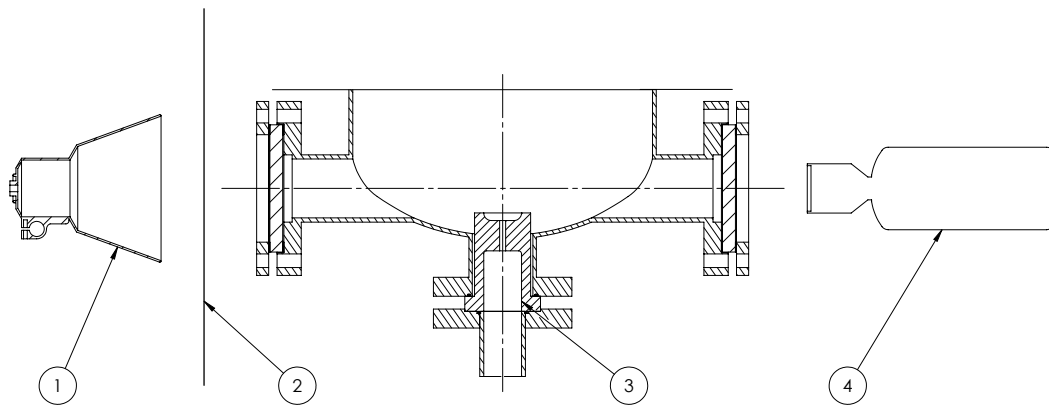


Figure 4.2: Schematic of near-nozzle spray visualisation setup
1. 500W Halogen lamp, 2. Light diffusion screen, 3. Acrylic nozzle, 4. High-speed camera

UNLESS OTHERWISE SPECIFIED: DIMENSIONS ARE IN MM SURFACE FINISH: TOLERANCES: ± 0.5	DEBUR AND BREAK SHARP EDGES	DO NOT SCALE DRAWING	REVISION: 2
	CONTACT	UNSW	
	DRAWN: Cameron Stanley PT: (02) 9385 6005	TITLE: PRESSURE VESSEL	
	DATE: 22/05/09	DWG NO. 01	
WEIGHT:		SCALE: 1:50	SHEET 1 OF 1

4.2.2 Camera Lens and Region of Interest

Careful selection of the camera region of interest (ROI) was important to ensure the trade off between frame rate and spatial resolution was optimised for the flow structures being recorded. Fundamental to this optimisation was the correct choice of camera lens. For internal nozzle flow analysis a 105mm Nikon Nikkor lens was used at a typical f-number of 11, providing maximum spatial resolution along the stream wise direction. With this lens the 800 pixel width of the camera CMOS chip was mapped as close as possible to the 40mm length of the nozzle, providing a spatial resolution of $\approx 0.055\text{mm}/\text{pix}$. In the lateral direction the camera region of interest (ROI) was reduced to just cover the width of the nozzle. This resulted in a ROI of 800 pixels x 160 pixels with a maximum frame rate capability of 23121fps. For near nozzle spray analysis a 70-200mm Carl Zeiss Jena f/2.8-4 MC Macro lens was used at a typical f-number of 8. A camera resolution of 608 x 400 pixels provided a suitable compromise between field of view and camera frame rate, allowing 12121fps with a spatial resolution of $\approx 0.092\text{mm}/\text{pix}$. A schematic illustrating the ROI for both configurations can be seen in figure 4.3.

In order to reduce the working distance of the camera using these high focal length lenses, lens spacers (extension tubes) were placed between the camera and the lens, artificially increasing the image distance. This allowed the camera to be mounted to a 3-axis translation stage attached to the rig frame, which aided with focusing and positioning the ROI with respect to the test section.

4.3 Image Processing Techniques

Once recordings were taken of the cavitation the extraction of pertinent flow details required digital processing of the images sequences. All recordings presented in this work represent recordings under steady flow conditions. Images recorded using the Phantom V7.3 camera were converted to 8-bit multtiff image sequences, a format suitable for processing using Matlab. A number of programs were written in Matlab for the extraction of different information from the video recordings such as; cavitation collapse length, shedding frequency, and spray an-

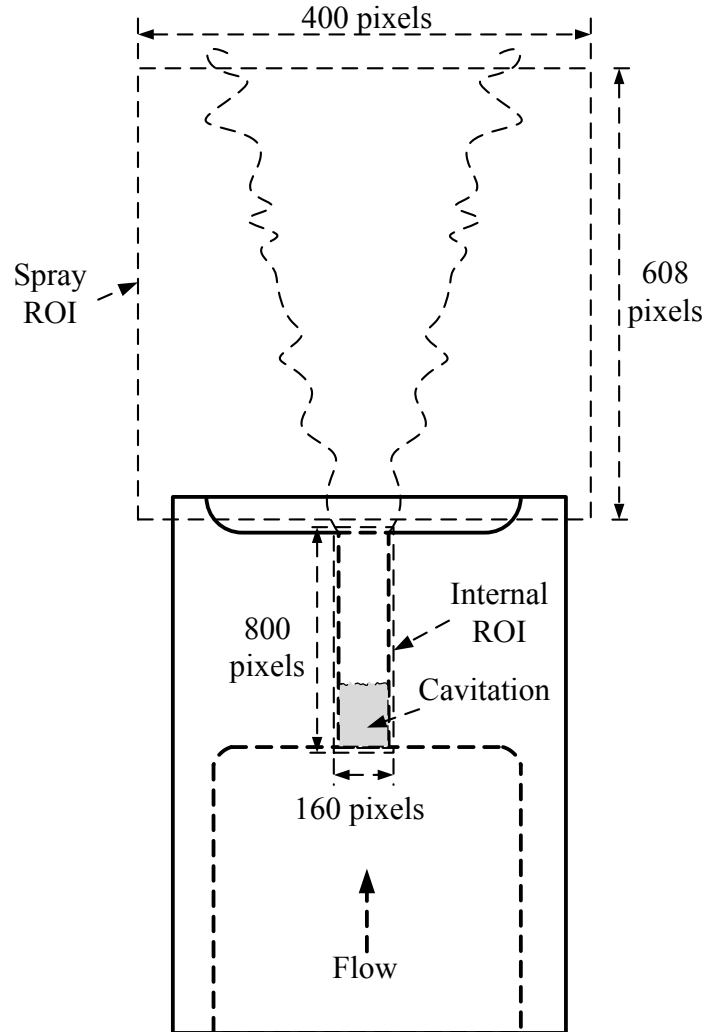


Figure 4.3: Schematic of visualisation ROI when investigating nozzle cavitation and for near-nozzle spray interrogation. Spatial resolution of $0.055\text{mm}/\text{pix}$ for internal ROI and $0.092\text{mm}/\text{pix}$ for spray ROI.

gles. The major interrogation methods employed during image processing for each of these measurements will be described in detail in the following sections.

4.3.1 Cavity Collapse length

The measurement of cavity collapse length is common for cavitation experiments for both internal and external flows. Often this measurement is via the analysis of photographs or video recordings. However, little attention is afforded to outlining the method used to identify a single collapse length for what is invariantly a 3-dimensional flow structure. For example, [Sou *et al.* \(2010\)](#) reports measurements of collapse length in 4mm diameter plain orifice nozzles as “the mean value obtained using 10 photographs for each flow rate”. Using a camera frame rate of 20,000fps, it is likely that this number of image frames would be insufficient to capture one full period of the cavitation shedding which could be expected for some of their flow conditions.

The highly transient nature of the bubble collapse process can result in significant frame-frame variation in observed cavity length. For the current work attempts were made to determine a collapse length that represented a spatially and temporally averaged value for each recording. The cavity length has been defined here as the distance from the nozzle entrance to the last point in the stream-wise direction at which the location of cavitation or bubbles can be identified.

To aid with the detection of cavities and bubbles the original recordings of the cavitation, typically 4500 frames in length, were converted to binary (white representing liquid phase, black representing vapour) by the application of a suitable greyscale threshold. This threshold was adjusted for each recording to ensure that fine bubble clouds that were still considered part of the cavitation structure were not eliminated during the conversion process. The Matlab program would then extract profiles of pixel value along 20 vertical lines extending the length of the nozzle, which were evenly spaced between the left and right walls. The uppermost interface between the vapour and liquid region was then identified as the last stream-wise pixel to have zero greyscale value (representing the edge of the black cavitation region). The temporal evolution of the cavity interface for each

of the 20 lateral positions was then averaged, both in time and space, to produce a nominal value for the mean cavity collapse length. The maximum, minimum and standard deviation of the cavity collapse length were also determined. A typical frame from an unprocessed image sequence and the corresponding binary frame can be seen in figure 4.4(a) and figure 4.4(b) respectively. Figure 4.4(c) shows the statistical collapse length measurements projected over the top of the original unprocessed frame

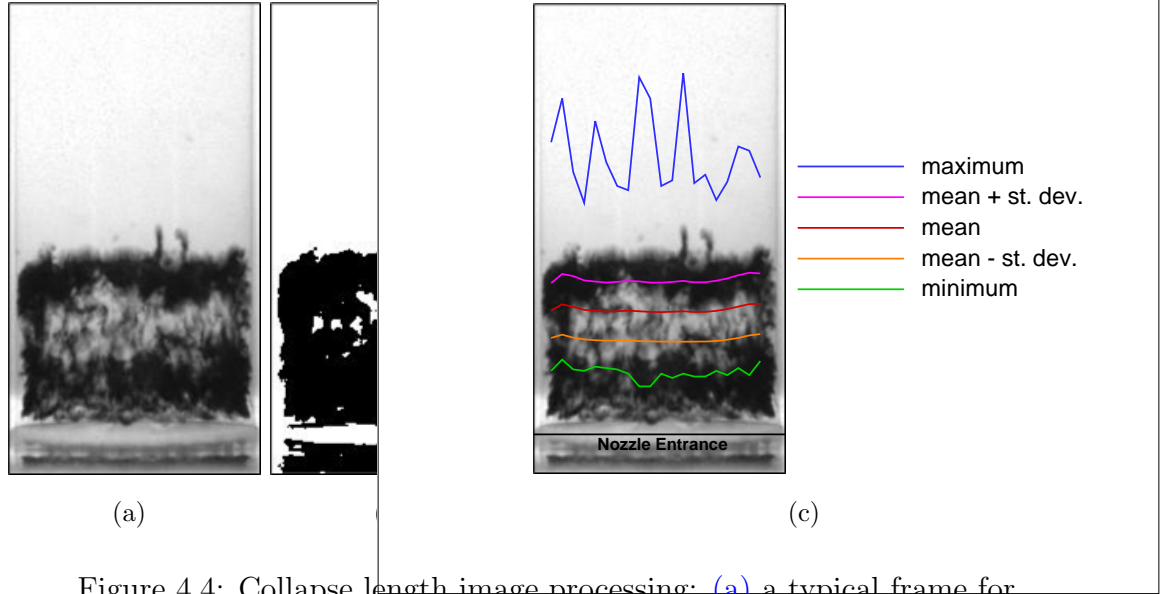


Figure 4.4: Collapse length image processing: (a) a typical frame for $Re = 9.3 \times 10^4$ and $K = 2.01$ before conversion, (b) the same frame represented as a binary image and (c) statistical collapse length over-layed on original frame. Note: a reduced length of nozzle shown only.

For developed cavitation, cavities tend to collapse very near the exit of the nozzle and it is common to observe clouds of cavitation bubbles being convected through the exit plane. The precise collapse length under these conditions cannot be determined accurately. The number of times the cavity was identified as reaching the nozzle exit was counted for each recording and gave an indication for the extent to which the true collapse length had been “clipped” by this limitation. Cases of supercavitation and hydraulic flip could not be processed as the cavities

are all exceeding the nozzle length. These cases were assigned a normalised collapse length of 1.

Refraction of the light passing through the nozzle for the cases with water as the working fluid significantly affected the contrast between the cavitation and the fluid. The conversion to binary was impossible whilst maintaining a true representation of the cavitation structure. To avoid this problem only the central core of the image ($\approx 1/3$ width), where cavitation could be easily distinguished from liquid, was used for estimation of the collapse length using an otherwise identical method to that described above. However, as the measurement was obtained for a smaller region of the flow, the estimate of collapse length is not as robust as for sodium iodide.

4.3.2 Spray Angle

Similarly to collapse length, spray angle is a parameter widely reported in the literature, but is often loosely defined. For small scale nozzles the spray angle is often estimated by the angle formed between tangent lines passing through the nozzle tip along the edge of the spray surface in the “steady” region (see for example [Desantes *et al.* \(2006\)](#)). This region describes the conical section of the spray immediately after the exit of the nozzle, the length of which varies based on injection conditions. [Payri *et al.* \(2004\)](#) estimate its length to equal 60% of the jet penetration and use this length of spray to estimate spray angle. Break-up lengths for large-scale nozzles are significantly greater than those for small nozzles. This makes visualising the entirety of the spray very difficult and means estimates of spray angles are generally made using the near-nozzle region of the jet.

For the current work the focus of the spray visualisations was on investigating the influence of the cavitation within the nozzle on the influence on the spray structures in the region immediately after the nozzle exit. As such, attempts were made to minimise the error in the estimate of spray angle taken from spray recordings encompassing a relatively short length of jet ($\approx 6D_n$). Video recordings were digitally averaged over the 4500 frame record length before being converted to binary by the application of a greyscale threshold. As for the determination of

collapse length, the threshold used for conversion to binary was manually chosen for each recording to suit the relative greyscale intensity of each averaged image. Repeated trials on the same injection image indicated the spray angle was insensitive to variations in this parameter within sensible limits (discussed in section 4.3.4). Figure 4.5 shows a representational spray image, the digitally averaged frame and the corresponding binary frame for the given conditions.

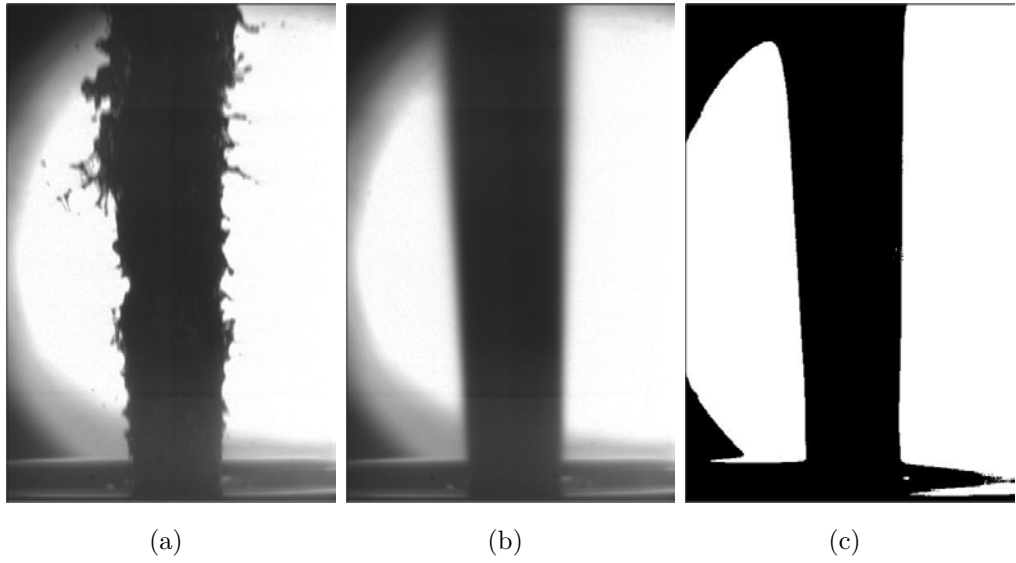


Figure 4.5: Spray images for $Re = 6.5 \times 10^4$ and $K = 1.83$ showing (a) Single frame from image sequence, (b) Average spray image, (c) Average spray converted to binary image.

Once converted to binary the upper and lower vertical limits for the measurement of the angle, denoted y_{UL} and y_{LL} respectively, were selected. These points formed the bounds for a series of 10 pairs of equally spaced horizontal lines passing through the spray image. A schematic representation of the spray indicating the half angles and relevant geometric points can be seen in figure 4.6.

The lateral locations of the gas/liquid interface for the i^{th} pair of horizontal intersecting line are denoted as $x_{LU}(i)$ and $x_{RU}(i)$ for the left and right upper points respectively, and $x_{LL}(i)$ and $x_{RL}(i)$ for the left and right lower points respectively. These values are obtained by determining the distance along the

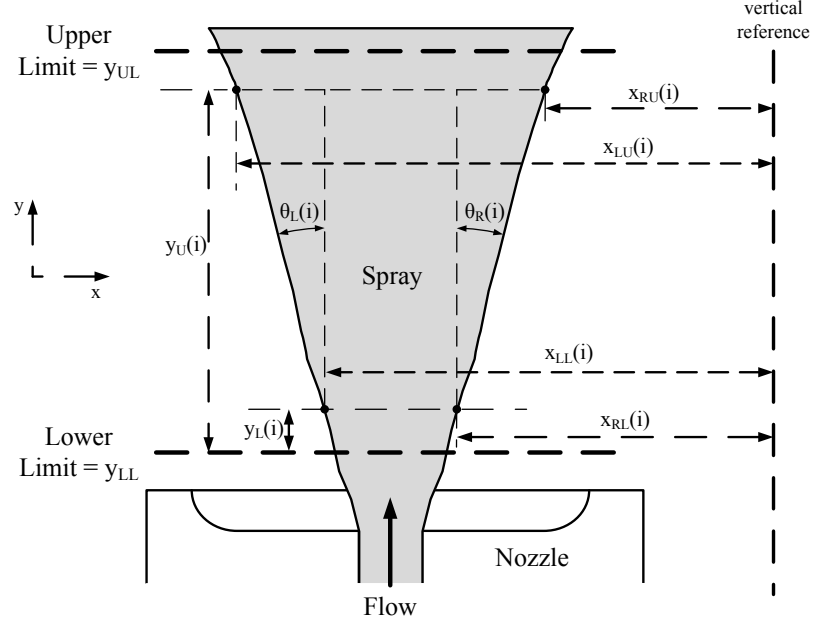


Figure 4.6: Spray angle definition - right side shown

horizontal transect from an arbitrary reference point to the first and last zero value elements through the binary spray.

The vertical translation between each pair of lines was set to five pixels, however the spacing between the upper and lower line was unique to each spray and set to provide maximum coverage of the spray without exceeding the bounds identified. In this fashion the vertical coordinate of the upper spray edge for the i^{th} line pair, $y_U(i)$, can be written in terms of the distance from the upper limit as,

$$y_U(i) = y_{UL} + 5(i - 1). \quad (4.7)$$

Similarly the lower spray edge for the i^{th} line pair, $y_L(i)$ can be expressed in terms of the distance from the lower limit as,

$$y_L(i) = y_{LL} - 5(10 - i). \quad (4.8)$$

Estimates for the half angle on both the left, θ_L , and right, θ_R , edges of the spray were then calculated as the mean angle determined between the upper and

lower gas/liquid interface for each of the 10 bisecting line pairs,

$$\theta_R = \frac{1}{10} \sum_{i=1}^{10} \arctan \left(\frac{x_{RU}(i) - x_{RL}(i)}{y_U(i) - y_L(i)} \right) \quad (4.9)$$

$$\theta_L = \frac{1}{10} \sum_{i=1}^{10} \arctan \left(\frac{x_{LL}(i) - x_{LU}(i)}{y_U(i) - y_L(i)} \right) \quad (4.10)$$

The overall estimate of the spray half angle could then be determined as,

$$\theta = \frac{1}{2} (\theta_L + \theta_R) \quad (4.11)$$

where averaging the half angle for the left and right sides of the spray eliminates errors introduced by possible vertical misalignment of the nozzle with respect to the axis of the camera. For highly divergent jets the reduction of image resolution required to achieve suitable frame rates meant that one side of the spray structure was analysed only. The measured half angle in these cases was corrected for nozzle misalignment using the mean angle of a number of hydraulically flipped cases for the same camera setup.

4.3.3 Signal Spectral Analysis

To determine the frequencies associated with the unsteady cloud shedding within the nozzle a spectral analysis technique was applied to the video recordings. The most common method of spectral analysis involves calculating the power spectral density (PSD) of the recording. Before describing the specific way in which this analysis was applied to the cavitation recordings, a brief technical description of the spectral analysis is given. The mathematical formulations within are derived mostly from [Mirchandani \(2011\)](#).

4.3.3.1 Power Spectral Density

In signal analysis the power spectral density provides a means of describing how the average power of a signal is distributed with frequency. For a discrete-time random process, $x(n)$ for $n = 0, \dots, N - 1$, the PSD can be expressed as

$$S_{XX}(\omega) = \lim_{M \rightarrow +\infty} E\left\{\frac{1}{2M+1} \left| \sum_{n=-M}^M x(n) e^{-j\omega n} \right|^2\right\} \quad (4.12)$$

where E is the expectation operator. It should be noted that the term “power” is used in PSD analysis in the sense of a squared variable and can be related to physical power in some cases by a dimensional scaling constant (Randall (1987)).

In simple terms equation 4.12 states that the power spectral density of a random process that has been discretely sampled in time can be estimated by taking the magnitude squared of the Discrete-time Fourier Transform (DTFT) of the data $x(n)$ and dividing by the length of the record. Then, since the Fourier transform will be a random variable (each new $x(n)$ will be different), the expected value (i.e. average value) is taken. Finally, since the random process is generally of infinite duration, the limit is taken.

The problem is that data records are always finite. One of the most common methods used for estimating the PSD for a finite length data signal is known as the Periodogram. Derived from equation 4.12, the summation is formed over a finite data length and by removing the expectation operator, it is defined as

$$\hat{S}_{PER}(\omega) = \frac{1}{N} \left| \sum_{n=0}^{N-1} x(n) e^{-j\omega n} \right|^2 \quad (4.13)$$

which is the DTFT squared and averaged. However the variance of the periodogram spectral estimator does not approach zero for $N \rightarrow \infty$, which may be due to the removal of the expectation operator, that is, a lack of averaging. To improve the variance of the estimator, the expectation operator from equation 4.12 can be replaced by averaging a set of periodograms. If we assume there are K independent records of the random process available for the interval $0 \leq n < L$ then we can define the averaged periodogram estimator as,

$$\hat{S}_{AVPER}(\omega) = \frac{1}{K} \sum_{m=0}^{K-1} \hat{S}_{PER}^{(m)}(\omega) \quad (4.14)$$

where $\hat{S}_{PER}^{(m)}(\omega)$ is the periodogram for the m th data set defined by,

$$\hat{S}_{PER}^{(m)}(\omega) = \frac{1}{L} \left| \sum_{n=0}^{L-1} x_m(n) e^{-j\omega n} \right|^2. \quad (4.15)$$

In the case that each $x_m(n)$ for $m = 0, 1, 2, \dots$ was a unique realisation of a random process, then the DTFT would be unique and the averaging results in a reduction of the variance of the PSD estimator by a factor of K . However more commonly the estimate of the PSD must be made from a single data record of length L . One means for reducing the variance of the PSD estimate from a single record is known as Welch's method (Welch (1967)). In this method an average is determined for the periodograms of a number of overlapping segments from the same data set offset by a separation D such that the k^{th} sequence can be written,

$$x_k(n) = x(n + (k - 1)D), \quad n = 0, 1, \dots, L - 1.$$

Visually this segmentation of the single data record can be seen in figure 4.7

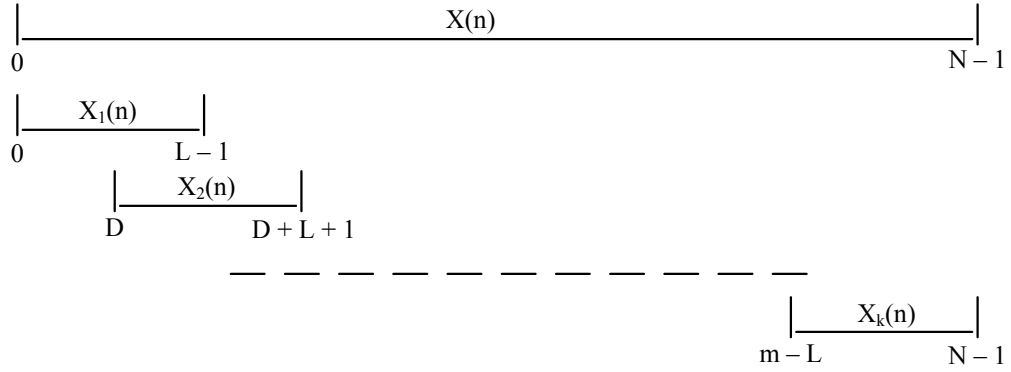


Figure 4.7: Schematic of the signal segmentation using Welch's averaged periodogram

The Fourier Transform, or in this case the Discrete-time Fourier Transform makes the implicit assumption that the signal is repetitive. In other words the segment of the record within the measured time repeats for all time. In reality, measured signals have discontinuities between the start and end of the record. Without correction the DTFT assumes these discontinuities are part of the repeating signal, which introduces artificial broad frequency spectra. By multiplying the time signal by a window function, $w(n)$, the record can be reduced smoothly to zero at each end enforcing end-point continuity.

Welch's averaged periodogram can be written in terms of the windowed data record as follows,

$$\hat{S}_W(\omega) = \frac{1}{KLU} \sum_{k=0}^{K-1} \left| \sum_{n=0}^{L-1} w(n) x_k(n) e^{-j\omega n} \right|^2 \quad (4.16)$$

where U is a constant accounting for the effect of the window on the power estimate, defined as

$$U = \frac{1}{L} \sum_{n=0}^{L-1} |w(n)|^2 \quad (4.17)$$

The primary advantage of Welch's method over other PSD methods is that by overlapping the segments the average can be conducted over more periodograms, improving the variance in the output.

4.3.3.2 Calculation Method

In order to evaluate the spectral properties of the cavity shedding the video recording was first analysed to select an appropriate position in the collapse region for the analysis. A stream-wise location was carefully selected that correspond to a point in the collapse region through which the shed cloud regularly passed as it was transported by the bulk flow, but was not a location permanently occupied by the fixed cavity. In other words, the greyscale values at these locations contain the temporal variations in intensity reflecting the large-scale cavity shedding process.

Once the stream-wise position was determined the images were then analysed using a program written in Matlab. Unlike the analysis techniques described in sections 4.3.1 and 4.3.2, the spectral analysis did not require conversion of the image to binary. The greyscale signal for 10 pixels spaced evenly across the width of the nozzle was then extracted from the image sequence. A schematic representation of the 10 chosen interrogation pixels is shown in figure 4.8. To eliminate the DC component in the spectral analysis the data records were adjusted to have zero mean value.

Welch's method was then used to determine the PSD for each of the 10 signals. Segment lengths equal to 10% of the original recording were used with 75% overlap (i.e. $D = 0.25L$ in figure 4.7) and a Hanning window. Typically the length of the image sequences used were 4500 frames as the detection of peak frequencies

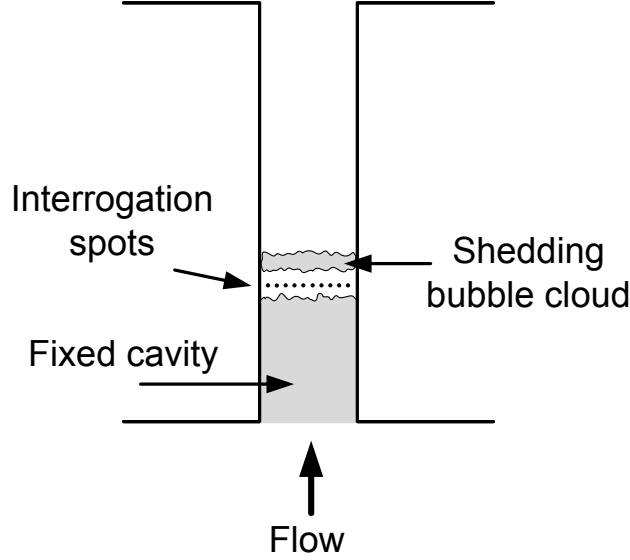


Figure 4.8: Schematic of interrogation spots used for cavitation frequency analysis

was found to be insensitive to further increases. To improve the efficiency of the fourier transform the record was zero padded (appended with zeros) untill the length was an integer power of 2. This is a well used technique for signal analysis and does not affect either the spectral content of the frequency resolution. The spectral resolution of the PSD estimate is equal to the sample frequency, f_s , divided by the length of the transform, L . The increased spectral resolution achieved by using a longer record length (> 4500 frames) did not justify the significantly longer processing time required.

To account for variations in the PSD estimate for the 10 radially spaced interrogations of the cavitation shedding, the individual PSD's were then averaged. In this way the final spectral output represents a spatially averaged estimate of the shedding frequencies of the three dimensional nozzle structures. The maximum frequency that could be identified using this method was half the sample rate ($23121Hz$), or approximately $11,500Hz$. Periodic shedding of water injections were also analysed to provide a source of comparison for the observed trends. As discussed in section 4.3.1 cavitation structures near the nozzle wall appeared

darker for water flows due to the refraction of light. However, the changes in greyscale intensity observed at an interrogation pixel due to the passing of a bubble cloud were sufficiently pronounced that the oscillations were easily identified. Typical PSD's for the cavitation recordings showed strong narrow-band spectral peaks with $3dB$ bandwidths of approximately $100Hz$, with diminishing peaks for higher harmonics.

4.3.4 Measurement Limitations

Irrespective of the apparent axisymmetry in the mean nozzle flow, cavitation and spray structures were inherently complex and 3-dimensional in nature. Whilst providing an excellent means of isolating the cavitation structures within the image, the back-lit images used for measurement represent a projection of these structures onto a 2-dimensional plane. In this way, the measurement of collapse length, spray angle and shedding frequencies are a macroscopic estimation for the given conditions and include “noise” introduced from this dimensional reduction.

For certain conditions it was observed that the light would refract around and partially obscure the spray structure. This was particularly obvious for the cases of hydraulic flip, where the jet appeared glassy smooth and cylindrical. However, it was also apparent in the measurement of some of the turbulent jets that had only minor surface disturbances. This distortion of the jet introduced only minimal errors to the calculations of spray angle, as the method adapted for the calculation could essentially straddle the affected regions.

Visualisation of the ligament formation on the surface of the jet was affected by a loss of resolution due to the presence of a thin liquid film on the inside of the glass. A residue of liquid remaining from the previous injection once the liquid was drained acted like a low-pass filter for the delicate features on the spray structure periphery. For spray angle measurements this loss of information had very little effect, however it presented a significant limitation to the ability to capture the small scale perturbations of the spray structure in the vicinity of the nozzle exit.

Finally, the reduction of the original video recording to binary introduces spatial errors in all measurements as it imposed an interpreted boundary to the

cavitation structures. The greyscale threshold somewhat arbitrarily defines this edge based on the relative contrast levels between the vapour and the liquid within the nozzle. The gradient in greyscale intensity across the vapour-liquid interface for internal visualisations was rather sharp in the original recording. As a result, the possible error in interface determination by the use of a threshold is minimal. Whereas greyscale variations in the lateral direction for the averaged spray image (see figure 4.5(b)) are substantial and continue to increase with increasing streamwise distance from the nozzle exit as the spray expands. These problems are obviously most pronounced for highly divergent spray structures associated with supercavitation. Application of a threshold to these images can result in a range of possible spray angles. To minimise this influence the threshold was often determined using an iterative approach, using repeated trials to obtain the best possible representation of the original structure.

4.4 Experimental Uncertainty

Measurement of experimental parameters involves a degree of error, usually defined as the difference between the true and measured value of the quantity. The term “uncertainty” is used to refer to the interval around the measured value in which we believe the true value to lie. The following sections outline the procedures used in this thesis to estimate uncertainties for all measured quantities. A summary table of all uncertainties is provided, however a comprehensive break-down of error analysis can be found in Appendix A.

4.4.1 Analysis Methodology

Estimations for the uncertainty of measured parameters within this work are based on the method outlined in Coleman & Steele (1995, 1999), using Stern *et al.* (1999) as a guide. Measurements are made of individual variables, X_i , to obtain a result, r , which is calculated by combining the data for various individual variables using a data reduction equation, $r = r(X_1, X_2, X_3, \dots, X_J)$. The total uncertainty of the result, U_r , is then determined as the root-sum-square (RSS) of

two components: a bias (systematic) error and a precision (random) error,

$$U_r^2 = B_r^2 + P_r^2 \quad (4.18)$$

where B_r is the bias error and P_r is the precision error. An error is classified as a precision error if it contributes to the scatter of the data, otherwise it is considered a bias error. Due to their systematic nature, bias errors are determined in the same fashion irrespective of the variable is measured once or many times. On the other hand, the method used to determine the precision error is dependent on how many times the measurement was conducted.

4.4.2 Bias Error

For both single and multiple tests the bias errors in the result (B_r from equation 4.18) are given by:

$$B_r^2 = \sum_{i=1}^J \theta_i^2 B_i^2 + 2 \sum_{i=1}^{J-1} \sum_{k=i+1}^J \theta_i \theta_k B_{ik} \quad (4.19)$$

where θ_i are the sensitivity coefficients defined as

$$\theta_i = \frac{\partial r}{\partial X_i} \quad (4.20)$$

and B_i is the bias error in X_i and B_{ik} is the correlated bias error between X_i and X_k .

$$B_{ik} = \sum_{\alpha=1}^L (B_{i\alpha}) (B_{k\alpha}) \quad (4.21)$$

where L is the number of correlated bias error sources that are common for the measurement of variables X_i and X_k . A typical source of correlated bias error arises when X_i and X_k have been calibrated on the same instrument. When several elemental bias error sources exist for say, the i th variable, X_i , the estimate for the bias error is determined as the RSS of the elemental sources;

$$B_i^2 = \sum_{k=1}^J (B_i)_k^2 \quad (4.22)$$

4.4.3 Precision Error for Single Measurements

Ideally measurement of all parameters would be repeated numerous times, with enough diverse equipment that the results can be assured using statistics. Unfortunately, as identified by Kline & McClintock (1953), in most engineering experiments it is not practical to estimate all of the uncertainties of observation by repetition, owing primarily to time and cost. In many experiments a measurement may be made once only and be comprised of a large number of samples at fixed conditions over a finite time period. Using the current method, under these conditions the precision error (P_r from eqn 4.18) can be estimated as;

$$P_r = tS_r \quad (4.23)$$

where t is the statistical coverage factor and S_r is the standard deviation of the sample of N readings.

It is also possible to estimate the precision error in the result as the RSS of the elemental precision error source (if known);

$$P_r^2 = \sum_{i=1}^J (\theta_i P_i)^2 \quad (4.24)$$

where θ_i are the sensitivity coefficients defined in equation 4.20 and $P_i = tS_i$ are the precision errors in the i th variable, X_i (where t_i and S_i are defined as per t and S_r in equation 4.23).

4.4.4 Precision Error for Multiple Measurements

Where possible precision errors were estimated using the statistical variance of the parameter over repeated measurement cycles. Where a measurement may be repeated an averaged result \bar{r} may be determined from the M sets of measurements $(X_1, X_2, \dots, X_J)_k$ at the same fixed test condition, such that

$$\bar{r} = \frac{1}{M} \sum_{k=1}^M r_k. \quad (4.25)$$

The bias error in the result is again determined using equation 4.19. If the M sets of measurements are taken over an appropriate time interval, the precision

error of a single result of the M measurements is

$$P_r = tS_{\bar{r}} \quad (4.26)$$

where t is determined with $M - 1$ degrees of freedom ($t \approx 2$ for $M \geq 10$) and $S_{\bar{r}}$ is the standard deviation of the M “sample” distribution of results

$$S_{\bar{r}} = \left[\sum_{k=1}^M \frac{(r_k - \bar{r})^2}{M - 1} \right]^{1/2} \quad (4.27)$$

The precision error for the average result is given by

$$P_{\bar{r}} = tS_{\bar{r}} = \frac{tS_r}{\sqrt{M}} \quad (4.28)$$

from which the total uncertainty for the average result can be calculated as;

$$U_{\bar{r}}^2 = B_r^2 + P_{\bar{r}}^2 = B_r^2 + \left(2S_r/\sqrt{M} \right)^2 \quad (4.29)$$

As mentioned above, a comprehensive break-down of the elemental error sources for each measured parameter is provided in Appendix A, however a summary of the estimated uncertainties for all measured parameters in this thesis can be seen in table 4.1. In general the levels of uncertainty are quite low which reflects the careful selection of appropriate instrumentation and measurement techniques.

Table 4.1: Measurement parameters and estimated uncertainties

Parameter	Symbol	Typical value	Bias Error		Precision Error		Uncertainty	
			value	%U	value	%U	value	%U
Injection Pressure (kPa) (see A.1)	P_1	684.8	13.84	99.9	0.41	0.1	13.85	2.02
Gas Pressure (kPa) (see A.1)	P_2	197.1	4.03	87.3	1.54	12.7	4.3	2.19
Nozzle Diameter (mm) (see A.2)	D_n	8.25	0.05	96.7	0.01	3.3	0.05	0.6
Liquid Temp ($^{\circ}C$) (see A.3)	T	21	0.13	29.3	0.20	70.7	0.23	1.1
NaI Concentration $\%(w/w)$ (see A.4)	C	63	0.0053	50	0.0053	50	0.0075	0.012
Viscosity (m^2/s) $\times 10^{-6}$ (see A.5)	ν	1.58	0.0418	99.7	0.0020	0.3	0.036	2.3
Density (see A.6)	ρ	1871.2	6.1	32.7	8.7	67.4	10.7	0.6
Vapour Pressure (kPa) (see A.7)	P_v	1.048	0.0115	79.7	0.0056	20.3	0.0124	1.2
Piston Velocity (m/s) (see A.8)	V_c	0.1003	0.0032	69.6	0.0021	30.4	0.0039	3.9
Nozzle Velocity (m/s) (see A.9)	V_n	16.35	0.53	72.4	0.33	27.6	0.62	3.8
Discharge Coefficient (see A.10)	C_d	0.852	0.028	96.2	0.006	3.8	0.029	3.4
Reynold Number (see A.11)	Re	79760	2625.5	73.1	1593.8	26.9	3071.4	3.9
Cavitation Number (see A.12)	K	1.847	0.016	4.2	0.078	95.8	0.08	4.3
Collapse Length (see A.13)	L_{cav}/L	0.25	0.005	0.8	0.059	99.2	0.006	23.7
Shedding Frequency (see A.14)	f	1600	51.38	99.44	3.87	0.56	51.53	3.2
Spray Angle ($^{\circ}$)(see A.15)	θ	9.72	0.75	35.5	1.01	64.5	1.26	13.0

Chapter 5

Results and Discussion

This chapter presents the results obtained from the cavitation rig presented in chapter 3. High-speed visualisation of an extensive range of conditions provided detailed characterisation of the orifice flow fields. Collapse length measurements are presented and indicate the complex nature of the orifice flow. Periodic shedding frequencies were measured for the partial cavitation regime. Extensive discharge coefficient measurements are also presented. Finally, the influence of the cavitation on the spray structure is also addressed.

5.1 Cavitating Flow Regimes

High speed visualisation was used to non-intrusively investigate the internal flow structures within the orifice for a wide range of conditions from single-phase turbulent flow through to hydraulic flip. A number of distinct cavitating flow regimes were identified. A typical image frame for each of these regimes is presented in figure 5.1. The distinguishing characteristics of each of these regimes will now be briefly discussed.

Incipient cavitation - figure 5.1(a) shows the typical cavitation structure for incipient conditions. Under these conditions the pressure at the nozzle entrance is just low enough for the largest nuclei present in the liquid to reach their critical radius and expand. Cavitation bubbles form sporadically around the nozzle entrance in the high-shear flow at the periphery of the separated boundary layer.

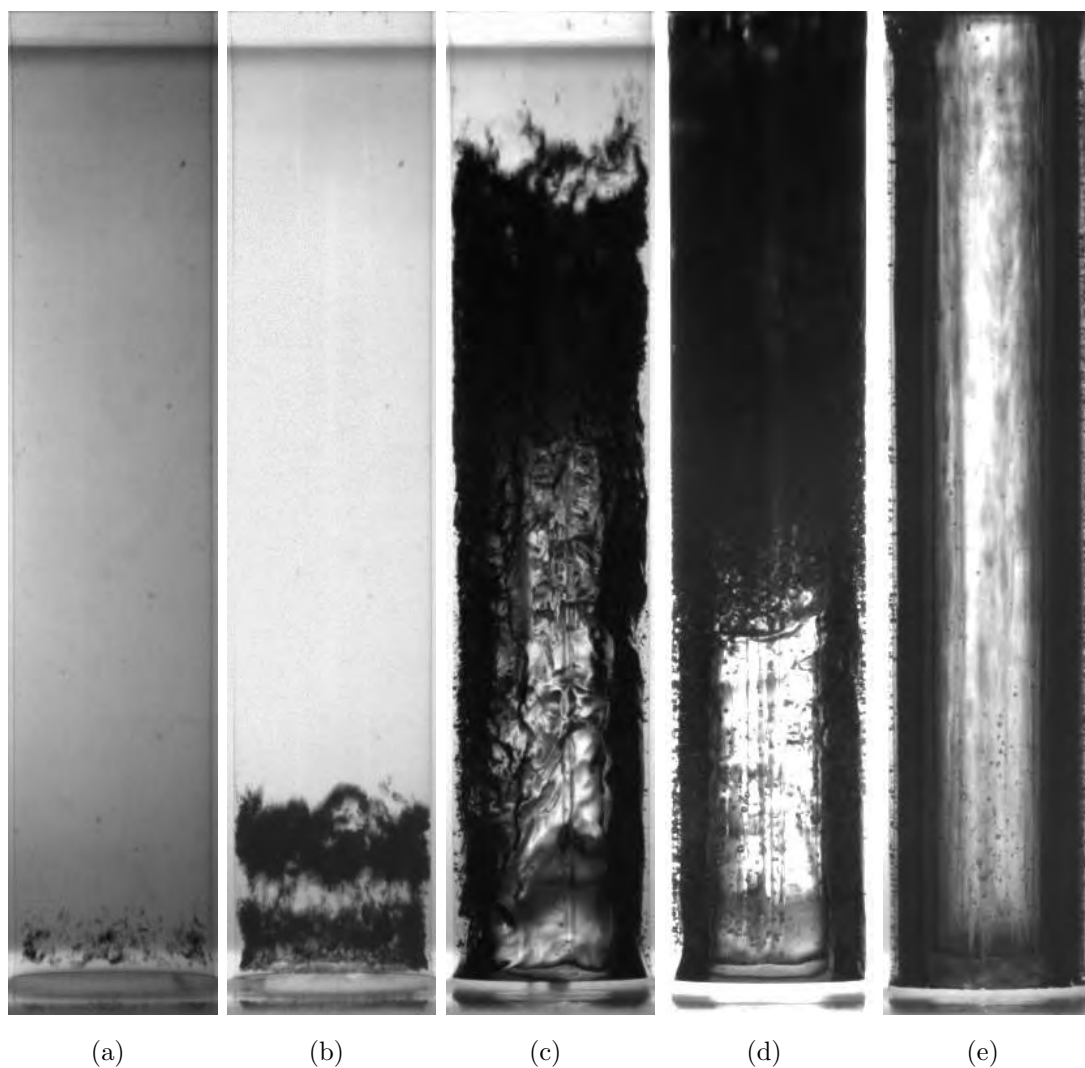


Figure 5.1: Representative nozzle cavitation structures for (a) incipient cavitation ($K = 2.27$, $Re = 6.57 \times 10^4$), (b) partial cavitation ($K = 1.93$, $Re = 9.80 \times 10^4$), (c) developed cavitation ($K = 1.76$, $Re = 1.06 \times 10^5$), (d) supercavitation ($K = 1.36$, $Re = 1.36 \times 10^5$) and (e) hydraulic flip ($K = 1.28$, $Re = 9.12 \times 10^4$).

The bubbles tend to remain as individual bubbles as they grow and extend a short distance into the nozzle before collapsing.

Partial cavitation - a reduction of cavitation number from the incipient conditions decreases the pressure at the nozzle entrance further. The higher number of bubbles forming at the nozzle entrance increases the void fraction of the cavity. The cavity attached to the nozzle entrance forms a well defined structure with a cloud like appearance which typically extends less than a third of the nozzle length. These cloud like cavitation structures consist of lots of small bubbles. These conditions are referred to as partial cavitation. The collapse of partial cavitation is a complex process and will be discussed in detail in section 5.4. Figure 5.1(b) shows a representational image frame for partial cavitation.

Developed cavitation - as the cavitation number is reduced further the void fraction of the cavitation increases significantly and the cavitation bubbles forming at the nozzle entrance extend into cavitation films. Figure 5.1(c) shows the typical structure of developed cavitation. The cavity attached to the nozzle entrance no longer consists of many small bubbles and has a glassy smooth appearance. As the cavity extends further the surface begins to become disturbed by the action of the liquid near the closure region. During the transition from partial cavitation to developed cavitation there is a sudden jump in the stream-wise length of the cavity. This will be discussed in more detail in section 5.3. For developed cavitation the cavitation film stretches from the nozzle entrance to the region preceding, but not quite at, the nozzle exit plane.

Supercavitation - further reductions in the cavitation number result in supercavitation, which is shown in figure 5.1(d). For nozzle flows, supercavitation refers to the conditions whereby cavitation bubbles forming at the entrance of the nozzle extend the entire length of the orifice and collapse at or beyond the exit plane of the nozzle. A clear distinction will be made in this work between supercavitation and developed cavitation which has not always been made in the literature (e.g. Sato & Saito (2002)). The cavity forming at the nozzle entrance appears glassy smooth as for developed cavitation. The highly turbulent region towards the nozzle exit cause the cavity to appear dark and rough.

Hydraulic Flip - as the cavitation number is reduced further the fixed cavity attached to the nozzle entrance reaches the nozzle exit. Ambient gas, which is at a

relatively high pressure compared with the vapour region, breaches the cavity and fills the separation zone producing a jet which separates at the nozzle entrance and remains detached from the nozzle wall for the entire length of the nozzle. This condition is referred to as hydraulic flip and is shown in figure 5.1(e). With the onset of hydraulic flip there is a complete cessation of cavitation within the nozzle. The wall regions of the nozzle now appear dark due to the refraction of the light as it passes through the separated region. A thin layer of liquid can often be observed between the wall and the separated jet, which will be discussed in detail in section 5.6.2.

5.2 Test Parameters

The experimental conditions explored within this work were chosen such that for all values of Re , the cavitation number, K could be adjusted to cover the range of flow conditions from single-phase flow through to hydraulic flip. Accordingly, the cavitation number range was $K \approx 1.1 \sim 3$. This allowed exploration of the differences in cavitation structure for a given K for different values of Re . The lowest Re in the range was that for which single phase flow could be achieved at ambient back pressure. However, the highest Re for which the cavitation within the nozzle could be suppressed by increasing the back pressure was limited by the maximum allowable pressure within the pressure vessel of 1.5MPa . A summary of the final range of test conditions can be seen in table 5.1.

5.3 Collapse Length

Non-dimensional collapse length, L_{cav}/L , was measured for cavitating flows of both water and sodium iodide. Figure 5.2 shows the results of these measurements plotted as a function of cavitation number, K . Generally the trend in the collapse length across the wide range of cavitation numbers were clearly established. The low degree of scatter in the data reflects the effectiveness of the technique employed to calculate the collapse length (see section 4.3.1).

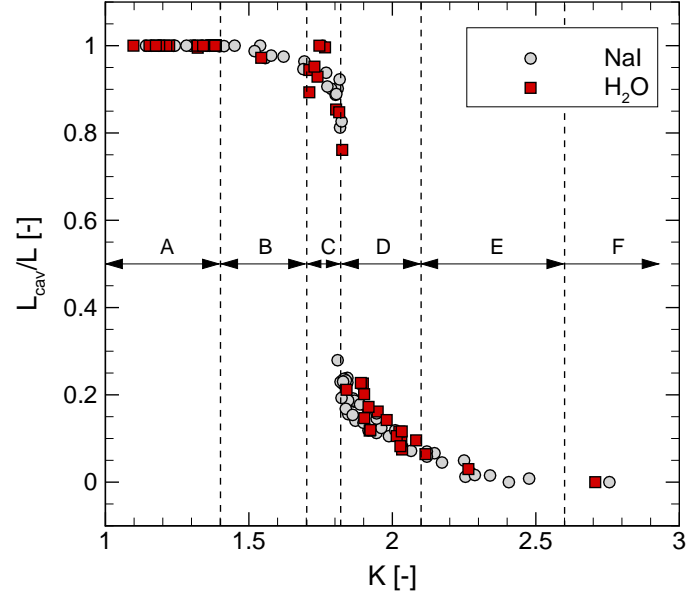
The plot has been indicatively divided into the different internal flow regimes observed for the respective range of K values, as outlined in section 5.1. Region

Table 5.1: Experimental Parameters

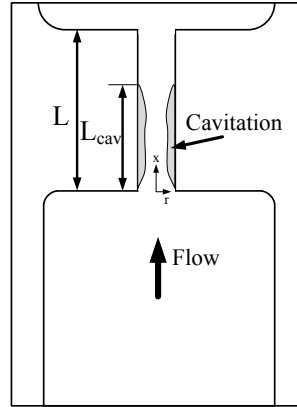
Parameter	Value
Reynolds Number (H_2O), Re	$7.4 \times 10^4 - 2.2 \times 10^5$
Reynolds Number (NaI), Re	$4.8 \times 10^4 - 1.5 \times 10^5$
Cavitation Number (H_2O), K	1.1 - 3.6
Cavitation Number (NaI), K	1.1 - 2.8
Weber Number (H_2O), We	$3.3 \times 10^4 - 3.1 \times 10^5$
Weber Number (NaI), We	$1.3 \times 10^4 - 1.0 \times 10^5$
Discharge Coefficient, C_d	0.63 - 0.87

F , with $K > 2.6$ corresponds to single phase flow through the nozzle, and thus $L_{cav}/L = 0$. Region E contains the onset of cavitation within the nozzle. Points to the far right in this region are for incipient cavitation, with tiny bubbles forming in the shear layer near the nozzle entrance and collapsing almost immediately. As the cavitation number is reduced the cavity begins to grow with length reaching approximately 5% of nozzle length. With further reductions in K the cavity length grows as the bubbles now begin to occupy the separated boundary layer. This region is labelled D and marks the partial cavitation region with normalised collapse lengths between approximately $0.05L$ for $K \approx 2.1$ and $0.25L$ for $K \approx 1.8$. The cloud cavities that form in this region exhibit periodic shedding, with large oscillations in the length of the cavity throughout the shedding cycle (see section 5.4.1 below).

As K is reduced below ≈ 1.8 the collapse length jumps discontinuously to approximately $0.8L$ as the flow transitions to developed cavitation, labelled region C . The developed cavitation region spans a very narrow range of cavitation numbers between approximately $K \approx 1.7 - 1.8$. The cavity length is prone to large oscillations in length and collapses in the highly turbulent region just before the nozzle exit. Sporadic shedding of clouds from the main fixed cavity attached to the nozzle entrance occur, with some of these clouds convecting through the nozzle exit. Cavity lengths were observed to fluctuate within the recording for



(a)



(b)

Figure 5.2: (a) Time-averaged, normalised cavitation collapse length for $Re = 5.3 \times 10^4 - 2.1 \times 10^5$ (b) Schematic illustrating the definition of L_{cav} . Regions: A = hydraulic flip, B = supercavitation, C = developed cavitation, D = partial cavitation, E = incipient cavitation, F = single phase.

developed cavitation conditions, which will be discussed in more detail in section 5.5.2. For $K < 1.7$ the nozzle rapidly transitions to either region A or B representing hydraulic flip and supercavitation respectively. Observations revealed a propensity for the flow to hydraulically flip (assigned $L_{cav}/L = 1$), before transitioning back to supercavitation. This reversion to supercavitation is unusual for sharp-edged orifices and will be discussed in detail in section 5.6.2. For supercavitation, region B , the cavity collapses at or just beyond the exit plane of the nozzle, with averaged collapse length just below $L_{cav}/L = 1$. Cavitation numbers of $K < 1.4$ correspond to hydraulic flip, with all cavitation ceasing.

Ostensibly there was no differences in the collapse length observed for the cavitating flows of water and sodium iodide. The transitions between the identified regions of the flow were invariant between the two fluids, suggesting the differences in properties between the two fluids, which were not accounted for by the cavitation number (i.e. viscosity and surface tension), had a minimal impact on the overall cavitation behaviour. The effects of dissolved gases and nucleation on the observed cavity length were also explored. To do so, liquid was left for many hours to reach equilibrium concentrations of dissolved gases within the supply tank. A sequence of injections at nominally identical conditions was then conducted, returning the fluid to the same tank from which it was extracted. While Re and K values cannot be matched exactly, due to changes to fluid temperatures and slight fluctuations in pressure, results indicated no noticeable effects on the collapse length. In fact the minimal scatter of the data further indicate that the effects of changes to the Re , even for each individual fluid, had very little effect on the collapse length behaviour.

Experimental measurements of collapse length conducted by Sato & Saito (2002) revealed similar trends in the collapse length for cavitating water flows in large nozzles (diameters up to 22mm). Their measurements of collapse length were normalised using nozzle diameter resulting in a unique curve for each nozzle L/D ratio. Despite observing a rapid jump in collapse length for 4 of the 5 nozzles they tested, the authors made no attempt to explain this. Figure 5.3 shows the collapse length data presented for the nozzles in their experiments. In this case it has been normalised using nozzle length rather than diameter. The first two series of data (labelled “NaI” and “H₂O”) corresponds to collapse length data

from the current work, for which $L/D = 4.85$. The remaining data, labelled A-E, correspond to the collapse length data from [Sato & Saito \(2002\)](#) for various nozzles with L/D ratios from 2.27 - 4.67. Series *D* from their work used a trip wire positioned just upstream of the nozzle entrance to initiate cavitation prematurely.

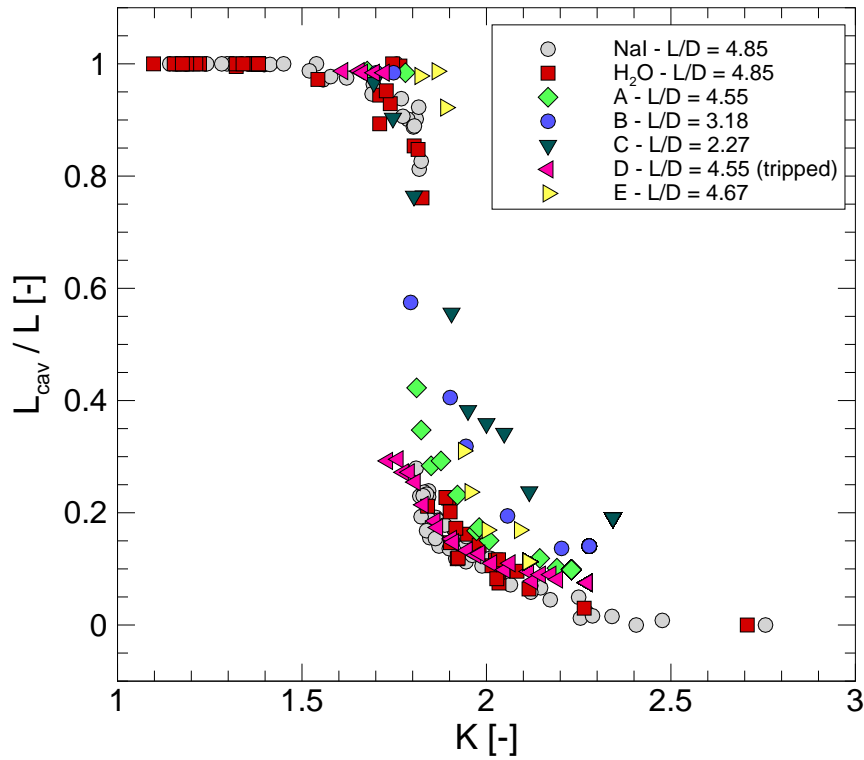


Figure 5.3: Cavitation collapse length comparison. Data labelled *NaI* and *H₂O* represent data from the current work. Data labelled series A-E is collapse length data for various nozzle geometries adapted from [Sato & Saito \(2002\)](#).

When plotted in this fashion, the cavitation collapse length for each of the various L/D ratio nozzles follows similar behaviour. Data series *C* from figure 5.3 is the only nozzle to demonstrate smooth collapse length variation across the plotted cavitation number range with no obvious discontinuities. The distinguishing feature of this nozzle is its shorter L/D ratio when compared to the other data

series exhibiting the discontinuous behaviour. It appears that the tendency of the cavity to suddenly lengthen as K is reduced below $K \approx 1.8$ is related to the pressure gradient in the proximity of the cavity closure region. From Bernoulli's principle it can be expected that the lowest pressure in the nozzle will correspond to the vena contracta. Following the vena contracta the pressure increases as the flow expands and re-attaches to the nozzle wall. Once the flow has re-attached the pressure can be expected to decay until the nozzle exit due to the viscous frictional losses, where the friction factor, f , can be estimated using the *Blasius* equation (Schlichting (1968));

$$f = \frac{0.3164}{Re^{1/4}} \quad (5.1)$$

The exact stream-wise location of the vena contracta will be a function of the Reynolds number, contraction ratio, and nozzle L/D ratio. However, for turbulent flow conditions it can be expected to occur approximately $0.5D$ from the entrance of the nozzle (Lichtarowicz *et al.* (1965), Daugherty & Franzini (1965)). For partial cavitation (region D in figure 5.3), bubbles initiating in the shear layer at the entrance of the nozzle occupy the recirculation region which results from flow separation. As more bubbles form they begin to fill this region and coalesce forming dense bubble clouds which appear to be bounded by the periphery of the recirculation region. Eventually the bubble cloud begins to extend into the region where the liquid flow is expanding after the vena contracta. The expanding flow exerts a shear force on the cavity. The flow re-attachment downstream from the cavity forms a re-entrant liquid jet which causes the fixed cavity to be pinched off from the nozzle entrance. The shed cavity forms a coherent bubble cloud, leaving behind a small cavity attached to the nozzle entrance. The adverse pressure gradient in the region of expanding flow promotes the rapid collapse of the bubble clouds. This growth and pinching cycle are highly periodic and will be discussed in detail in section 5.4.

As the cavitation number decreases for a fixed Re , the vapour production increases and the bubbles forming at the nozzle entrance coalesce into a single cavity. The pressure in the separated region is now more conducive to maintaining the cavity and allow it to extend further into the nozzle preventing the flow from

reattaching. At this point the length of the cavity is influenced by two counter acting forces. Firstly, the increased void fraction and greater stream-wise length of the low pressure region act to increase the length of the cavity and prevent the flow from reattaching to the nozzle wall. Secondly, the flow in the core of the nozzle attempts to expand after the vena contracta and exerts a shear force on the cavity surface. These two influences result in a rapid extension of the cavity length, resulting in the transition to developed cavitation (region *C* in figure 5.3). The highly turbulent flow in the core causes the cavity to sporadically break into smaller bubble clouds which collapse in the higher pressure region near the nozzle exit.

In the case of nozzles with short L/D ratios, such as data series *C* ($L/D = 2.27$) in figure 5.3, the length of the flow recirculation region represents a significant portion of the nozzle length. For this reason the rapid transition to developed cavitation cannot occur and so the collapse length exhibits a gradual increase towards $L_{cav}/L = 1$ as K is reduced. The location of the cavity closure region was also seen to have a significant influence on the stability of the cavity, which will be discussed in detail in the following sections.

5.4 Partial Cavitation

5.4.1 Periodic Cloud Shedding

The growth and pinching cycle mentioned for partial cavitation in section 5.3 results in periodic shedding of cavitation clouds. This periodic behaviour was observed for cavitation numbers between approximately $K = 1.8$ and $K = 2.1$. A representative image sequence illustrating this periodic shedding process can be seen in figure 5.4 for $K = 1.97$ at $Re = 1.1 \times 10^5$. Image (a) reveals a bubble cloud (labelled B) beginning to be separated from the fixed cavity (labelled A) attached to the nozzle entrance. Image(b) shows the gap between the two structures, A & B, beginning to expand as bubbles within the bubble cloud coalesce. By image (c) the bubble cloud has been entirely shed from the fixed cavity at the entrance of the nozzle and has formed what appears to be a vortex of cavitation bubbles. Surface tension forces and coalescence draw the bubble cloud together, while

momentum imparted on the cloud from the core flow cause it to roll as a tight vortex. These effects increases the gap between the two large-scale structures which can be seen in image (d). The cavitation at the entrance continues to grow during this process. The bubble cloud begins to collapse as it is convected into the high pressure wake region, and by image (e) very little of the apparent vortex structure remains. The fixed cavity at the nozzle entrance appears uniform across the nozzle cross-section and varies very little in length between image (d) and image (e). However it continues to expand as bubbles forming at the entrance coalesce together. Only remnants of the shed bubble cloud can be seen in image (f), whilst the fixed cavity continues to grow. The formation, growth, coalescence, shedding and collapse processes now repeat themselves, with images (g)-(j) analogous to images (a)-(d), illustrating the periodicity of the process.

5.4.2 Re-entrant Jet

It is widely believed that the periodic shedding process presented in figure 5.4 is controlled by motion of the re-entrant jet which is formed during the flow re-attachment with the nozzle wall. In order to investigate the influence of the re-entrant jet motion on this process recordings of the entrance region of the nozzle were taken at frame rates up to 100,000 *fps*. The much greater temporal resolution provided significant insight into the role that the re-entrant jet has on the periodic shedding motion. To achieve this frame rate the camera ROI was reduced significantly, as is shown schematically in figure 5.5(a). A typical image sequence of the periodic shedding process for these conditions can be seen in figure 5.5(b). Image 1 shows a fixed cavity attached to the entrance of the nozzle, labelled *A*, and a bubble cloud labelled *B*, which has been shed from the fixed cavity. Images 2 and 3 show the fixed cavity continue to grow while the shed cloud is convected into the higher pressure region (outside the ROI) and begin to collapse. The collapse of the bubble cloud and reattachment of the core flow establishes the re-entrant jet (labelled *C*) in image 4 and 5. However, identifying the exact location of the re-entrant jet is very difficult. The influence of the re-entrant jet can clearly be seen to deform the under side of the fixed cavity. This deformation can be traced and can be seen to move steadily towards

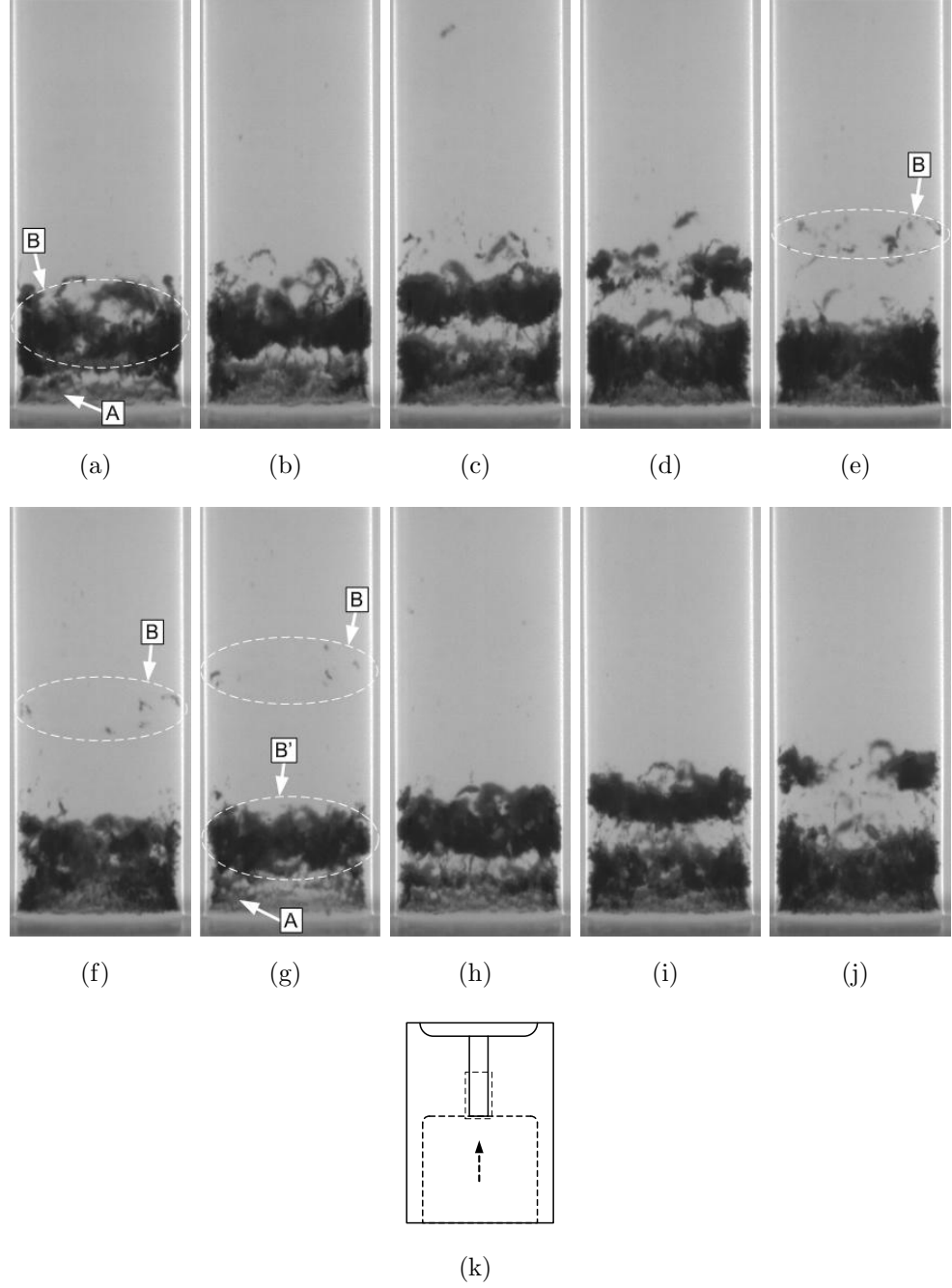


Figure 5.4: Periodic cavitation shedding sequence recorded at $f = 20,052\text{Hz}$, $Re = 1.1 \times 10^5$, $K = 1.97$. Time between images, $\Delta t \approx 100\mu\text{s}$. Schematic indicates location of images (a) - (j). Annotations: *A* - identifies the fixed-type cavity at the entrance of the nozzle. *B* and *B'* - identifies the old and new bubble cloud.

the nozzle entrance in images 6-10 as indicated by the diagonal line following its position. In image 11, the re-entrant jet impinges on the lower point of the fixed cavity and severs it from the nozzle entrance. The initial fixed cavity, A , is now separated from the new fixed cavity, labelled A' , and begins to form the new cloud, labelled B' . Images 12-14 show the bubbles within the two-phase cloud structure coalescing, while the length from the entrance to the farthest stream-wise point of this new cloud remains essentially constant. During the same period, the new fixed cavity grows from the entrance and extends towards the nozzle exit. Finally, image 15 shows the cloud being shed and beginning to roll up as a vortex of bubbles as the central flow imparts rotational momentum on the cloud structure.

Whilst these observations confirm that the action of growth and pinching of the cloud cavitation is indeed linked to the motion of the re-entrant jet impinging on the fixed cavity, they reveal the continual presence of a liquid sublayer throughout the duration of the cycle. The thickness of this layer fluctuates with the complex motion of the cavitation clouds within the recirculation zone, but remains visible for all partial cavitation conditions. This revelation provides some great insight into the re-entrant jet mechanism and validates the use of the refractive index matching technique, which allowed unabated optical access to the near wall region of the flow. Depictions of partial cavitation instabilities in the literature (see for example [Le *et al.* \(1993\)](#), [De Lange & De Bruin \(1998\)](#), [Callenaere *et al.* \(2001\)](#)) tend to suggest the fixed cavity remains attached to the body until the re-entrant jet forces liquid under the cavity and towards the entrance. The high fidelity images presented here have demonstrated that the motion of the re-entrant jet does not conform to this common description, but is rather more complex.

5.4.2.1 Re-entrant Jet Motion

The motion of the re-entrant jet, inferred from the deformation of the cavity interface and subsequent disruption of the fixed cavity, appeared to behave more as a travelling wave than a constant velocity liquid jet. Although the fixed cavity and cloud actually consist of a large number of small bubbles, as a simplification, they

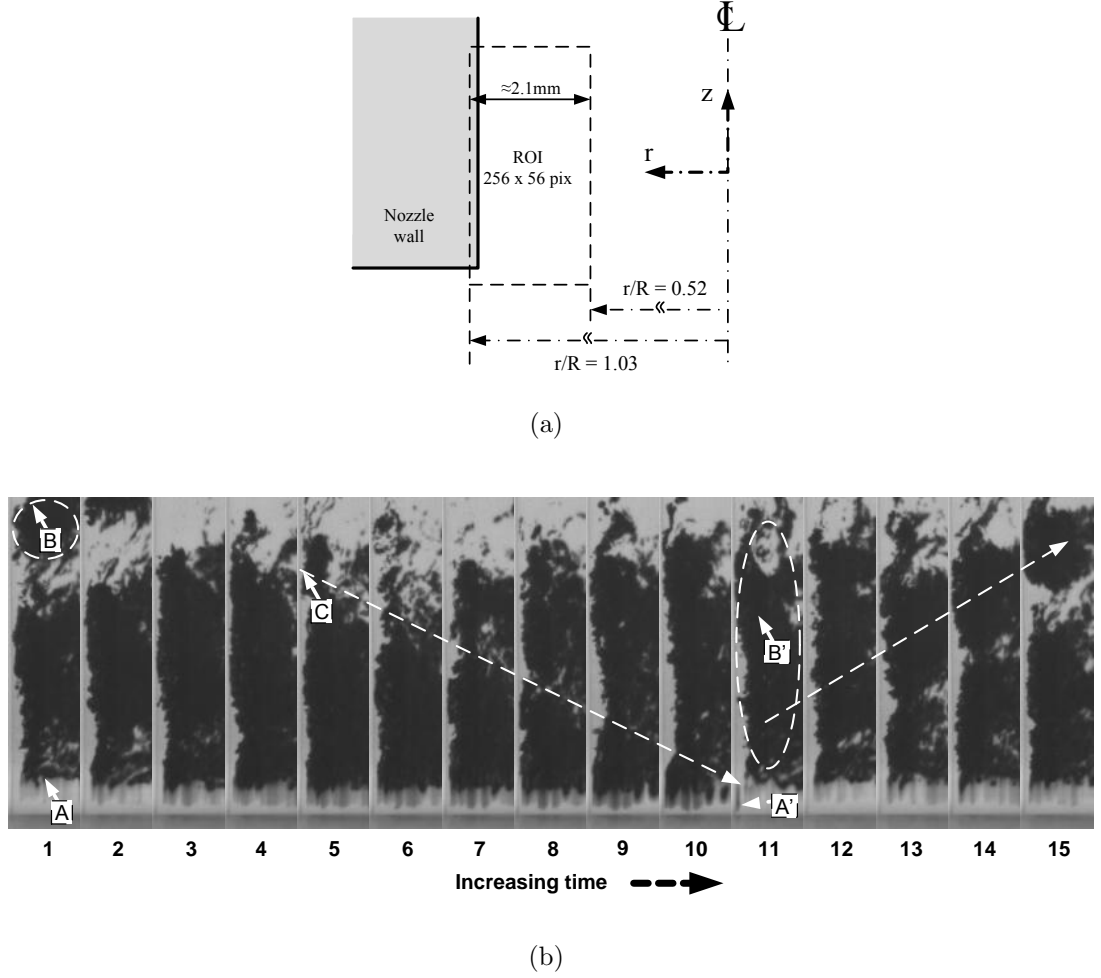


Figure 5.5: Cavitation shedding sequence showing detailed re-entrant jet motion for $K = 1.80$, $Re = 6.9 \times 10^4$ recorded at $f = 100000\text{Hz}$. (a) Camera region of interest showing resolution and position in nozzle (b) Image sequence, time between images, $\Delta t = 110\mu\text{s}$. Annotations: A, B & C identify the fixed cavity, bubble cloud and re-entrant jet respectively where an apostrophe implies a new structure.

can be thought of as a coherent vapour bubble. The outer surface of this cavity be thought of as a free surface above a liquid sublayer. Flow reattachment during the periods following cloud shedding, provide transient pulses of momentum which drive liquid flow beneath the cavity towards the nozzle entrance. Supplementary to this are pressure pulses created during the collapse of the shed bubble cloud. These two influences combine to produce periodic impulses of liquid, which seem to produce a travelling wave style motion for the re-entrant jet. A schematic illustrating the sequence of this motion for one period of the shedding is shown in figure 5.6.

At the instance $t/T = 0$ the bubble cloud (labelled B) is collapsing downstream from the cavity closure region. The flow reattachment creates an over-pressure at the stagnation point and causes the formation of the re-entrant jet (labelled C). The initial pulse of momentum creates a deformation of the underside of the cavity surface, which is shown at $t/T = 1/6$. This deformation moves towards the nozzle entrance at approximately constant velocity and has the appearance of a travelling wave moving along the cavity interface. Although shown schematically as a coherent vapour cavity, the fixed cavity (labelled A) is actually a two phase region composed of small vapour bubbles and liquid.

At the instance when the wave reaches the nozzle entrance ($t/T = 1/3$) the disturbance is sufficient to disrupt the fixed cavity causing it to break off from the entrance. Immediately a new cavity begins to grow from the nozzle entrance (labelled A') while the original fixed cavity forms the new bubble cloud (labelled B'). The new cloud is then entrained by the flow and begins to be convected downstream, shown at $t/T = 1/2$. The counter-directional velocity of the core-flow and the re-entrant jet imparts rotational momentum on the bubble cloud causing it rotate as it is convected downstream. This vortical motion is clearly evident in the video recordings. The bubbles within the cloud also appear to coalesce and form larger cavities which draws the cloud together. By $t/T = 2/3$ the bubble cloud has been drawn together and has formed a coherent structure. As the cloud is convected into the wake region behind the flow re-attachment point the cloud has formed a tight annular vortex ring around the nozzle ($t/T = 5/6$). Meanwhile the new fixed cavity (A') has grown and by this point has reached its

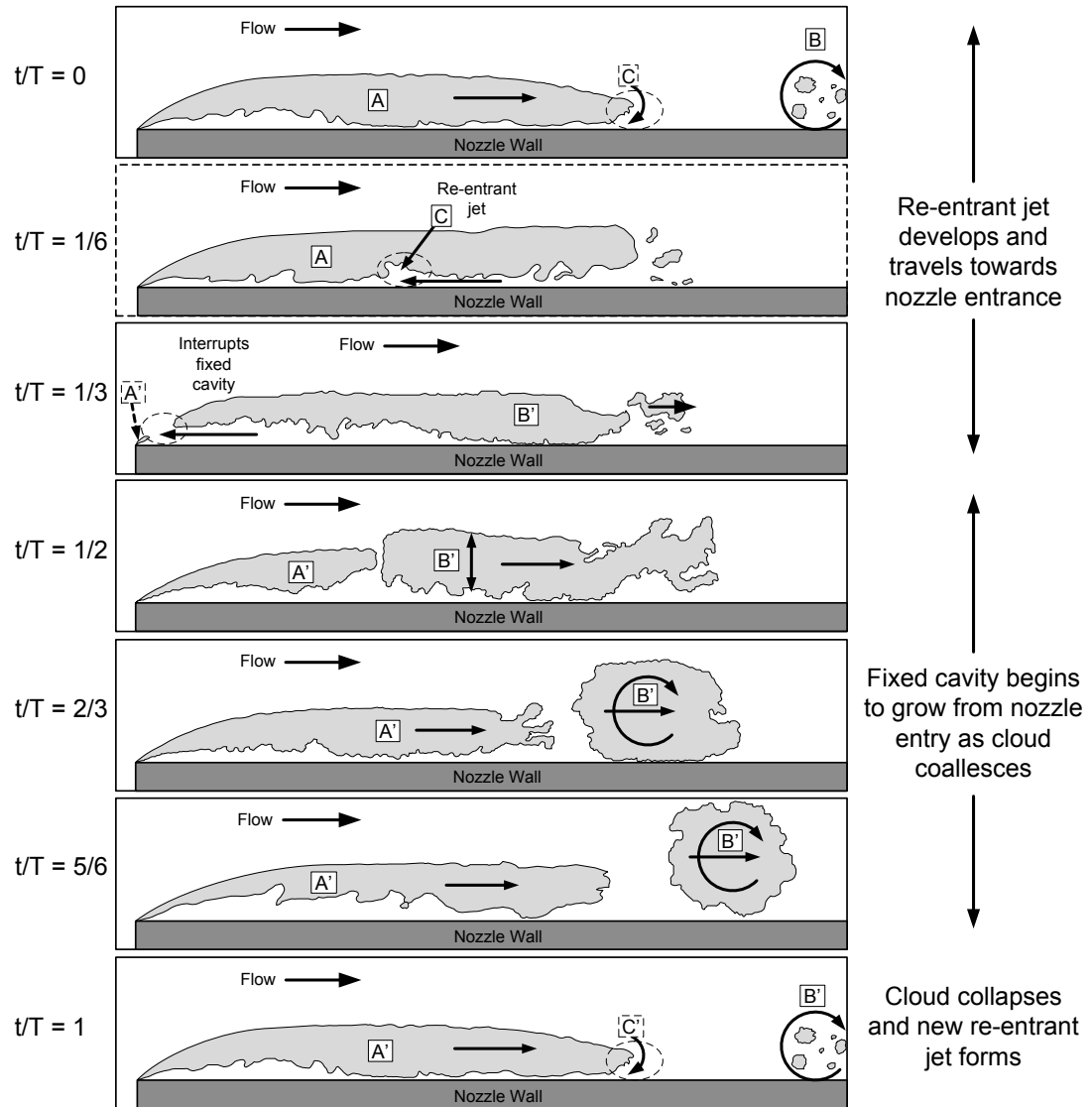


Figure 5.6: Schematic illustration of typical re-entrant jet motion, adapted and modified from [Le *et al.* \(1993\)](#). Note: the nozzle orientation has been turned horizontal for convenience. Annotations: A, B & C identify the fixed cavity, bubble cloud and re-entrant jet respectively where an apostrophe implies a new structure. Note: vapour appears grey.

characteristic length. Following this, the cloud continues to convect into the high-pressure region downstream from the cavity and collapses violently ($t/T = 1$). Occasionally, rebound and collapse cycles for the bubbles within the cloud can be observed (see section 1.3.3). The flow can now re-attach to the nozzle wall, forming a new re-entrant jet (C') and the shedding process is repeated.

5.4.2.2 Estimation of Re-entrant Jet Velocity

As discussed above, the travelling deformation of the underside of the cavity interface could be identified in the recordings and was directly related to the cloud shedding. While this deformation was highly recurrent and often clearly visible within an image sequence, measuring the velocity of this travelling wave was an extremely difficult process. Due to the complex motion of the sublayer, and the recirculation present in the separated layer, identification of the leading edge of the travelling wave was not always possible. Often the cavity disturbance was visible at the downstream end of the cavity but became obscured by the motion of bubbles within the recirculation region. Figure 5.7 shows an example of the deformation of the interface discernible between adjacent frames of a recording. However, in order to provide a good estimate of velocity the deformation needed to be largely visible for the entire passage beneath the fixed cavity.

High-speed recordings, each 50,000 frames in length, were scoured to find 10 exemplary motion sequences, for which the interface could be effectively tracked. Figure 5.8(a) shows the position of the deformation as a function of time a recording at $K = 1.78$, $Re = 6.8 \times 10^4$ for the 10 sequences. The scatter of the data in the vertical direction is due the variation in the initial stream-wise location for which the jet could be observed to commence its motion under the cavity, which was highly dependent on the individual structures present. The velocity estimation for each of the 10 sequences was determined from the slope of a linear curve fit (not shown in figure 5.8(a) for clarity). An example of this curve fit for series 3 of figure 5.8(a) can be seen in figure 5.8(b).

The jet velocity estimate was then determined as the average of the 10 events. This calculation process was repeated for a number of partial cavitation conditions, the results of which are summarised in table 5.2. Jet velocity for each

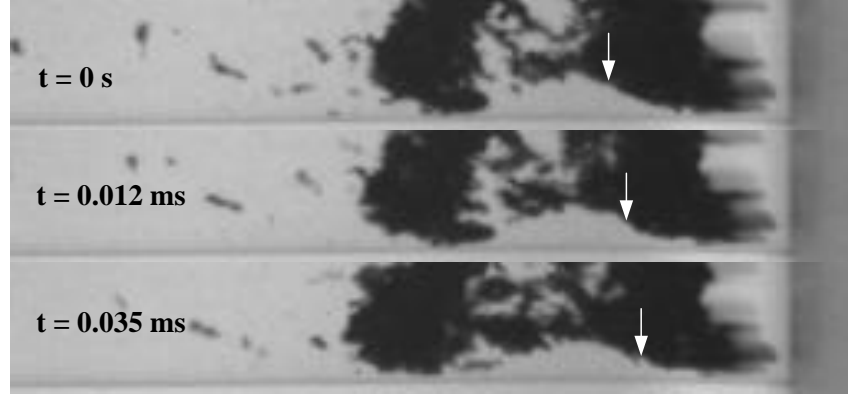


Figure 5.7: Re-entrant jet interface deformation image sequence recorded at 86956fps for $K = 1.78$, $Re = 6.8 \times 10^4$. The location of the deformation within each frame is indicated by the white arrow.

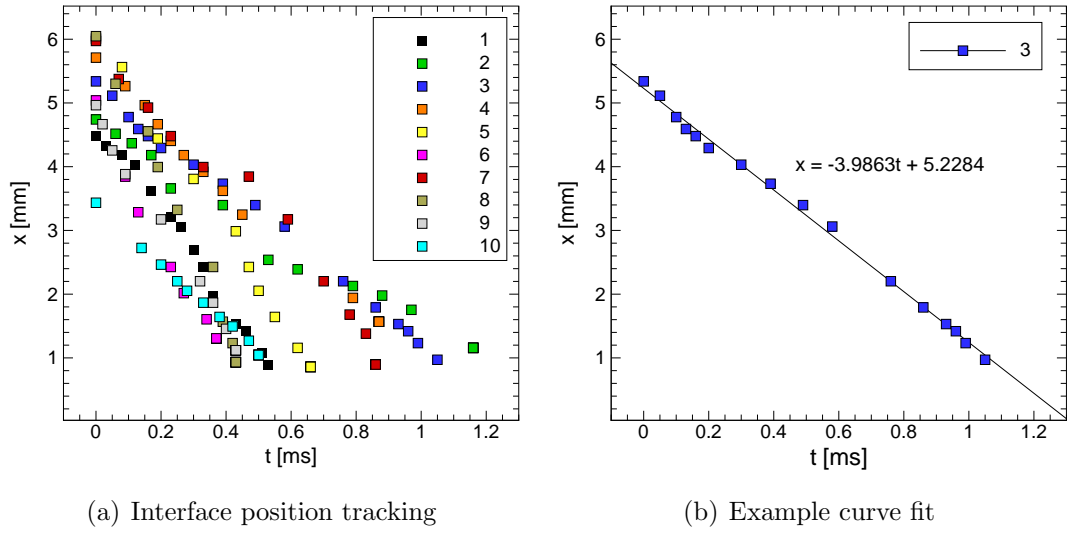


Figure 5.8: Re-entrant jet interface tracking for $K = 1.78$, $Re = 6.8 \times 10^4$. (a) shows the position with time of the interface disturbance caused by the re-entrant jet for 10 periods of the motion. (b) shows an example linear curve fit to series 3.

individual sequence within a recording was found to be highly linear, however significant fluctuations could be observed in the velocity magnitude between the individual re-entrant jets within a recording. The standard deviation in the velocity estimate provides an indication of the scatter in the individual jet velocity approximations.

Table 5.2: Measured re-entrant jet velocity, V_j , for various conditions. V_n is the mean nozzle velocity. S_{V_j} is the standard deviation of the jet velocity.

#	Re	K	V_n [m/s]	V_j [m/s]	$ V_j/V_n $	S_{V_j} [m/s]
1	62764	1.882	12.822	-10.853	0.846	1.969
2	69027	1.804	13.545	-6.575	0.485	1.625
3	68214	1.784	13.742	-6.634	0.483	2.730
4	64100	1.847	13.103	-8.637	0.659	0.990
5	83230	2.001	16.479	-21.481	1.304	2.329
6	83343	2.002	16.470	-19.223	1.167	2.030

The ratio of the magnitude of re-entrant jet velocity to mean nozzle velocity, $|V_j/V_n|$, can be seen in figure 5.9. Typically the jet velocity is of the same order of magnitude as the free-stream velocity, which is consistent with other studies (eg [Le *et al.* \(1993\)](#), [Kawanami *et al.* \(1997\)](#)). For the cases with $K > 2$ the ratio $|V_j/V_n| > 1$. Using electrical impedance measurements on the surface of a hydrofoil, [Pham *et al.* \(1999\)](#) also observed the re-entrant jet velocity to exceed the free-stream velocity, found that the jet slowed as it travelled beneath the cavity. The current measurements indicated the motion of the interface deformation was essentially constant (see figure 5.8(a)). These observations support the notion that the actual mechanism causing the break off and shedding of the fixed cavity is not so much the coherent motion of a thin liquid layer, but is rather due to a surge of liquid created by the travelling wave which disrupts the fixed cavity in the vicinity of the the nozzle entrance. The wave motion is essentially superimposed on the translational motion of the physical re-entrant jet. The wave travels along

the cavity interface at velocities greater than the motion of the liquid itself, which is slowed by the viscous interaction with the wall.

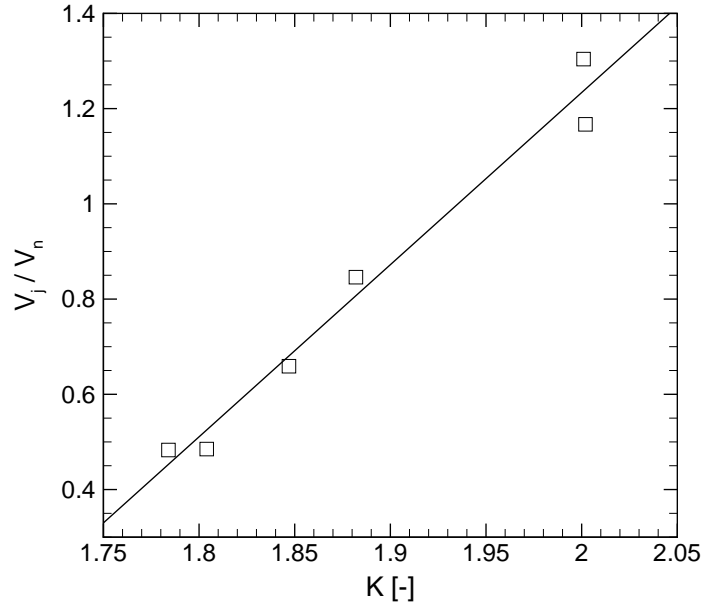


Figure 5.9: Ratio of re-entrant jet travelling wave velocity, V_j to mean nozzle velocity, V_n , plotted as a function of cavitation number. Data from table 5.2.

In one recording of the partial cavitation, small vapour bubbles were seen moving in the re-entrant jet liquid layer below the cavity. By tracking the motion of these bubbles between the frames it was possible to approximate the bubble velocity, from which the liquid velocity was then inferred. Figure 5.10 shows the frame-by-frame position of one such bubble. The horizontal axis, x , is distance from the nozzle entrance and the vertical axis, y , is distance from the nozzle wall. The bubble appeared to be formed as a small bubble cloud collapsed at the end of the fixed cavity following the shedding of a bubble cloud. In fact, it appeared to coincide with the initial pulse of the re-entrant jet. Initially the bubble moves horizontally in what can be assumed to be a laminar sub-layer adjacent to the wall. At $x \approx 3.4mm$ from the nozzle entrance the bubble was convected away from the wall illustrating the complex flow fields within the re-

entrant jet. Most significant was the interaction of the liquid layer and the cloud as it rolls up and was convected down-stream after detaching from the fixed cavity at the entrance. As the disturbance travels much faster than the liquid, the shed cloud is convected down-stream as the liquid sub layer continues moving towards the nozzle entrance. The bubble is entrained into the vortical flow in the wake of the shed cloud and at $x \approx 2.4\text{mm}$ it is rapidly convected away from the wall. Eventually the bubble reaches the interface with the fixed cavity and is obscured from vision.

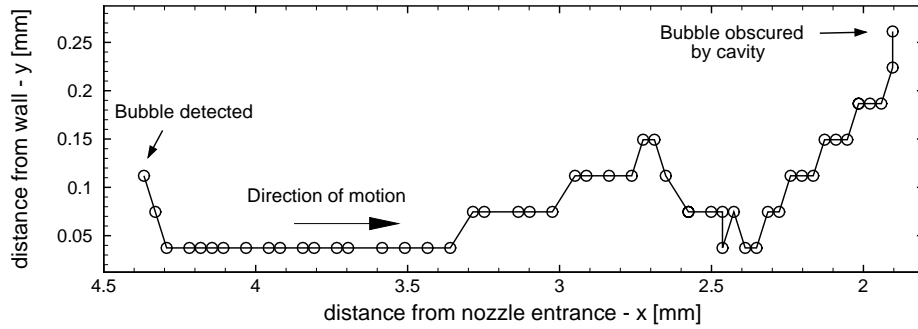


Figure 5.10: Bubble motion in the re-entrant jet for $K = 1.88$, $Re = 6.3 \times 10^4$ recorded at $f = 86,956\text{Hz}$. Time between images, $\Delta t \approx 115\mu\text{s}$.

The instantaneous stream-wise velocity of the bubble was determined for each frame making the assumption the inter-frame motion was linear. Averaging these values gave an estimate for the liquid velocity, which was determined to be $V_{liq} \approx -4.2\text{m/s}$. For the same period within the recording the travelling deformation causing bubble shedding was determined to have a velocity of $V_j = -11.5\text{m/s}$. Although the motion of one bubble cannot fully describe the liquid within the re-entrant jet the large difference between the inferred fluid velocity and the velocity of the cavity interface disturbance further supports the idea of a travelling wave style instability mechanism.

5.4.2.3 Asymmetric Cloud Shedding

Very rarely asymmetric cloud shedding could be seen for partial cavitation. For these injections the cloud shedding was far less periodic and would oscillate shed-

ding clouds on alternate sides of the nozzle. The asymmetric shedding appeared to be initiated by the convection of large gas bubbles through the nozzle which were initially resting on the face of the contraction below the nozzle. As these bubbles convected into the low pressure region in the nozzle entrance they violently expanded and significantly altered the cavitation structure within their vicinity. This momentarily causes an inclination of the cavity closure line and allows the re-entrant jet to form on a diagonal to the axis of the nozzle. There are parallels between the asymmetric motion of the re-entrant jet observed here and the three-dimensionality of the re-entrant jets observed on swept hydrofoils (e.g. De Lange *et al.* (1994), Duttweiler & Brennen (1998)). Figure 5.11 shows a sequence of diagonal re-entrant jet motion.

The jet (or cavity disturbance) travels towards the nozzle entrance, but has a circumferential velocity component. Initially it can be seen travelling to the right and is identified by red lines. It then reflects and travels to the left, which is identified by green lines. The diagonal re-entrant jet impinges with the fixed cavity at different times around the nozzle circumference causing asymmetrical cloud shedding. The collapse of these clouds maintains the imbalance in the re-entrant jet motion sets up an auto-oscillation of the asymmetric shedding. Generally the size of the cloud structures which are shed is significantly smaller than for symmetric re-entrant jet motion. The asymmetric shedding behaviour was highly transient and conditional on the location and size of the initial disturbance which caused it. Gradually the circumferential motion of the re-entrant was diminished and cavitation reverted to symmetric periodic shedding. The differences in the jet breakup due to asymmetric cloud shedding was not directly observed. However, it is reasonable to assume the influence on the spray structure would be minimal when compared to symmetric periodic cloud shedding. This would be primarily the result of the distance from the closure region to the nozzle exit being sufficient to allow dissipation of the increased turbulent kinetic energy introduced by the cloud collapse.

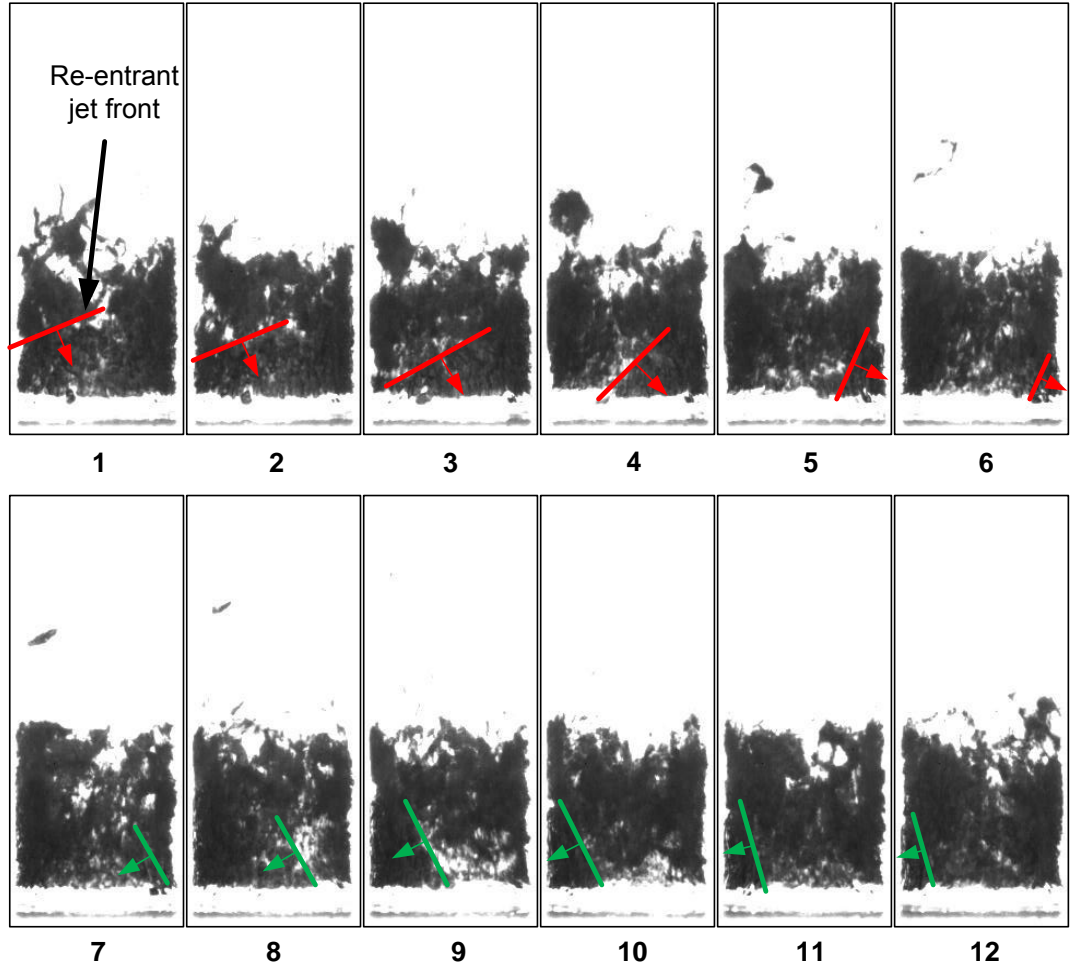


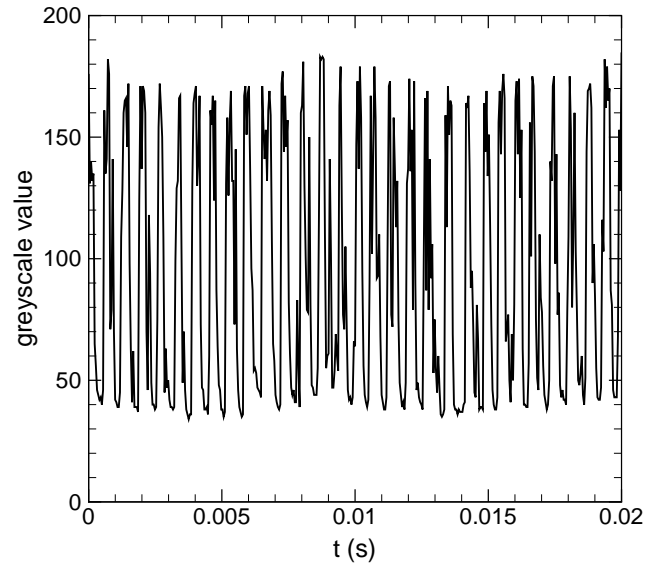
Figure 5.11: Image sequence showing asymmetric motion of re-entrant jet for $K = 1.83$, $Re = 8.7 \times 10^4$ recorded at $f = 23,121 Hz$. Time between images, $\Delta t \approx 130 \mu s$. Red lines indicate the re-entrant jet wave front travelling to the right, green lines indicate the re-entrant jet wave front travelling to the left.

5.4.3 Measurement of Periodic Shedding Frequencies

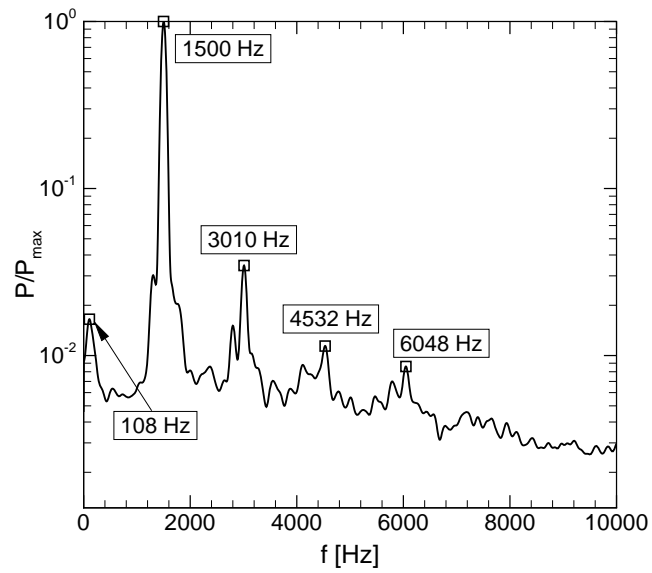
Measurements were conducted of the periodic shedding frequencies for partial cavitation conditions using the method outlined in section 4.3.3. Injections for both water and sodium iodide were conducted providing a source of comparison for the observed shedding behaviour. Figure 5.12(a) shows a 20ms record of the greyscale variation for a pixel located at non-dimensional axial and radial distances of $x/L = 0.12$ and $r/R = 2/3$ respectively for the cavitation recording shown sequentially in figure 5.4. Rapid greyscale variation can be seen modulated by a longer period oscillation. The averaged frequency spectrum for the 10 pixels interrogated at $x/L = 0.12$ is shown in figure 5.12(b), where the vertical axis is normalised power spectral density. The spectrum reveals a fundamental frequency of $1500Hz$ with second, third and fourth harmonics visible as diminishing peaks. A low frequency peak appears at $108Hz$ corresponding to the longer period pixel intensity oscillation in figure 5.12(a). This component is from the mains power oscillation of the halogen light illumination source.

The greyscale oscillations and singular narrow band frequency peak shown in figure 5.12 are typical for all periodic cavitation observed in the range $1.8 \leq K \leq 2.1$, for which $L_{cav} < 0.25L$. Fundamental frequencies identified had a typical 3dB bandwidth of the order of 100-150Hz. Axial vibrations of the piston were recorded for piston velocities covering the working range using a Bruel and Kjaer (B&K) accelerometer, signal amplifier and B&K 2035 800 point signal analyser unit. The vibration power spectrum indicated peak frequencies at 300 and 600Hz with spectral peaks above 1kHz roughly two orders of magnitude lower, thus ruling out the piston motion as a possible influence on the observed shedding periodicity.

Figure 5.13(a) is a compilation of the peak frequency extracted from the averaged power spectral density for each injection with periodic shedding properties. Linear curve fits for both data sets are also shown to suggest indicative trends. The data presented is far more extensive than any previously published for cavitating orifice flows, and represents the first data known to the authors for shedding frequencies in a liquid other than water. The shedding frequency indicates a strong linear dependence with cavitation number for both water and sodium

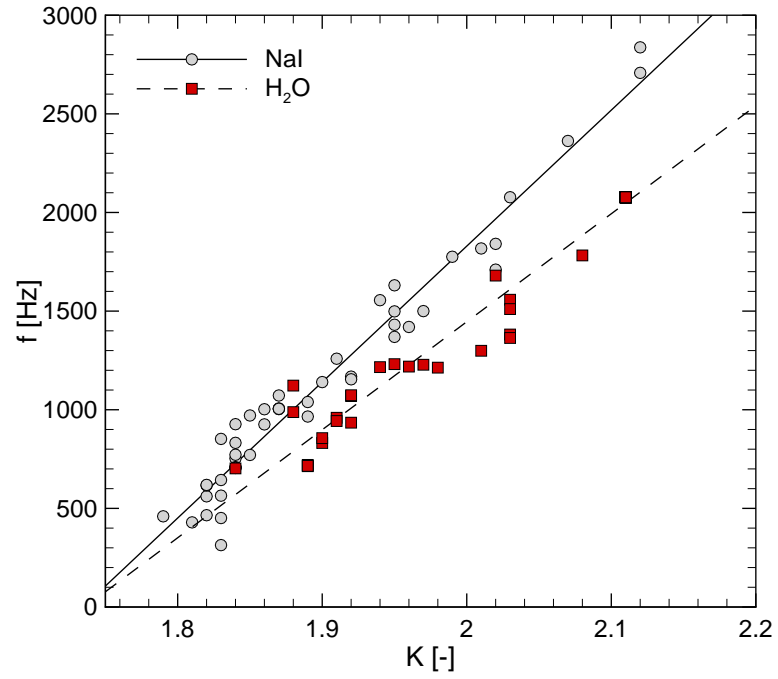


(a) typical pixel greyscale variation

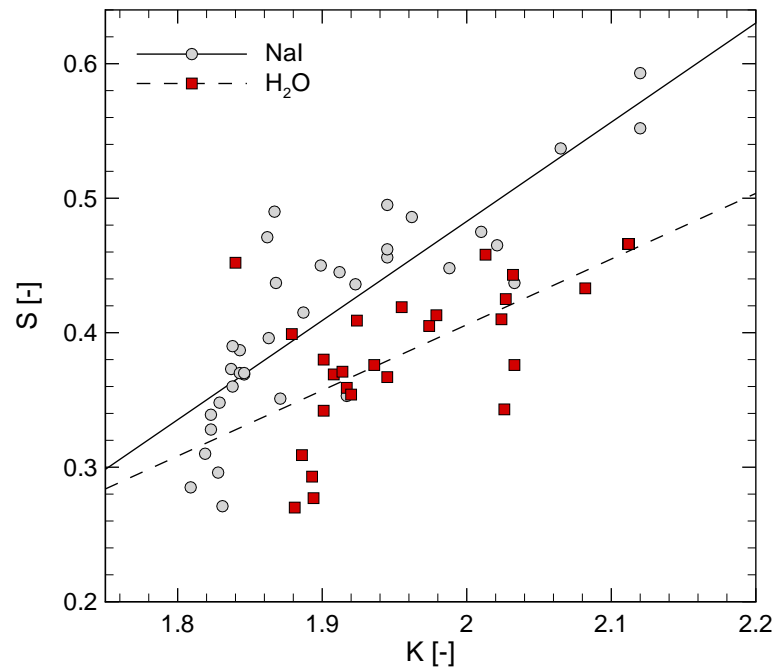


(b) average frequency spectrum

Figure 5.12: Power spectral density analysis for an flow conditions of $K = 1.97$, $Re = 1.1 \times 10^5$ extracted at a non-dimension stream-wise position $x/L = 0.12$.



(a)



(b)

Figure 5.13: Periodic shedding spectral analysis. (a) Peak frequency versus cavitation number (b) Strouhal number versus cavitation number.

iodide, with values ranging between approximately 500 - 2000 Hz. The higher values of this range correspond to the shorter timescales associated with the shorter collapse lengths observed in figure 5.2(a). As K approaches 1.8 and the cavity lengthens, the timescales for the re-entrant jet and cavity growth increase causing a reduction in the frequency of cloud shedding. Across the entire range of partial cavitation, the shedding frequencies measured for water were consistently below those for sodium iodide for the same cavitation numbers. The differences in the slope of the curves in figure 5.13(a) appears to be related to the differences in the Weber number, We for the two different fluids. There may also have been some minor influence from the differing degrees of dissolved gases within the liquid affecting the free-stream nuclei present and hence the cavity structure which forms. Comparison of the influence of variations in the Re revealed this influence had no affect on the slope of the shedding frequency curve, and so did not contribute to the difference in the slope of the curves.

The range of frequencies agree well with those obtained by Chandra & Collicott (1999) for measurements of large-scale cavitation instabilities in slots with a height of $H = 0.889mm$, which were of the order of 1-2 kHz. Their experiments were conducted for relatively short lengths of cavitation ($L_{cav} \approx 0.06L$). With this in mind, the shedding frequencies obtain here for $K \approx 2.1$, which indicated averaged collapse lengths of $L_{cav} \approx 0.05L$, matched their results very closely. Higher frequencies identified in their study (10-12 kHz), which were associated with individual bubble collapse, could not be effectively detected using this digital post-processing method due to the limitations imposed by the Nyquist sampling criterion.

Figure 5.13(b) presents the Strouhal number distribution with cavitation number, where Strouhal numbers were based on the mean cavity collapse length, $S = fL_{cav}/V_n$. For sodium iodide the Strouhal numbers ranged from approximately $S = 0.27$ at $K = 1.83$ to $S = 0.59$ at $K = 2.12$. Strouhal numbers for water injections were generally lower than this and ranges from approximately $S = 0.27$ at $K = 1.88$ to $S = 0.46$ at $K = 2.11$. These values are higher than those reported in the literature for cloud shedding on hydrofoils (Le *et al.* (1993), Sato & Saito (2002), Stutz & Reboud (1997a)), which are typically around $S = 0.2 \sim 0.3$. External flows have generally found that the Strouhal number

is largely independent of the cavitation number. The results presented in figure 5.13(b) indicate that changes in internal flow structure with cavitation number alter the shedding spectrum. The greater degree of scatter is due to the product of length and frequency, both of which have experimental variability (see appendix A).

5.5 Developed Cavitation

5.5.1 Cavity Appearance

The typical appearance for developed cavitation, $1.7 \leq K \leq 1.8$, within the nozzle can be seen in figure 5.14. A liquid layer can clearly be seen separating the cavity from the nozzle wall and extending the entire length of the cavity. The entrance region of the fixed cavity appears glassy smooth and unless disturbed by the motion of the liquid sublayer or the internal flow, remains so throughout the duration of the injection. Occasionally localised disturbances of the interface can be seen, created by the counterflow motion of the sublayer, or the convection of bubbles through the nozzle. Regularly the inner surface of the cavity can be seen to be disturbed by the advection of bubbles in the core liquid flow. These localised disruptions can then last for extended periods and produce long wakes stretching along the cavity interface towards the collapse region.

The cavity interface becomes increasingly rippled and disturbed as it extends to $0.3 \sim 0.40.3L$. Analysis of the recordings reveals the rippling is caused by the turbulent motion within the liquid sublayer, which is discussed in more detail below. As the cavity nears the closure region it can be seen to thin as the internal flow expands. This thinning allows interactions between the sublayer and the turbulent motion of the expanding core flow, breaking it into smaller bubble clouds. The transition from a single cavity near the nozzle entrance to a multitude of smaller bubble clouds makes the cavity appear much darker. Once shed from the main structure, these clouds quickly collapse as they convect towards the nozzle exit.

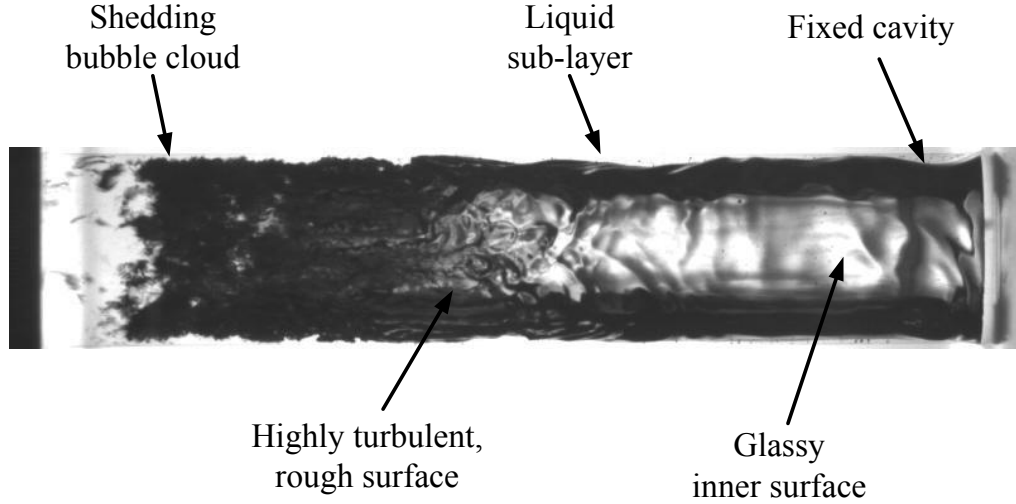
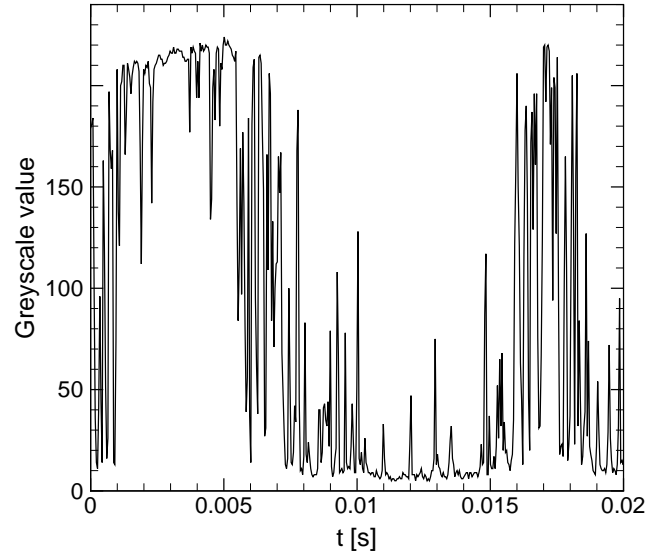


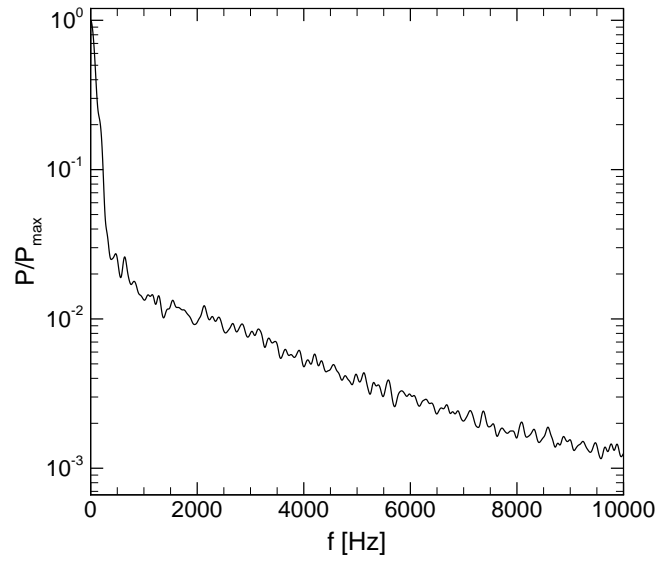
Figure 5.14: Turbulent reattachment with sporadic cavitation shedding,
 $K = 1.79$, $Re = 6.9 \times 10^4$

5.5.2 Transient Motion of Closure Region

Cavity closure for developed cavitation occurs in the region of the nozzle with rather flat stream-wise pressure gradient. As a result the collapse length of the cavity is particularly susceptible to slight changes in static pressure. This phenomenon has been observed for convergent-divergent nozzles and hydrofoil cavitation, but has not been addressed for plain orifice nozzles. Cavity collapse length regularly fluctuated up to 20% over short time spans but could not be correlated to appreciable changes in the injection pressure. These large but inconsistent fluctuations in cavity length made spectral analysis of developed cavitation flows particularly difficult as interrogation points corresponding to repeatable cavity oscillation were difficult to achieve. Figure 5.15 shows the power spectrum for the recording with example frame shown in figure 5.14. The peaks observed are considerably less pronounced and typically power spectra covered a broad range of frequencies. Similar broad spectrum shedding frequencies were measured by Sou *et al.* (2007) for developed cavitation in slots with heights of $H = 4mm$.



(a) Example greyscale variation



(b) Averaged power spectrum

Figure 5.15: Power spectral density analysis for $K = 1.79$, $Re = 6.9 \times 10^4$ at $x/L = 0.86$.

5.5.3 Sublayer Motion

The motion of the liquid sublayer separating the cavity from the nozzle wall was highly transient and dependent on the steam-wise position. Despite the absence of a well defined closure region and subsequent stagnation point re-entrant jets can be seen as rapid waves of motion travelling upstream on the cavity interface. However, unlike the re-entrant jets that form for partial cavitation, there is a complex interplay between the counter-flowing sublayer and the internal liquid core. Turbulent fluctuations of the liquid core regularly break through the thin cavity and cause transient shedding of smaller bubble clouds. These observations correlate well to the regular pinching off of small bubble clouds for thin cavities forming behind a step (Callenaere *et al.* (2001)).

The intermittent but strong pulses of re-entrant jet drive streams of liquid upstream. Once beneath the fixed cavity the jets cause a rippling of the cavity interface, which can be seen in the middle region of the cavity in figure 5.14. The ripples continue to slowly travel upstream along the interface and often reach the nozzle entrance. In the region near the nozzle entrance the motion of the liquid layer, inferred from the motion of small bubbles, is typically slow moving and laminar in nature. Occasionally weak rotation is imparted on the liquid by the turbulent down-stream flow. The liquid jet travelling towards the nozzle entrance seems to accumulate over the duration of the injection causing a thickening of the liquid sublayer. Unlike the flows behind the backward facing step, the re-entrant jet was never seen to impinge on the fixed cavity at the nozzle entrance with sufficient force to cause large-scale shedding of the fixed cavity.

5.6 Nozzle Discharge Coefficient

Measurements of discharge coefficient, C_d , can be seen in figure 5.16 for both sodium iodide and water flows. This data represents a significant improvement to the data available within the literature, both in terms of the comprehensive range of conditions and the low experimental scatter (see figure 2.6 in section 2.3.3). Also plotted is the 1-D theory presented in section 2.3.3, which has been adjusted to account for the actual nozzle contraction ratio, discussed below. For

cavitation numbers above $K \approx 1.8$ the C_d is roughly constant and independent of Re , as observed by [Lichtarowicz *et al.* \(1965\)](#), with a value of $C_d \approx 0.85$ for sodium iodide and $C_d \approx 0.86$ for water. For $K > 1.8$ a single linear curve fit is shown to illustrate the trend, however the C_d behaviour in this region is discussed in more detail below. The critical cavitation number, K_{crit} , below which the discharge coefficient begins to be affected by the cavitation was found to be approximately $K = 1.8$ for both water and sodium iodide. For $K < K_{crit}$ the discharge coefficient data closely matches the 1-dimensional theory (see section [5.6.1](#)).

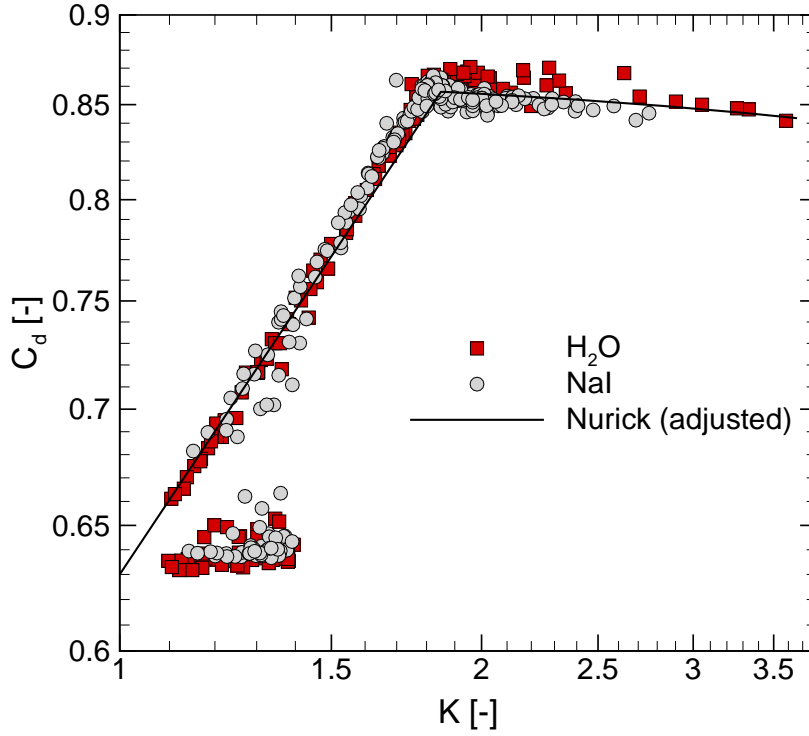


Figure 5.16: Nozzle discharge coefficient for both NaI and Water. The solid inclined line is a 1D model developed by [Nurick \(1976\)](#), with the contraction coefficient, C_c adjusted for inlet rounding. For a comparison to previous experimental data see figure [2.6](#).

For $K < 1.4$ the discharge coefficient was measured to have one of two values.

Under hydraulically flipped conditions the discharge coefficient discontinuously fell to the contraction coefficient of the nozzle, C_c . The contraction coefficient was measured to be slightly higher than the theoretical limit for a sharp entrance orifice, with a value of $C_c \approx 0.63$. The difference is due to the effects of the pipe diameter and possible slight inlet rounding at the nozzle entrance. If the flow re-attached to the nozzle and reverted to supercavitation then the discharge coefficient was very close to that predicted from the 1D theory. Typically sharp edged nozzles demonstrate a strong hysteresis and require substantial reductions of injection pressure to cause this transition. The causes for the observed trends in this work are discussed in more detail in section 5.6.2. Applying the correction for C_c above, the theoretical relationship plotted can be expressed as $C_d = 0.63\sqrt{K}$.

5.6.1 Comparison to 1-dimensional theory

The 1-dimensional model of Nurick (1976) is based on the assumption that the static pressure across the vena contracta section is constant. At the point of cavitation inception this pressure is assumed to be equal to the vapour pressure of the fluid. This represents a minimum value (practically) and so imposes a limit on the flow rate in this region. The flow through the nozzle is then “choked” by the cavitation. In reality, the pressure across the vena contracta is not constant and will be lowest at the peripheries of the contraction where the velocities are highest. Locally the pressure in the separated boundary layer can reach the vapour pressure of the liquid, initiating cavitation, while mean pressures across the vena contracta remain above the vapour pressure. The choking, and subsequent reduction in discharge coefficient with further reductions in cavitation number, will only occur once the pressure across the entire nozzle section has reached the vapour pressure. At this point the flow rate through the nozzle will remain constant for further reductions in the downstream pressure and represents the “critical” conditions. In fact K_{crit} is experimentally determined by observing the stabilisation of mass flow rate with increasing injection pressure (see for example Payri *et al.* (2004)).

Despite numerous authors reporting discharge coefficient measurements for cavitating nozzles, few have simultaneously visualised the nozzle to verify the

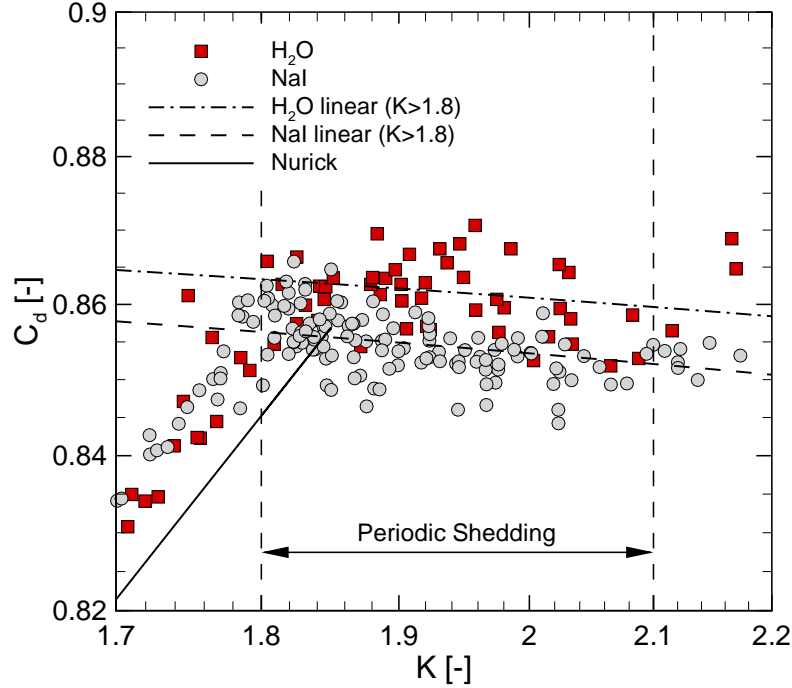


Figure 5.17: Discharge coefficient for partial cavitation showing deviation from predicted values. Also plotted are linear curve fits to the both the H_2O and NaI data for cavitation numbers, $K > 1.8$.

presence of cavitation. Visualisation in this work has clearly shown cavitation present for cavitation numbers up to $K \approx 2.3$, well in excess of the $K_{crit} = 1.8$. Partial cavitation, discussed in section 5.4, also occurs at conditions above the critical cavitation number and so has very little influence on the discharge coefficient of the nozzle. Figure 5.17 shows the experimental data for discharge coefficient for the partial cavitation conditions. The complete suppression of cavitation, particularly for sodium iodide was particularly difficult, with $K > 2.5$ required. This seemed to be related to dissolved gases within the sodium iodide. It should be noted, that above the critical cavitation number the cavitation structures observed will be a combination of true cavitation bubbles (vapour filled bubbles) formed by localised reduction of pressure to the vapour pressure, and

bubbles formed due to the release of dissolved gases, which will occur above the vapour pressure. It is difficult, it not impossible, to distinguish the difference between these two using the visual techniques presented.

5.6.2 Transition from Hydraulic Flip to Supercavitation

High speed visualisation together with injection pressure records indicated a tendency for the flow to transition from hydraulic flip to supercavitation during an injection. Figure 5.18 shows the pressure trace for an injection of sodium iodide in which the flow transitions between hydraulic flip and supercavitation a number of times. This behaviour is uncharacteristic of sharp-edged plain orifice nozzles, which tend to show strong hysteresis once flipped (see [Hiroyasu \(2000\)](#) and [Ramamurthi *et al.* \(2001\)](#)). In a typical orifice the liquid is injected vertically downwards, or horizontally. Once flipped, the flow separates from the nozzle wall at the entrance and remains detached until the exit. A complete absence of surface disturbance from within the nozzle results in substantially increased breakup length. Flow reattachment requires a substantial reduction in velocity, allowing the jet to expand, become wavy and attach to the nozzle wall before the exit plane.

The current configuration, injecting liquid vertically upwards, introduces an external disturbance to the flow which helps the nozzle make this transition. During injection liquid falling from the top of the pressure vessel collects in the volume surrounding the protruding nozzle at the base as the injection continues. Eventually the level of the liquid reaches a point where it begins to interfere with the jet leaving the nozzle. Liquid falls down the internal wall of the nozzle occupying the separated region between the jet surface and wall. As this liquid interacts with the jet it creates a disturbance to the jet surface, which eventually becomes sufficiently influential that the resulting fluctuations allow the jet to reattach to the orifice wall. The subsequent introduction of frictional losses due to viscous interaction with the wall reduce the pressure upstream and allow the discharge coefficient of the nozzle to increase. The flow reattachment causes cavitation to initiate at the nozzle inlet, which rapidly grows and settles into the supercavitation regime.

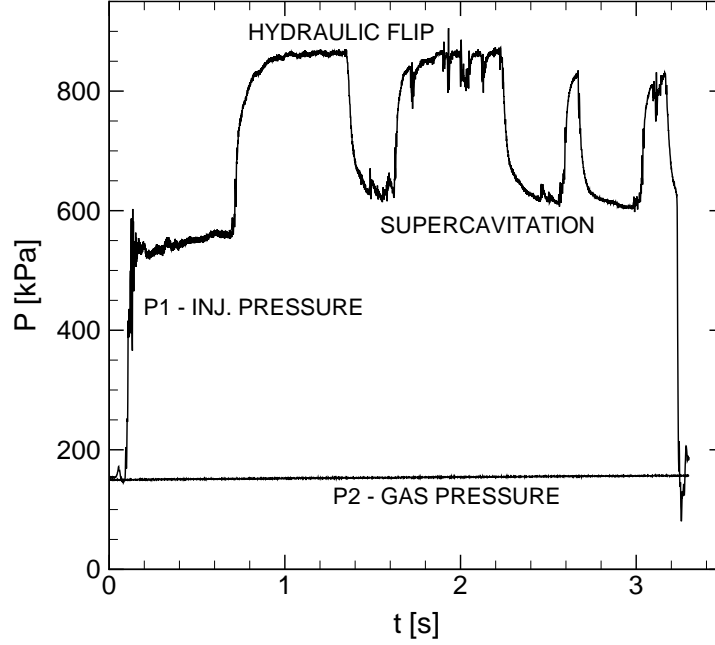


Figure 5.18: Pressure data showing fluctuations between hydraulic flip and supercavitation for $Re = 8.7 \times 10^4$ and $1.36 < K < 1.64$. Peaks of injection pressure above $P_1 = 800 \text{ kPa}$ correspond to observed hydraulic flip, where when $P_1 = 600 \text{ kPa}$ the nozzle was observed to supercavitate.

Figure 5.19 shows the discharge coefficient data for cases in which this transition was noticed. As mentioned in section 4.1, the pressure data for these injections was divided into the distinct regions and the discharge coefficient for each section determined individually. Points for both water and sodium iodide are plotted, where the solid symbols represent the early conditions of the data record and open symbols those for late in the record.

The vast majority of flow transitions were singular with the nozzle moving from the flipped conditions back to supercavitation, as discussed above. Very rarely cases were observed in which the nozzle would move back and forth between the flipped and supercavitation regimes a number of times, as in figure 5.18. This behaviour is not representative of a hydraulic condition of the nozzle geometry

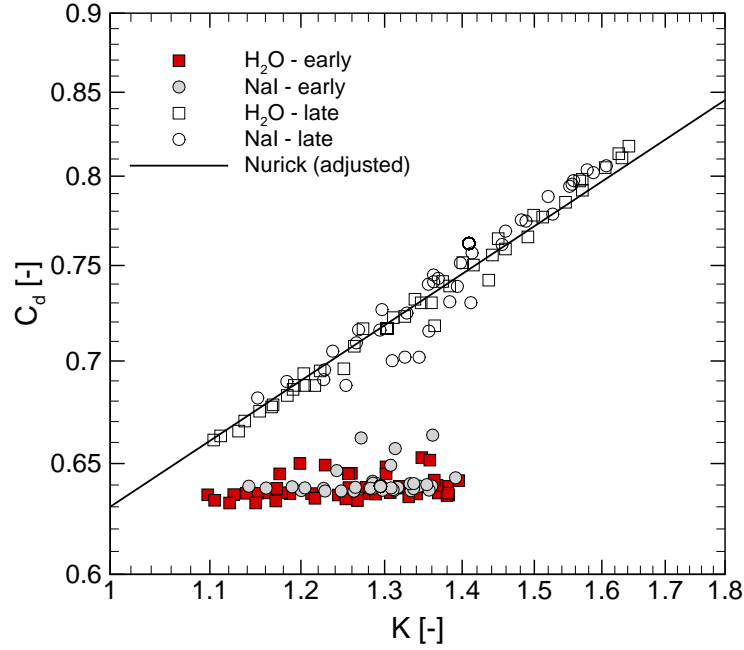


Figure 5.19: Nozzle discharge coefficient comparison for both NaI and Water.

itself, but rather a construct of the unusual conditions of its operation. The slight deviation of the C_d values for the “late” data from figure 5.19 are the result of the highly disturbed and unsteady nature of the flow after it has transitioned from the hydraulically flipped state. It is also influenced by the reduced length of the data used to calculate the C_d values, which increases the variability in the result.

5.7 Near-Nozzle Spray Structure Visualisation

5.7.1 Spray Surface Appearance

The surface appearance of the jet was dependent on a number of parameters including Reynolds number, cavitation number and gas pressure. Results were recorded across the entire range of cavitation numbers from single phase conditions through to hydraulically flipped. Typical spray structures for the different

5.7 Near-Nozzle Spray Structure Visualisation

regimes can be seen in figure 5.20.

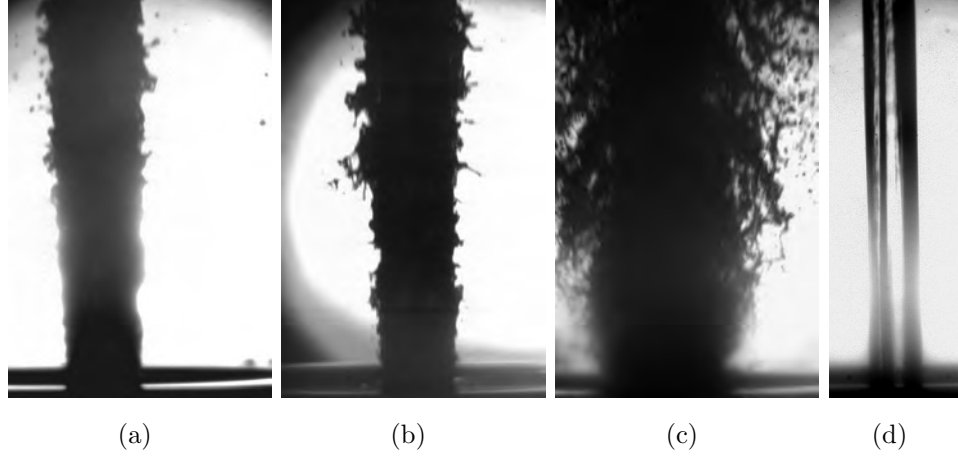


Figure 5.20: Representative images of spray structure recorded at $f = 12,021fps$ for (a) incipient cavitation ($K = 2.29$, $Re = 6.3 \times 10^4$), (b) partial cavitation ($K = 1.83$, $Re = 6.5 \times 10^4$), (c) supercavitation ($K = 1.66$, $Re = 7.1 \times 10^4$), and (d) hydraulic flip ($K = 1.36$, $Re = 7.5 \times 10^4$).

Figure 5.20(a) shows the typical spray structure for incipient cavitation conditions. The jet surface is wavy and rough with small ligaments and droplets forming by the mid-point of the visible spray ($\approx 3D$). The spray angles for these conditions are only slightly divergent, and the presence of cavitation has little effect on the overall spray structure. Partial cavitation, figure 5.20(b), results in slightly more divergence of the spray as ligaments form closer to the nozzle exit ($\approx 1 \sim 1.5D$). The periodic shedding and collapse of bubble clouds increases the turbulence of the flow. This can be seen to increase the magnitude of the perturbations on the surface of the jet as it emerges from the nozzle. As the cavitation collapse region approaches the nozzle exit this effect is magnified. Figure 5.20(c) shows the spray appearance for supercavitation. For these conditions the bubble clouds are collapsing directly at or slightly through the nozzle exit. The turbulent fluctuations created by this collapse imparts substantial lateral velocity components on the spray. Ligaments form directly from the nozzle exit and are rapidly broken into droplets as the spray diverges. The typical appearance of a

hydraulically flipped spray can be seen in figure 5.20(d). As the flow has separated from the nozzle at the entrance the mechanisms for surface perturbation are completely removed, as discussed by Soteriou *et al.* (1995). The result is a jet that appears glassy smooth, with negligible divergence angle.

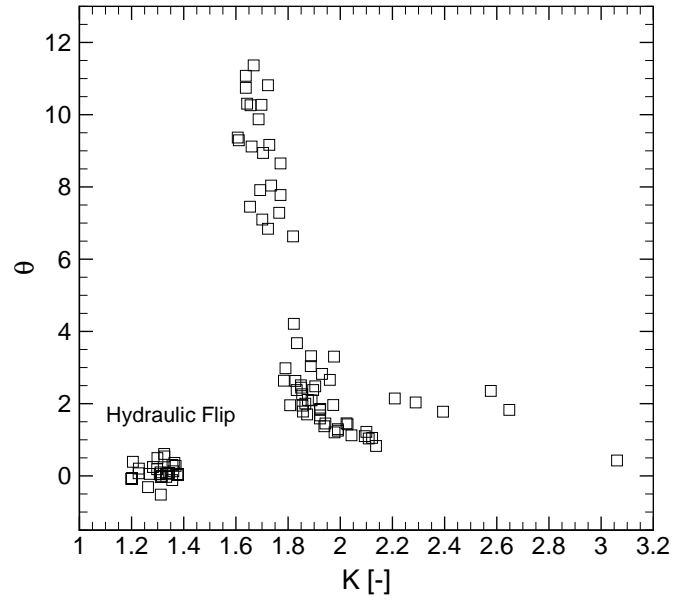
5.7.2 Measurements of Spray Angle Variation with Cavitation

Figure 5.21(a) shows half cone spray angles plotted against K , with half cone angle measured as per section 4.3.2 and shown schematically in figure 5.21(b). For values of $K > 2$ there is very little variation in angle with increases in K , with the angle approaching a nearly constant value of $\theta \approx 2^\circ$. These values coincide with conditions of short collapse lengths of $L_{cav} < 0.15L$ with the highest values of K representing single phase flow conditions. The additional turbulence generated by the cavitation collapse process is diminished prior to reaching the exit and has minimal influence on the spray structure. All surface perturbations that are visible result from turbulent velocity fluctuations within the nozzle.

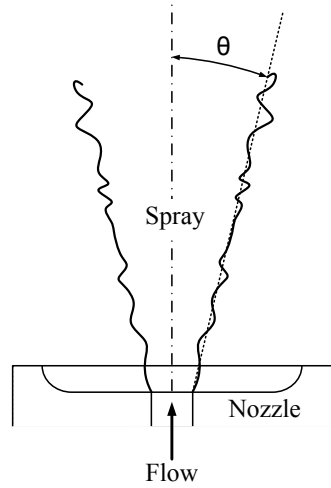
For $K < 2$ the spray angle begins to rise with a significant increase in the observed spray angles for $K < 1.8$. These increases relate directly to the sudden increases in collapse length as the flow transitions from partial to developed cavitation. Spray angles continue to increase as the cavitation collapse region approaches the nozzle exit plane, reaching a peak value of around $\theta \approx 11.5^\circ$ for the supercavitation condition. This value compares well to the peak spray angles observed by Sou *et al.* (2007) for large scale 2D nozzles with width of $4mm$. The trend for steady increase of spray angle with peak values corresponding to supercavitation reflect the findings of Chaves *et al.* (1995) for $0.2mm$ nozzles with $L/D = 5$. Whereas for small nozzles the spray angle plateaus off for further reductions of K , large scale nozzles hydraulically flip. This results in a sudden discontinuity with spray angles dropping to a value of $\theta \approx 0^\circ$ ($K < 1.5$ in figure 5.21(a)).

The absence of spray angles for the range of cavitation numbers between $K \approx 1.4 - 1.6$ is a result of the shift in cavitation number observed with transition between supercavitation and hydraulic flip. This is again a consequence of

5.7 Near-Nozzle Spray Structure Visualisation



(a) spray angle variation with K



(b) Spray angle definition

Figure 5.21: Near nozzle spray angle as a function of cavitation number

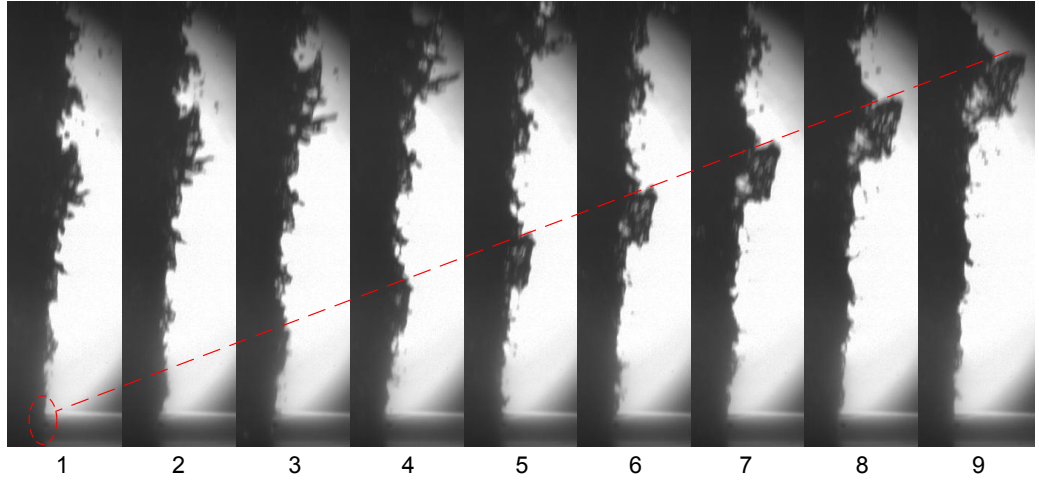
the current experimental setup, in which the piston driving the injection ensures constant mass flow through the nozzle. When the nozzle transitions from super-cavitation to hydraulic flip there is a significant reduction in the nozzle discharge coefficient. For the flipped condition, the velocity coefficient, C_v , approaches unity, meaning that discharge coefficient is entirely constituted by the head loss due to the contraction of the jet from the approach to the vena-contracta. As the back pressure remains constant, this increased head loss through the nozzle requires an increase in upstream pressure, P_1 , in order to maintain continuity, which lowers the cavitation number. Experimental results for nozzles driven by supply pressure, not constant mass flow do not follow this behaviour. For those conditions, the onset of hydraulic flip results in a direct reduction of C_d with no change in K and a choking of the nozzle.

5.7.3 Ligament and Droplet Formation

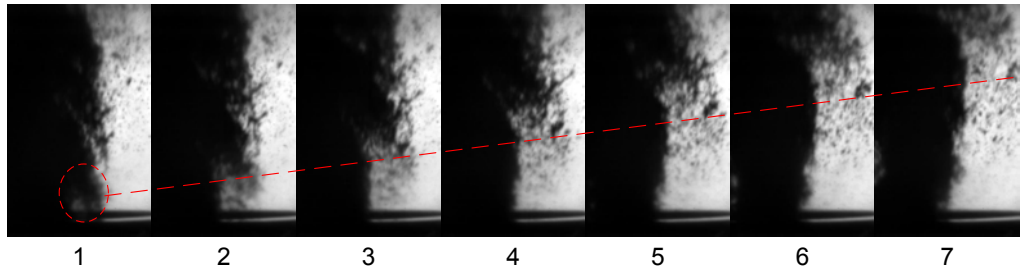
As discussed above, the driving force behind the increase in spray angle as the cavitation approaches the nozzle exit is enhanced levels of lateral velocity produced by the turbulence around the collapse region. It is this effect which causes the surface to expand and form ligaments of fluid stretching out from the main spray. As these ligaments expand they are stretched and distorted by aerodynamic shear forces and eventually fragment into droplets under the action of surface tension. Figure 5.22 shows ligament formation sequences for different partial and super-cavitation and highlights the significance of the cavitation in the breakup of the jet.

The formation of a ligament for partial cavitation conditions is shown in figure 5.22(a). In image 1 the perturbation driving the ligament formation is exiting the nozzle. The following 3 frames, Images 2-4, show the surface of the jet beginning to protrude due to the lateral momentum imparted by turbulent fluctuations as the jet travels in the stream-wise direction. By image 5 of the sequence, the leading edge of the protrusion is beginning to separate from the main liquid core as it is retarded by aerodynamic shear force. Images 6-10 show the ligament forming as it continues to expand laterally and separate from the main spray. This kind of ligament growth is common for the partial cavitation regime, expected for this

5.7 Near-Nozzle Spray Structure Visualisation



(a) $K = 1.79$, $Re = 6.7 \times 10^4$



(b) $K = 1.58$, $Re = 9.4 \times 10^4$

Figure 5.22: Ligament formations sequence for (a) partial cavitation and (b) supercavitation. Time between images, $\Delta t \approx 0.33ms$. Dashed red lines indicate the progression of the surface disturbance as it breaks away from the spray structure.

5.7 Near-Nozzle Spray Structure Visualisation

cavitation number. A number of small droplets can also be seen around the spray, which have been pinched off the smaller ligaments and surface perturbations.

To contrast this, figure 5.22(b) shows the ligament formation for supercavitation conditions. As above, image 1 captures the surface disturbance as it is leaving the nozzle. The significant lateral velocity of the ligament is obvious as it rapidly expands and separated from the main spray in image 2. Unlike the ligament for partial cavitation the perturbation does not remain intact, but is immediately broken up into droplets. By image 3, the main body of the ligament is significantly reduced and a fine mist of small droplets can be seen trailing the ligament. Following this initial thrust and breakup, the main ligament continues to diverge as it expands from the nozzle exit. Images 4-7 shows the continued breakup of the ligament due to surface tension as it travels.

The frequency at which ligaments are formed on the surface is much higher for supercavitation than the partial cavitation. This is directly related to the sporadic shedding of smaller bubble clouds immediately before or through the exit for during supercavitation. Compared to the partial cavitation spray, there is a much greater number of droplets surrounding the spray structure. It is obvious that the presence of cavitation near the nozzle exit dramatically alters the spray. The highly turbulent bubble collapse results in much higher divergence angles and dramatically improved jet breakup. It should be remembered that while these comparisons are stark for the results presented here, the relative magnitude of these effects can be expected to be different for different scale nozzles.

Chapter 6

Conclusions and Recommendations

A new cavitation research rig was designed and built for the experimental investigation of cavitation within a large-scale cylindrical orifice. Optical access to the orifice wall region was significantly enhanced by the use of a refractive index matching technique. High-speed visualisation was used to thoroughly characterise the cavitation structures that formed within the orifice for conditions that ranged from single-phase flow to hydraulic flip. Digital post-processing techniques were used to extract pertinent information from the recordings, such as cavity collapse length, periodic shedding frequencies and spray divergence angles. The influence of cavitation on the nozzle discharge coefficient was also extensively investigated. The significant findings from the results presented in this work will now be outlined, followed by suggestions for possible future work.

6.1 Key Findings

The transition from partial cavitation to developed cavitation was accompanied by significant changes to the cavitation structure. A sudden and dramatic increase in collapse length was shown to occur, which coincided with a reduction of discharge coefficient and the onset of flow choking. The transition point between these two regimes was highly repeatable and found to occur at a cavitation number of $K = 1.8$. The observed lengthening of the cavity was shown to be related

to the position of the flow re-attachment point with respect to the nozzle exit. Comparison of the results obtained here to those of other studies with varying L/D ratios indicated the rapid lengthening is related to the flow dynamics related to the vena contracta. The increase vapour production at this cavitation number lengthens the cavity and restrict the internal liquid core from re-attaching to the nozzle wall.

Spectral analysis of partial cavitation demonstrated that periodic shedding frequencies had a rather strong linear relationship with cavitation number. Frequencies for the large-scale cloud shedding ranged between $500 \sim 2700 Hz$ for a $K \approx 1.8 \sim 2.1$. As cavitation number was reduced and the length of the cavity increased, the frequencies of oscillation also reduced. Strouhal numbers for these oscillations were higher in magnitude than similar shedding regimes for external flows and indicated a greater dependence on cavitation number, with values ranging from $S = 0.27 \sim 0.59$.

The re-entrant jet mechanism responsible for the shedding was shown to be more complex than previously suggested within the literature. Visualisation revealed a constantly present liquid layer beneath the fixed cavity. The re-entrant jet was formed by the momentum of the flow re-attaching to the wall and may be complemented by the collapse of the bubble cloud, as previously suggested. However, the motion of the re-entrant jet is a complex combination of liquid translating towards the nozzle entrance and a travelling wave motion. The influence of this wave motion could be seen as a deformation of the cavity interface which travelled with approximately constant velocity. The interruption of the fixed cavity by the travelling wave was directly responsible for shedding of the fixed cavity and formation of a bubble cloud. This new detail presented has provided an improved understanding of the physics behind the partial cavitation instability and will assist with future attempts to accurately model these phenomena using computational fluid dynamics.

Measurements of the nozzle discharge coefficient indicated that generally the 1D models within the literature accurately describe the influence of cavitation once flow choking has been established. Deviations from this curve occur for hydraulic flip cases, where the discharge coefficient dropped immediately to the flow contraction coefficient, measured to be $C_c \approx 0.63$. The vertical inclination of

the nozzle was shown to introduce a mechanism by which liquid injected from the nozzle could interfere with hydraulically flipped jets and cause a reversion back to supercavitation. This transition was accompanied by an increase in discharge coefficient and a dramatic improvement to the spray divergence. Partial cavitation was found to occur for cavitation numbers above the critical point at which choking occurs and was shown to have minimal influence on the discharge coefficient. Slightly more scatter was apparent in the data and a marginal difference in C_d value was observed between sodium iodide and water.

Finally, spray angle measurements indicated the divergence of the jet was directly related to the magnitude of the lateral velocities created by the flow within the nozzle. Conditions of developed and supercavitation, for which the bubbles collapse in close proximity to the nozzle exit had a profound influence on the observed spray structure and breakup. Ligament formation and subsequent secondary breakup into droplets was significantly enhanced by the turbulence introduced by bubble collapse. Measurements indicated spray angles were optimised for supercavitation conditions. Due to the tendency for large-scale plain orifice atomizers to hydraulically flip, the results indicate the need to characterise the flow and determine the conditions for which the nozzle transitions to developed cavitation. Operation in the developed cavitation regime represents the optimal trade-off between the enhancements to spray breakup and the increased hydraulic resistance due to the reduction of nozzle discharge coefficient.

6.2 Recommendations for Future Work

The results presented within this study thoroughly characterised the cavitation structures that form within a cylindrical orifice and the influence the various flow regimes have on the nozzle flow. Trends were established for a number of important parameters such as collapse length and periodic shedding frequency. Considering the use of large-scale orifices to validate computational models, there is now scope for a quantitatively focused study, which aims to measure the influence of the cavitation on the turbulence generation within the nozzle. Particle Image Velocimetry or Laser Doppler Velocimetry could be used to measure the

6.2 Recommendations for Future Work

turbulence resulting from the bubble collapse for various cavitation regimes. The influence of cavitation on spray divergence and ligament growth could then be assessed quantitatively.

One phenomenon of interest that could be explored further is the re-entrant jet cloud shedding mechanism. Exploration of the liquid layer observed to lie between the cavity and the nozzle wall would help to further the understanding of periodic cloud shedding. These experiments could further address the void in quantitative experimental data for CFD model validation.

Appendix A

Uncertainty Analysis

This chapter outlines the elemental error sources used in the calculation of uncertainty estimates for all measured parameters. The methods used below have been outlined in Section 4.4 and will not be repeated here for brevity. Many parameters are derived quantities for which the uncertainty of each constituent variable propagates through a data reduction equation to the final result. In these cases a nominal value for each variables is required in order to generate sensitivity coefficients. The nominal value used represents a typical value with the resulting uncertainty providing a representative estimate in each case.

Attempts have been made to identify and describe all known and assumed sources of both systematic (bias) and random (precision) errors. Bias error sources typically arrive from manufacturer specifications, the calibration process and regression equation fitting. Where possible precision errors were calculated from the standard deviation, however for a number of quantities, the precision error was determined using the elemental precision errors measured statistically for each of the constituent variables. In some cases, both bias and precision errors were estimated based on experience and engineering judgment.

A.1 Pressure Measurements

Injection Pressure, P_1 [kPa]

Nominal value: 684.8

Sensor: Honeywell 24PCGFM6G

full scale output (FSO): 0-250psi = 0-1723 kPa (gauge)

Bias errors:

Regression bias - from calibration ($2S_r$), $B_{reg} = 2.01kPa$

Thermal sensitivity shift bias (2% reading for $\pm 10^\circ C$ range), $B_{th1} = 13.69kPa$

Applying equation 4.22 the total bias error in P_1 is;

$$\begin{aligned} B_{P_1}^2 &= (2.01)^2 + (13.69)^2 \\ \Rightarrow B_{P_1} &= 13.84 \end{aligned} \tag{A.1}$$

Precision error:

Standard deviation ($2S_r$), $P_{P_1} = 0.41$

Total Uncertainty:

Combining the bias and precision errors, the total uncertainty in P_1 from equation 4.18 is;

$$\begin{aligned} U_{P_1}^2 &= (13.84)^2 + (0.41)^2 \\ \Rightarrow U_{P_1} &= 13.85 kPa (2.02\%P_1) \end{aligned} \tag{A.2}$$

Gas Pressure, P_2 [kPa]

Nominal value: 197.1

Sensor: Honeywell 24PCGFM6G

full scale output (FSO): 0-250psi = 0-1723 kPa (gauge)

Bias errors:

Regression bias - from calibration ($2S_r$), $B_{reg} = 0.84kPa$

A.2 Diameter Measurements

Thermal sensitivity shift bias (2% reading for $\pm 10^\circ C$ range), $B_{th1} = 3.94 kPa$
Applying equation 4.22 the total bias error in P_2 is;

$$\begin{aligned} B_{P_2}^2 &= (0.84)^2 + (3.94)^2 \\ \Rightarrow B_{P_2} &= 4.03 \end{aligned} \quad (A.3)$$

Precision error:

Standard deviation ($2S_r$), $P_{P_2} = 1.54$

Total Uncertainty:

Combining the bias and precision errors, the total uncertainty in P_2 from equation 4.18 is;

$$\begin{aligned} U_{P_2}^2 &= (4.03)^2 + (1.54)^2 \\ \Rightarrow U_{P_2} &= 4.31 kPa (2.19\% P_2) \end{aligned} \quad (A.4)$$

A.2 Diameter Measurements

Diameter measurements for the cylinder bore, supply pipe and nozzle section are all used throughout the analysis. The uncertainty in each of these is covered below.

Nozzle Diameter, D_n [mm]

Nominal value: 8.246

Measurements of the internal nozzle diameter were conducted 10 times and the entrance, mid-point and exit plane using an internal bore-gauge. The diameter was then measured from the bore-gauge using a micrometer.

Bias errors:

Measurement bias (Half-scale of micrometer), $B_{D_n} = 0.05 mm$

Precision error:

Standard deviation ($2S_r$), $P_{D_n} = 0.0092 mm$

Total Uncertainty:

A.2 Diameter Measurements

Combining the bias and precision errors, the total uncertainty in D_n from equation 4.18 is;

$$\begin{aligned} U_{D_n}^2 &= (0.05)^2 + (0.0092)^2 \\ \Rightarrow U_{D_n} &= 0.051 \text{ mm } (0.618\% D_n) \end{aligned} \quad (\text{A.5})$$

Cylinder Bore, D_c [mm]

Nominal value: 101.689

As the cylinder was not dismantled for measurement, the error sources for the cylinder bore were taken from the engineering drawing and machining tolerances used in its fabrication.

Bias errors:

Bore tolerance bias ($\pm 0.0025\text{in}$), $B_{D_c} = 0.0635\text{mm}$

Precision error:

No precision error is accounted for as the machine tolerance will encompass the true value of diameter.

Total Uncertainty:

In this case the total uncertainty in D_c from equation 4.18 is;

$$\begin{aligned} U_{D_c}^2 &= (0.0635)^2 \\ \Rightarrow U_{D_c} &= 0.0635 \text{ mm } (0.062\% D_c) \end{aligned} \quad (\text{A.6})$$

Pipe Diameter, D_p [mm]

Nominal value: 52.506

Pipe: 2" nominal bore Schedule 40 pipe

The internal diameter of the supply pipe was not measured. A nominal bias error was estimated which was believed to encompass the uncertainty in the diameter. This parameter is included in one derived quantity, the discharge coefficient C_d , and has negligible influence on the uncertainty for this parameter.

Bias errors:

Estimated bias, $B_{D_p} = 1\text{mm}$

Precision error:

A.3 Temperature Measurements

As the diameter was not measured, the bias error was estimated to be sufficiently large to encompass the true value. As such there was no precision error for D_p .

Total Uncertainty:

Combining the bias and precision errors, the total uncertainty in D_P from equation 4.18 is;

$$\begin{aligned} U_{D_p}^2 &= (1)^2 \\ \Rightarrow U_{D_p} &= 1 \text{ mm } (1.9\%D_p) \end{aligned} \tag{A.7}$$

A.3 Temperature Measurements

Liquid Temp, T [$^{\circ}C$]

Nominal value: 21

Thermocouple type: K

Temperature was measured in the supply pipe below the nozzle at 1 sample/min.

Bias errors:

Regression bias - from thermocouple calibration ($2S_r$), $B_{reg} = 0.13$

Precision error:

Standard deviation for repeated measurements ($2S_r$), $P_T = 0.20$

Total Uncertainty:

Combining the bias and precision errors, the total uncertainty in T from equation 4.18 is;

$$\begin{aligned} U_T^2 &= (0.13)^2 + (0.02)^2 \\ \Rightarrow U_T &= 0.024 \text{ } ^{\circ}C (0.11\%T) \end{aligned} \tag{A.8}$$

A.4 Solution Concentration

Mixing of the sodium iodide solution was quite a complex process. The final batch volume of 22L was measured in 6 batches to accommodate the limited volume of a mixing beaker. A beaker was required, as the solution needed to be

A.4 Solution Concentration

heated during the process to aid with dissolving the salts into the water. Each batch required multiple measurements of both water and sodium iodide, which is reflected in the bias error estimates. The solution concentration was determined by accurately weighing the quantities of crystallised NaI and water used to make the batches.

Solution Concentration, C [%w/w]

Nominal value: 63

Total NaI mass, M_{NaI} : 25589.2 g

Total H₂O mass, M_{H_2O} : 15028.4 g

Total Na₂S₂O₃ mass, M_{Th} : 40.7 g

The total sodium iodide and water masses above required 50 and 33 batches respectively.

Average mass of NaI sample to make up the total 22L, $M_{NaI_{avg}} = 511.8g$

Average mass of H₂O sample to make up the total 22L, $M_{H_2O_{avg}} = 455.4g$

Data reduction equation:

$$C = 100 \times \frac{M_{NaI}}{(M_{NaI} + M_{H_2O} + M_{Th})} \quad (A.9)$$

From this data reduction equation, the sensitivity coefficients for each variable are:

$$\begin{aligned} \frac{\partial C}{\partial M_{NaI}} &= 100 \times \frac{M_{H_2O} + M_{Th}}{(M_{NaI} + M_{H_2O} + M_{Th})^2} \\ &= 9.16 \times 10^{-4} \text{ 1/g} \end{aligned} \quad (A.10)$$

$$\begin{aligned} \frac{\partial C}{\partial M_{H_2O}} &= -100 \times \frac{M_{NaI}}{(M_{NaI} + M_{H_2O} + M_{Th})^2} \\ &= -1.5 \times 10^{-3} \text{ 1/g} \end{aligned} \quad (A.11)$$

and

$$\begin{aligned} \frac{\partial C}{\partial M_{Th}} &= -100 \times \frac{M_{NaI}}{(M_{NaI} + M_{H_2O} + M_{Th})^2} \\ &= -1.5 \times 10^{-3} \text{ 1/g} \end{aligned} \quad (A.12)$$

Bias errors:

Measurement scale bias (manufacturer specs.), $B_{scale} = 0.1g$

Mass bias for NaI (50 meas. required, $\therefore \sqrt{50}B_{scale}$), $B_{NaI_{sc}} = 0.707g$

Mass bias for H₂O (33 meas. required, $\therefore \sqrt{33}B_{scale}$), $B_{H_2O_{sc}} = 0.575g$

Mass bias for Na₂S₂O₃ (6 meas. required, $\therefore \sqrt{6}B_{scale}$), $B_{Th_{sc}} = 0.245g$

Hygroscopy bias (see below), $B_{NaI_{hyg}} = 3.32g$

NaI left in beaker bias (crystal NaI stuck to walls - measured), $B_{NaI_{bk}} = 0.037g$

H₂O left in beaker bias (total water - measured), $B_{H_2O_{bk}} = 0.65g$

Na₂S₂O₃ left in beaker bias (crystal Na₂S₂O₃ stuck to walls - estimated from NaI, is additive as this is added to the final batch solution, $\therefore 6B_{NaI_{bk}}$), $B_{Th_{bk}} = 0.222g$

Water mass loss bias (due to spill/evaporation - estimated), $B_{loss} = 5g$

Due to its *hygroscopic* nature, quantities of dry NaI powder tended to increase in mass during the weighing process. To estimate the influence of this on the final concentration, the water absorption of a test sample was evaluated. An initial mass of 17.429g was left for a period of time equivalent to the time required to mix the NaI solution. The final sample weight was 17.445g, a 0.0918% increase. Projecting this gain onto the total M_{NaI} yields: $0.000918 \times 511.8\sqrt{50} = 3.32g$. This is then used as an estimate of the bias due to hygroscopy.

Applying equation 4.22 the total bias error in the measurement of NaI is;

$$\begin{aligned} B_{M_{NaI}}^2 &= (0.707)^2 + (3.32)^2 \\ \Rightarrow B_{M_{NaI}} &= 3.39 \text{ g} \end{aligned} \tag{A.13}$$

Similarly, the total bias error in the measurement of water is;

$$\begin{aligned} B_{M_{H_2O}}^2 &= (0.575)^2 + (0.65)^2 + (5)^2 \\ \Rightarrow B_{M_{H_2O}} &= 5.07 \text{ g} \end{aligned} \tag{A.14}$$

and the total bias error in the measurement of Na₂S₂O₃ is;

$$\begin{aligned} B_{M_{Th}}^2 &= (0.245)^2 + (0.222)^2 + (5)^2 \\ \Rightarrow B_{M_{Th}} &= 0.33 \text{ g} \end{aligned} \tag{A.15}$$

Applying equation 4.19 the total bias error in C is;

$$\begin{aligned}
 B_C^2 &= \left(\frac{\partial C}{\partial M_{NaI}} \right)^2 B_{M_{NaI}}^2 + \left(\frac{\partial C}{\partial M_{H_2O}} \right)^2 B_{M_{H_2O}}^2 + \left(\frac{\partial C}{\partial M_{Th}} \right)^2 B_{M_{Th}}^2 \\
 &\quad + 2 \left(\frac{\partial C}{\partial M_{NaI}} \right) \left(\frac{\partial C}{\partial M_{H_2O}} \right) B_{M_{NaI}} B_{M_{H_2O}} \\
 &\quad + 2 \left(\frac{\partial C}{\partial M_{NaI}} \right) \left(\frac{\partial C}{\partial M_{Th}} \right) B_{M_{NaI}} B_{M_{Th}} \\
 &\quad + 2 \left(\frac{\partial C}{\partial M_{H_2O}} \right) \left(\frac{\partial C}{\partial M_{Th}} \right) B_{M_{H_2O}} B_{M_{Th}} \\
 &= (9.16 \times 10^{-4})^2 (3.39)^2 + (-1.5 \times 10^{-3})^2 (5.07)^2 + (-1.5 \times 10^{-3})^2 (0.33)^2 \\
 &\quad + 2 (9.16 \times 10^{-4}) (-1.5 \times 10^{-3}) (3.39) (5.07) \\
 &\quad + 2 (9.16 \times 10^{-4}) (-1.5 \times 10^{-3}) (3.39) (0.33) \\
 &\quad + 2 (-1.5 \times 10^{-3}) (-1.5 \times 10^{-3}) (5.07) (0.33) \\
 \Rightarrow B_C &= 0.0053
 \end{aligned} \tag{A.16}$$

Precision errors:

As the measurement for each batch was only made once, the precision error was estimated to be of the same order as the bias error.

$$\Rightarrow P_C = B_C = 0.0053$$

Total Uncertainty:

Combining the bias and precision errors, the total uncertainty in C from equation 4.18 is;

$$\begin{aligned}
 U_C^2 &= (0.0053)^2 + (0.0053)^2 \\
 \Rightarrow U_C &= 0.0075 \text{ (0.012\% } C)
 \end{aligned} \tag{A.17}$$

A.5 Viscosity

Viscosity measurements were conducted for a range of fluid temperatures using a Cannon-Fenske viscometer.

Kinematic Viscosity, ν [$10^{-6}m^2/s$]

Nominal value: 1.5778

Nominal concentration: 63 %

Nominal temperature: 21 °C

Data reduction equation:

$$\nu = 0.008t \quad (\text{A.18})$$

where ν is the kinematic viscosity in centi-stokes, cSt ($10^{-6}m^2/s$), and $t(s)$ is the time taken for the liquid to traverse the capillary passage. The uncertainty of the viscometer was noted as 0.16% for kinematic viscosities <10 cSt. The viscosity for each concentration was measured twice at each temperature to bolster confidence in the result.

$$\frac{\partial \nu}{\partial t} = 0.008 \text{ cSt}/s \quad (\text{A.19})$$

Experimental viscosities were measured for temperatures from 13°C to 26°C and for concentrations from 57% to 66%. The following regression equation was then fit to the data;

$$\nu = 8.575 \times 10^{-6} e^{(-0.014T)} C^3 \quad (\text{A.20})$$

with sensitivity coefficients:

$$\begin{aligned} \frac{\partial \nu}{\partial C} &= 2.573 \times 10^{-5} e^{(-0.014T)} C^2 \\ &= 0.0761 \text{ cSt} \end{aligned} \quad (\text{A.21})$$

$$\begin{aligned} \frac{\partial \nu}{\partial T} &= -1.201 \times 10^{-7} e^{(-0.014T)} C^3 \\ &= -0.0224 \text{ cSt}/^\circ\text{C} \end{aligned} \quad (\text{A.22})$$

Bias errors:

Bias in time (\pm half scale), $B_t = 0.005 \text{ s}$

Bias in viscometer (from manufacturer $\pm 0.16\%$), $B_{\nu_{man}} = 0.00252 \text{ cSt}$

Bias in regression eqn ($2S_r$), $B_{reg} = 0.03545 \text{ cSt}$

Applying equation 4.22 the bias error in ν due to the experimental measurement

of traverse time is;

$$\begin{aligned}
 B_{\nu t}^2 &= \left(\frac{\partial \nu}{\partial t} \right)^2 B_t^2 \\
 &= (0.008)^2 (0.005)^2 \\
 \Rightarrow B_{\nu t} &= 4 \times 10^{-5} \text{ m}^2/\text{s}
 \end{aligned} \tag{A.23}$$

$$\begin{aligned}
 B_{\nu eqn}^2 &= \left(\frac{\partial \nu}{\partial T} \right)^2 U_T^2 + \left(\frac{\partial \nu}{\partial C} \right)^2 B_C^2 \\
 &= (-0.0224)^2 (0.024)^2 + (0.0761)^2 (0.2816)^2 \\
 \Rightarrow B_{\nu eqn} &= 0.0067 \text{ cSt}
 \end{aligned} \tag{A.24}$$

$$\begin{aligned}
 B_{\nu}^2 &= B_{\nu eqn}^2 + B_{reg}^2 + B_{\nu t}^2 + B_{\nu man}^2 \\
 &= (0.0067)^2 + (0.03545)^2 + (4 \times 10^{-5})^2 + (0.00252)^2 \\
 \Rightarrow B_{\nu} &= 0.0362 \text{ cSt}
 \end{aligned} \tag{A.25}$$

Precision error:

Precision error in time ($2S_r$), $P_t = 0.25\text{s}$

Applying equation 4.24 the total precision error in ν is;

$$\begin{aligned}
 P_{\nu}^2 &= \left(\frac{\partial \nu}{\partial t} \right)^2 P_t^2 \\
 &= (0.008)^2 (0.25)^2 \\
 \Rightarrow P_{\nu} &= 0.002 \text{ cSt}
 \end{aligned} \tag{A.26}$$

Total Uncertainty:

Combining the bias and precision errors, the total uncertainty in ν from equation 4.18 is;

$$\begin{aligned}
 U_{\nu}^2 &= (0.0362)^2 + (0.002)^2 \\
 \Rightarrow U_{\nu} &= 0.0362 \text{ cSt } (2.30\% \nu)
 \end{aligned} \tag{A.27}$$

A.6 Density

Density measurements were made by measuring the mass of 20mL samples of NaI solution.

Density, ρ [kg/m³]

Nominal density value: 1871.2

Nominal mass: $36.013 \times 10^{-3} \text{ kg}$

Nominal volume: $19.994 \times 10^{-6} \text{ m}^3$

Data reduction equation:

$$\rho = \frac{M}{V} \quad (\text{A.28})$$

From this data reduction equation, the sensitivity coefficients for each variable are:

$$\begin{aligned} \frac{\partial \rho}{\partial M} &= \frac{1}{V} \\ &= 50015 \text{ 1/m}^3 \end{aligned} \quad (\text{A.29})$$

and

$$\begin{aligned} \frac{\partial \rho}{\partial V} &= \frac{-M}{V^2} \\ &= -9.0087 \times 10^7 \text{ kg/m}^6 \end{aligned} \quad (\text{A.30})$$

Bias errors:

Measurement scale bias (\pm half res.), $B_{m1} = 0.0005 \times 10^{-3} \text{ kg}$

Scale error, $B_{m1} = 0.01 \times 10^{-3} \text{ kg}$

Temp change bias ($0.2\% \rho$ for $20 \pm 5^\circ \text{C}$), $B_{temp} = 3.742 \text{ kg/m}^3$

Pipette manufacturer error ($\pm 0.03 \text{ ml}$), $B_{V1} = 0.03 \times 10^{-6} \text{ m}^3$

Pipette scale bias (\pm half res.), $B_{V2} = 0.01 \times 10^{-6} \text{ m}^3$

Regression bias ($2S_r$), $B_{reg} = 3.834 \text{ kg/m}^3$

Applying equation 4.22 the total bias error in the measurement of the volume is;

$$\begin{aligned} B_V^2 &= (0.03 \times 10^{-6})^2 + (0.01 \times 10^{-6})^2 \\ \Rightarrow B_V &= 3.162 \times 10^{-8} \text{ m}^3 \end{aligned} \quad (\text{A.31})$$

and the total bias error in the measurement of the mass is;

$$\begin{aligned} B_M^2 &= (0.005 \times 10^{-3})^2 + (0.01 \times 10^{-3})^2 \\ \Rightarrow B_M &= 1.118 \times 10^{-5} \text{ kg} \end{aligned} \quad (\text{A.32})$$

The total bias error for the reduction equation for B_ρ can be determined as;

$$\begin{aligned} B_{\rho_{red}}^2 &= \left(\frac{\partial \rho}{\partial M} \right)^2 B_M^2 + \left(\frac{\partial \rho}{\partial V} \right)^2 B_V^2 \\ &= (50015)^2 (1.118 \times 10^{-5})^2 + (-9.0087 \times 10^7)^2 (3.162 \times 10^{-8})^2 \\ \Rightarrow B_{\rho_{red}} &= 2.9031 \text{ kg/m}^3 \end{aligned} \quad (\text{A.33})$$

Applying equation 4.22 the total bias error in ρ is;

$$\begin{aligned} B_\rho^2 &= B_{\rho_{red}}^2 + B_{reg}^2 + B_{temp}^2 \\ &= (2.9031)^2 + (3.834)^2 + (3.742)^2 \\ \Rightarrow B_\rho &= 6.093 \text{ kg/m}^3 \end{aligned} \quad (\text{A.34})$$

Precision error:

Precision error ($2S_r$), $P_\rho = 8.742 \text{ kg/m}^3$

Total Uncertainty:

Combining the bias and precision errors, the total uncertainty in ρ from equation 4.18 is;

$$\begin{aligned} U_\rho^2 &= (6.093)^2 + (8.742)^2 \\ \Rightarrow U_\rho &= 10.656 \text{ kg/m}^3 \text{ (0.57\%}\rho) \end{aligned} \quad (\text{A.35})$$

A.7 Vapour Pressure

Vapour Pressure, P_v [kPa]

Nominal density value: 1.048

fractional concentration, $x = 0.63$

Molar mass of NaI, $M = 149.89$

Antoine equation constants:

$$\begin{aligned}
 A_0 &= 6.6418220, A_1 = 0.4914986, A_2 = -0.1008282, A_3 = 0.0051828 \\
 B_0 &= -1340.4910, B_1 = -323.2146, B_2 = 63.0511, B_3 = -3.2720 \\
 C_0 &= -146462.900, C_1 = 51849.160, C_2 = -10123.010, C_3 = 525.534
 \end{aligned}$$

$$m = 1000 \times \frac{x}{M(1-x)} \quad (\text{A.36})$$

$$\begin{aligned}
 \frac{\partial m}{\partial x} &= 1000 \times \frac{1-2x}{M(1-x)^2} \\
 &= -12.671 \text{ mol/kg}
 \end{aligned} \quad (\text{A.37})$$

$$\begin{aligned}
 A &= A_0 + A_1(m) + A_2(m)^2 + A_3(m)^3 \\
 B &= B_0 + B_1(m) + B_2(m)^2 + B_3(m)^3 \\
 C &= C_0 + C_1(m) + C_2(m)^2 + C_3(m)^3 \\
 \frac{dA}{dm} &= A_1 + 2A_2(m) + 3A_3(m)^2 \\
 \frac{dB}{dm} &= B_1 + 2B_2(m) + 3B_3(m)^2 \\
 \frac{dC}{dm} &= C_1 + 2C_2(m) + 3C_3(m)^2
 \end{aligned} \quad (\text{A.38})$$

Data reduction equation:

$$P_v = e^{\left(A + \frac{B}{T(K)} + \frac{C}{T(K)^2}\right)} \quad (\text{A.39})$$

From this data reduction equation, the sensitivity coefficients for each variable are:

$$\begin{aligned}
 \frac{\partial P_v}{\partial m} &= e^{\left(A + \frac{B}{T(K)} + \frac{C}{T(K)^2}\right)} \left(dA + \frac{dB}{T(K)} + \frac{dC}{T(K)^2} \right) \\
 &= -0.0864
 \end{aligned} \quad (\text{A.40})$$

$$\begin{aligned}
 \frac{\partial P_v}{\partial T} &= e^{\left(A + \frac{B}{T(K)} + \frac{C}{T(K)^2}\right)} \left(\frac{-B}{T(K)^2} - \frac{2C}{T(K)^3} \right) \\
 &= 0.0279
 \end{aligned} \quad (\text{A.41})$$

Bias errors:

$$\begin{aligned}
 B_m^2 &= \left(\frac{\partial m}{\partial x} \right)^2 B_x^2 \\
 \Rightarrow B_m &= 6.6785 \times 10^{-4}
 \end{aligned} \tag{A.42}$$

Applying equation 4.22 the total bias error in P_v is;

$$\begin{aligned}
 B_{P_{veqn}}^2 &= \left(\frac{\partial P_v}{\partial m} \right)^2 B_m^2 + \left(\frac{\partial P_v}{\partial T} \right)^2 B_T^2 \\
 &= (-0.0864)^2 (6.6785 \times 10^{-4})^2 + (0.0279)^2 (0.1288)^2 \\
 \Rightarrow B_{P_{veqn}} &= 0.0036
 \end{aligned} \tag{A.43}$$

$$B_{P_{vreg}} = 0.01P_v$$

$$\begin{aligned}
 B_{P_v}^2 &= (B_{P_{veqn}})^2 + (B_{P_{vreg}})^2 \\
 &= (0.0036)^2 + (0.0105)^2 \\
 \Rightarrow B_{P_v} &= 0.0111 \text{ kPa}
 \end{aligned} \tag{A.44}$$

Precision error:

Applying equation 4.24 the total precision error in P_v is;

$$\begin{aligned}
 P_{P_v}^2 &= \left(\frac{\partial P_v}{\partial T} \right)^2 P_T^2 \\
 &= (0.0279)^2 (0.2)^2 \\
 \Rightarrow P_{P_v} &= 0.0056 \text{ kPa}
 \end{aligned} \tag{A.45}$$

Total Uncertainty:

Combining the bias and precision errors, the total uncertainty in P_v from equation 4.18 is;

$$\begin{aligned}
 U_{P_v}^2 &= (0.0111)^2 + (0.0056)^2 \\
 \Rightarrow U_{P_v} &= 0.0124 \text{ kPa} \text{ (1.18\% } P_v)
 \end{aligned} \tag{A.46}$$

A.8 Piston Velocity

Piston Velocity, V_c [m/s]

Nominal value: 0.1003

Nominal input voltage: 8.2V

LDT output is between 4-20mA. A 250Ω resistor then converts this input to a 1 – 5V input to the data acquisition system. The output of sensor voltage as a function of position was then used to determine a regression expression relating these two parameters.

The equation relating piston axial position, $x_p[m]$ in terms of LDT output voltage, $V_o[V]$;

$$x_p = 0.0921947V_o - 0.0937527 \quad (\text{A.47})$$

For the nominal input voltage the linear curve fit for output voltage, V_o as a function of time (sampling rate of 1000Hz) was determined to be;

$$V_o = 1.0777t + 1.0018 \quad (\text{A.48})$$

Applying the chain rule, we can determine the piston velocity;

$$V_c = \frac{dx_p}{dt} = \frac{dx_p}{dV_o} \frac{dV_o}{dt} \quad (\text{A.49})$$

Letting $x_V = \frac{dx_p}{dV_o}$ and $\dot{V}_o = \frac{dV_o}{dt}$ we can write

$$V_c = x_V \dot{V}_o \quad (\text{A.50})$$

Bias errors:

Bias in regression equation for x_V ($2S_r$), $B_{x_V} = 0.000655619 \text{ m/V}$

Bias in regression equation for \dot{V}_o ($2S_r$), $B_{\dot{V}_o} = 0.027076 \text{ V/s}$

Applying equation 4.22 the total bias error in V_c is;

$$\begin{aligned} B_{V_c}^2 &= \left(\frac{\partial V_c}{\partial x_V} \right)^2 B_{x_V}^2 + \left(\frac{\partial V_c}{\partial \dot{V}_o} \right)^2 B_{\dot{V}_o}^2 \\ &\quad + 2 \left(\frac{\partial V_c}{\partial x_V} \right) \left(\frac{\partial V_c}{\partial \dot{V}_o} \right) B_{x_V} B_{\dot{V}_o} \\ &= (1.0777)^2 (6.556 \times 10^{-4})^2 + (0.0921947)^2 (0.027076)^2 \\ &\quad + 2(1.0777)(0.0921947)(6.556 \times 10^{-4})(0.027076) \\ \Rightarrow B_{V_c} &= 3.204 \times 10^{-3} \text{ m/s} \end{aligned} \quad (\text{A.51})$$

Precision error:

Precision error in velocity ($2S_r$), $P_{V_c} = 0.002134 \text{ m/s}$

Total Uncertainty:

Combining the bias and precision errors, the total uncertainty in V_c from equation 4.18 is;

$$\begin{aligned} U_{V_c}^2 &= (0.003204)^2 + (0.002134)^2 \\ \Rightarrow U_{V_c} &= 3.848 \times 10^{-3} \text{ m/s} \end{aligned} \quad (\text{A.52})$$

A.9 Nozzle Velocity

Nozzle Velocity, V_n [m/s]

Nominal value: 15.192

Piston velocity: 0.1003 m/s

Cylinder bore: $101.689 \times 10^{-3} \text{ m}$

Nozzle diameter: $8.246 \times 10^{-3} \text{ m}$

The equation relating nozzle velocity, V_n to piston velocity, V_c is;

$$V_n = V_c \left(\frac{D_c}{D_n} \right)^2 \quad (\text{A.53})$$

where D_c and D_n represent the cylinder bore and nozzle diameters respectively.

From this data reduction equation, the sensitivity coefficients for each variable are:

$$\begin{aligned} \frac{\partial V_n}{\partial V_c} &= \left(\frac{D_c}{D_n} \right)^2 \\ &= 152.076 \end{aligned} \quad (\text{A.54})$$

$$\begin{aligned} \frac{\partial V_n}{\partial D_c} &= 2 \frac{V_c D_c}{D_n^2} \\ &= 299.998 \text{ 1/s} \end{aligned} \quad (\text{A.55})$$

and

$$\begin{aligned}\frac{\partial V_n}{\partial D_n} &= -2 \frac{V_c D_c^2}{D_n^3} \\ &= -3699.55 \text{ 1/s}\end{aligned}\tag{A.56}$$

Bias errors:

Bias error in piston velocity (see section A.8), $B_{V_c} = 3.204 \times 10^{-3} \text{ m/s}$

Bias error in cylinder bore diameter (see section A.2), $B_{D_c} = 0.0635 \times 10^{-3} \text{ m/s}$

Bias error in nozzle diameter (see section A.2), $B_{D_n} = 0.05 \times 10^{-3} \text{ m/s}$

Applying equation 4.22 the total bias error in V_n is;

$$\begin{aligned}B_{V_n}^2 &= \left(\frac{\partial V_n}{\partial V_c}\right)^2 B_{V_c}^2 + \left(\frac{\partial V_n}{\partial D_c}\right)^2 B_{D_c}^2 + \left(\frac{\partial V_n}{\partial D_n}\right)^2 B_{D_n}^2 \\ &= (152.076)^2 (3.204 \times 10^{-3})^2 + (299.998)^2 (6.35 \times 10^{-5})^2 \\ &\quad + (-3699.55)^2 (5 \times 10^{-5})^2 \\ \Rightarrow B_{V_n} &= 0.5243 \text{ m/s}\end{aligned}\tag{A.57}$$

Precision error:

Precision error in piston velocity (see section A.8), $P_{V_c} = 0.002134 \text{ m/s}$

Precision error in nozzle diameter (see section A.2), $P_{D_n} = 9.2 \times 10^{-6} \text{ m}$

Applying equation 4.24 the total precision error in V_n is;

$$\begin{aligned}P_{V_n}^2 &= \left(\frac{\partial V_n}{\partial V_c}\right)^2 P_{V_c}^2 + \left(\frac{\partial V_n}{\partial D_n}\right)^2 P_{D_n}^2 \\ &= (152.076)^2 (0.002134)^2 + (-3699.55)^2 (9.2 \times 10^{-6})^2 \\ \Rightarrow P_{V_n} &= 0.3260 \text{ m/s}\end{aligned}\tag{A.58}$$

Total Uncertainty:

Combining the bias and precision errors, the total uncertainty in V_n from equation 4.18 is;

$$\begin{aligned}U_{V_n}^2 &= (0.5243)^2 + (0.3260)^2 \\ \Rightarrow U_{V_n} &= 0.6164 \text{ m/s (4.06\% } V_n)\end{aligned}\tag{A.59}$$

A.10 Discharge Coefficient

Discharge Coefficient, C_d

Nominal value: 0.7756

Nominal Gas Pressure, P_1 : 458.313 kPa

Nominal Gas Pressure, P_1 : 95.863 kPa

Nominal density, ρ : 1871.2 kg/m^3

Piston velocity, V_c : 0.1003 m/s

Cylinder bore, D_c : $101.689 \times 10^{-3} m$

Nozzle diameter, D_n : $8.246 \times 10^{-3} m$

Nominal Δz : $-0.202 m$

Data reduction equation:

$$C_d = \frac{D_c^2 V_c}{\frac{D_n^2}{\sqrt{1-\beta^4}} \sqrt{\frac{2000(P_1-P_2)+\rho g \Delta z}{\rho}}} \quad (A.60)$$

where $\beta = \frac{D_n}{D_p}$

From this data reduction equation, the sensitivity coefficients for each variable are:

$$\begin{aligned} \frac{\partial C_d}{\partial V_c} &= \frac{D_c^2}{\frac{D_n^2}{\sqrt{1-\beta^4}} \sqrt{\frac{2000(P_1-P_2)+\rho g \Delta z}{\rho}}} \\ &= 7.736 \text{ s/m} \end{aligned} \quad (A.61)$$

$$\begin{aligned} \frac{\partial C_d}{\partial D_c} &= \frac{2D_c V_c}{\frac{D_n^2}{\sqrt{1-\beta^4}} \sqrt{\frac{2000(P_1-P_2)+\rho g \Delta z}{\rho}}} \\ &= 15.223 \text{ 1/m} \end{aligned} \quad (A.62)$$

$$\begin{aligned} \frac{\partial C_d}{\partial D_n} &= \frac{-2D_c^2 V_c (D_n^4 - D_p^4 (1 - \beta^4))}{D_p^4 D_n^3 \sqrt{1 - \beta^4} \sqrt{\frac{2000(P_1-P_2)+\rho g \Delta z}{\rho}}} \\ &= 187.513 \text{ 1/m} \end{aligned} \quad (A.63)$$

$$\begin{aligned}\frac{\partial C_d}{\partial D_p} &= \frac{2D_c^2 V_c D_n^2}{D_p^3 \sqrt{1-\beta^4} \sqrt{\frac{2000(P_1-P_2)+\rho g \Delta z}{\rho}}} \\ &= 5.091 \times 10^{-5} \text{ 1/m}\end{aligned}\tag{A.64}$$

$$\begin{aligned}\frac{\partial C_d}{\partial P_1} &= \frac{-1000 D_c^2 V_c \sqrt{1-\beta^4}}{\rho D_n^2 \frac{2000(P_1-P_2)+\rho g \Delta z}{\rho}^{3/2}} \\ &= -0.0011 \text{ 1/kPa}\end{aligned}\tag{A.65}$$

$$\begin{aligned}\frac{\partial C_d}{\partial P_2} &= \frac{1000 D_c^2 V_c \sqrt{1-\beta^4}}{\rho D_n^2 \frac{2000(P_1-P_2)+\rho g \Delta z}{\rho}^{3/2}} \\ &= 0.00111 \text{ 1/kPa}\end{aligned}\tag{A.66}$$

$$\begin{aligned}\frac{\partial C_d}{\partial \rho} &= \frac{1000 D_c^2 V_c (P_1 - P_2) \sqrt{1-\beta^4}}{D_n^2 \rho^2 \left(\frac{2000(P_1-P_2)+\rho g \Delta z}{\rho} \right)^{\frac{3}{2}}} \\ &= 2.078 \times 10^{-4} \text{ m}^3/\text{kg}\end{aligned}\tag{A.67}$$

and

$$\begin{aligned}\frac{\partial C_d}{\partial \Delta z} &= \frac{-D_c^2 V_c g \sqrt{1-\beta^4}}{D_n^2 \left(\frac{2000(P_1-P_2)+\rho g \Delta z}{\rho} \right)^{\frac{3}{2}}} \\ &= -0.0197 \text{ 1/m}\end{aligned}\tag{A.68}$$

Bias errors:

Bias in piston velocity (see section A.9), $B_{V_c} = 3.204 \times 10^{-3} \text{ m/s}$

Bias in cylinder bore (see section A.2), $B_{D_c} = 6.35 \times 10^{-5} \text{ m}$

Bias in nozzle diameter (see section A.2), $B_{D_n} = 5 \times 10^{-5} \text{ m}$

Bias in pipe diameter (see section A.2), $B_{D_p} = 5 \times 10^{-5} \text{ m}$

Bias in injection pressure, P_1 (see section A.1), $B_{P_1} = 13.84 \text{ kPa}$

Bias in gas pressure, P_2 (see section A.1), $B_{P_2} = 4.03 \text{ kPa}$

Bias in density (see section A.6), $B_\rho = 6.093 \text{ kg/m}^3$

Bias in Δz (\pm half scale res.), $B_{\Delta z} = 5 \times 10^{-4} m$

Applying equation 4.22 the total bias error in C_d is;

$$\begin{aligned}
 B_{C_d}^2 &= \left(\frac{\partial C_d}{\partial V_c} \right)^2 B_{V_c}^2 + \left(\frac{\partial C_d}{\partial D_c} \right)^2 B_{D_c}^2 + \left(\frac{\partial C_d}{\partial D_n} \right)^2 B_{D_n}^2 \\
 &+ \left(\frac{\partial C_d}{\partial D_p} \right)^2 B_{D_p}^2 + \left(\frac{\partial C_d}{\partial P_1} \right)^2 B_{P_1}^2 + \left(\frac{\partial C_d}{\partial P_2} \right)^2 B_{P_2}^2 \\
 &+ \left(\frac{\partial C_d}{\partial \rho} \right)^2 B_{\rho}^2 + \left(\frac{\partial C_d}{\partial \Delta z} \right)^2 B_{\Delta z}^2 \\
 &= (7.736)^2 (3.204 \times 10^{-3})^2 + (15.223)^2 (6.35 \times 10^{-5})^2 + (187.513)^2 (5 \times 10^{-5})^2 \\
 &+ (5.091 \times 10^{-5})^2 (5 \times 10^{-5})^2 + (-0.0011)^2 (13.84)^2 + (0.0011)^2 (4.03)^2 \\
 &+ (2.078 \times 10^{-4})^2 (6.093)^2 + (-0.0197)^2 (5 \times 10^{-4})^2 \\
 \Rightarrow B_{C_d} &= 0.0281
 \end{aligned} \tag{A.69}$$

Precision error:

Precision error in discharge coefficient ($2S_r$), $P_{C_d} = 0.0056 m/s$

This was determined from the standard deviation of repeated injections at nominally identical conditions. **Total Uncertainty:**

Combining the bias and precision errors, the total uncertainty in C_d from equation 4.18 is;

$$\begin{aligned}
 U_{C_d}^2 &= (0.0281)^2 + (0.0056)^2 \\
 \Rightarrow U_{C_d} &= 0.0286 \text{ (3.36\% } C_d)
 \end{aligned} \tag{A.70}$$

A.11 Reynolds Number

Reynolds Number, Re

Nominal value: 78631

Nominal nozzle velocity, V_n : 15.238 m/s

Nominal nozzle diameter, D_n : $8.246 \times 10^{-3} m$

Nominal viscosity, ν : $1.598 \times 10^{-6} m^2/s$

A.11 Reynolds Number

Data reduction equation:

$$Re = \frac{V_n D_n}{\nu} \quad (\text{A.71})$$

From this data reduction equation, the sensitivity coefficients for each variable are:

$$\begin{aligned} \frac{\partial Re}{\partial V_n} &= \frac{D_n}{\nu} \\ &= 5160.2 \text{ s/m} \end{aligned} \quad (\text{A.72})$$

$$\begin{aligned} \frac{\partial Re}{\partial D_n} &= \frac{V_n}{\nu} \\ &= 9.536 \times 10^6 \text{ 1/m} \end{aligned} \quad (\text{A.73})$$

and

$$\begin{aligned} \frac{\partial Re}{\partial \nu} &= V_n D_n \ln \nu \\ &= -1.6771 \text{ s/m}^2 \end{aligned} \quad (\text{A.74})$$

Bias errors:

Bias in velocity (see section A.9), $B_{V_n} = 0.5243 \text{ m/s}$

Bias in diameter (see section A.2), $B_{D_n} = 0.05 \text{ mm}$

Bias in viscosity (see section A.5), $B_\nu = 0.0362 \times 10^{-6} \text{ m}^2/\text{s}$

Applying equation 4.22 the total bias error in Re is;

$$\begin{aligned} B_{Re}^2 &= \left(\frac{\partial Re}{\partial V_n} \right)^2 B_{V_n}^2 + \left(\frac{\partial Re}{\partial D_n} \right)^2 B_{D_n}^2 + \left(\frac{\partial Re}{\partial \nu} \right)^2 B_\nu^2 \\ &= (5160.2)^2 (0.5243)^2 + (9.536 \times 10^6)^2 (0.05)^2 + (-1.6771)^2 (0.0362 \times 10^{-6})^2 \\ \Rightarrow B_{Re} &= 2747.1 \end{aligned} \quad (\text{A.75})$$

Precision error:

Precision error in velocity (see section A.9), $P_{V_n} = 0.3260 \text{ m/s}$

Precision error in diameter (see section A.2), $P_{D_n} = 9.2 \times 10^{-6} \text{ m}$

Precision error in viscosity (see section A.5), $P_\nu = 0.002 \times 10^{-6} \text{ m}^2/\text{s}$

Applying equation 4.24 the total precision error in Re is;

$$\begin{aligned} P_{Re}^2 &= \left(\frac{\partial Re}{\partial V_n} \right)^2 P_{V_n}^2 + \left(\frac{\partial Re}{\partial D_n} \right)^2 P_{D_n}^2 + \left(\frac{\partial Re}{\partial \nu} \right)^2 P_\nu^2 \\ &= (5160.2)^2 (0.3260)^2 + (9.536 \times 10^6)^2 (9.2 \times 10^{-6})^2 + (-1.6771)^2 (0.002 \times 10^{-6})^2 \\ \Rightarrow P_{Re} &= 1684.4 \end{aligned} \quad (\text{A.76})$$

Total Uncertainty:

Combining the bias and precision errors, the total uncertainty in Re from equation 4.18 is;

$$\begin{aligned} U_{Re}^2 &= (2747.1)^2 + (1684.4)^2 \\ \Rightarrow U_{Re} &= 3222.4 \text{ (4.098\% } Re) \end{aligned} \quad (\text{A.77})$$

A.12 Cavitation Number

Cavitation number, K

Nominal value: 1.852

Nominal injection pressure, P_1 : 370.797 kPa

Nominal gas pressure, P_2 : 116.558 kPa

Nominal vapour pressure, P_v : 1.064 kPa

Nominal atmospheric pressure, P_{atm} : 100.984 kPa

Data reduction equation:

$$K = \frac{(P_1 + P_{atm}) - P_v}{P_1 - P_2} \quad (\text{A.78})$$

From this data reduction equation, the sensitivity coefficients for each variable are:

$$\begin{aligned} \frac{\partial K}{\partial P_v} &= \frac{-1}{P_1 - P_2} \\ &= -3.933 \times 10^{-3} \text{ 1/kPa} \end{aligned} \quad (\text{A.79})$$

$$\begin{aligned}\frac{\partial K}{\partial P_1} &= \frac{P_v - P_2 - P_{atm}}{P_1 - P_2^2} \\ &= -3.349 \times 10^{-3} \text{ 1/kPa}\end{aligned}\tag{A.80}$$

and

$$\begin{aligned}\frac{\partial K}{\partial P_2} &= \frac{P_1 + P_{atm} - P_v}{P_1 - P_2^2} \\ &= 7.284 \times 10^{-3} \text{ 1/kPa}\end{aligned}\tag{A.81}$$

Bias errors:

Bias in vapour pressure (see section A.7), $B_{P_v} = 0.011 \text{ kPa}$

Bias in injection pressure (see section A.1), $B_{P_1} = 13.84 \text{ kPa}$

Bias in gas pressure (see section A.1), $B_{P_2} = 4.03 \text{ kPa}$

Applying equation 4.22 the total bias error in K is;

$$\begin{aligned}B_K^2 &= \left(\frac{\partial K}{\partial P_v}\right)^2 B_{P_v}^2 + \left(\frac{\partial K}{\partial P_1}\right)^2 B_{P_1}^2 + \left(\frac{\partial K}{\partial P_2}\right)^2 B_{P_2}^2 \\ &= (-3.933 \times 10^{-3})^2 (0.011)^2 + (-3.349 \times 10^{-3})^2 (13.84)^2 + (7.284 \times 10^{-3})^2 (4.03)^2 \\ \Rightarrow B_K &= 0.0164\end{aligned}\tag{A.82}$$

Precision error:

Precision error in cavitation number ($2S_r$), $P_K = 0.0781 \text{ m/s}$

This was determined from the standard deviation of repeated injections at nominally identical conditions.

Total Uncertainty:

Combining the bias and precision errors, the total uncertainty in K from equation 4.18 is;

$$\begin{aligned}U_K^2 &= (0.0164)^2 + (0.0781)^2 \\ \Rightarrow U_K &= 0.0798\end{aligned}\tag{A.83}$$

A.13 Cavity Collapse Length

Cavity collapse length was determined using the method outlined in section 4.3.1.

Cavity Collapse Length, L_{cav}/L

Nominal value: 0.25

Bias errors:

Image resolution bias - (± 1 pixel), $B_{res} = 1.375 \times 10^{-3}$

Threshold conversion bias - estimated (± 3 pixel), $B_{th} = 4.125 \times 10^{-3}$

Entrance detection bias - estimated (± 2 pixel), $B_{det} = 2.75 \times 10^{-3}$

Applying equation 4.22 the total bias error in L_{cav}/L is;

$$\begin{aligned} B_{L_{cav}/L}^2 &= B_{res}^2 + B_{th}^2 + B_{det}^2 \\ &= (1.375 \times 10^{-3})^2 + (4.125 \times 10^{-3})^2 + (2.75 \times 10^{-3})^2 \\ \Rightarrow B_{L_{cav}/L} &= 0.005 \end{aligned} \quad (A.84)$$

Precision error:

Standard deviation ($2S_r$), $P_{L_{cav}/L} = 0.059$

Total Uncertainty:

Combining the bias and precision errors, the total uncertainty in L_{cav}/L from equation 4.18 is;

$$\begin{aligned} U_{L_{cav}/L}^2 &= (0.005)^2 + (0.059)^2 \\ \Rightarrow U_{L_{cav}/L} &= 0.0592 \text{ (23.7\% } L_{cav}/L) \end{aligned} \quad (A.85)$$

A.14 Shedding Frequency

Periodic shedding frequency was determined using the method outlined in section 4.3.3.

Shedding Frequency, f [Hz]

Nominal value: 1600

Bias errors:

PSD resolution bias - (width of frequency bin), $B_{bin} = 51.38$

Precision error:

Standard deviation ($2S_r$), $P_f = 3.87$ Measured as the standard deviation of the frequency determined for the individual interrogation points

Total Uncertainty:

Combining the bias and precision errors, the total uncertainty in f from equation 4.18 is;

$$\begin{aligned} U_f^2 &= (51.38)^2 + (3.87)^2 \\ \Rightarrow U_f &= 51.52 \text{ (3.22\%}f\text{)} \end{aligned} \quad (\text{A.86})$$

A.15 Spray Angle

Spray angle was determined using the method outlined in section 4.3.2.

Spray Angle, θ [°]

Nominal value: 9.72

Bias errors:

Bias due to thresholding - (averaged from various trials), $B_{th} = 0.75$

Precision error:

Standard deviation ($2S_r$), $P_\theta = 1.012$ Measured from repeated measurements of the same image

Total Uncertainty:

Combining the bias and precision errors, the total uncertainty in θ from equation 4.18 is;

$$\begin{aligned} U_\theta^2 &= (0.75)^2 + (1.01)^2 \\ \Rightarrow U_\theta &= 1.26 \text{ (12.96\%}\theta\text{)} \end{aligned} \quad (\text{A.87})$$

Appendix B

Instrumentation Calibration

Pressure Sensors

All pressure sensors used for this work was calibrated using a dead weight pressure tester. Sensor output voltage was measured using the National Instruments PCI 6221 data acquisition card and TBX-68 I/O connector block to ensure end-to-end calibration. Weights were gradually applied to the dead weight tester in increments of 100 kPa equivalence. The entire process was repeated 3 times for each sensor and the output voltages averaged to further reduce sample to sample error. Figure [B.1](#) shows the regression curve obtained for the gas pressure sensor, while figure [B.2](#) shows the regression curve obtained for the liquid injection pressure sensor.

Thermocouples

Temperature measurements for ambient gas and liquid were measured using K-type thermocouple probes located in measurement ports in the top of the pressure vessel and in the supply pipe respectively. Calibration of these sensors was conducted across a broad range of temperature and compared to a platinum resistance thermometer. Figure [B.3](#) shows the calibration curve for the gas temperature thermocouple, while figure [B.4](#) shows the calibration curve for the liquid temperature thermocouple.

Piston velocity

Determination of the piston velocity require the linear position of the piston to

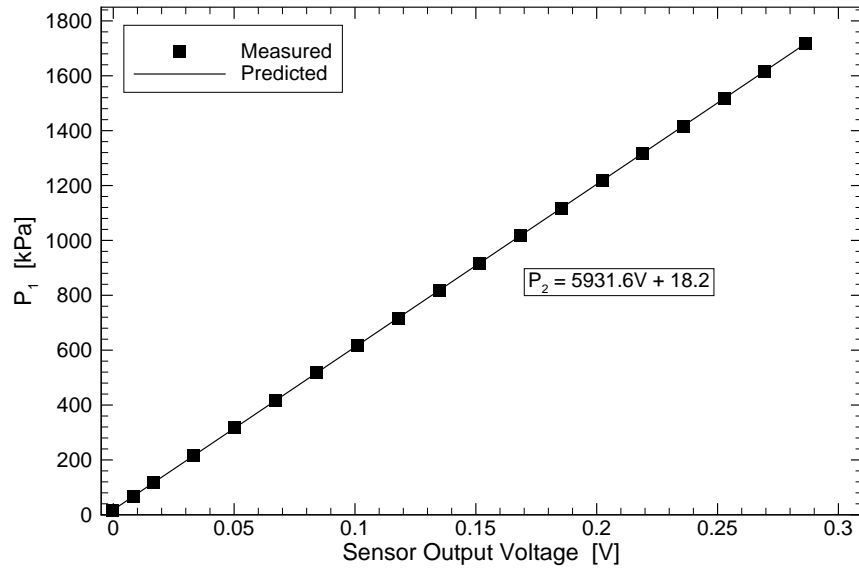


Figure B.1: Pressure vessel gas pressure sensor calibration

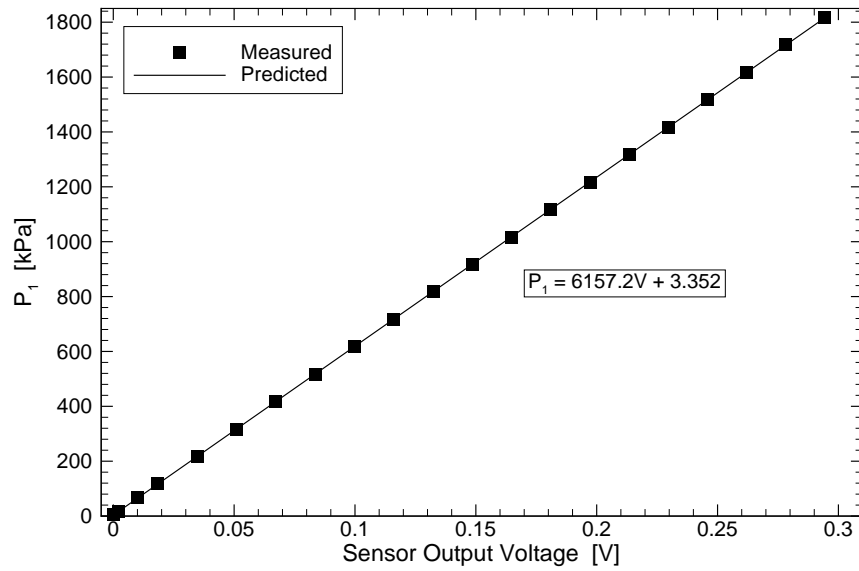


Figure B.2: Injection pressure sensor calibration

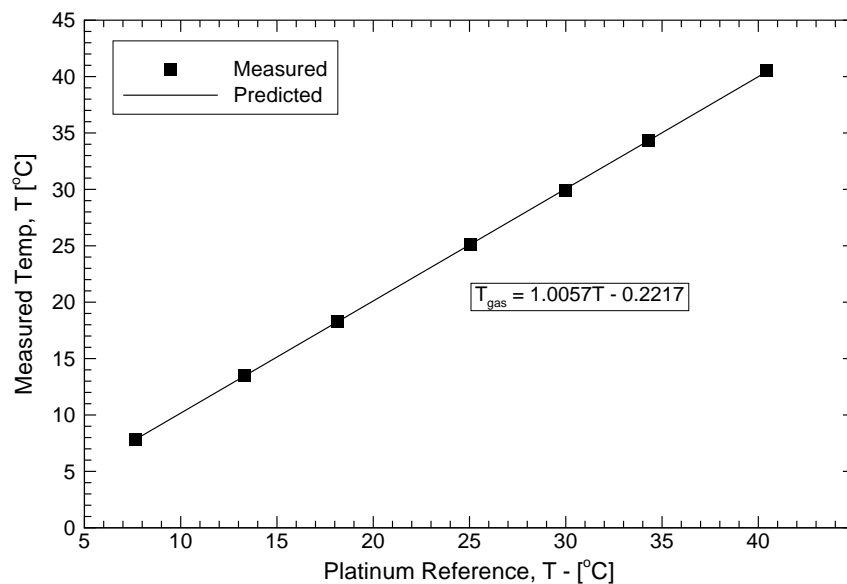


Figure B.3: Gas temperature thermocouple calibration

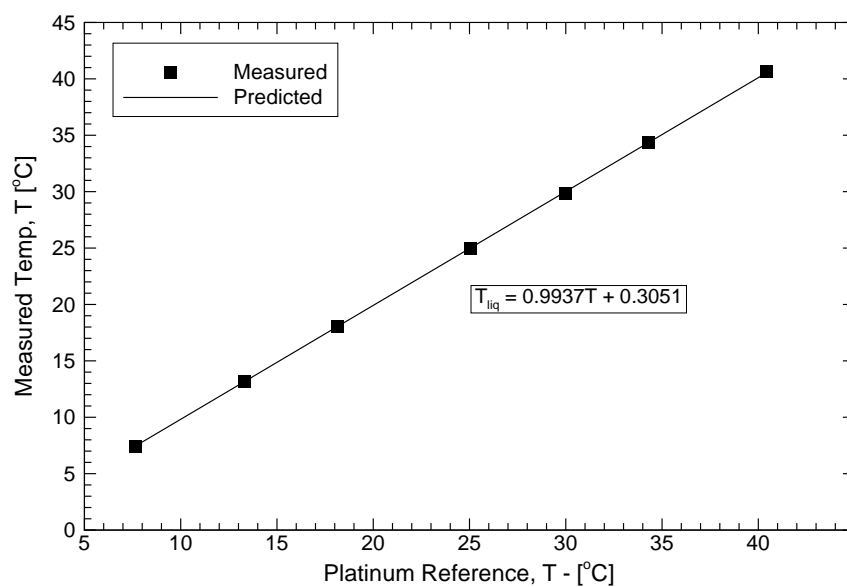


Figure B.4: Liquid temperature thermocouple calibration

be differentiated. The LDT generated an analog current output ($4 - 20mA$) proportional to the piston position. This current output was input across a 250Ω resistor to produce a range of output spanning $1 - 5V$ for the entire piston stroke length. Figure B.5 shows the calibration of the piston position, measured as distance in meters from zero position, against the converted LDT voltage. The linear curve fit shows the expression relating these parameter. The relationship predicting the piston velocity as a function of input voltage was then obtained by applying the chain rule expression (see section A.8). The resulting curve was then fit with a quadratic regression curve, as shown in figure B.6.

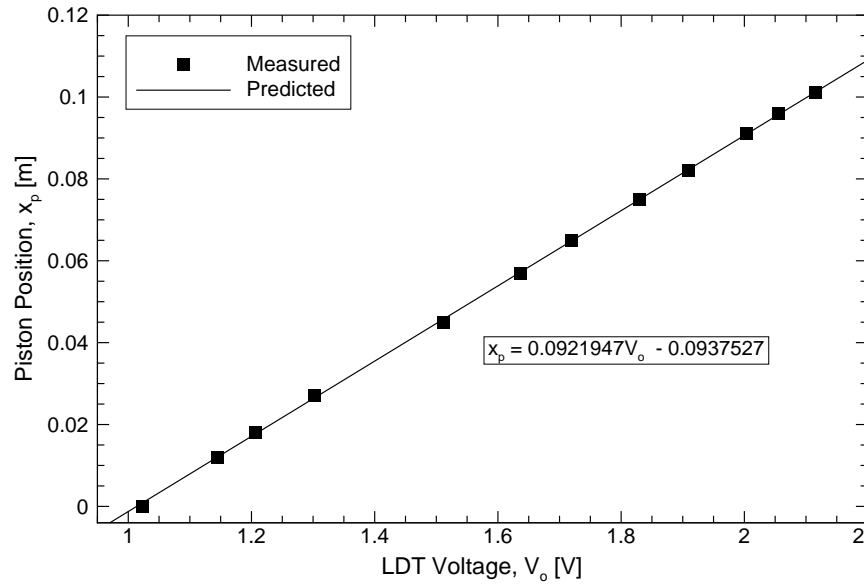


Figure B.5: LDT piston position calibration

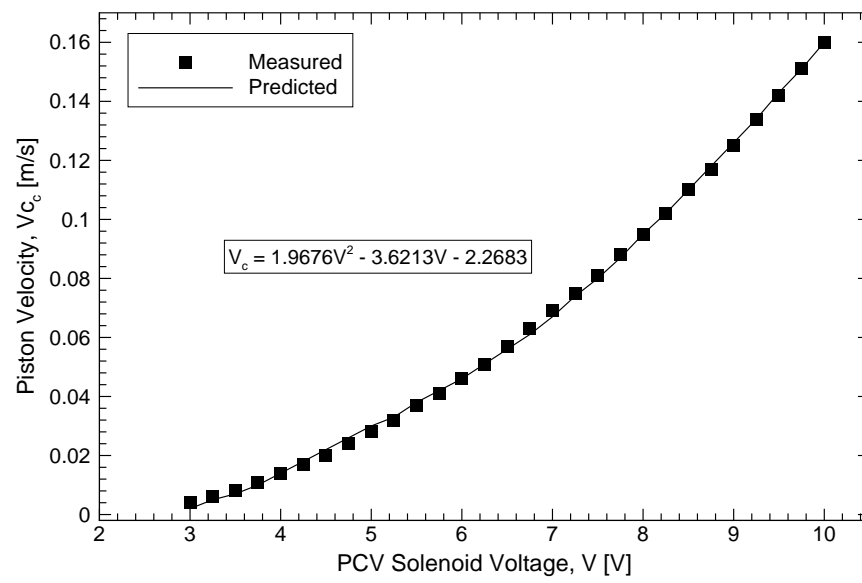


Figure B.6: Piston velocity calibration

Appendix C

Pressure Vessel Drawings

As presented in Chapter 3, the design of an optical access pressure vessel formed a major component of the development of the experimental rig used for this work. The concept and design of the vessel was entirely conducted by the author, the key features of which were discussed in section 3.5. Verification of material stresses and fabrication of the vessel was completed by *L & A Pressure Welding*. Further to this, registration of the pressure vessel with WorkCover NSW which is a legal requirement for operation, required the design to be independently verified to comply to the regulations outlined in the *Occupational Health and Safety Regulation 2001*. The design was found to comply to the Australian Standard AS1210-1997 and registered with WorkCover NSW on 14/08/2009 - Registration No: PV 6-120613/09.

The engineering drawings used for manufacture can be seen in the following pages.

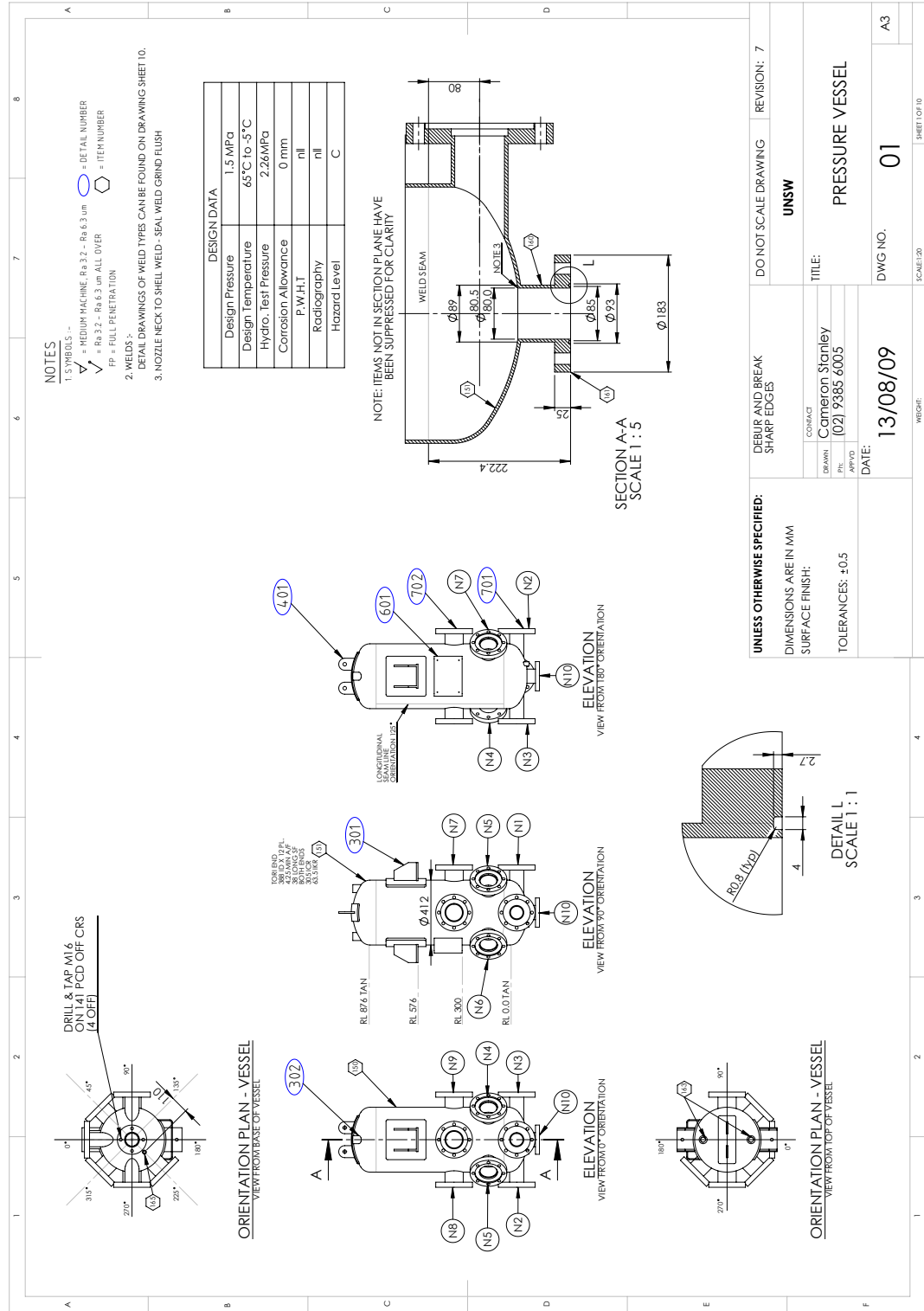
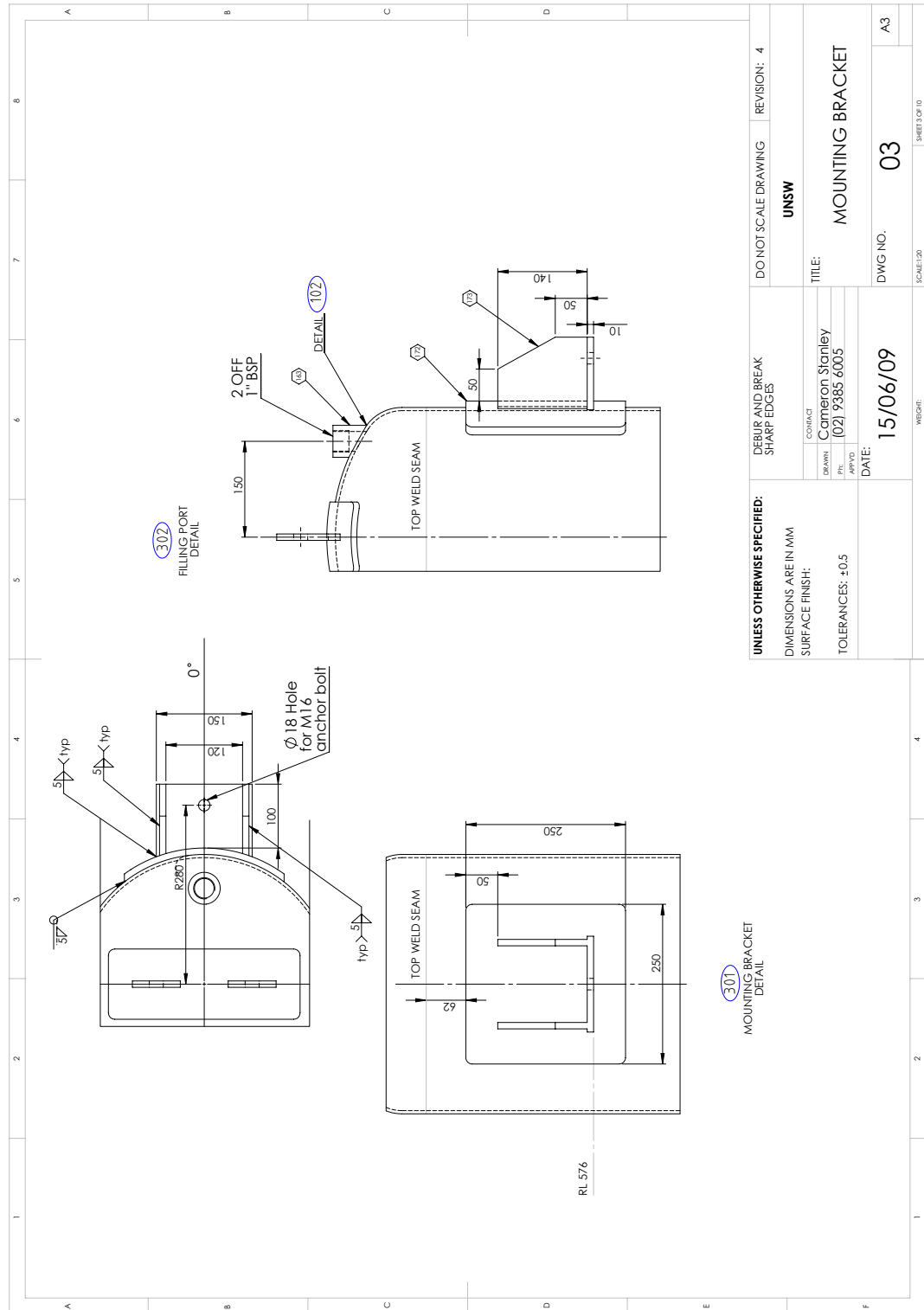


Figure C.1: Pressure vessel - drawing sheet 1

1	2	3	4	5	6	7	8
BILL OF MATERIALS							
ITEM	DESCRIPTION	QTY	MATERIAL SPECIFICATION	NOTES:			
150	CYLINDRICAL SHELL - Ø 412 OD x 800 LG x 12 PL.	1	ASTM A240-304	1. ITEM 171 IS TO BE SUPPLIED BY UNSW AND THEN WELDED TO ITEM 164 BY L&A ACCORDING TO DRAWING 09. 2. ELEVATION OF NOZZLES IS MEASURED FROM THE BOTTOM SHELL-HEAD CIRCUMFERENTIAL WELD SEAM. 3. ELEVATION FOR NOZZLE N10 IS MEASURED TO THE FLANGE FACE.			
151	TORI HEAD - Ø 412 OD x 38 S.F. X 12 PL.	2	ASTM A240-304				
152	N1-N3 NECK - 80 NB SCH 40S x 184 LG	3	ASTM A312-TP304				
153	N1-N3 FLANGE - Ø 230 OD x Ø 91 ID x 32 PL.	3	ASTM A240-304				
154	N1-N9 BLIND - Ø 230 OD x 16 PL.	9	ASTM A240-304				
155	N1-N9 SIGHTGLASS - Ø 169 OD x 17 THK	9	BOROSILICATE				
156	N4-N9 NECK - 100 NB SCH 40S x 76 LG	6	ASTM A312-TP304				
157	N4-N9 FLANGE - Ø 230 OD x Ø 116 ID x 32 PL.	6	ASTM A240-304				
158	N1-N9 GASKET - Ø 169 OD x Ø 143 ID x 1.5 THK	18	CNAF				
159	N1-N9 HEX HEAD BOLTS AND NUTS - M16 x 120 LG.	72	ASTM A193-B7M/ASTM A194M-2H				
160	N10 NECK - 80 NB SCH 40S x 75 LG.	1	ASTM A312-TP304	B			
161	N10 FLANGE - Ø 183 OD x Ø 91 ID x 25 PL.	1	ASTM A240-304				
162	N10 GASKET (O-RING - Ø 92.15 OD x 3.15 WIDE)	1	VITON				
163	GAS PORT - 1" BSP HALF COUPLING, 300# 1	2	ASTM A182-F304				
164	PIPE FLANGE - Ø 183 OD x Ø 63 ID x 32 PL.	1	ASTM A240-304				
165	PIPE PORT - 3/8" BSP, 3000# HALF COUPLING	2	ASTM A182-F304				
166	NOZZLE INSERT FLANGE - Ø 183 OD x Ø 50 ID x 32 PL.	1	ASTM A240-304				
167	PIPE PORT - 1/4" BSP, 3000# HALF COUPLING	1	ASTM A182-F304				
168	LIFTING LUG - 10 PL. x 75 x 110	2	ASTM A240-304				
169	LIFTING LUG PAD - 10 PL. x 110 X 315	1	ASTM A240-304				
170	NAMING PLATE BRACKET - 6 PL. x 175 x 430	1	ASTM A240-304	C			
171	SUPPLY PIPE - 50NB SCH 40S**	1	ASTM A312-TP304				
172	MOUNTING BRACKET PAD - 10 PL. x 250 x 270	2	ASTM A240-304				
173	MOUNTING BRACKET LUG - 10 PL. x 150 x 350	2	ASTM A240-304				
				D			
REF	RL ELEVATION	ORIENTATION	OD	ID	POSITION SHELL/HEAD	HORIZONTAL/VERTICAL	
N1	-42	0°	88.9	77.9	HEAD	HORIZONTAL	
N2	-42	90°	88.9	77.9	HEAD	HORIZONTAL	
N3	-42	270°	88.9	77.9	HEAD	HORIZONTAL	
N4	135	315°	114.3	102.26	SHELL	HORIZONTAL	
N5	135	45°	114.3	102.26	SHELL	HORIZONTAL	
N6	135	225°	114.3	102.26	SHELL	HORIZONTAL	
N7	350	0°	114.3	102.26	SHELL	HORIZONTAL	
N8	350	90°	114.3	102.26	SHELL	HORIZONTAL	
N9	350	270°	114.3	102.26	SHELL	HORIZONTAL	
N10	-184.4	-	88.9	80	HEAD	VERTICAL	
UNLESS OTHERWISE SPECIFIED:							DERUR AND BREAK SHARP EDGES
DIMENSIONS ARE IN MM							DO NOT SCALE DRAWING
SURFACE FINISH:							REVISION: 6
TOLERANCES: ±0.5							UNSW
							TITLE:
							Cameron Stanley
							02 9385 6005
							DATE:
							13/08/09
							DWG NO.
							02
							A3
							SHEET 2 OF 10

Figure C.2: Pressure vessel - drawing sheet 2



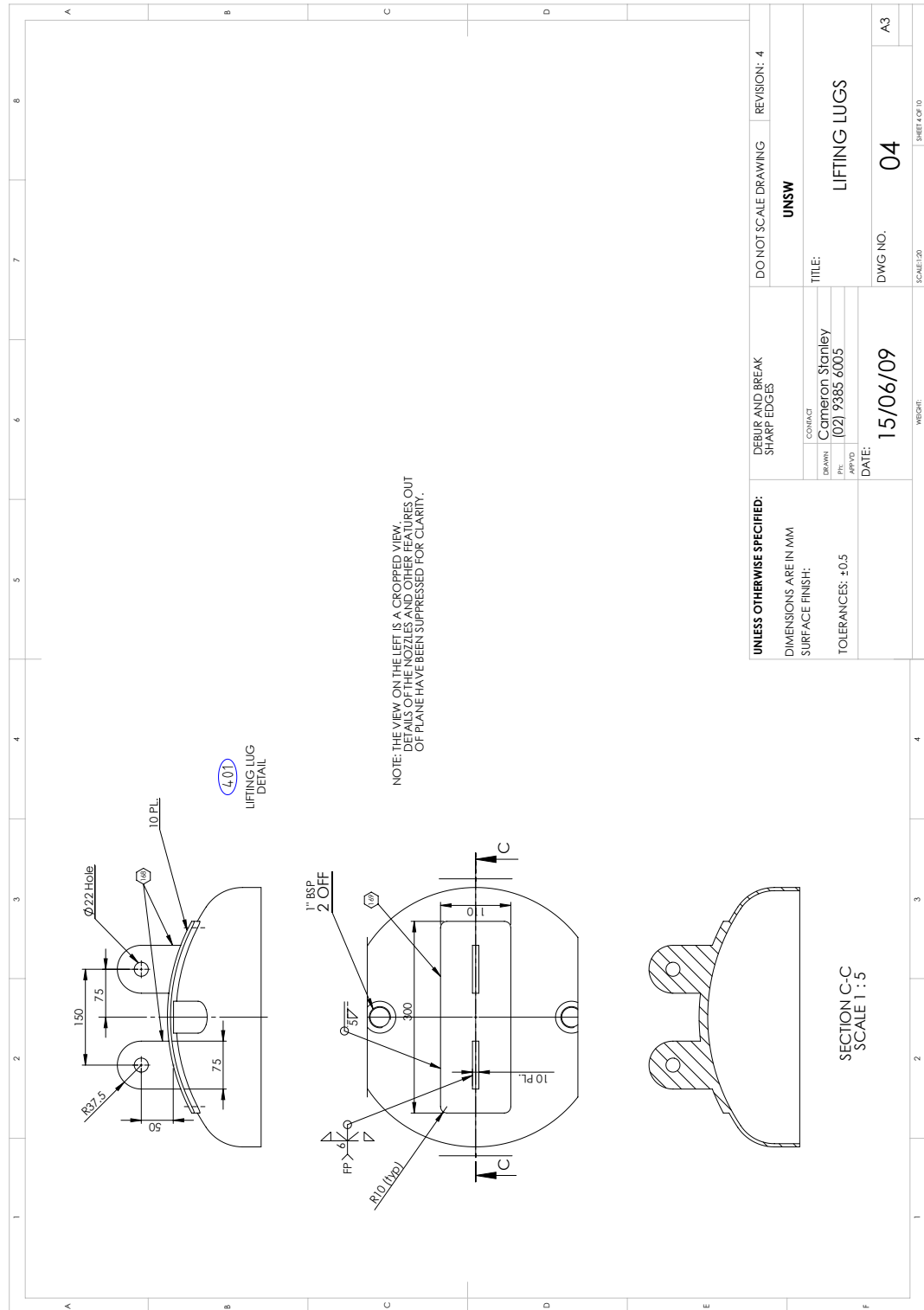


Figure C.4: Pressure vessel - drawing sheet 4

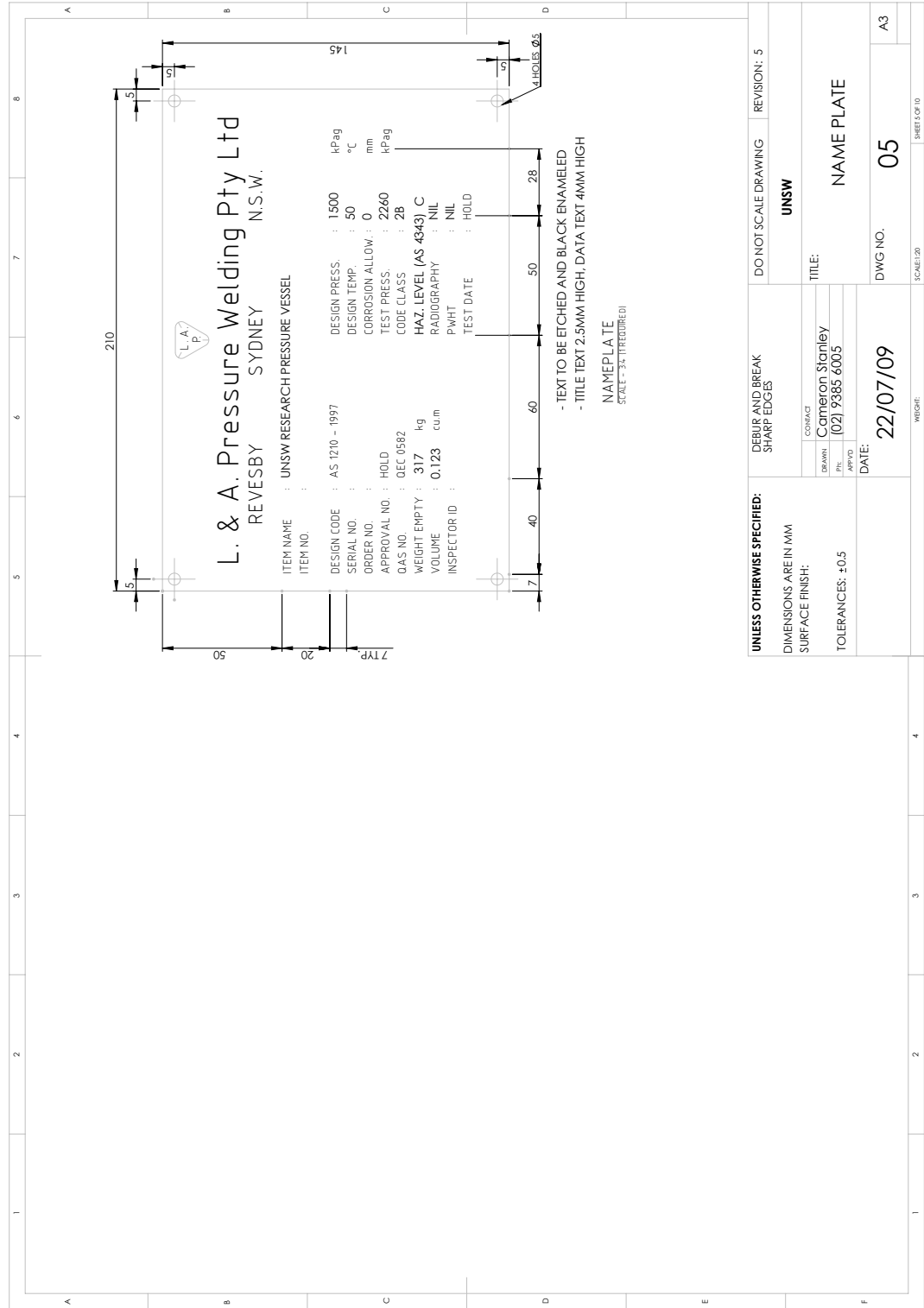


Figure C.5: Pressure vessel - drawing sheet 5

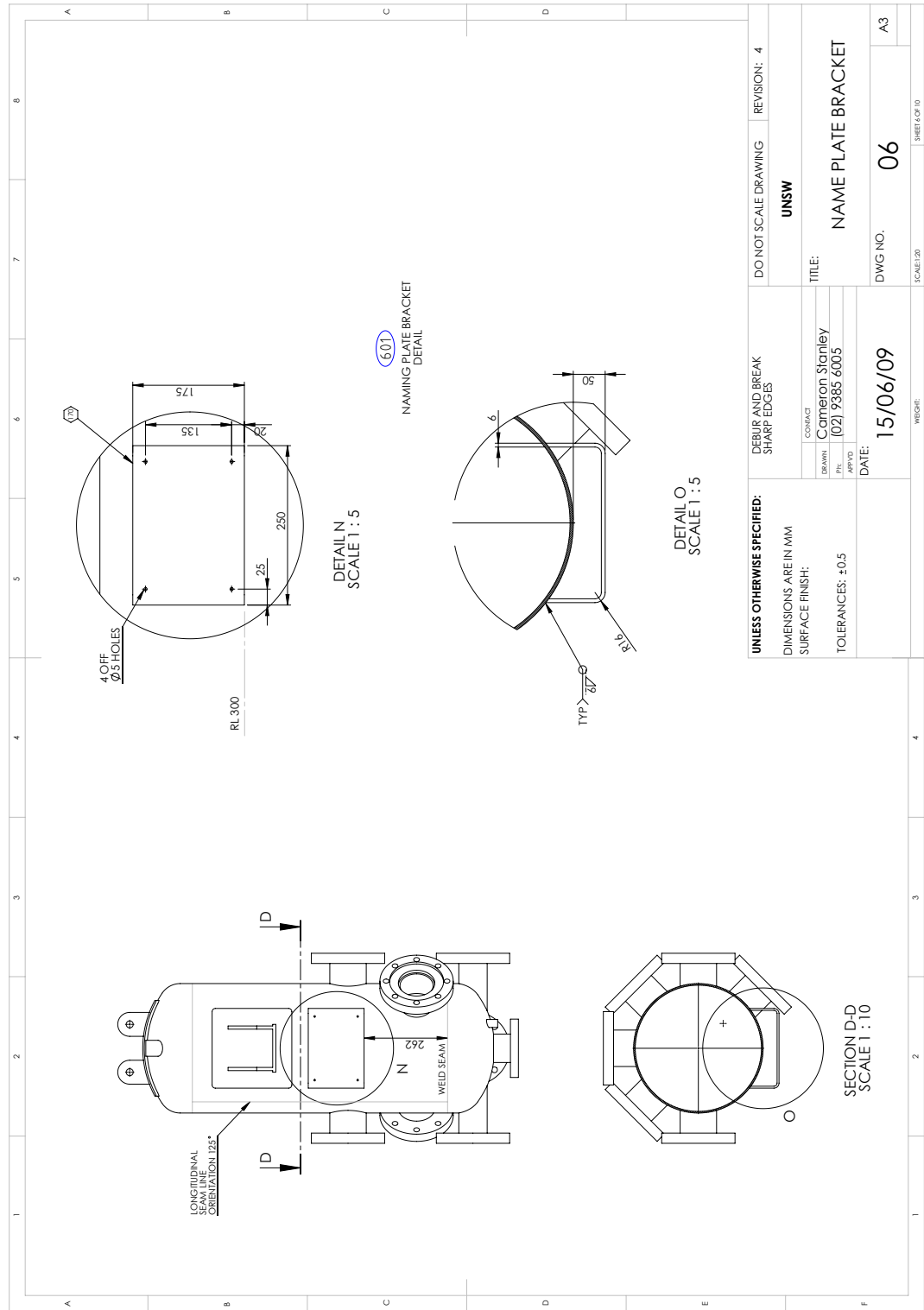


Figure C.6: Pressure vessel - drawing sheet 6

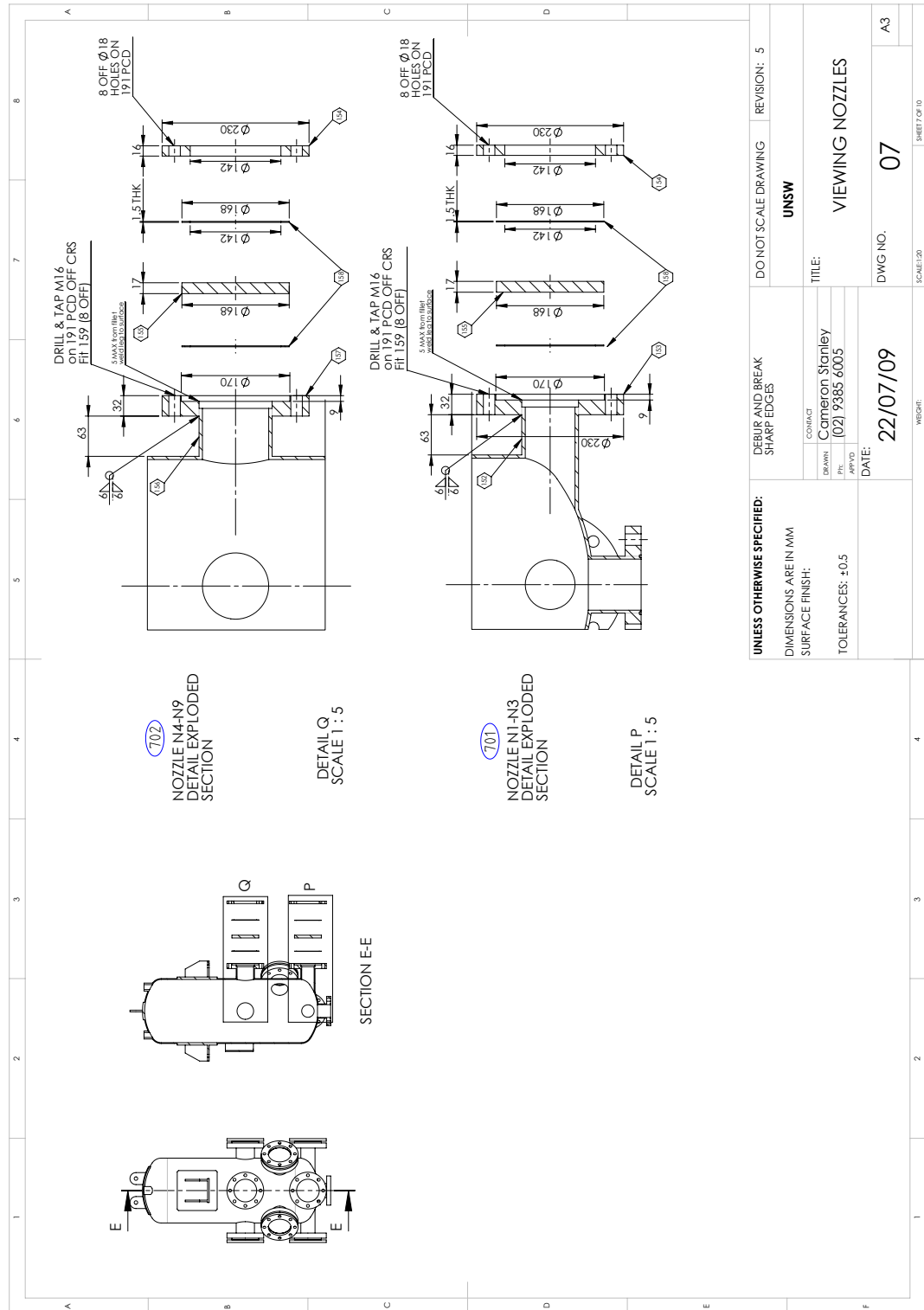


Figure C.7: Pressure vessel - drawing sheet 7

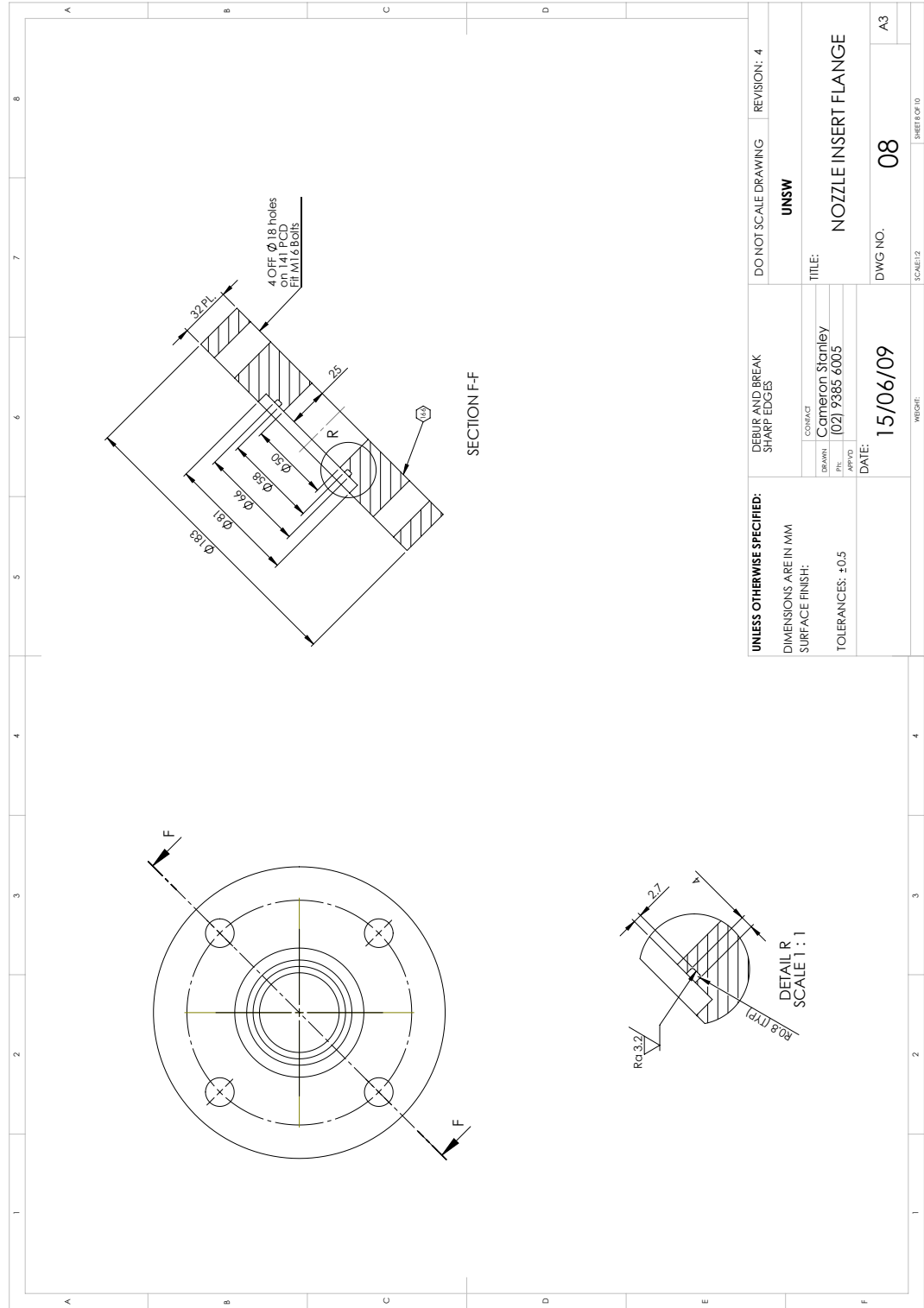


Figure C.8: Pressure vessel - drawing sheet 8

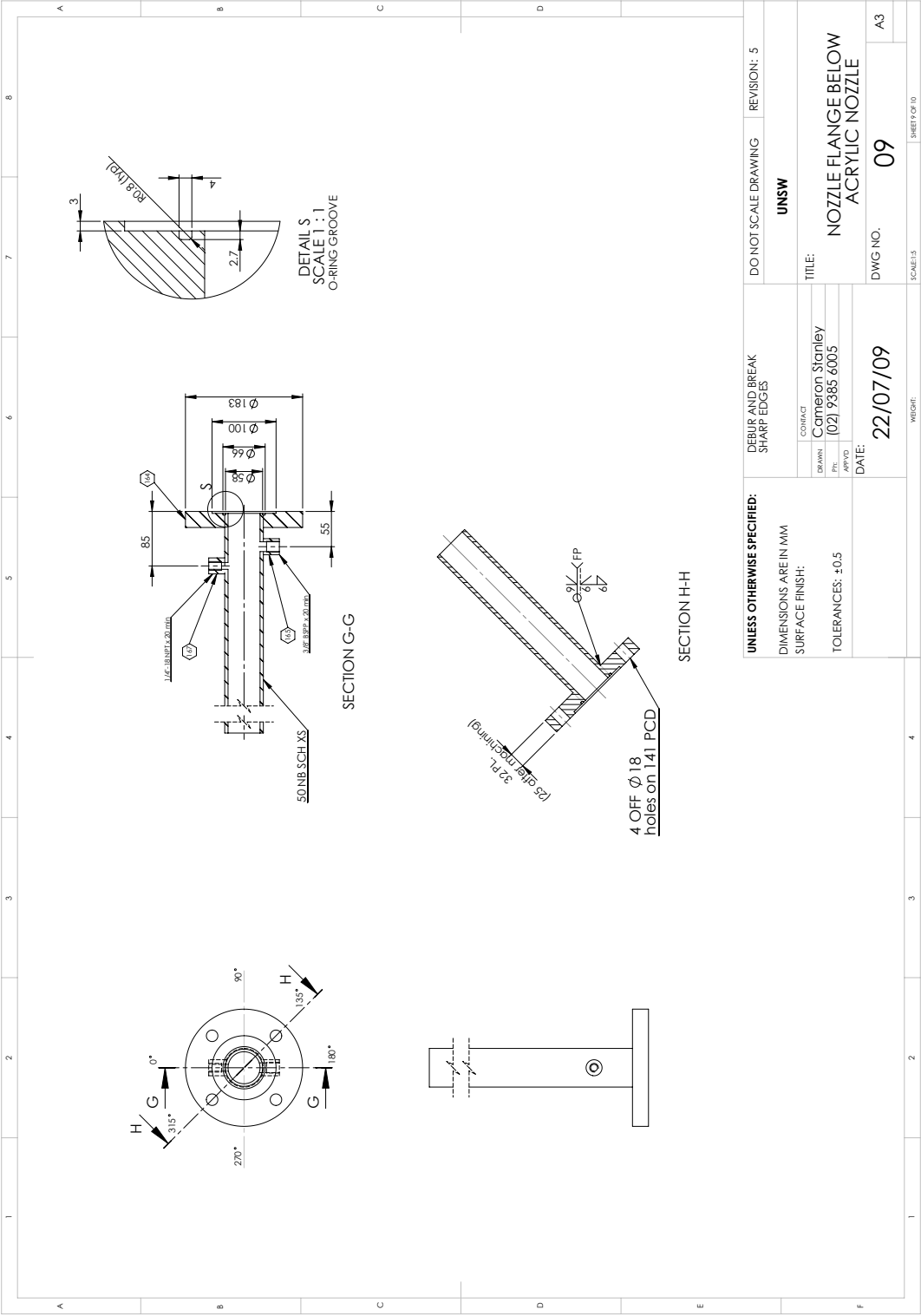


Figure C.9: Pressure vessel - drawing sheet 9

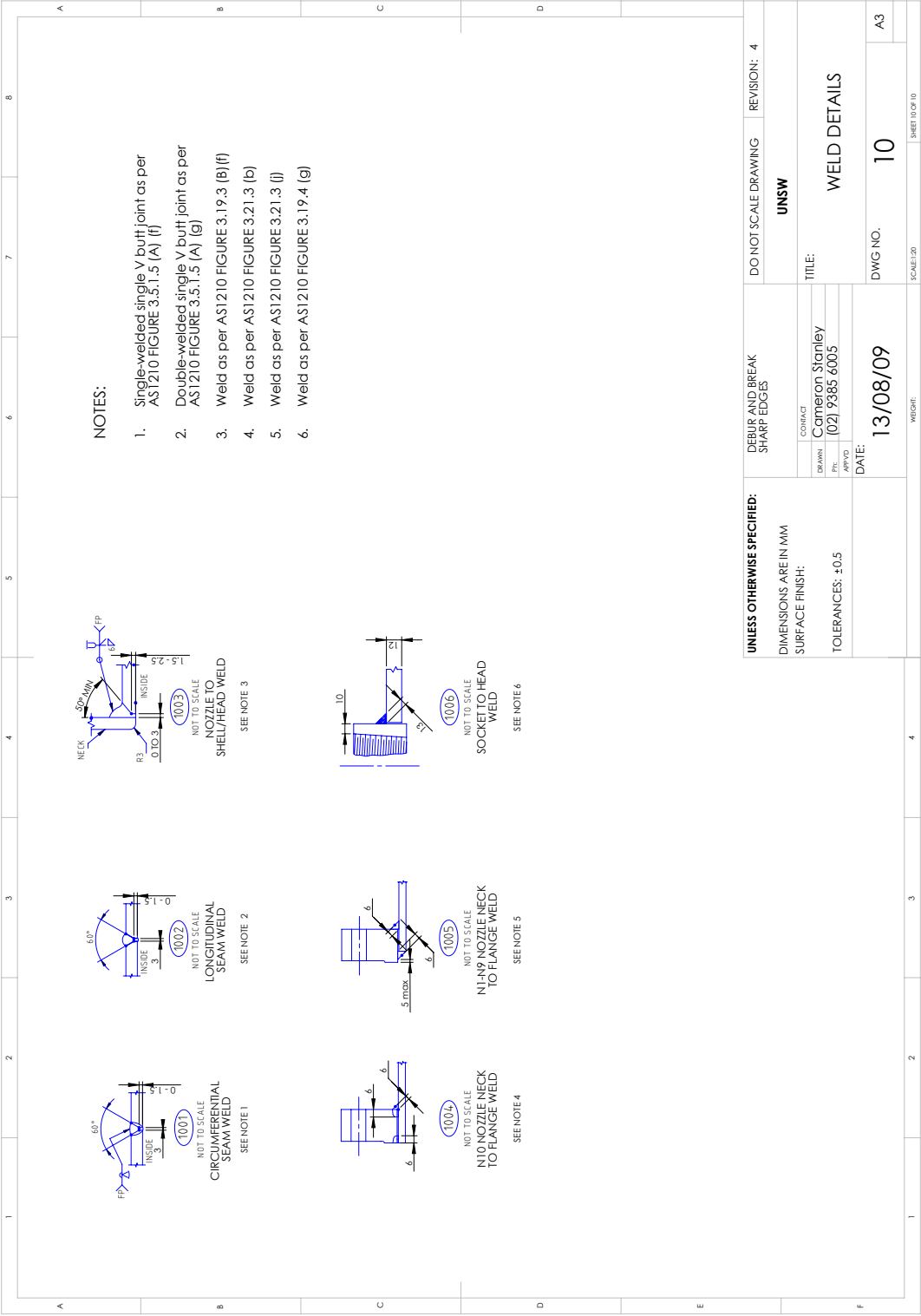


Figure C.10: Pressure vessel - drawing sheet 10

Appendix D

Hydraulic Equipment

The propulsion of liquid through the test section was accomplished using hydraulic cylinders, as described in Chapter 3. All hydraulic components used for this work were purchased from *Parker Hannifin Australia*. Where possible standard hydraulic components were used. Special attention was given to the corrosive properties of the Sodium Iodide test fluid, which required the test cylinder to be manufactured from Stainless Steel and use non-standard piston seals. A Schematic showing the arrangement of the hydraulic system and a list of key components can be seen in figure D.1.

As mentioned in section 3.4 the cylinder end-cap for the test fluid cylinder was custom designed by the author to minimise the flow separation in the contraction from the cylinder bore to the supply piping entry. Figure D.2 shows the engineering drawing of this end cap.

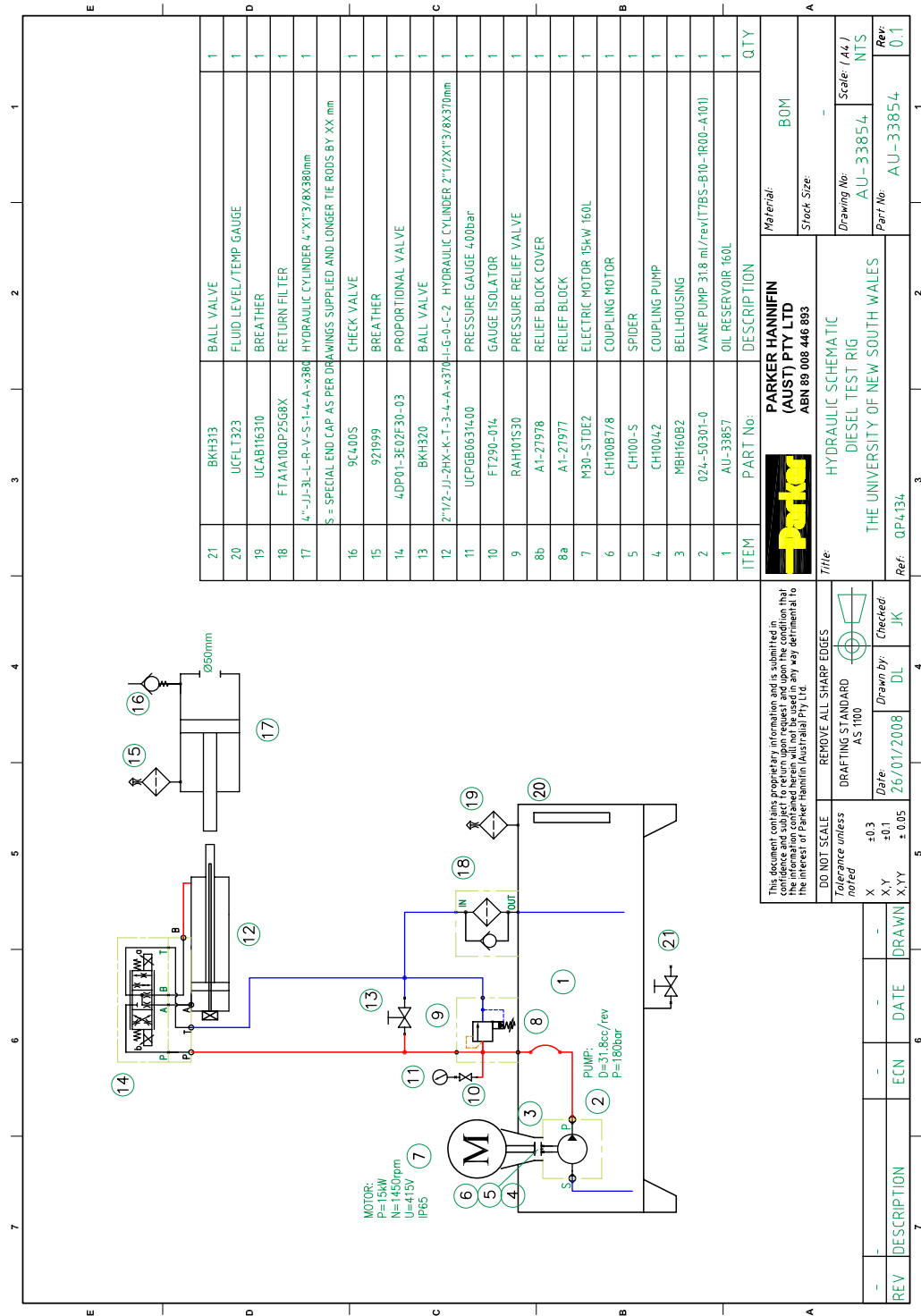


Figure D.1: Hydraulic System Schematic

References

- AFZAL, H., ARCOUMANIS, C., GAVAISES, M. & KAMPANIS, N. (1999). Internal flow in diesel injector nozzles - modelling and experiments. *Proc. IMechE Seminar on Fuel Injection Systems*, **London**, 25–44. [26](#), [34](#), [35](#)
- ANDRIOTIS, A., GAVAISES, M. & ARCOUMANIS, C. (2008). Vortex flow and cavitation in diesel injector nozzles. *Journal of Fluid Mechanics*, **610**, 195–215. [35](#)
- ARAI, M., TABATA, M., HIROYASU, H. & SHIMIZU, M. (1984). Disintegrating process and spray characterisation of fuel jet injected by a diesel nozzle. *SAE Technical Paper*, **840275**. [18](#), [22](#), [28](#)
- ARCOUMANIS, C. & GAVAISES, M. (1998). Cavitation in diesel injectors: modelling and experiments. In *Proc. ILASS-Europe*, 248–255. [26](#)
- ARCOUMANIS, C. & WHITELAW, J. (2002). Is cavitation important in diesel engine injectors? 145–159. [27](#)
- ARCOUMANIS, C., FLORA, H., GAVAISES, M., KAMPANIS, N. & HORROCKS, R. (1999). Investigation of cavitation in a vertical multi-hole injector. *SAE Technical Paper*, **1999-01-0524**. [24](#), [27](#), [34](#)
- ARCOUMANIS, C., BADAMI, M., FLORA, H. & GAVAISES, M. (2000). Cavitation in real-size multi-hole diesel injector nozzles. *SAE Technical Paper*, **2000-01-1249**. [27](#), [35](#)

REFERENCES

- ARNDT, R., SONG, C., KJELDSSEN, M., HE, J., KELLER, A. *et al.* (2000). Instability of partial cavitation: a numerical/experimental approach. In *23rd Symposium on Naval Hydrodynamics, September, Rouen, France*. [41](#)
- ASI, O. (2006). Failure of a diesel engine injector nozzle by cavitation damage. *Engineering Failure Analysis*, **13**, 1126–1133. [36](#)
- BADOCK, C., WIRTH, R., FATH, A. & LEIPERTZ, A. (1999). Investigation of cavitation in real size diesel injection nozzles. *International Journal of Heat and Fluid Flow*, **20**, 538–544. [24](#), [26](#)
- BAE, C., YU, J., KANG, J., KONG, J. & OOK LEE, K. (2002). Effect of nozzle geometry on the common-rail diesel spray. *SAE Technical Paper*, **2002-01-1625**. [2](#)
- BENAJES, J., PASTOR, J., PAYRI, R. & PLAZAS, A. (2004). Analysis of the influence of diesel nozzle geometry in the injection rate characteristics. *Journal of Fluids Engineering*, **Vol. 126**, 63–71. [28](#), [33](#)
- BERGER, S., TALBOT, L. & YAO, L. (1983). Flow in curved pipes. *Annual Review of Fluid Mechanics*, **15**, 461–512. [59](#)
- BERGWERK, W. (1959). Flow pattern in diesel nozzle spray holes. *Proc Inst Mech Eng*, **173**, 655–660. [26](#)
- BILLET, M. (1985). Cavitation nuclei measurements-a review. In *Proc. 1985 ASME Cavitation and Multiphase Flow Forum*, 31–38. [8](#)
- BILLET, M. & HOLL, J. (1981). Scale effects on various types of limited cavitation. *Journal of Fluids Engineering*, **103**, 405. [27](#)
- BLAKER, A. (1965). *Photography for Scientific Publication - A Handbook*. W. H. Freeman and Company. [81](#)
- BLESSING, M., KONIG, G., KRUGER, C., MICHELS, U. & SCHWARZ, V. (2003). Analysis of flow and cavitation phenomena in diesel injection nozzles and its effects on spray and mixture formation. In *Two day conference on fuel*

REFERENCES

- injection systems: organized by the Combustion Engines and Fuels Group of the Automobile Division of the Institution of Mechanical Engineers (IMEchE)*, vol. 610, 21, Professional Engineering for the Institution of Mechanical Engineers. [35](#), [36](#)
- BRANDNER, P., WALKER, G., NIEKAMP, P. & ANDERSON, B. (2007). An investigation of cloud cavitation about a sphere. *16th Australasian Fluid Mechanics Conference (AFMC)*, 1392–1398. [41](#)
- BRENNEN, C. (1995). *Cavitation and bubble dynamics*. Oxford University Press. [5](#), [7](#), [27](#), [35](#)
- BUDWIG, R. (1994). Refractive index matching methods for liquid flow investigations. *Experiments in fluids*, **17**, 350–355. [70](#)
- BUNNELL, R., HEISTER, S., YEN, C. & COLLICOTT, S. (1999). Cavitating injector flows: validation of numerical models and simulations of pressure atomizers. *Atomization and Sprays*, **9**, 445–465. [42](#)
- CALLENAERE, M., FRANC, J., MICHEL, J. & RIONDET, M. (2001). The cavitation instability induced by the development of a re-entrant jet. *Journal of Fluid Mechanics*, **444**, 223–256. [36](#), [37](#), [39](#), [113](#), [131](#)
- CASTLEMAN, R. (1932). The mechanism of atomization accompanying solid injection. *N.A.C.A, Report No. 440*. [15](#), [16](#)
- CHANDRA, B. & COLLICOTT, S. (1999). Experimental investigation of cavitation frequency in a slot orifice. *12th Annual conference of ILASS, Americas*, 379–383. [41](#), [127](#)
- CHAVES, H., KNAPP, M., KUBITZEK, A., OBERMEIER, F. & SCHNEIDER, T. (1995). Experimental study of cavitation in the nozzle hole of diesel injectors using transparent nozzles. *SAE Technical Paper*, **950290**. [24](#), [25](#), [26](#), [28](#), [139](#)
- CHEN, R. & FAN, L. (1992). Particle image velocimetry for characterizing the flow structure in three-dimensional gas-liquid-solid fluidized beds. *Chemical Engineering Science*, **47**, 3615–3622. [71](#)

REFERENCES

- COLEMAN, H. & STEELE, W. (1995). Engineering application of experimental uncertainty analysis. *AIAA journal*, **33**, 1888–1896. [96](#)
- COLEMAN, H. & STEELE, W. (1999). *Experimentation and uncertainty analysis for engineers*. Wiley-Interscience. [96](#)
- COUTIER-DELGOSHA, O., STUTZ, B., VABRE, A. & LEGOUPIL, S. (2007). Analysis of cavitating flow structure by experimental and numerical investigations. *Journal of Fluid Mechanics*, **578**, 171. [39](#)
- DAN, T., YAMAMOTO, T., SENDA, J. & FUJIMOTO, H. (1997). Effect of nozzle configurations for characteristics of non-reacting diesel fuel spray. *SAE transactions*, **106**, 581–596. [26](#)
- DAUGHERTY, R. & FRANZINI, J. (1965). *Fluid mechanics with engineering applications*. McGraw-Hill, 6th edn. [109](#)
- DE LANGE, D. & DE BRUIN, G. (1998). Sheet cavitation and cloud cavitation, re-entrant jet and three-dimensionality. *Applied scientific research*, **58**, 91–114. [42](#), [113](#)
- DE LANGE, D., BRUIN, G. & WIJNGAARDEN, L. (1994). On the mechanism of cloud cavitation - experiment and modelling. *The 2nd international symposium on Cavitation, Tokyo, Japan*, 45–49. [40](#), [122](#)
- DEJUHASZ, K. (1931). Dispersion of sprays in solid injection oil engines. *Trans. ASME Oil and Gas Power*. [17](#)
- DESANTES, J., PASTOR, J. & DOUDOU, A. (2001). Study of the steady flow produced by direct injection diesel engine intake ports. *Proc Inst Mech Eng*, **215**, 285 – 298. [28](#)
- DESANTES, R., J.M. AND, SALVADOR, F. & GIL, A. (2006). Development and validation of a theoretical model for diesel spray penetration. *Fuel*, **85**, 910–917. [87](#)
- DODGE, L., RYAN III, T. & M.G, R. (1992). Effects of different injector hole shapes on diesel sprays. *SAE Technical Paper*, **920623**. [19](#), [23](#)

REFERENCES

- DUMONT, N., SIMONIN, O. & HABCHI, C. (2000). Cavitating flow in diesel injectors and atomization: a bibliographic review. *Proceedings of the 8th International Conference on Liquid Atomization and Spray Systems*, **Pasadena, California**. 28
- DUTTWEILER, M. & BRENNEN, C. (1998). Partial cavity instabilities. *US-Japan Seminar on Abnormal Flow Phenomena in Turbomachines*, *Osaka, Japan*. 40, 122
- FRANC, J. & MICHEL, J. (2004). *Fundamentals of Cavitation*. Springer. 5, 7, 27
- GANIPPA, L., BARK, G., ANDERSSON, S. & CHOMIAK, J. (2004). Cavitation: a contributory factor in the transition from symmetric to asymmetric jets in cross-flow nozzles. *Experiments in Fluids*, **36**, 627–634. 29
- GAVAISES, M. (2008). Flow in valve covered orifice nozzles with cylindrical and tapered holes and link to cavitation erosion and engine exhaust emissions. *International Journal of Engine Research*, **9**, 435–447. 36
- GAVAISES, M. & ANDRIOTIS, A. (2006). Cavitation inside multi-hole injectors for large diesel engines and its effect on the near-nozzle spray structure. *SAE Technical Paper*, **2006-01-1114**. 35
- GAVAISES, M., PAPOULIAS, D., ANDRIOTIS, A., GIANNADAKIS, E. & THEODORAKAKOS, A. (2007). Link between cavitation development and erosion damage in diesel fuel injector nozzles. *SAE Technical paper*, 2007–01–0246. 35
- GAVAISES, M., ANDRIOTIS, A., PAPOULIAS, D., MITROGLOU, N. & THEODORAKAKOS, A. (2009). Characterization of string cavitation in large-scale diesel nozzles with tapered holes. *Physics of Fluids*, **21**, 052107. 3, 35, 36
- GELALLES, A. (1930). Effect of orifice length-diameter ratio on spray characteristics. *N.A.C.A, Technical Note No. 352*. 15

REFERENCES

- GELALLES, A. (1932). Coefficients of discharge of fuel injection nozzles for compression-ignition engines. *N.A.C.A, Report No. 373*. [15](#)
- GIFFEN, E. & MURASZEW, A. (1953). *The Atomization of Liquid Fuels*. John Wiley and Sons, Inc., NY. [1](#)
- HAENLEIN, A. (1932). Disintegration of a liquid jet. *N.A.C.A, Technical Memorandum No. 659*. [16](#)
- HE, L. & RUIZ, F. (1995). Effect of cavitation on flow and turbulence in plain orifices for high-speed atomization. *Atomization and Sprays*, **5**, 569–584. [28](#)
- HENRY, M. & COLLICOTT, S. (2000). Visualization of internal flow in a cavitating slot orifice. *Atomization and Sprays*, **10**, 545–563. [26](#)
- HIROYASU, H. (1991). Experimental and theoretical studies on the structure of fuel sprays in diesel engines. *proceedings of the International Conference on Liquid Atomization and Spray Systems (ICLASS 91)*, **Gaithersburg, Maryland, 15-18 July**, 17–31. [4](#)
- HIROYASU, H. (2000). Spray breakup mechanism from the hole-type nozzle and its applications. *Atomization and Sprays*, **10**, 511–527. [26](#), [135](#)
- HIROYASU, H., SHIMIZU, M. & ARAI, M. (1982). The breakup of high speed jet in a high pressure gaseous atmosphere. *Proceedings of ICLASS-82*. [18](#)
- HIROYASU, H., ARAI, M. & SHIMIZU, M. (1991). Break-up length of a liquid jet and internal flow in a nozzle. *Proceedings of the International Conference on Liquid Atomization and Spray Systems (ICLASS 91)*, **Gaithersburg, Maryland, 15-18 July**, 275–282. [22](#), [26](#), [28](#)
- ITO, H. (1960). Pressure losses in smooth pipe bends. *J. Basic Eng*, **82**, 43. [59](#)
- IYER, V. & ABRAHAM, J. (1997). Penetration and dispersion of transient gas jets and sprays. *Combustion Science and Technology*, **130**, 315–334. [21](#)

REFERENCES

- JOUSSELLIN, F., DELANNOY, Y., SAUVAGE-BOUTAR, E. & GOIRAND, B. (1991). Experimental investigations on unsteady attached cavities. *ASME FED*, **116**, 61–66. [38](#)
- KARASAWA, T., TANAKA, M., ABE, K., SHIGA, S. & KURABAYASHI, T. (1992). Effect of nozzle configuration on the atomization of a steady spray. *Atomization and Sprays*, vol **2**, 411–426. [19](#), [20](#)
- KAWANAMI, Y., KATO, H., YAMAGUCHI, H., TANIMURA, M. & TAGAYA, Y. (1997). Mechanism and control of cloud cavitation. *Journal of fluids engineering*, **119**, 788. [38](#), [39](#), [41](#), [119](#)
- KENT, J. & BROWN, G. (1982). Nozzle exit flow characteristics for square-edged and rounded inlet geometries. *Combustion Science and Technology*, **30**, 121–132. [19](#), [20](#)
- KIM, J., NISHIDA, K., YOSHIKAWA, T. & HIROYASU, H. (1997). Characterization of flows in the sac chamber and the discharge hole of a d.i. diesel injection nozzle by using a transparent model nozzle. *SAE Technical Paper*, **972942**. [34](#), [35](#)
- KLINE, S. & MCCLINTOCK, F. (1953). Describing uncertainties in single-sample experiments. *Mechanical engineering*, **75**, 3–8. [98](#)
- KNAPP, R. (1955). Recent investigations of the mechanics of cavitation and cavitation damage. *Trans. ASME*, **77**, 1045–1054. [36](#), [37](#)
- KNAPP, R. (1957). *Investigation of the Mechanics of Cavitation and Cavitation Damage*. California Institute of Technology, Hydrodynamics Laboratory. [35](#)
- KNAPP, R., DAILY, J. & HAMMITT, F. (1970). *Cavitation*. McGraw-Hill New York. [5](#)
- KNOX-KELECY, A. (1992). *Turbulent Flow in a Scale Model of a Diesel Fuel Injector Nozzle Hole*. Ph.D. thesis, University of Wisconsin. [21](#)
- KNOX-KELECY, A. & FARRELL, P. (1992). Internal flow in a scale model of a diesel fuel injector nozzle. *SAE Technical paper*, **922308**. [21](#)

REFERENCES

- KNOX-KELECY, A. & FARRELL, P. (1993). Spectral characteristics of turbulent flow in a scale model of a diesel fuel injector nozzle. *SAE Technical Paper*, **930924**. [21](#)
- KUBOTA, A., KATO, H., YAMAGUCHI, H. & MAEDA, M. (1989). Unsteady structure measurement of cloud cavitation on a foil section using conditional sampling technique. *Journal of fluids engineering*, **111**, 204–210. [37](#), [40](#)
- KUEHN, R. (1925). Atomization of liquid fuels. *N.A.C.A, T.M. Nos.* **329**, **330**, **331**. [15](#), [16](#)
- LABERTEAUX, K. & CECCIO, S. (2001a). Partial cavity flows. part 1. cavities forming on models without spanwise variation. *Journal of Fluid Mechanics*, **431**, 1–41. [39](#)
- LABERTEAUX, K. & CECCIO, S. (2001b). Partial cavity flows. part 2. cavities forming on test objects with spanwise variation. *Journal of Fluid Mechanics*, **431**, 43–63. [40](#)
- LAUTERBORN, W. & OHL, C. (1997). The peculiar dynamics of cavitation bubbles. *Applied scientific research*, **58**, 63–76. [82](#)
- LE, Q., FRANC, J. & MICHEL, J. (1993). Partial cavities: global behavior and mean pressure distribution. *Journal of fluids engineering*, **115**, 243–248. [37](#), [38](#), [40](#), [113](#), [116](#), [119](#), [127](#)
- LEE, D. (1933). The effect of nozzle design and operating conditions on the atomization and distribution of fuel sprays. *N.A.C.A, Report No.* **425**. [15](#), [21](#)
- LEE, D. & SPENCER, R. (1934). Photomicrographic studies of fuel sprays. *N.A.C.A, Report No.* **454**. [15](#), [16](#)
- LEFEBVRE, A. (1989). *Atomization and sprays (Combustion: An International Series)*. Hemisphere Publishing Corporation. [1](#)
- LEROUX, J. (2004). An experimental study of unsteady partial cavitation. *Journal of fluids engineering*, **126**, 94. [39](#), [41](#)

REFERENCES

- LEROUX, J., COUTIER-DELGOSHA, O. & ASTOLFI, J. (2005). A joint experimental and numerical study of mechanisms associated to instability of partial cavitation on two-dimensional hydrofoil. *Physics of Fluids*, **17**, 052101. [39](#)
- LICHTAROWICZ, A., DUGGINS, R. & MARKLAND, E. (1965). Discharge coefficients for incompressible non-cavitating flow through long orifices. *Journal Mechanical Engineering Science*, **Vol 7**, 210–219. [32](#), [58](#), [109](#), [132](#)
- LIM, W., CHEW, Y., CHEW, T. & LOW, H. (1994). Particle image velocimetry in the investigation of flow past artificial heart valves. *Annals of biomedical engineering*, **22**, 307–318. [72](#)
- MARCER, R. & LEGOUEZ, J. (2001). Simulation of unsteady cavitating flows in diesel injector with an improved VOF-method. In *Proc of 17th ILASS-Eu Conf.* [19](#)
- MCCARTHY, M. & MOLLOY, N. (1974). Review of stability of liquid jets and the influence of nozzle design. *The Chemical Engineering Journal*, **7**, 1–20. [18](#), [22](#)
- MCKENNEY, E. & BRENNEN, C. (1994). On the dynamics and acoustics of cloud cavitation on an oscillating hydrofoil. In *ASME*, 190, 195–202, American Society of Mechanical Engineers. [39](#)
- MILLER, H. & BEARDSLEY, E. (1926). Spray penetration with a simple fuel injection nozzle. *NACA, Report No. 222*. [15](#), [21](#)
- MILLER, P., DANIELSON, K., MOODY, G., SLIFKA, A., DREXLER, E. & HERTZBERG, J. (2006). Matching index of refraction using a diethyl phthalate/ethanol solution for in vitro cardiovascular models. *Experiments in Fluids*, **41**, 375–381. [70](#), [72](#)
- MIRCHANDANI, G. (2011). Spectral analysis in matlab - part ii. *Laboratory notes for Digital Signal Processing, The University of Vermont*. [90](#)
- NARROW, T., YODA, M. & ABDEL-KHALIK, S. (2000). A simple model for the refractive index of sodium iodide aqueous solutions. *Experiments in Fluids*, **28**, 282–283. [71](#)

REFERENCES

- NOURI, J., MITROGLOU, N., YAN, Y. & ARCOUMANIS, C. (2007). Internal flow and cavitation in a multi-hole injector for gasoline direct-injection engines. *SAE Technical Paper*, **2007-01-1405**. [35](#)
- NURICK, W. (1976). Orifice cavitation and its effect on spray mixing. *Journal of Fluids Engineering*, **98**, 681–687. [13](#), [31](#), [132](#), [133](#)
- OHRN, T., SENSER, D. & LEFEBVRE, A. (1991a). Geometric effects on spray cone angle for plain-orifice atomizers. *Atomization and Sprays*, **Vol 1**, 253–268. [19](#), [23](#)
- OHRN, T., SENSER, D. & LEFEBVRE, A. (1991b). Geometrical effects on discharge coefficients for plain-orifice atomizers. *Atomization and Sprays*, **1**. [33](#)
- PATIL, K., TRIPATHI, A., PATHAK, G. & KATTI, S. (1991). Thermodynamic properties of aqueous electrolyte solutions. 2. Vapor pressure of aqueous solutions of sodium bromide, sodium iodide, potassium chloride, potassium bromide, potassium iodide, rubidium chloride, cesium chloride, cesium bromide, cesium iodide, magnesium chloride, calcium chloride, calcium bromide, calcium iodide, strontium chloride, strontium bromide, strontium iodide, barium chloride, and barium bromide. *Journal of Chemical and Engineering Data*, **36**, 225–230. [75](#)
- PAYRI, F., BERMUDEZ, V., PAYRI, R. & SALVADOR, F. (2004). The influence of cavitation on the internal flow and the spray characteristics in diesel injection nozzles. *Fuel*, **83**, 419–431. [28](#), [33](#), [87](#), [133](#)
- PAYRI, R., GARCIA, J., SALVADOR, F. & GIMENO, J. (2005). Using spray momentum flux measurements to understand the influence of diesel nozzle geometry on spray characteristics. *Fuel*, **Vol. 84**, 551–561. [33](#)
- PAYRI, R., SALVADOR, F., GIMENO, J. & ZAPATA, L. (2008). Diesel nozzle geometry influence on spray liquid-phase fuel penetration in evaporative conditions. *Fuel*, **87**, 1165–1176. [33](#)

REFERENCES

- PEARCE, I. & LICHTAROWICZ, A. (1971). Discharge performance of long orifices with cavitating flow. In *Proceedings of the 2nd Fluid Power Symposium*, vol. 2, 13–35. [30](#), [31](#)
- PHAM, T., LARRARTE, F. & FRUMAN, D. (1999). Investigation of unsteady sheet cavitation and cloud cavitation mechanisms. *Journal of fluids engineering*, **121**, 289. [38](#), [119](#)
- PLATEAU, J. (1945). Statique experimentale et theorique des liquides soumis aux seules forces moleculaires. In L. Rayleigh, ed., *Theory of Sound*, vol. Vol. II, Dover, New York. [15](#)
- PLESSET, M. (1949). The dynamics of cavitation bubbles. *Trans. ASME J. Appl. Mechanics*, **16**, 228–231. [11](#)
- RAMAMURTHI, K. & PATNAIK, S. (2002). Influence of periodic disturbances on inception of cavitation in sharp-edged orifices. *Experiments in Fluids*, **33**, 720–727. [26](#)
- RAMAMURTHI, K., NANDAKUMAR, K., SHANKAR, S. & PATNAIK, R. (2001). Hysteresis and bifurcation of flow in fuel injector nozzles. *Proc Inst Mech Eng*, **215**, 49–59. [26](#), [135](#)
- RANDALL, L. (1952). Rocket applications of the cavitating venturi. *American Rocket Society Journal*, **January-February**, 28–31. [31](#)
- RANDALL, R. (1987). *Frequency Analysis*. Brüel & Kjær, 3rd edn. [91](#)
- RANZ, W. (1958). Some experiments on orifice sprays. *Can J. Chem. Engng*, **August**, 175–181. [17](#)
- RAY, S. (2002). *High speed photography and photonics*. SPIE - The International Society for Optical Engineering. [82](#)
- RAYLEIGH, L. (1917). On the pressure development in a liquid during the collapse of a spherical cavity. *Phil. Mag.*, **Vol. 34**, pp. 94–98. [11](#), [15](#)

REFERENCES

- REESE, J., CHEN, R. & FAN, L. (1995). Three-dimensional particle image velocimetry for use in three-phase fluidization systems. *Experiments in Fluids*, **19**, 367–378. [71](#)
- REISMAN, G. & BRENNEN, C. (1996). Pressure pulses generated by cloud cavitation. *Proc. ASME Symp. on Cavitation and Gas-Liquid Flows in Fluid Machinery and Devices. FED Vol. 236*, 319–328. [39](#)
- REISMAN, G., WANG, Y. & BRENNEN, C. (1998). Observations of shock waves in cloud cavitation. *Journal of Fluid Mechanics*, **355**, 255–283. [39](#), [41](#)
- REITZ, R. & BRACCO, F. (1979a). On the dependence of spray angle and other spray parameters on nozzle design and operating conditions. *SAE Technical Paper*. [22](#), [28](#)
- REITZ, R. & BRACCO, F. (1979b). Ultra-high-speed filming of atomizing jets. *Physics of Fluids*, **22**, 1054. [22](#)
- REITZ, R.D. & BRACCO, F. (1982). Mechanisms of atomization of a liquid jet. *Phys. Fluids*, **25**, 1730–1742. [16](#), [17](#), [18](#), [19](#), [21](#), [22](#)
- ROTH, H., GAVAISES, M. & ARCOUMANIS, C. (2002). Cavitation initiation, its development and link with flow turbulence in diesel injector nozzles. *SAE TRANSACTIONS*, **111**, 561–580. [29](#), [35](#)
- ROTH, H., GIANNADAKIS, E., GAVAISES, M., ARCOUMANIS, C., OMAE, K., SAKATA, I., NAKAMURA, M. & YANAGIHARA, H. (2005). Effect of multi-injection strategy on cavitation development in diesel injector nozzle holes. *SAE transactions*, **114**, 1029–1045. [35](#)
- RUIZ, F. (1991). A few useful relations for cavitating orifices. *Proceedings of the International Conference on Liquid Atomization and Spray Systems (ICLASS 91)*, Gaithersburg, Maryland, 15-18 July, 595–602. [33](#)
- RUIZ, F. & HE, L. (1999). Turbulence Under Quasi-cavitating Conditions: A New Species? *Atomization and Sprays*, **9**, 419–430. [28](#)

REFERENCES

- SAKODA, M., YAKUSHIJI, R., MAEDA, M. & YAMAGUCHI, H. (2001). Mechanism of cloud cavitation generation on a 2-d hydrofoil. In *4th International Symposium on Cavitation*. 38
- SATO, K. & SAITO, Y. (2002). Unstable cavitation behavior in a circular-cylindrical orifice flow. *JSME International Journal Series B*, **45**, 638–645. 38, 40, 41, 42, 103, 107, 108, 127
- SCHLICHTING, H. (1968). *Boundary-layer theory*. McGraw-Hill, 6th edn. 58, 109
- SCHMIDT, D. & CORRADINI, M. (1997). Analytical prediction of the exit flow of cavitating orifices. *Atomization and Sprays*, **Vol. 7**, 603–616. 33
- SCHMIDT, D. & CORRADINI, M. (2001). The internal flow of diesel fuel injector nozzles: a review. *Int. J. Engine Research*, **Vol. 2**, 1–22. 22, 23, 33
- SCHMIDT, D., SU, T.F., GONEY, K., FARRELL, P. & CORRADINI, M. (1995). Detection of cavitation in fuel injector nozzles. In *8th ISTP Conference, San Francisco, California*, 1521–1532. 33
- SCHWEITZER, P.H. (1937). Mechanism of disintegration of liquid jets. *Journal of Applied Physics*, **8**, 513–521. 17
- SOTERIOU, C., ANDREWS, R. & SMITH, M. (1995). Direct injection diesel sprays and the effect of cavitation and hydraulic flip on atomization. *SAE Technical Paper*, **950080**. 24, 28, 31, 33, 34, 139
- SOTERIOU, C., ANDREWS, R. & SMITH, M. (1999). Further studies of cavitation and atomization in diesel injection. *SAE Technical Paper*, **1999-01-1486**. 24, 25, 61
- SOU, A., HOSOKAWA, S. & TOMIYAMA, A. (2006). Cavitation in a two-dimensional nozzle and liquid jet atomization. *JSME International Journal, Series B*, **49**, 1253–1259. 28, 29
- SOU, A., HOSOKAWA, S. & TOMIYAMA, A. (2007). Effects of cavitation in a nozzle on liquid jet atomisation. *International Journal of Heat and Mass Transfer*, **50**, 3575–3582. 29, 129, 139

REFERENCES

- SOU, A., MAULANA, M., HOSOKAWA, S. & TOMIYAMA, A. (2008). Ligament formation induced by cavitation in a cylindrical nozzle. *Journal of Fluid Science and Technology*, **3**, 633–644. [29](#)
- SOU, A., HOSOKAWA, S. & TOMIYAMA, A. (2010). Cavitation in nozzles of plain orifice atomizers with various length-diameter-ratios. *Atomization and Sprays*, **20**. [85](#)
- SPIKES, R. & PENNINGTON, G. (1959). Discharge coefficient of small submerged orifices. *Proceedings of the Institution of Mechanical Engineers*, **173**, 661–674. [30](#), [31](#)
- STERN, F., MUSTE, M., BENINATI, M. & EICHINGER, W. (1999). Summary of Experimental Uncertainty Assessment Methodology with Example. *IIHR Report, Iowa Institute of Hydraulic Research, The University of Iowa, Iowa City, IA*. [96](#)
- STUTZ, B. & REBOUD, J. (1997a). Experiments on unsteady cavitation. *Experiments in fluids*, **22**, 191–198. [39](#), [127](#)
- STUTZ, B. & REBOUD, J. (1997b). Two-phase flow structure of sheet cavitation. *Physics of Fluids*, **9**, 3678. [39](#)
- SUGIMOTO, Y. & SATO, K. (2009). Visualization of unsteady behavior of cavitation in circular cylindrical orifice with abruptly expanding part. *The 13th International Topical Meeting on Nuclear Reactor Thermal Hydraulics*. [38](#), [42](#)
- SUH, H.K., PARK, S.H. & LEE, C.S. (2008). Experimental investigation of nozzle cavitating flow characteristics for diesel and biodiesel fuels. *International Journal of Automotive Technology*, **9**, 217–224. [26](#)
- TAMAKI, N., SHIMIZU, M., NISHIDA, K. & HIROYASU, H. (1998). Effects of cavitation and internal flow on atomization of a liquid jet. *Atomization and Sprays*, **3**, pp.179–197. [28](#)
- TAYLOR, G. (1963). Generation of ripples by wind blowing over a viscous fluid. *The Scientific Papers of G.I. Taylor*, **Vol. 3**. [16](#)

REFERENCES

- UZOL, O., CHOW, Y., KATZ, J. & MENEVEAU, C. (2002). Unobstructed particle image velocimetry measurements within an axial turbo-pump using liquid and blades with matched refractive indices. *Experiments in Fluids*, **33**, 909–919. [71](#), [73](#)
- WADE, R. & ACOSTA, A. (1966). Experimental observations on the flow past a plano-convex hydrofoil. *ASME J. Basic Eng*, **88**, 273–283. [37](#)
- WEBER, C. (1931). Disintegration of liquid jets. *Z. Angew. Math. Mech.*, **11**, 136–154. [15](#)
- WELCH, P. (1967). The use of fast fourier transform for the estimation of power spectra: a method based on time averaging over short, modified periodograms. *Audio and Electroacoustics, IEEE Transactions on*, **15**, 70–73. [92](#)
- WU, K., REITZ, R. & BRACCO, F. (1986). Measurements of drop size at the spray edge near the nozzle in atomizing liquid jets. *Physics of Fluids*, **29**, 941. [22](#)
- WU, K.J., SU, C.C., STEINBERGER, R., SANTAVICCA, D. & BRACCO, F. (1983). Measurement of the spray angle of atomizing jets. *Trans. ASME J. Fluids Eng.*, **Ser. I**, 406–413. [18](#), [27](#), [28](#)
- YOUNG, W. & BUDYNAS, R. (2002). *Roark's Formulas for Stress and Strain*. London: McGrath-Hill, New York, 7th edn. [53](#)